amU
Aix Marseille Université

NNT : 2025AIXM0000

# THÈSE DE DOCTORAT

Soutenue à AMU — Aix-Marseille Université
le 22 janvier 2026 par


## Xiangyi LI


# Widefield linear and non-linear optical microscopies using random illumination and temporal focusing

**Discipline**
Physique et science de la Matière

**Spécialité**
Optique, Photonique et Traitement d'Image

**École doctorale**
ED 352 Physique et science de la matière

**Laboratoire/Partenaires de recherche**
CBI (Toulouse)
LS2N (Nantes)

**Composition du jury**

| | |
|---|---|
| Marc Guillon<br>SPPIN, Université Paris Cité, Paris | Rapporteur |
| Eirini Papagiakoumou<br>Institute De La Vision, CNRS, Sorbonne Université, Paris | Rapporteure |
| Hilton Barbosa de Aguiar<br>Kastler Brossel Laboratory, CNRS, ENS Paris | Examinateur |
| Martin Oheim<br>SPPIN, CNRS, Paris | Président du jury |
| Hervé Rigneault<br>Institut Fresnel, CNRS, Marseille | Examinateur |
| Anne Sentenac<br>Institut Fresnel, CNRS, Marseille | Directrice de thèse |


INSTITUT FRESNEL
CBI Toulouse Centre de Biologie Intégrative
Funded by the European Union
erc European Research Council Established by the European Commission
cnrs

# Affidavit

Je soussignée, Xiangyi Li, déclare par la présente que le travail présenté dans ce manuscrit est mon propre travail, réalisé sous la direction scientifique d'Anne Sentenac, dans le respect des principes d'honnêteté, d'intégrité et de responsabilité inhérents à la mission de recherche. Les travaux de recherche et la rédaction de ce manuscrit ont été réalisés dans le respect à la fois de la charte nationale de déontologie des métiers de la recherche et de la charte AMU relative à la lutte contre le plagiat.

Ce travail n'a pas été précédemment soumis en France ou à l'étranger dans une version identique ou similaire à un organisme examinateur.

Fait à Marseille le 4 novembre 2025

LI Xiangyi

# Liste de publications et participation aux conférences

## Liste des publications et brevets réalisées dans le cadre du projet de thèse :

1. "Optical sectioning in wide-field two-photon microscopy using temporal focusing and random illumination", under review by Optics Letters, Xiangyi Li, Federico Vernuccio, Michal Marynowski, Assia Benachir, Sandro Heuke, Herve Rigneault, and Anne Sentenac
2. "Super-resolved live imaging of thick biological samples with 3D Random Illumination Microscopy (3D-RIM)", under review by Nature Methods, Thomas Mangeat, Lorry Mazzella, Benoît Rogez, Guillaume Giroussens, Xiangyi Li, Mathilde Bernard, Pablo Vargas, Marc Allain, Simon Labouesse, Jérôme Idier, Loïc LeGoff, and Anne Sentenac
3. "Speckle illumination temporal focusing two-photon excited fluorescence microscopy", under review by Optica, Federico Vernuccio, Michal Marynowski, Xiangyi Li, Assia Benachir, Luca Genchi, Randy Bartels, Sandro Heuke, Anne Sentenac, and Hervé Rigneault
4. "Widefield two-photon random illumination microscopy (2P-RIM)", under review by Light : Science & Applications, Assia Benachir, Xiangyi Li, Eric M. Fantuzzi, Guillaume Giroussens, Thomas Mangeat, Federico Vernuccio, Hervé Rigneault, Anne Sentenac, and Sandro Heuke

## Participation aux conférences et écoles d'été au cours de la période de thèse :

1. Optica Imaging Congress 2024 : "Improving Optical Sectioning in Wide-field Two-Photon Excitation Microscopy using Random Illumination"- Oral presentation

# Résumé

La microscopie optique à grand champ, dans laquelle l'échantillon entier est éclairé en une seule fois et l'image est enregistrée par une caméra, est largement utilisée pour observer des structures micrométriques et submicrométriques en raison de sa rapidité, de sa robustesse et de son impact minimal sur les échantillons. Cependant, elle souffre de deux limitations majeures : une résolution transversale limitée (au mieux, la moitié de la longueur d'onde) et, plus grave encore, l'absence de sectionnement optique. Comme l'échantillon est également éclairé en profondeur, la lumière provenant des plans défocalisés dégrade le contraste de l'image, rendant cette technique inefficace pour les échantillons épais. Cette thèse explore comment les éclairages par speckle aléatoire et la focalisation temporelle peuvent introduire le sectionnement optique dans la microscopie à grand champ, en particulier pour la microscopie à fluorescence à excitation à un et deux photons et pour l'imagerie non linéaire.

Tout d'abord, ces travaux portent sur la microscopie à illumination aléatoire (RIM) pour la fluorescence à photon unique. La RIM est une méthode de microscopie à champ large qui utilise la variance de plusieurs images acquises sous différents motifs de speckle pour reconstruire numériquement une image à super-résolution, sectionnée optiquement. Alors que la RIM a été initialement développée pour l'imagerie 2D, cette thèse étend l'algorithme à la 3D, en introduisant une procédure de déconvolution itérative adaptée aux images comportant peu de plans optiques. L'approche 3D offre une meilleure résolution et un meilleur contraste que la reconstruction 2D tranche par tranche.

Ensuite, l'étude aborde la microscopie à fluorescence à excitation à deux photons (2PM), qui repose généralement sur le balayage d'un faisceau fortement focalisé pour obtenir une résolution submicrométrique et un sectionnement optique. Cependant, la modalité de balayage s'avère lente lors de l'imagerie de grands champs de vision. Pour surmonter ce problème, nous avons étendu les principes de la RIM à la microscopie à deux photons à champ large (2PE-RIM). Nous démontrons théoriquement et expérimentalement une amélioration de la résolution et du sectionnement optique. Une deuxième approche a consisté à développer un nouveau schéma d'excitation pour la modalité de balayage. Nous avons montré qu'un faisceau concentré et moucheté est capable de former un volume d'excitation 2P avec une largeur transversale et une largeur axiale de quelques micromètres. Ce schéma d'illumination est susceptible de fournir des balayages plus rapides de grands champs de vision (au prix d'une résolution réduite).

Dans le troisième chapitre, nous explorons également le potentiel de la focalisation temporelle (TF) pour générer des coupes optiques en microscopie à champ large non linéaire. Pour créer un faisceau focalisé temporellement, une impulsion est envoyée

sur un réseau et les longueurs d'onde dispersées sont recombinées de manière à ce que leur interférence ne soit constructive qu'au niveau du plan focal. Alors que le TF à réseau standard nécessite un fort grossissement, sa combinaison avec un éclairage par speckle aléatoire (TF à réseau rugueux) permet un sectionnement optique au niveau micrométrique à faible grossissement, adapté aux grands champs de vision. Nous avons montré que la combinaison du TF à réseau rugueux avec le RIM améliorait à la fois les résolutions transversale et axiale de la 2PM à champ large.

Enfin, nous avons étudié l'intérêt de l'illumination TF pour la microscopie par diffusion Raman anti-Stokes cohérente (CARS), une technique sans marquage permettant d'étudier des liaisons chimiques spécifiques. Nous avons démontré théoriquement et expérimentalement qu'en focalisant temporellement les faisceaux de pompage et Stokes, nous pouvions obtenir des images CARS à section optique dans une configuration à champ large.

Mots clés : Microscopie non linéaire, Super résolution, Focalisation temporelle, Microscopie à deux photons, Coupe optique, Microscopie à diffusion Raman anti-Stokes cohérente

# Abstract

Wide-field optical microscopy, in which the whole sample is illuminated in one shot and the image is recorded on a camera, is widely used for observing micrometric and submicrometric structures due to its speed, robustness, and minimal impact on samples. However, it suffers from two major limitations: limited transverse resolution (at best, half the wavelength) and, more critically, a lack of optical sectioning. Because the sample is also illuminated in depth, light from out-of-focus planes degrades image contrast, making the technique ineffective for thick samples. This thesis explores how random speckle illuminations and temporal focusing can introduce optical sectioning in wide-field microscopy, particularly for one and two-photon excitation fluorescence microscopy and for nonlinear imaging.

First, the work investigates Random Illumination Microscopy (RIM) for one-photon fluorescence. RIM is a widefield microscopy method that uses the variance of multiple images acquired under different speckle patterns to numerically reconstruct a super-resolved, optically sectioned image. While RIM was originally developed for 2D imaging, this thesis extends the algorithm to 3D, introducing an iterative deconvolution procedure tailored for images with few optical planes. The 3D approach yields better resolution and contrast than slice-by-slice 2D reconstruction.

Next, the study addresses two-photon excitation fluorescence microscopy (2PM), which typically relies on scanning a tightly focused beam for sub-micrometer resolution and optical sectioning. However, the scanning modality proves slow when imaging large fields of view. To overcome this issue, we extended RIM principles to two-photon wide-field microscopy (2PE-RIM) . We theoretically and experimentally demonstrate an improved resolution and optical sectioning. A second approach consisted in developing a novel excitation scheme for the scanning modality. We showed that a focused speckled beam is able to form a 2P excitation volume with a transverse width and axial width of a few micrometers. This illumination scheme is susceptible to provide faster scans of large fields of view (at the cost of a reduced resolution).

In the third chapter, we also explore the potential of Temporal Focusing (TF), for generating optical sectioning in non-linear widefield microscopy. To create a temporally focused beam, a pulse is sent onto a grating and the dispersed wavelengths are recombined in such a way that their interference are constructive only at the focal plane. While standard grating-TF requires high magnification, combining it with random speckle illumination (roughness-grating TF) enables micrometer-level optical sectioning at low magnification, suitable for large fields of view. We showed that combining roughness-grating TF with RIM improved both the transverse and axial resolutions of widefield 2PM.

Finally, we studied the interest of TF illumination for Coherent Anti-Stokes Raman

Scattering (CARS) microscopy, a label-free technique for probing specific chemical bonds. We showed theoretically and experimentally that by temporally focusing both the pump and Stokes beams, we could obtain optically sectioned CARS images in a widefield configuration.

Keywords: Non-linear microscopy, Super-resolution, Temporal focusing, Two-photon microscopy, Optical sectioning, Coherent anti-Stokes Raman scattering microscopy

# Résumé étendu en Français

La microscopie optique est l'outil le plus utile en biologie, dans les domaines des matériaux ou de la médecine pour observer des échantillons à l'échelle (sub)micrométrique en raison de sa facilité d'utilisation, de sa résolution et de sa capacité à observer l'intérieur des échantillons (lorsqu'ils sont suffisamment transparents) sans être invasive. Au cours des trente dernières années, de nombreuses modalités de microscopie ont été développées, soit pour être sensibles à de nouveaux contrastes (indice de réfraction, susceptibilités non linéaires, fluorescence, polarisation), soit pour améliorer sa résolution. Quelle que soit l'approche choisie, l'amélioration de la capacité de sectionnement optique du microscope est une question clé qui a suscité beaucoup d'attention. Le sectionnement optique en microscopie est la capacité à obtenir une image des structures appartenant à un plan spécifique (essentiellement le plan focal) d'un échantillon épais sans avoir besoin de le découper physiquement. Il est obtenu en rejetant physiquement ou numériquement le signal provenant des régions hors foyer. Sans sectionnement optique, le signal hors foyer et le bruit qui lui est associé polluent l'image des structures dans le foyer. Pour certains échantillons épais, le signal hors foyer peut être si élevé qu'il rend l'image incompréhensible.

Une façon de vérifier si un microscope présente un sectionnement optique consiste à enregistrer les images d'une fine couche homogène lorsque celle-ci est placée à différentes distances du plan focal. Si les images enregistrées ne dépendent pas de la position de la couche, il n'y a pas de sectionnement optique. Dans la configuration de microscopie à champ large, chaque plan transversal de l'espace échantillon est éclairé de manière homogène avec la même puissance. Évidemment, avec cette définition, la microscopie à champ large à excitation par photon unique, 1PM, (ainsi que les microscopes à transmission standard) ne dispose pas de sectionnement optique. La fluorescence émise par la couche homogène (ou l'intensité transmise) étant proportionnelle à la puissance d'éclairage (VALEUR 2002 ; LAKOWICZ 2006), l'image sera la même quelle que soit la position de la couche le long de l'axe optique.

De nombreuses techniques différentes ont été proposées pour améliorer la capacité de sectionnement optique de la microscopie, en particulier pour la microscopie à un photon. Afin de réduire physiquement le signal provenant des zones défocalisées, des techniques de balayage ont été développées. Elles consistent à focaliser un faisceau à l'intérieur de l'échantillon sous la forme d'un point (microscopie confocale (PAWLEY 2006)) ou d'une ligne (IM et al. 2005) et à limiter la détection du signal à un détecteur à seau couvrant un domaine conjugué à la zone excitée. En microscopie non linéaire, lorsque le signal enregistré n'est pas proportionnel à la puissance d'illumination (microscopie à fluorescence à excitation deux photons, génération de seconde harmonique, diffusion Raman stimulée, diffusion Raman anti-Stokes cohérente...), la plupart

des implémentations consistent à balayer une illumination focalisée. Contrairement à la microscopie linéaire, telle que la 1PM, la non-linéarité de l'excitation permet d'obtenir un sectionnement optique même sans limiter la détection à la région excitée. Le détecteur à seau recueille autant que possible le signal émis.

Malheureusement, l'amélioration de la capacité de sectionnement optique apportée par la modalité de balayage s'accompagne d'une détérioration des performances du microscope en termes de vitesse et de phototoxicité. En effet, pour réduire le temps d'acquisition d'une image, il faut scanner plus rapidement. Pour obtenir un rapport signal/bruit suffisant avec un temps d'intégration plus court, il faut augmenter la puissance d'éclairage. Or, pour maintenir une phototoxicité raisonnable, il faut maintenir la puissance en dessous d'un certain seuil. Ainsi, les méthodes de balayage sont intrinsèquement limitées à l'imagerie rapide de petits champs de vision ou à l'imagerie lente de grands champs de vision.

Pour contourner cette limitation, d'autres approches utilisant des éclairages étendus couvrant l'ensemble de l'échantillon et la détection par caméra ont été proposées pour permettre le sectionnement optique.

Une technique populaire consiste à limiter l'éclairage à une fine couche autour du plan d'intérêt de l'échantillon à l'aide d'une feuille de lumière (STELZER et al. 2021). Cependant, cela nécessite une mise en œuvre complexe avec deux objectifs qui n'est pas toujours adaptée aux échantillons étudiés. Plus récemment, des méthodes qui rejettent numériquement le signal hors foyer ont démontré leur intérêt tant pour l'imagerie 1PM (VENTALON et al. 2005) que pour l'imagerie CARS non linéaire (FANTUZZI et al. 2023). En enregistrant plusieurs images de l'échantillon sous des éclairages périodiques/aléatoires (comme dans la microscopie à éclairage structuré ou la microscopie à éclairage aléatoire), une reconstruction optiquement sectionnée peut être obtenue grâce à divers traitements numériques (GUSTAFSSON et al. 2008; VENTALON et al. 2005; MANGEAT et al. 2021; FANTUZZI et al. 2023). De plus, ces approches améliorent considérablement les résolutions transversale et axiale par rapport aux approches par balayage ou par feuille de lumière. Cependant, elles sont ralenties par la nécessité d'enregistrer plusieurs images et peuvent échouer lorsque le bruit lié au signal défocalisé de chaque image brute est trop important pour que la reconstruction numérique aboutisse. Enfin, une technique qui n'est adaptée qu'à l'excitation non linéaire a montré son intérêt : la focalisation temporelle (TF). La TF permet de former une impulsion lumineuse dont la durée varie au fur et à mesure de sa propagation. Une courte durée au niveau du plan focal et une longue durée à l'extérieur induisent un pic d'excitation localisé dans une couche autour du plan focal. À notre connaissance, cette approche a été essentiellement mise en œuvre dans la microscopie à fluorescence à excitation deux photons (2PM) pour les petits champs de vision (quelques dizaines de microns) (Michael E DURST et al. 2006; ORON et SILBERBERG 2005; PAPAGIAKOUMOU, RONZITTI et al. 2020).

L'objectif de cette thèse est de proposer des solutions pour améliorer le sectionnement optique des microscopies linéaires (1PM) et non linéaires (imagerie 2PM et CARS) qui sont spécifiquement adaptées à l'imagerie rapide de grands champs de vision. Mon travail a été essentiellement théorique et numérique, mais la plupart des

analyses et des simulations sont accompagnées de résultats expérimentaux obtenus par Assia Benachir et Federico Vernuccio à l'Institut Fresnel et par Thomas Mangeat au CBI à Toulouse. La thèse est divisée en quatre chapitres.

Dans le premier chapitre, je me concentre sur l'approche de la microscopie à illumination aléatoire (RIM). La RIM consiste à enregistrer plusieurs images à basse résolution sous un éclairage aléatoire moucheté et fournit une reconstruction optiquement sectionnée à super-résolution à partir de la variance des images brutes (MANGEAT et al. 2021 ; GIROUSSENS et al. 2024). La reconstruction est basée sur un algorithme de correspondance des écarts types qui dépend uniquement de la fonction d'étalement du point d'observation et de l'autocorrélation des taches. Au départ, le modèle RIM supposait que l'échantillon et l'éclairage étaient bidimensionnels, le signal hors foyer étant considéré comme du bruit. La reconstruction 3D de l'échantillon a été obtenue en empilant des coupes reconstruites en 2D, comme le montre la Fig. 1. Dans la première partie, j'ai adapté la technique RIM à la microscopie à excitation deux photons (2PM). Cette tâche a nécessité l'étude de l'autocorrélation de l'intensité d'excitation deux photons, qui est proportionnelle au carré de l'intensité lumineuse. Les reconstructions RIM sur des images speckle expérimentales à deux photons ont montré que cette technique permet d'obtenir des images sectionnées optiquement avec une résolution supérieure à celle des approches de balayage standard dans une configuration à champ large. Dans la deuxième partie, j'ai amélioré l'algorithme de reconstruction RIM (GIROUSSENS et al. 2024) en tenant compte de la nature 3D de l'échantillon et du modèle de formation d'image, suivant les développements de Guillaume Giroussens. Il est démontré que la version 3D de l'algorithme RIM permet d'obtenir des reconstructions 3D mieux contrastées et mieux résolues que la version 2D.

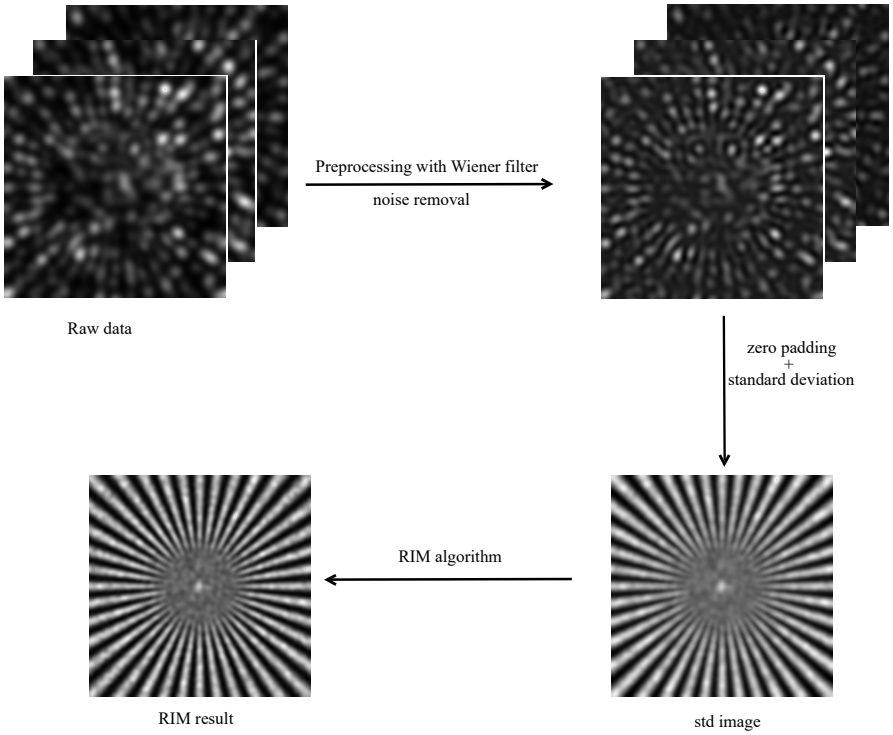


FIGURE 1 – Procédé RIM

Au chapitre 2, nous avons proposé d'adapter le balayage 2PM à l'imagerie rapide de grands champs de vision. Le balayage 2PM a été introduit comme alternative au 1PM confocal pour l'imagerie en profondeur d'échantillons hétérogènes. Premièrement, son éclairage infrarouge peut se focaliser plus profondément dans les échantillons biologiques que la lumière visible du 1PM confocal. Deuxièmement, grâce au processus d'excitation non linéaire, le sectionnement optique est obtenu même sans aucun sténopé de collecte. Toute la lumière émise étant collectée sur le détecteur, le balayage 2PM est insensible à l'aberration et à la diffusion du côté de la collecte, contrairement à la 1PM confocale. Actuellement, le balayage 2PM est réalisé à l'aide d'objectifs à ouverture numérique élevée (high-NA), ces derniers étant nécessaires pour obtenir un sectionnement optique de quelques microns, comme illustré à la Fig. 2. Pour balayer un grand champ de vision sans augmenter le temps d'acquisition, réduire l'ouverture numérique n'est pas une option, car cela entraîne une détérioration spectaculaire de la section optique. Dans ce travail, nous proposons de remplacer le faisceau focalisé dans le balayage 2PM par un éclairage focalisé à taches aléatoires, tout en continuant à utiliser un objectif à haute ouverture numérique. Nous avons démontré théoriquement et numériquement qu'en jouant sur la longueur de corrélation du speckle, il est possible d'augmenter la largeur transversale du volume d'excitation à deux photons sans détériorer la largeur axiale. J'ai dérivé une formule simple reliant les largeurs axiale et transversale du faisceau speckled focalisé, qui a été confirmée par des simulations et des expériences. La grande dimension transversale du spot généré par un éclairage aléatoire focalisé devrait faciliter le balayage d'un grand champ de vision

sans compromettre la section optique.

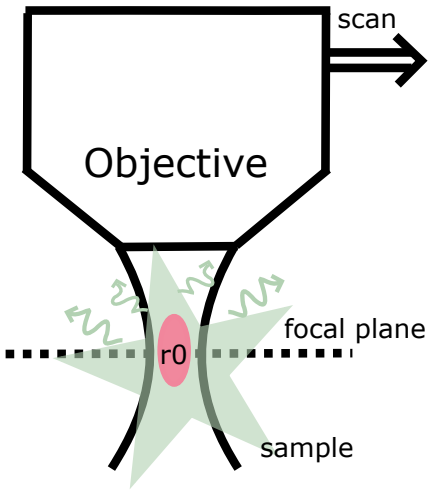


FIGURE 2 – Configuration du balayage 2PM

Dans le chapitre 3, j'étudie plusieurs implémentations de la focalisation temporelle (TF) pour améliorer la section optique de la 2PM dans une configuration à champ large. La TF consiste à utiliser un réseau blazé (diffractant la lumière essentiellement selon son ordre moins un, par exemple) pour disperser spatialement, sous la forme d'un éventail arc-en-ciel, les longueurs d'onde (couleurs) d'une impulsion collimatée. Après avoir traversé la lentille tubulaire et l'objectif, les différentes couleurs n'interfèrent de manière constructive qu'au niveau du plan focal de l'objectif (Fig. 3). En dehors de ce plan, le déphasage croissant entre les couleurs se propageant dans différentes directions allonge la durée de l'impulsion, réduisant ainsi l'intensité maximale. L'analyse théorique du sectionnement optique du TF à réseau est une tâche difficile en raison de la complexité des dérivations proposées (ORON, TAL et al. 2005; ZHU et al. 2005; Michael E DURST et al. 2006; CHOI et al. 2013; LESHEM et al. 2014). Dans ce chapitre, je présente une formule simple montrant que le sectionnement optique est inversement proportionnel au carré de l'ouverture numérique effective du réseau, $NA_G$, cette dernière étant liée à l'angle de divergence des couleurs dispersées (l'angle de l'arc-en-ciel après grossissement par le microscope). J'ai ensuite proposé une nouvelle configuration, appelée TF à réseau multi-ordres, dans laquelle plusieurs ordres du réseau sont collectés par l'objectif ou plusieurs impulsions sont incidentes sur le réseau et collectées par l'objectif (ces deux configurations sont équivalentes d'un point de vue théorique). Dans ce cas, j'ai démontré analytiquement et par des simulations que le sectionnement optique ne dépend pas de la dispersion de la vitesse de groupe (GVD) d'une impulsion, comme dans le TF à réseau standard, mais dépend de la différence entre les vitesses de groupe des impulsions. Ainsi, le TF à réseau multi-ordres offre un sectionnement optique nettement meilleur que le TF à réseau lorsque la largeur de bande de la longueur d'onde de l'impulsion ou le grossissement du microscope sont faibles. Pour mettre en œuvre cette configuration avec plusieurs

impulsions incidentes, j'ai étudié une configuration appelée TF à réseau de rugosité, dans laquelle l'impulsion collimatée est d'abord diffusée de manière aléatoire par une surface rugueuse avant d'éclairer le réseau. J'ai démontré théoriquement que, dans ce cas, le sectionnement optique est inversement proportionnel à $NA_G$, ce qui confirme qu'un sectionnement optique micrométrique peut être obtenu dans des conditions de faible grossissement et de bande passante étroite qui étaient inaccessibles avec le TF à réseau standard. L'analyse théorique a été validée par des simulations numériques et des expériences. Elle prouve qu'un TF efficace peut être mis en œuvre sur des microscopes 2PM à faible grossissement et à large champ, ouvrant ainsi la voie à l'imagerie rapide de grands champs de vision avec sectionnement optique micrométrique. De plus, le motif d'excitation speckled focalisé temporellement généré par la configuration TF à réseau de rugosité est particulièrement adapté à l'approche RIM. Comme il élimine physiquement le signal défocalisé, il permet d'observer des échantillons plus denses et plus épais. Nous avons montré expérimentalement que la procédure de reconstruction RIM permet d'améliorer encore la résolution transversale et le sectionnement optique du TF-2PM à réseau de rugosité.

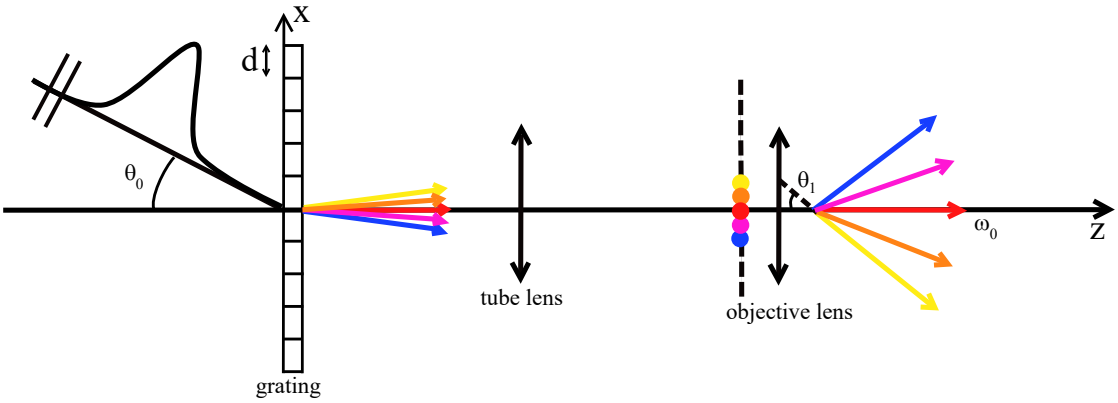


FIGURE 3 – Configuration du réseau TF

Enfin, le quatrième chapitre est consacré à l'imagerie CARS non linéaire. CARS est un processus de mélange à quatre ondes sans marquage capable de sonder des liaisons chimiques spécifiques dans des échantillons. Lorsqu'un faisceau de pompage et un faisceau de Stokes illuminent simultanément l'échantillon, un signal CARS intense apparaît si la différence de fréquence laser correspond à une fréquence moléculaire. En général, la microscopie CARS fonctionne en mode balayage (ZUMBUSCH et al. 1999), où les faisceaux de pompage et de Stokes sont focalisés (et superposés) à l'intérieur de l'échantillon. Comme pour la 2PM, le mode balayage peut s'avérer trop lent lorsque l'échantillon est de grande taille. L'avènement de lasers puissants rend la microscopie CARS à large champ possible, mais celle-ci reste entravée par l'absence de sectionnement optique (HEINRICH et al. 2004). Récemment, une microscopie CARS à sectionnement optique sans balayage utilisant le RIM (FANTUZZI et al. 2023) a été proposée, mais elle nécessite l'enregistrement de nombreuses images. Nous avons proposé ici d'introduire le TF dans un microscope CARS à large champ. J'ai étudié

deux configurations distinctes. La première approche utilise deux réseaux séparés et deux chemins d'illumination pour focaliser temporairement les impulsions de pompage et de Stokes au niveau du plan focal. La principale difficulté consiste à s'assurer que les deux faisceaux se superposent au niveau du plan focal. J'ai dérivé une expression analytique du sectionnement optique montrant qu'il pouvait être meilleur que celui obtenu en 2PM. Les résultats théoriques ont été confirmés numériquement et expérimentalement. Nous avons obtenu un sectionnement optique au niveau micrométrique avec des impulsions femtosecondes et un grossissement relativement élevé. De plus, nous avons observé que cette technique améliorait considérablement la résolution spectrale CARS. La deuxième approche s'inspire de l'analyse concernant le TF à réseau multi-ordres. Elle consiste à envoyer les impulsions superposées de pompage et de Stokes sur un seul réseau et à jouer sur les vitesses de groupe des différentes impulsions pour former un pic d'intensité autour du plan focal. Cette configuration devrait permettre d'obtenir des sections optiques de quelques micromètres avec des impulsions picosecondes et un faible grossissement du microscope.

# Remerciements

First of all, I would like to thank Eirini Papagiakoumou and Marc Guillon for agreeing to evaluate my thesis as reviewers. I would also like to thank Hilton Barbosa de Aguiar and Martin Oheim for agreeing to participate in the jury.

Next, I would like to thank Guillaume Giroussens, Thomas Mangeat, and Simon Labouesse at the Centre de Biologie Intégrative (CBI) from Toulouse, Jérôme Idier at Laboratoire des Sciences du Numérique (LS2N) from Nantes, and Marc Allain for their help in understanding the RIM algorithm in the first stages, adapting RIM to the two-photon and 3D-RIM cases. And I would like to thank Thomas Mangeat again for providing the 3D experimental data during the extension of the 3D-RIM algorithm, which allows me to better test the practicality of this method.

Next, I would also like to thank Assia Benachir for providing experimental data on two-photon RIM, which enable me to integrate two-photon RIM from both theoretical and experimental perspectives, and for offering initial experimental validation within the focused speckles. Then, I would like to thank Federico Vernuccio and Michal Marynowski for providing the experimental data on focused speckles, temporal focusing, and the combination of temporal-focused speckle with RIM, which made it possible for me to validate the theory. Then, I would like to thank Sandro Heuke and Hervé Rigneault for their assistance with several projects in my research, which permitted us to smoothly apply the theory to the experiments.

Finally, I would like to thank my supervisor, Anne Sentenac for her support and guidance over the past three years. She sparked my interest in theoretical modeling, encouraged the progress, and helped me to apply the theoretical work to experimental applications.

# Table des matières

**Affidavit** 2

**Liste de publications et participation aux conférences** 3

**Résumé** 4

**Abstract** 6

**Résumé étendu en Français** 8

**Remerciements** 15

**Table des matières** 16

**Introduction** 19

**1 Random Illumination Microscopy (RIM)** 24
- 1.1 Introduction . . . 24
- 1.2 Principle of RIM . . . 25
- 1.3 Extending one-photon RIM to two-photon RIM . . . 31
  - 1.3.1 Two-photon speckle . . . 31
  - 1.3.2 Simulations . . . 32
  - 1.3.3 Experiments . . . 35
- 1.4 Adapting 2D RIM to 3D RIM . . . 36
  - 1.4.1 An iterative filter for preprocessing the raw speckled images . . . 38
  - 1.4.2 Experiments . . . 40
- 1.5 Conclusion . . . 42

**2 Scalable isotropic resolution in scanning two-photon microscopy using focused random illumination** 44
- 2.1 Introduction . . . 44
- 2.2 Scanning two-photon microscopy . . . 46
- 2.3 Enlarging the excitation volume quasi-isotropically using speckled focused beams . . . 48
  - 2.3.1 Modeling a focused speckled beam and its analytical optical sectioning . . . 50
  - 2.3.2 Simulations . . . 52

2.4 Experiments . . . 55
2.4.1 A diffuser is placed at a conjugated Fourier plane before a field diaphragm . . . 55
2.4.2 The diffuser is moved throughout a slightly focused beam to control the speckle correlation at the pupil plane . . . 58
2.5 Conclusion . . . 62

**3 Improving optical sectioning in widefield two-photon microscopy by combining temporal focusing with random illumination 63**
3.1 Introduction . . . 64
3.2 Principle of grating TF . . . 65
3.2.1 Modeling Temporally Focused laser pulses . . . 66
3.2.2 Exciting the fluorescence with a temporally focused laser pulse . 70
3.2.3 Numerical Simulation . . . 72
3.2.4 Grating TF with a chirped pulse . . . 76
3.3 Collecting two or many orders diffracted by the grating : Multi-order-grating TF . . . 77
3.3.1 multi-order grating TF : Two diffracted orders are collected . . . 77
3.3.2 multi-order grating TF : Three diffracted orders are collected . . 85
3.4 Optical sectioning obtained from a pulse diffracted by a rough surface : Roughness TF . . . 90
3.5 Improving optical sectioning by combining grating TF with random illumination : Roughness-grating TF . . . 94
3.5.1 Theory of Temporal-Focused Speckle (TF-speckle) . . . 94
3.6 Experiments . . . 104
3.6.1 Modeling grating TF when using a reflection grating in Littrow configuration . . . 104
3.6.2 Modeling roughness-grating TF using a reflection grating in Littrow configuration . . . 106
3.6.3 Experimental implementation of grating TF and roughness-grating TF . . . 107
3.7 Using temporal-focused speckles in Random Illumination Microscopy 110
3.8 Conclusion . . . 114

**4 Adapting temporal focusing to Coherent Anti-Stokes Raman Scattering microscopy (TF-CARS) 115**
4.1 Introduction . . . 115
4.2 Applying TF-CARS using two gratings . . . 120
4.2.1 Theory of TF-CARS with two gratings . . . 121
4.2.2 Simulations . . . 124
4.2.3 Experiments on the optical sectioning of TF-CARS using two gratings . . . 125
4.3 Spectroscopy in the TF-CARS configuration with two gratings . . . 128
4.3.1 Analysis of the pupil plane . . . 128

4.3.2 How to select configuration parameters to improve spectral resolution? . . . 131
4.3.3 Experiments on TF-CARS spectral resolution . . . 133
4.4 Forming TF-CARS using only one grating . . . 134
4.4.1 Theory of TF-CARS with one grating . . . 134
4.4.2 How can an objective collect all the light in TF-CARS using one grating? . . . 137
4.4.3 Field behavior at the pupil plane . . . 137
4.4.4 Simulations . . . 138
4.5 Conclusion and perspective . . . 141

**Conclusion and perspective** **142**

**Bibliographie** **144**

# Introduction

Optical microscopy is the most useful tool in biology, material or medical domains for observing samples at the (sub)-micrometer scale due to its ease of use, resolution, and ability to observe inside the samples (when they are transparent enough) without being invasive. In the last thirty years, many different microscopy modalities have been developed, either for being sensitive to novel contrasts (refraction index, non-linear susceptibilities, fluorescence, polarization) or for improving its resolution. Whatever the chosen approach, improving the microscope optical sectioning capability is a key issue that has attracted a lot of attention. Optical sectioning in microscopy is the ability to image the structures belonging to a specific plane (basically the focal plane) of a thick sample without the need for physical slicing. It is obtained by physically or numerically rejecting the signal coming from the out-of-focus regions. Without optical sectioning, the out-of-focus signal and its associated noise pollute the image of the in-focus structures. For certain thick samples, the out-of-focus signal can be so high that it renders the image meaningless.

One way to check if a microscope exhibits optical sectioning is to record the images of a thin homogeneous layer when the latter is placed at different distances from the focal plane. If the recorded images do not depend on the layer position, there is no optical sectioning. In the widefield microscopy configuration, each transverse plane of the sample space is illuminated homogeneously with the same power. Obviously, with this definition, one-photon excitation fluorescence widefield microscopy, 1PM, (and also standard transmission microscopes) lacks optical sectioning. The fluorescence emitted from the homogeneous layer (or the transmitted intensity) being proportional to the illumination power (VALEUR 2002; LAKOWICZ 2006), the image will be the same whatever the layer's position along the optical axis.

Many different techniques have been proposed for improving the optical sectioning capability of microscopy especially for 1PM. For physically decreasing the signal coming from out-of-focus regions, scanning techniques which involve focusing a beam inside the sample either in the form of a spot (confocal microscopy (PAWLEY 2006)) or a line (IM et al. 2005) and restricting the signal detection on a bucket detector covering a domain conjugated to the excited region, have been developed. In non-linear microscopy, when the recorded signal is not proportional to the illumination power, (two-photon excitation fluorescence microscopy, Second Harmonic Generation, Stimulated Raman Scattering, Coherent AntiStokes Raman Scattering ...), most implementations consist in scanning a focused illumination. Contrary to linear microscopy, such as 1PM, the non-linearity of the excitation permits to obtain optical sectioning even without restricting the detection to the excited region. As much of the emitted signal as possible is collected by the bucket detector.

Unfortunately, the improvement in the optical sectioning capability brought by the scanning modality come with a deterioration of the performances of microscope with respect to speed and phototoxicity. Basically, to lessen the acquisition time of an image, one needs to scan faster. To obtain a sufficient signal to noise ratio with a smaller integration time, one needs to increase the illumination power. Now, to keep a reasonable phototoxicity, one needs to keep the power below a certain threshold.Thus, scanning methods are inherently limited to the fast imaging of small FOVs or to the slow imaging of large FOV.

To bypass this limitation, other approaches which use extended illuminations covering the whole sample and camera detection have been proposed to provide optical sectioning.

A popular technique consists in restricting the illumination to a thin layer about the sample plane of interest with a light sheet (STELZER et al. 2021). However, it requires a complex implementation with two objectives that is not always adapted to the samples under study. More recently, methods that numerically reject the out-of-focus signal have demonstrated their interest both for 1PM (VENTALON et al. 2005) and non-linear CARS imaging (FANTUZZI et al. 2023). By recording several images of the sample under periodic/random illuminations (as in Structured Illumination Microscopy or Random Illumination Microscopy) an optically sectioned reconstruction can be obtained through diverse numerical treatments (GUSTAFSSON et al. 2008; VENTALON et al. 2005; MANGEAT et al. 2021; FANTUZZI et al. 2023). In addition, these approaches improve significantly the transverse and axial resolutions compared to the scanning or light-sheet approaches. However, they are slowed down by the need to record multiple images and they can fail when the noise relevant to the out-of-focus signal of each raw image is too important for the numerical reconstruction to succeed. Last, a technique that is only adapted to non-linear excitation, has shown its interest : Temporal Focusing (TF). TF permits to form a light pulse whose duration changes as it propagates. A short duration at the focal plane and long duration outside induce a localized excitation peak within a layer about the focal plane. To our knowledge, this approach has been essentially implemented in two-photon excitation fluorescence microscopy (2PM) for small (tens of microns) FOV (Michael E DURST et al. 2006; ORON et SILBERBERG 2005; PAPAGIAKOUMOU, RONZITTI et al. 2020).

The aim of this thesis is to propose solutions for improving the optical sectioning of linear (1PM) and non-linear microscopies (2PM and CARS imaging) that are specifically adapted to the fast imaging of large FOV. My work has been essentially theoretical and numerical but most of the analysis and simulations are accompanied by experimental results obtained by Assia Benachir and Federico Vernuccio at the Fresnel Institute and by Thomas Mangeat at the CBI in Toulouse. The thesis is divided in four chapters.

In the first chapter, I focus on the Random Illumination Microscopy approach. RIM consists in recording multiple low-resolution images under random speckled illumination and provides a super-resolved optically sectioned reconstruction from the variance of the raw images (MANGEAT et al. 2021; GIROUSSENS et al. 2024). The reconstruction is based on a standard deviation matching algorithm that depends only

on the observation point spread function and the speckle autocorrelation. Initially, RIM model assumed that the sample and illumination were two-dimensional, the out-of-focus signal being considered noise. The 3D reconstruction of the sample was obtained by stacking 2D reconstructed slices. In the first part, I adapted RIM to two-photon excitation microscopy (2PM). This task required studying the auto-correlation of the two-photon excitation intensity, which is proportional to the square intensity of the light. RIM reconstructions on experimental two-photon speckled images showed that this technique permits to obtain optically sectioned images with a resolution better than that of standard scanning approaches in a widefield configuration. In the second part, I improved RIM reconstruction algorithm (GIROUSSENS et al. 2024) by accounting for the 3D nature of the sample and of the image formation model following Guillaume Giroussens' development. It is shown that the 3D version of algoRIM permits to obtain better contrasted and resolved 3D reconstructions than the 2D version.

In chapter 2, we proposed to adapt scanning 2PM to fast imaging of large FOV. Scanning 2PM has been introduced as an alternative to confocal 1PM for imaging deep inside inhomogeneous samples. First, its infrared illumination can focus deeper in biological samples than the visible light of confocal 1PM. Second, thanks to the non-linear excitation process, optical sectioning is obtained even without any collection pinhole. All the emitted light being collected on the detector, scanning 2PM is insensitive to aberration and scattering on the collection side, contrary to confocal 1PM. Presently, scanning 2PM is performed using objectives with high Numerical Aperture (high-NA), the latter being necessary to obtain an optical sectioning of a few microns. To scan large FOV without increasing the acquisition time, reducing the NA is not an option as it leads to a dramatic deterioration of the optical sectioning. In this work, we propose to replace the focused beam in scanning 2PM with a focused random speckled illumination, while still using a high-NA objective. We showed theoretically and numerically that by playing on the correlation length of the speckle, one can increase the transverse width of two-photon excitation volume without deteriorating the axial width. I derived a simple formula linking the axial and transverse widths of the focused speckled beam which was confirmed by simulations and experiments. The large transverse dimension of the spot generated by a focused random illumination should make the scanning of large FOV easier without compromising the optical sectioning.

In chapter 3, I study several implementations of Temporal Focusing for improving the optical sectioning of 2PM in a widefield configuration. TF consists in using a blazed grating (diffracting light essentially along its minus one order for example) for spatially dispersing, in the shape of a rainbow fan, the wavelengths (colors) of a collimated pulse. After passing through the tube lens and objective, the different colors interfere constructively only at the focal plane of the objective. Outside this plane, the increasing phase mismatch between the colors propagating along different directions stretches the pulse duration, thus reducing the peak intensity. Analysing theoretically the optical sectioning of grating-TF is a difficult task due to the complexity of the proposed derivations (ORON, TAL et al. 2005; ZHU et al. 2005; Michael E DURST et al.

2006; CHOI et al. 2013; LESHEM et al. 2014). In this chapter, I provide a simple formula showing that the optical sectioning is inversely proportional to the square of the grating effective numerical aperture, $NA_G$, the latter being related to the divergence angle of the dispersed colors (the angle of the rainbow fan after magnification by the microscope). Then, I proposed a novel configuration, called multi-order grating TF, in which several orders of the grating are collected by the objective or several pulses are incident on the grating and collected by the objective (these two configurations are equivalent from the theoretical point of view). In this case, I demonstrated analytically and through simulations that the optical sectioning does not depend on the Group Velocity Dispersion (GVD) of one pulse, as in standard grating TF but depends on the difference between the group velocities of the pulses. Thus, multi-order grating TF provides a significantly better optical sectioning than grating TF when the pulse wavelength bandwidth or the microscope magnification are small. To implement this configuration with multiple incident pulses, I studied a configuration, called roughness-grating TF, in which the collimated pulse is first randomly scattered by a rough surface before illuminating the grating. I showed theoretically that, in this case, the optical sectioning is inversely proportional to $NA_G$, which confirms that a micrometric optical sectioning can be achieved under conditions of low magnification and narrow bandwidth that were inaccessible with standard grating TF. The theoretical analysis was validated with numerical simulations and experiments. It proves that efficient TF can be implemented on low magnification widefield 2PM microscopes thus paving the way to the fast imaging of large FOV with micrometric optical sectioning. In addition, the temporal focused speckled excitation pattern generated by the roughness-grating TF configuration is particularly adapted to the RIM approach. As it removes physically the out-of-focus signal, it permits to observe denser labeled and thicker samples. We showed experimentally that RIM reconstruction procedure permits to further improve the transverse resolution and the optical sectioning of roughness-grating TF-2PM.

Finally the fourth chapter is devoted to non-linear CARS imaging. CARS is a label-free four-wave mixing process able to probe specific chemical bonds in samples. When a pump and Stokes beams simultaneously illuminate the sample, an intense CARS signal emerges if the laser frequency difference matches a molecular frequency. Typically, CARS microscopy works in a scanning mode (ZUMBUSCH et al. 1999), where both pump and Stokes beams are focused (and superimposed) inside the sample. As for 2PM, the scanning mode may prove too slow when the sample is large. The advent of powerful lasers make wide-field CARS microscopy feasible but still plagued by the absence of optical sectioning (HEINRICH et al. 2004). Recently, scanless optically sectioned CARS microscopy using RIM (FANTUZZI et al. 2023) have been proposed but requires the recording of many images. Here, we proposed to introduce TF in a widefield CARS microscope. I studied two distinct configurations. The first approach employs two separate gratings and two illumination paths to temporally focus both the pump and Stokes pulses at the focal plane. The key difficulty is to make sure that both beams are superimposed at the focal plane. I derived an analytical expression of the optical sectioning showing that it could be better than that obtained

in 2PM. The theoretical results were confirmed numerically and experimentally. We obtained optical sectioning at a micrometer-level with femto-second pulses and relatively high magnification. In addition, we observed that this technique improved significantly CARS spectral resolution. The second approach is inspired from the analysis concerning the multi-order grating TF. It consists in sending the superposed pump and stokes pulses onto a single grating and playing on the group velocities of the different pulses for forming an intensity peak about the focal plane. This configuration should permit to obtain optical sections of a few micrometers with picosecond pulses and low microscope magnification.

# 1 Random Illumination Microscopy (RIM)

## Sommaire


1.1 Introduction . . . . . 24
1.2 Principle of RIM . . . . . 25
1.3 Extending one-photon RIM to two-photon RIM . . . . . 31
1.3.1 Two-photon speckle . . . . . 31
1.3.2 Simulations . . . . . 32
1.3.3 Experiments . . . . . 35
1.4 Adapting 2D RIM to 3D RIM . . . . . 36
1.4.1 An iterative filter for preprocessing the raw speckled images . . 38
1.4.2 Experiments . . . . . 40
1.5 Conclusion . . . . . 42


## 1.1 Introduction

In wide-field standard fluorescence microscopy and in a 2D configuration the sample (considered as a thin slice about the focal plane) is excited by a homogeneous illumination. The spatial frequencies of the recovered sample are limited to a disk of radius $\frac{2}{\lambda}$ where $\lambda$ denotes the emitted light wavelength, corresponding to the Fourier support of the point spread function (PSF) of the microscope. It is possible to recover the sample with spatial frequencies exceeding this diffraction limit by using structured illumination. Structured Illumination Microscopy uses periodic light grids (periodic SIM) or scanning focused spots (Image Scanning Microscopy) that down-modulate high spatial frequencies of the sample into the accessible frequency domain of the microscope (GUSTAFSSON 2000; DERTINGER et al. 2009), yielding a two-fold resolution gain. These super-resolved approaches requiring multiple illuminations are, up to now, the best compromise between resolution, speed, and gentleness for the samples. However, they are plagued by one major drawback : they require a precise knowledge of the illumination patterns.

To address this issue, RIM has been proposed as a super-resolution fluorescence microscopy technique in which the illuminations are uncontrolled speckles. The super-resolved image is reconstructed by matching the empirical variance or standard deviation of the speckled illuminated images and their expected variance or standard

deviation. It was shown mathematically and confirmed experimentally that this approach yielded a resolution gain comparable to that of periodic-SIM or scanning-SIM (LABOUESSE, IDIER, ALLAIN et al. 2024; IDIER et al. 2018; MANGEAT et al. 2021). Up to now, RIM has been implemented in one-photon excitation fluorescence microscopy (AFFANNOUKOUÉ et al. 2023; MANGEAT et al. 2021; MAZZELLA et al. 2024). In the first part of this chapter we extend RIM to two-photon excitation microscopy. Furthermore, apart from a study on an extended FOV configuration (MAZZELLA et al. 2024) RIM has been developed in the two-dimensional configuration (the sample is a thin slice about the focal plane, the speckle and PSFs are 2D functions) (MANGEAT et al. 2021; AFFANNOUKOUÉ et al. 2023). In the second part of this chapter, we present an implementation of RIM in 3D configuration (the sample, PSF, and speckles are 3D functions).

## 1.2 Principle of RIM

In this section, we review the theoretical principles of RIM described in (IDIER et al. 2018; LABOUESSE, IDIER, ALLAIN et al. 2024; GIROUSSENS et al. 2024) in the context of fluorescence microscopy. RIM involves collecting multiple images of the sample under uncontrolled speckled illuminations, where the illumination wavelength $\lambda_{\text{il}}$ and observation wavelength $\lambda_{\text{ob}}$ are assumed to be identical. Moreover, the RIM derivation process described in the following applies to both 2D and 3D imaging. One speckled image can be modeled as :

$$y(\boldsymbol{R}) = \int h(\boldsymbol{R}-\boldsymbol{r})\rho(\boldsymbol{r})|E|^2(\boldsymbol{r})\mathrm{d}\boldsymbol{r} + b(\boldsymbol{R}) \tag{1}$$

where $\boldsymbol{R}$ and $\boldsymbol{r}$ represent the coordinates in the camera space and object space respectively, $\rho$ is the sample, $b$ is the noise contribution to the measurement, $|E|^2(\boldsymbol{r})$ describes the illumination intensity, and $h$ is the incoherent PSF, which can be expressed as :

$$h(\boldsymbol{r}) = \left| \int p(\boldsymbol{\kappa}) e^{i\boldsymbol{k}_{\text{ob}}\cdot\boldsymbol{r}} \mathrm{d}\boldsymbol{\kappa} \right|^2 \tag{2}$$

where $\boldsymbol{k}_{\text{ob}}$ presents the spatial frequency, $p$ is the pupil function that is equal to 1 if $\boldsymbol{\kappa} < \frac{2\pi \text{NA}}{\lambda_{\text{ob}}}$ and 0 elsewhere, and $\boldsymbol{\kappa}$ is the transverse component of the spatial frequency. Generally, the Fourier transform of $h$ is a solid torus with a 'missing cone', as shown in Fig. 1.1a.

In RIM, the illumination light is considered as a fully developed speckle (GOODMAN 1975), whose field can be understood as a sum of plane waves with random phases :

$$E(\boldsymbol{r}) = \int p(\boldsymbol{\kappa}) e^{i\phi(\boldsymbol{\kappa})} e^{i\boldsymbol{k}_{\text{il}}\cdot\boldsymbol{r}} \mathrm{d}\boldsymbol{\kappa} \tag{3}$$

where $\boldsymbol{k}_{\text{il}}$ and $p$ describe the spatial frequency and the illumination pupil function, respectively. $\phi(\boldsymbol{\kappa})$ represents uncorrelated random complex variable that is uniformly

distributed between $[0, 2\pi]$, which satisfies $\langle e^{i\phi(\boldsymbol{\kappa})} e^{-i\phi(\boldsymbol{\kappa}')} \rangle = \delta(\boldsymbol{\kappa} - \boldsymbol{\kappa}')$, and zero mean : $\langle e^{i\phi(\boldsymbol{\kappa})} \rangle = 0$ , where $\langle\rangle$ is the averaging,

For the RIM reconstruction process, the autocorrelation of the illumination light intensity is critical and is considered prior information. One-photon speckled intensity with the illumination wavelength can be written as :

$$I(\boldsymbol{r}) = |E|^2(\boldsymbol{r}) \tag{4}$$

Due to the property of this circular Gaussian random variable (GOODMAN 1975), the autocorrelation of one photon speckle intensity can be represented by : $\langle I(\boldsymbol{r}_1) I(\boldsymbol{r}_2) \rangle \propto 2 |\langle E(\boldsymbol{r}_1) E^*(\boldsymbol{r}_2) \rangle|^2$, where the autocorrelation of the field reads

$$\begin{aligned} C(\boldsymbol{r}_1 - \boldsymbol{r}_2) &= \langle E(\boldsymbol{r}_1) E^*(\boldsymbol{r}_2) \rangle \\ &= \int |p|^2(\boldsymbol{\kappa}) e^{i \boldsymbol{k}_{\text{il}} \cdot \boldsymbol{r}} \mathrm{d}\boldsymbol{\kappa} \end{aligned} \tag{5}$$

Thus, the autocorrelation of speckle intensity can be expressed as

$$\langle I(\boldsymbol{r}_1) I(\boldsymbol{r}_2) \rangle \propto |C|^2(\boldsymbol{r}_1 - \boldsymbol{r}_2) \tag{6}$$

The reconstruction procedure of RIM requires forming the variance of the multiple speckled images $y(\boldsymbol{R})$ (GIROUSSENS et al. 2024) :

$$\begin{aligned} \sigma_y^2(\boldsymbol{R}) &= \int t(\boldsymbol{R} - \boldsymbol{r}_1, \boldsymbol{R} - \boldsymbol{r}_2) \rho(\boldsymbol{r}_1) \rho(\boldsymbol{r}_2) \mathrm{d}\boldsymbol{r}_1 \mathrm{d}\boldsymbol{r}_2 + \nu_\epsilon \\ &= \sigma^2(\boldsymbol{R}) + \nu_\epsilon \end{aligned} \tag{7}$$

with the kernel

$$t(\boldsymbol{r}_1, \boldsymbol{r}_2) = h(\boldsymbol{r}_1) h(\boldsymbol{r}_2) |C|^2(\boldsymbol{r}_1 - \boldsymbol{r}_2) \tag{8}$$

where $\nu_\epsilon$ the variance of the noise.

Observing $t$ as a positive definite operator, which can be decomposed on the orthonormal basis of its eigenvectors as (GOHBERG et al. 2013) :

$$t(\boldsymbol{r}_1, \boldsymbol{r}_2) = \sum_{n=1}^{+\infty} \beta_n \phi_n(\boldsymbol{r}_1) \phi_n(\boldsymbol{r}_2) \tag{9}$$

where $\phi_n$ and $\beta_n$ present the orthogonal functions and real-valued eigenvalues, more details could be found in (GIROUSSENS et al. 2024).

Therefore, the variance $\sigma^2$ in equ(7) can be derived as [1] :

$$\sigma^2 = \sum_{n=1}^{+\infty} (\rho * u_n)^2 \tag{10}$$

where $u_n = \sqrt{\beta_n} \phi_n$.

1. $*$ denotes convolution

Generally, the first 10 eigenvectors in the kernel decomposition are enough to provide an accurate variance estimation (LABOUESSE, IDIER, SENTENAC et al. 2021). The first reconstruction RIM procedure was a variance-based matching algorithm (LABOUESSE, IDIER, SENTENAC et al. 2021). This algorithm minimizes the distance between the empirical variance $\hat{\sigma}^2$ and the variance model $\sigma^2$ in Eq. (7) to build the following cost function :

$$F_v(\rho;\mu) = ||\hat{\sigma}^2 - \sigma^2||_2^2 + \mu||\rho||_2^2 \tag{11}$$

Recently, (GIROUSSENS et al. 2024) proposed a closed-form (CF) RIM estimator and a faster standard deviation (std)-based matching algorithm. The RIM-CF estimator is based on a rough estimate for the model variance : $\sigma^2 \approx (\rho * u_1)^2$, because the first eigenvector holds nearly 90% energy of the kernel $T$.

Therefore, the theoretical standard deviation $\sigma$ can be approximated as :

$$\sigma \approx \rho * u_1 \tag{12}$$

Because of this linear dependence between the sample and theoretical $\sigma$, the RIM-CF estimator reads[2]

$$\rho_{\mathrm{CF}} = \mathscr{F}^{-1}\left(\mathscr{F}(\hat{\sigma})\frac{\tilde{u}_1}{|\tilde{u}_1|^2 + \mu}\right) \tag{13}$$

For more accurate sample reconstruction, the distance between the empirical standard deviation $\hat{\sigma}$ and the expected standard deviation $\sigma$. The cost functional reads,

$$F_s(\rho;\mu) = ||\hat{\sigma} - \sigma||_2^2 + \mu||\rho||_2^2. \tag{14}$$

To solve the minimization problem Eq. (14), a preconditioned conjugate gradient algorithm was developed in (GIROUSSENS et al. 2024). Thanks to the significant acceleration of algorithm convergence achieved by this preconditioner, the std-RIM algorithm has been demonstrated to converge much faster than variance-based methods.

Noting that at the beginning of this chapter, we assumed that the illumination wavelength $\lambda_{\mathrm{il}}$ and the observation wavelength $\lambda_{\mathrm{ob}}$ are identical, so $h$ and $|C|^2(\boldsymbol{r}_1 - \boldsymbol{r}_2)$ have the same expressions. In addition, (LABOUESSE, IDIER, ALLAIN et al. 2024) has shown that there is a bijection between the variance $\sigma^2(\boldsymbol{R})$ and the sample frequencies in the Fourier support of $h^2$ when PSF and the autocorrelation of intensity have the same Fourier support.

2. $\mathscr{F}$ and $\mathscr{F}^{-1}$ present the Fourier transform and inverse Fourier transform, respectively. The variable with wavy lines denotes its frequency domain representation : $\tilde{h}$ is the Fourier transform of $h$.

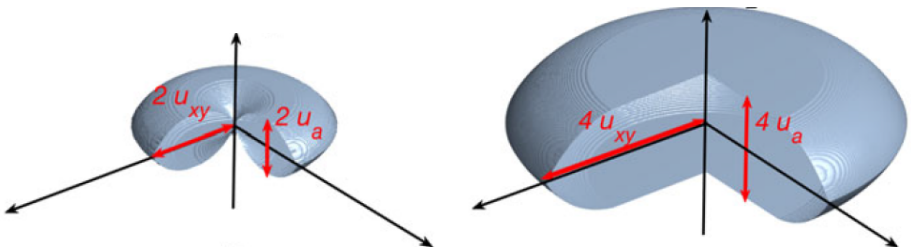


(a) 3D OTF (b) Fourier support of 3D RIM result

FIGURE 1.1 – Understanding of 3D RIM (IDIER et al. 2018) ($u_{xy} = \frac{NA}{\lambda}$, $u_a = \frac{NA^2}{\lambda}$). Fig a presents the Fourier transform of PSF ($\tilde{h}$) in 3D, Fig b shows the Fourier support of a 3D RIM result, which are twice larger than $\tilde{h}$ at transverse plane, and solve the missing cone problem.

Therefore, RIM can reconstruct the sample in the Fourier support of $h^2$, which reveals an important property of RIM : its ability to achieve optical sectioning. Fig. 1.1a describes the 3D OTF $\tilde{h}$, and the missing cone explains why there is no optical sectioning in wide-field fluorescence microscopy, as its Fourier transform along the z-axis is constant. However, RIM can retrieve the sample in the Fourier support of $h^2$ without missing cone in 3D, as shown in Fig. 1.1b. This explains the optical sectioning property of the variance or standard deviation for many images, which was proposed in (VENTALON et al. 2005; OH et al. 2013).

More specifically, when the sample is a thin slice placed at the objective focal plane,we refer to it as a 2D RIM problem. The Fourier support of the recoverable sample frequency for RIM corresponds to a disk of radius $\frac{4NA}{\lambda}$, whereas the Fourier support of the PSF is only a disk of radius $\frac{2NA}{\lambda}$, as Fig. 1.2 shows.

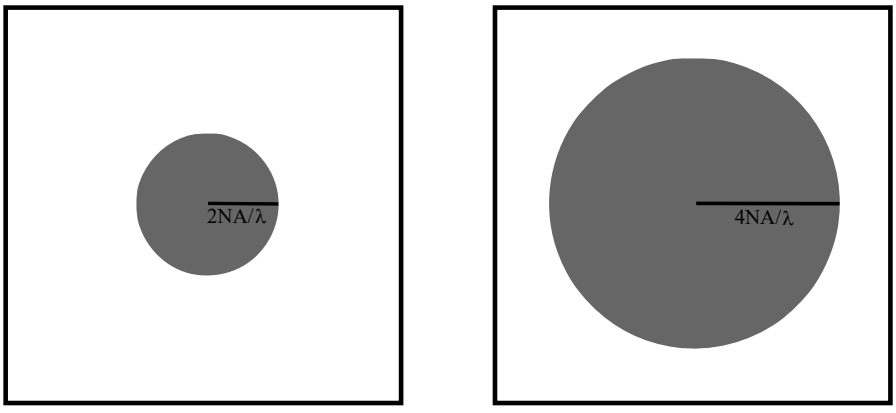


Fourier support of PSF Fourier support of RIM result

FIGURE 1.2 – Fourier supports in 2D. The left image shows the Fourier support of PSF $\tilde{h}$, the right image shows the Fourier support of RIM result.

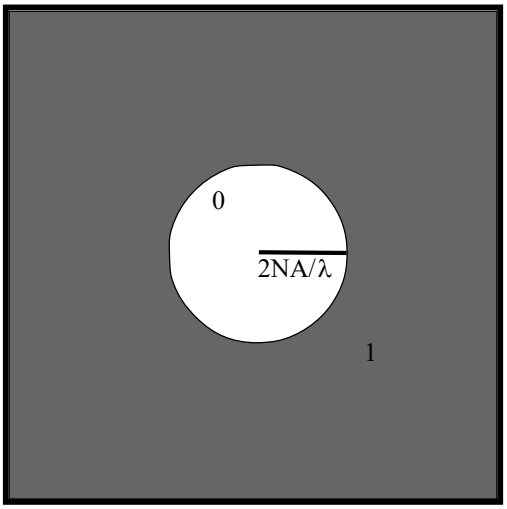


FIGURE 1.3 – Fourier support of the noise removing filter.

The variance model requires the knowledge of the noise variance $v_\epsilon$, Eq. (7). S. Labouesse proposed in (LABOUESSE, IDIER, SENTENAC et al. 2021) a technique for estimating this noise variance. Noting that the noise (essentially Poisson noise) is uncorrelated so that its spectrum spreads well beyond the Fourier support of the PSF, he introduced a filter $m$ whose Fourier support is zero when $\tilde{h}$ is nonzero and one when $\tilde{h}$ is zero. Fig. 1.3 shows its Fourier support in 2D, which is exactly the opposite of the left plot in Fig. 1.2.

By forming $y' = m * y$ where $y$ represents one raw speckled image, we discard all the information stemming from the sample and get an estimate of the noise. The variance of $y$ is equal to the variance of the noise convolved with $h^2$ : $v' = v_\epsilon * m^2$. Then the noise variance $v_\epsilon$ can be estimated as

$$\tilde{v}_\epsilon = \frac{\tilde{v}_{y'}}{\tilde{m} * \tilde{m}}. \tag{15}$$

(Note that, $\tilde{m} * \tilde{m}$ is never null). This estimation of the noise variance can be used in the variance or standard deviation model taken in the cost functional for improving the accuracy of the model and limiting the influence of noise.

Another important preprocessing is performed on the raw data for improving the signal to noise ratio and enhance the sample high spatial frequencies. We recall that each raw speckled image $y$ is modeled as the convolution of $\rho|E|^2$ with $h$, Eq. (1). To cut the noise outside the Fourier support of $h$ and enhance the high-frequency part, we apply a wiener filter with $\tilde{g} = \frac{\tilde{h}^*}{|\tilde{h}|^2+\eta}$ [3] to each raw image. Therefore, each prefiltered raw image reads

$$y^{'} = y * g. \tag{16}$$

Then each filtered raw image can be interpreted as the convolution of $\rho|E|^2$ with

3. $h^*$ is the conjugate of $h$

$h' = h * g$. An illustration for the original OTF $\tilde{h}$ and the filtered OTF $\tilde{h'}$ can be found in Fig. 1.4. This preprocessing not only reduces the impact of noise but also increases the weight of high frequencies, thereby accelerating the convergence speed of the iterative algorithm. Then the inversion scheme is performed by changing $h$ by $h'$ in the formula. Note that the noise variance of the filtered raw images $y'$ is also different from the previously estimated variance $v_\epsilon$ of the raw images, we have $\tilde{v}_\epsilon^{y'} = \tilde{v}_\epsilon \tilde{g} * \tilde{g}$.

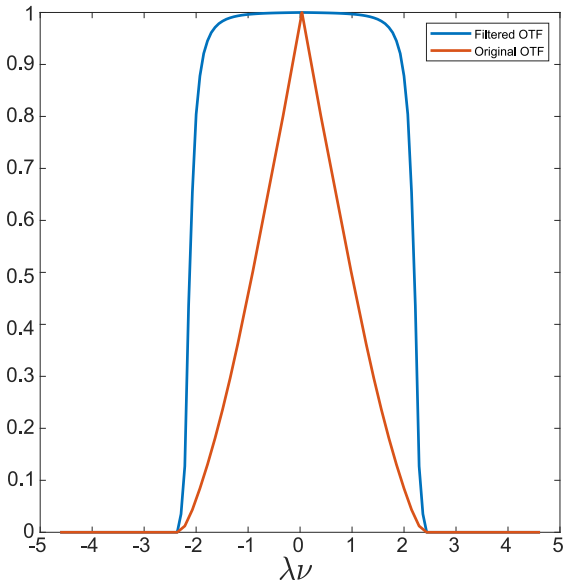


FIGURE 1.4 – Fourier supports in 1D during preprocessing with Wiener filter. Red line illustrates the OTF $\tilde{h}$; the blue line illustrates the filtered OTF $\tilde{h}'$. This preprocess filter not only reduces the influence of noise, but also enhances the weight of high frequency.

Finally, RIM reconstruction process requires two critical parameters to be tuned : one is the parameter $\eta$ during the preprocessing of the raw data, and the other is the Tikhonov parameter $\mu$ within the iterative inversion scheme algoRIM (minimizing the cost function Eq. (14)). The whole RIM reconstruction process can be described as Fig. 1.5.

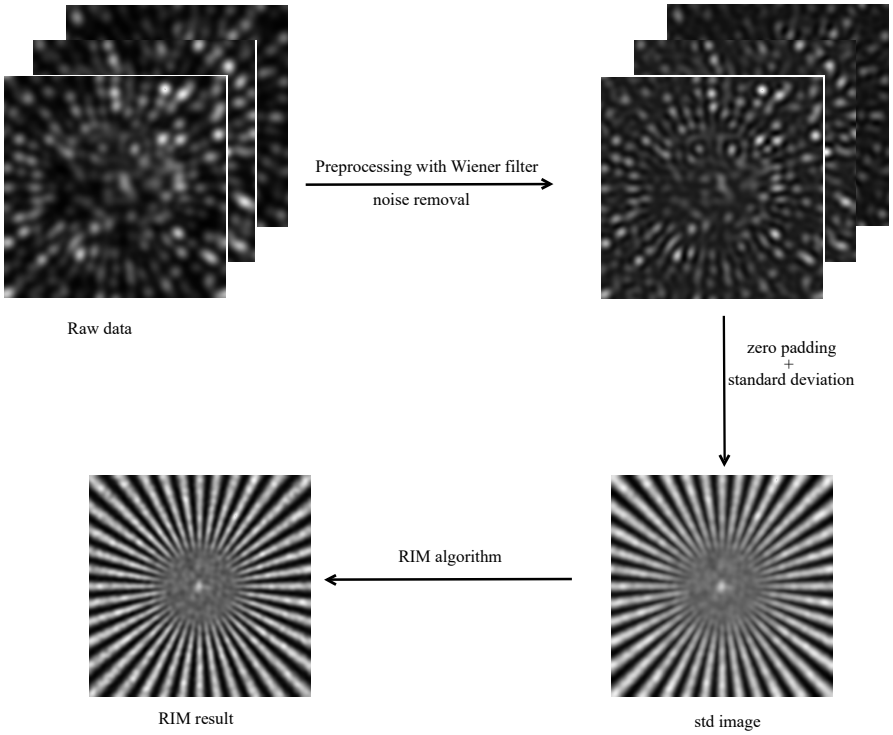


FIGURE 1.5 – RIM process. First, we preprocess all raw images using a Wiener filter and get the filtered standard deviation image, which has less noise and higher high-frequency weights. Subsequently, we obtain RIM results from the the filtered standard deviation image through the RIM algorithm.

## 1.3 Extending one-photon RIM to two-photon RIM

In this section, we present the theoretical model and experimental results for extending one-photon RIM to two-photon RIM, and analyze the properties of two-photon RIM in 2D.

### 1.3.1 Two-photon speckle

Typically, two photon uncorrelated speckle intensity $I_{2\mathrm{PE}}$ can be modeled as the squared one-photon speckle with a twice larger excitation wavelength (NEGASH et al. 2018) :

$$I_{2\mathrm{PE}}(\boldsymbol{r}) = |E|^4(\boldsymbol{r}; 2\lambda_{\mathrm{il}}) \tag{17}$$

where $2\lambda_{\mathrm{il}}$ is two-photon excitation wavelength[4].

Even though the excitation wavelength of a two-photon excitation beam is twice that of a one-photon excitation beam, their 2D Fourier support is nearly identical because the square of the intensity compensates the difference in wavelength. The

4. Here, we still keep the assumption : $\lambda_{\mathrm{il}} = \lambda_{\mathrm{ob}}$

illustrations of one-photon speckles and two-photon speckles at the transverse plane can be found in Fig. 1.6.

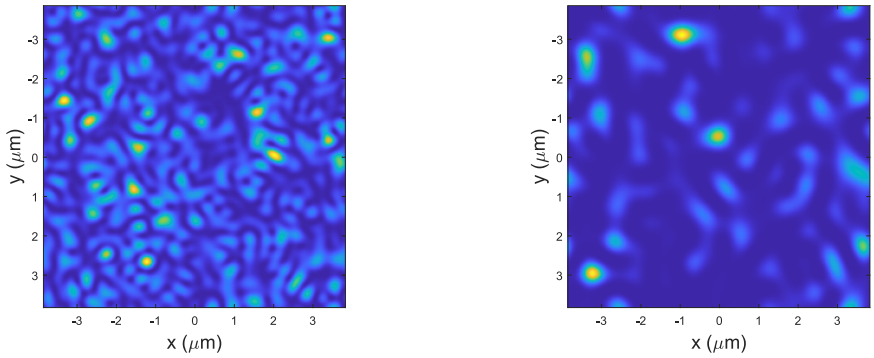


(a) One photon (b) Two photon

FIGURE 1.6 – Illustration of one photon speckle (intensity of speckles at $\lambda_{il} = 500$ nm) and two photon speckle (square intensity of speckles at $2\lambda_{il} = 1000$ nm). (a) : xy map of one-photon speckle. (b) : xy map for two-photon speckle, two-photon speckle grains are more sparse because two-photon intensity is sensitive to the square of one-photon intensity.

As we mentioned before, the autocorrelation of illumination intensity is a key input of the RIM reconstruction procedure. Due to the property of complex Gaussian circular variable, the autocorrelation of two-photon speckled intensity can be expressed as (GOODMAN 2007)

$$\langle I_{2PE}(\boldsymbol{r}_1) I_{2PE}(\boldsymbol{r}_2)\rangle = 16|C|^2(\boldsymbol{r}_1 - \boldsymbol{r}_2; 2\lambda_{il}) + 4|C|^4(\boldsymbol{r}_1 - \boldsymbol{r}_2; 2\lambda_{il}) \tag{18}$$

Moreover, the assumption $\lambda_{ob} = \lambda_{il}$ indicates that the excitation wavelength is about twice larger than the emitted wavelength in two photon fluorescence microscopy. And $|C|^4(\boldsymbol{r}_1 - \boldsymbol{r}_2; 2\lambda_{il})$ has roughly the same Fourier support as PSF $h$ (Eq. (2)) and one-photon autocorrelation $|C|^2(\boldsymbol{r}_1 - \boldsymbol{r}_2; \lambda_{il})$, thus RIM can recover the sample in the Fourier support of $h^2$. Theoretically, two-photon RIM can reconstruct the sample frequency in a Fourier support corresponding to a disk of radius $\frac{4NA}{\lambda_{il}}$.

## 1.3.2 Simulations

To investigate the super-resolution capabilities of two-photon 2D RIM and one-photon 2D RIM in numerical simulations, we simulate 500 two-photon speckled images taking the emitted wavelength at $\lambda_{ob} = 515nm$ and the excitation wavelength at $1030nm$, and 500 one-photon speckled images with $\lambda_{il} = \lambda_{ob} = 515nm$. The sample is assumed to be a thin slice about the focal plane with a fluorescence density reproducing a spoke pattern. By following the RIM procedures in Fig. 1.5, one-photon RIM result and two-photon RIM result are shown in Fig.1.7(a), which demonstrates

that the resolution of two-photon RIM is slightly lower than that of one-photon RIM. This aligns with our expectations, because although theoretically $|C|^4$ in Eq. (18) can provide a Fourier support of the same size as $h$, its weight is far smaller than that of $|C|^2$. Therefore, the effective Fourier support of the autocorrelation of the two-photon speckle $\langle I_{2\mathrm{PE}}(\boldsymbol{r}_1) I_{2\mathrm{PE}}(\boldsymbol{r}_2)\rangle$ is smaller than that of the observation PSF $h$.

In addition, we demonstrate in Fig.1.7(b) that both one-photon RIM and two-photon RIM can theoretically recover the same range of sample frequencies, typically represented as the convolution of the ground truth for the sample $\rho^*$ with the first eigenvector $u_1$, respectively.

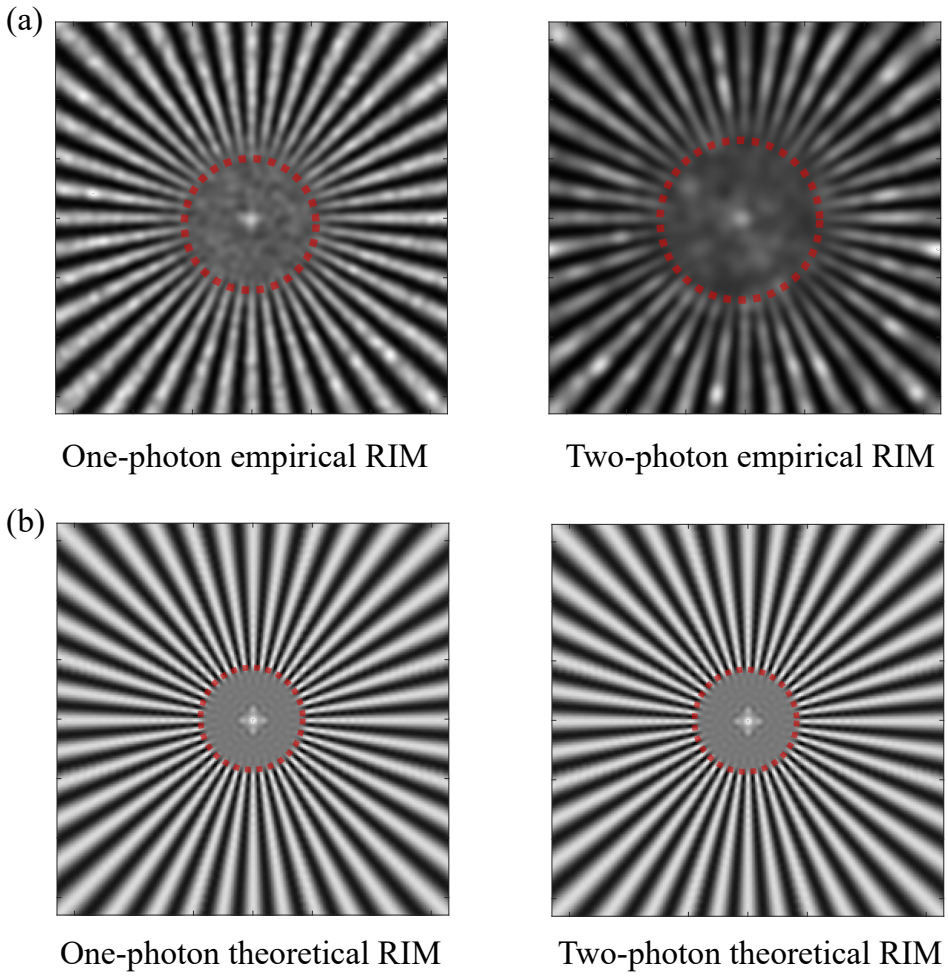


FIGURE 1.7 – Comparative analysis of one-photon RIM and two-photon RIM. First, we irradiated the same sample with 500 one-photon and 500 two-photon speckles respectively. The collection wavelength was 515 nm for both of them, identical to the one-photon illumination wavelength, while the two-photon illumination wavelength was twice that, at 1030 nm. (a) Empirical RIM results obtained from 500 simulated images demonstrate superior performance for one-photon illumination. This arises because the weight of $|C|^2$ in Eq. (18) significantly exceeds that of $|C|^4$, resulting in a smaller effective Fourier support for the autocorrelation of two-photon speckles compared to OTF. (b) During the RIM derivation, we learn that the sample frequency range recoverable by RIM nearly corresponds to the Fourier support of the first eigenvalue $\tilde{u}_1$. Therefore, we represent the convolution of the sample ground truth $\rho^*$ and their first eigenvalues : $\rho^* * u_1$, demonstrating that their theoretical super-resolution is identical.

### 1.3.3 Experiments

In this section, we show two-photon RIM results for different samples on FOVs greater than 100 microns. These experiments were conducted by Assia Benachir, PhD student of H. Rigneault and S. Heuke.

The speckled illumination is generated by illuminating with a collimated beam (a pulsed laser beam ①) a diffuser (Spatial Light Modulator, SLM, ② combined with a zero-stop ③) placed at the Fourier plane of the microscope objective. The camera ⑤ records multiple speckled images of the sample produced by changing the SLM random pattern, as shown in Fig. 1.8.

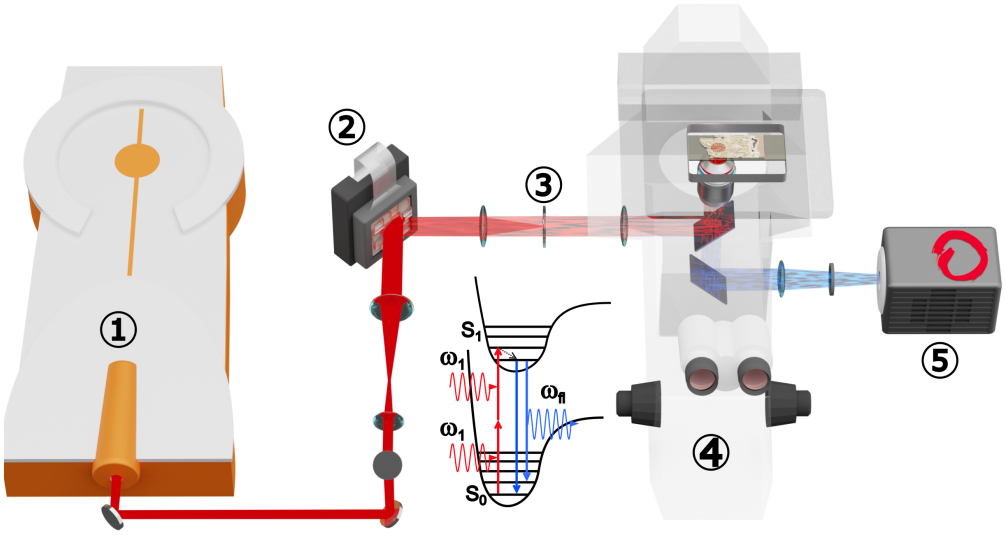


FIGURE 1.8 – Experimental setup of 2P-RIM. (1) A pulsed laser beam (low repetition rate fs-laser, 20W, 100kHz, 350fs, 1030nm) goes through a (2) diffuser (Spatial light modulator displaying random patterns, combined with (3) a zero-order stop) placed at a conjugated back-focal plane of the objective of a (4) standard microscope in epi-configuration. The 2P fluorescence is collected on a (5) scientific camera.

About 500 to 1000 raw speckled images are generally recorded. The sample placed at the focal plane, consist in U2OS cells or fern leaves. The excitation wavelength is $1030nm$ and emitted wavelength is $600nm$. The RIM reconstruction process consisted in prefiltering each raw images, forming the standard deviation and using the std-matching procedure presented in (GIROUSSENS et al. 2024) with the speckle autocorrelation function and PSF adapted to the two-photon configuration.

We display the averaged prefiltered speckled images and RIM recosntructions in Fig. 1.9. The average image can be considered as the image of a standard wide-field two-photon or equivalently one-photon microscopy (under homogeneous illumination) because the average of the speckle intensity or square of intensity is quasi-homogeneous. It serves as a basis for estimating the resolution gain. In Fig. 1.9(a), RIM can distinguish two filamentous structures separated by $300nm$ that are inseparable

in the averaged image. In Fig. 1.9(b), RIM achieves visualization of granular structures within chloroplasts. It demonstrates a significant improvement in lateral resolution for two-photon RIM in wide-field microscopy.

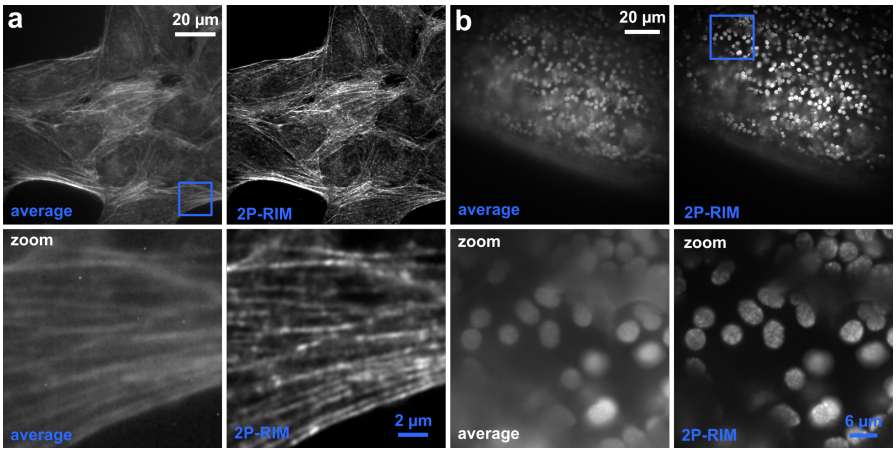


FIGURE 1.9 – Comparison of 2P-average and 2P-RIM images of fixed biological samples : (a) Images of actin labeled (AlexaFluor 568 phalloidin) U2OS cells illuminated at $2\lambda_{il} = 1030nm$. 500 raw speckled images were recorded. In the zooms, we can see that 2P-RIM can distinguish several actin filaments in places where 2P-average shows only one large filament. (b) Images of the autofluorescence of a fern leaf illuminated at $2\lambda_{il} = 1030nm$. 500 raw speckled images were recorded. Contrary to 2P-average, 2P-RIM enables the visualization of the grana inside the chromoplasts.

## 1.4 Adapting 2D RIM to 3D RIM

We have discussed the fundamentals of RIM, its reconstruction process, and the extension of one-photon RIM to two-photon RIM. But these implementation assume that the sample is a thin slice localized at the focal plane, the signal coming from out-of-focus planes being regarded as noise. However, in most cases, the sample is 3D. So, how can we access the 3D information of a sample with RIM?

An intuitive approach consists in translating the sample or objective lens through the focal plane and reconstructing each slice independently. The 3D reconstruction is then obtained by stacking the different reconstructed slices, as shown in (MANGEAT et al. 2021). Although this method is feasible, it is not optimal, as the out-of-focus signal, which carries useful information on the out-of-focus fluorophores is discarded. Also, 2D RIM is based on a 2D modeling of the speckle, sample and PSF. Now, even if only one image at the focal plane is recorded, the speckle, sample and PSF are 3D. Accounting for the 3D nature of these features should improve the accuracy of the model and hopefully the reconstruction.

To obtain accurate 3D sample information, it has been proposed to form volumetric

reconstruction using hundreds of 3D images captured under 3D random illumination (GIROUSSENS 2024). To adapt the RIM reconstruction to the 3D configuration, the 3D images were recorded using a remote focusing technique which ensures that the speckled illumination of the sample remains the same during the 3D recording. The configuration is depicted on Fig. 1.10.

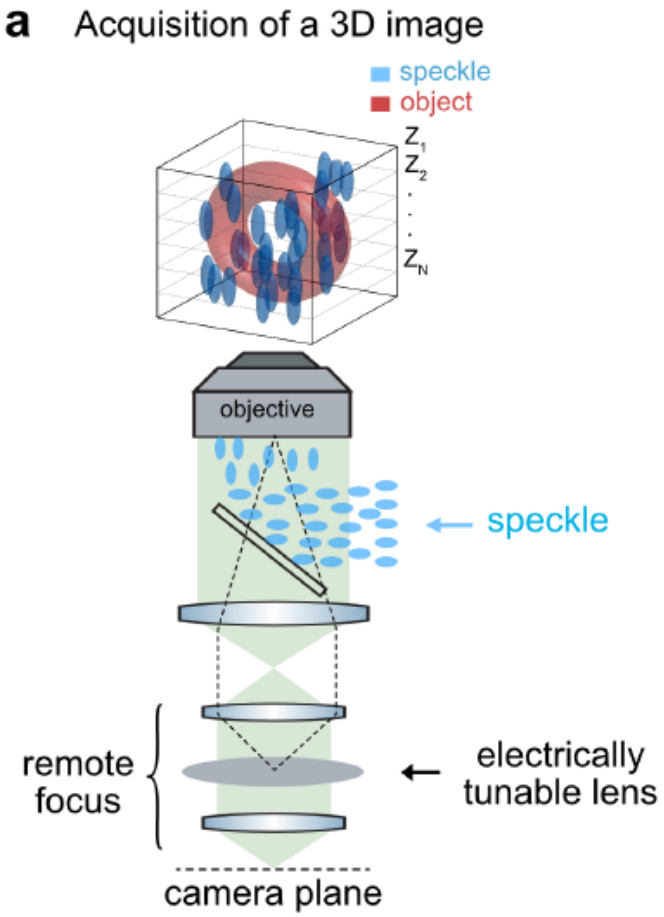


FIGURE 1.10 – Schematic of the 3D-RIM set-up. The sample (here a FtsZ : GFP fusion in a live Streptococcus pneumonia bacterium during cell division ring) is excited by a speckled illumination. A remote focusing unit, using an electrically tunable lens, permits to record z-stack images while keeping the illumination of the sample unchanged. Multiple (100 to 200) low-resolution 3D speckled images of a sample are recorded under different random speckled illuminations. The super-resolved 3D image is obtained from the variance of the speckled images using the RIM algorithm.

Using this specific recording configuration, the modeling of each 3D speckled image can be modeled as Eq. (1). The adaptation of the 2D RIM reconstruction scheme to the 3D configuration amounts to replacing the 2D sample, PSF and speckle autocovariance

by their 3D counterparts. This work was initiated by Guillaume Giroussens during his thesis and he obtained the first 3D reconstructions of 3D samples (GIROUSSENS 2024). It was observed that the preprocessing of the 3D raw speckled images was a key step for the success of the reconstruction as it removed the noise and enhanced the fluorescence signal stemming from the bright speckle grains.

### 1.4.1 An iterative filter for preprocessing the raw speckled images

Up to now, the preprocessing of the raw speckled images consisted in a Wiener filtering, Eq. (16). One way to perform this Wiener filtering is to minimize a quadratic criterion that reads

$$F(x) = ||y - Hx||^2 + \eta||x||^2 \tag{19}$$

where $x = \rho|E|^2$, $y$ is the observed image, $H$ is defined as a convolution operator so that $Hx = h * x$. The reconstructed sample $\rho$, PSF $h$, speckled illumination $|E|^2$, and the collected data belong to the same domain $\Omega_{\text{obs}}$.

When the criterion reaches its minimum, $\hat{x} = (H^\dagger H + \eta)^{-1} H^\dagger y$, where $H^\dagger$ is the adjoint operator of $H$. In the Fourier domain, the minimizer $\tilde{\hat{x}}$ reads $\tilde{\hat{x}} = \frac{\tilde{h}^* \tilde{y}}{|\tilde{h}|^2 + \eta}$, which is the same as adding the Wiener filter in Eq. (16).

Now this fast Fourier processing can, in principle, be used only if $y$ (and consequently $\rho E$) are equal to zero at the edges of the images (and beyond). In other terms, the image $y$ should be recorded over a domain that is larger that the whole size of the sample. This is generally not the case : $y$ is not equal to zero at the edges of the image because of the fluorescence signal coming from fluorophores laying outside the domain of observation. In 2D imaging, this is not a significant issue because the FOV is sufficiently large, typically 1000 by 1000 pixels. On the other hand, it becomes a major problem in 3D imaging especially along the $z$ axis, as only a few z-planes (10-100) are generally recorded. In the following, we have developed an iterative prefilter that enables preprocessing within the limited z-layer information.

As shown in Fig. 1.11, we consider a configuration in which the sample (i.e. the unknowns) belongs to a large domain $\Omega$, while the observation image (i.e. the data) belongs to a smaller domain $\Omega_{\text{obs}}$. The preprocessing is performed through a minimisation procedure, following Eq. (19) in which the fluorescence signal $I$ and object $\rho E$ are defined over $\Omega$ while the norm is defined over $\Omega_{\text{obs}}$.

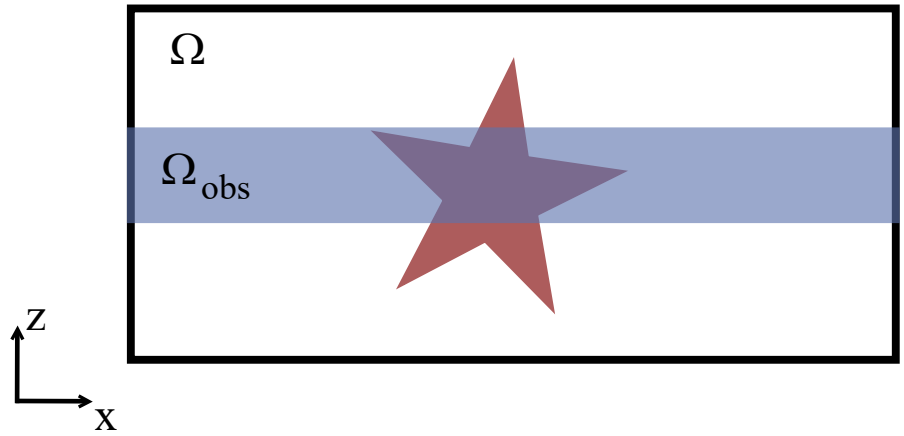


FIGURE 1.11 – In 3D RIM data acquisition, we typically collect only data from domain $\Omega_{\text{obs}}$, whereas the fluorescence process occurs in domain $\Omega$. Therefore, the recorded image can be understood as data collected in the larger domain $\Omega$ times a mask, which belongs to domain $\Omega$ and is zero everywhere except in $\Omega_{\text{obs}}$ where it equals one.

More precisely, the criterion (Eq. (19)) of the preprocessing minimization problem becomes :

$$F(x) = ||M(y - Hx)||^2 + \eta||x||^2 \tag{20}$$

where the operator $M$ is built such that $M(r) = 1$ if $r \in \Omega_{\text{obs}}$ and 0 elsewhere. The minimizer of Eq. (20) is explicit and reads

$$\hat{x} = (H^\dagger M^\dagger M H + \eta)^{-1} H^\dagger M y \tag{21}$$

However, due to the expensive computation, the minimizer Eq. (21) cannot be directly obtained by FFT, as in the minimizer of Eq. (19). Therefore, the state-of-the-art approach to solve this least-square problem is by preconditioned conjugate gradient method. In our case, the preconditioner is taken as, $N = H^\dagger M^\dagger M H + \eta$.

The detailed algorithm is as follows :

**Algorithm 1** Preconditioned conjugate gradient algorithm

Initialization : $r_0 = q - QX_0$, $z_0 = N^{-1}r_0$, $p_0 = z_0$, $k = 0$
**repeat**
  $\alpha_k = \frac{r_k^\top z_k}{p_k^\top Q p_k}$
  $X_{k+1} = X_k + \alpha P_k$
  $r_{k+1} = r_k - \alpha Q p_k$
  $z_{k+1} = N^{-1} r_{k+1}$
  $\beta_k = \frac{z_{k+1}^\top r_{k+1}}{z_k^\top r_k}$
  $p_{k+1} = z_{k+1} + \beta_k p_k$
  $k \leftarrow k+1$
**until** convergence

where $Q = H^\dagger M^\dagger M H$, $q = H^\dagger M^\dagger y$, and neither the computation nor the storage of $Q$ is actually required, and $Qp_k$ can be performed by FFTs. This approach yielded a significant improvement in the prefiltering of the raw 3D speckled images. A comparison with the preprocessing method using a Wiener filter will be presented in the next subsection. This method better deals with the case where data exists at the boundaries of the image, a common occurrence in 3D RIM.

## 1.4.2 Experiments

In this section, we demonstrate the transverse and axial resolution of 3D-RIM reconstructions and compare them with the 3D widefield image and the image formed by stacking multiple 2D-RIM reconstructions. The experiment were performed by T. Mangeat at the CBI Toulouse.

Fig. 1.10 shows the experimental configuration in which the axial scan is performed remotely using a tunable lens. The sample consists in live Streptococcus pneumonia bacteria. We used 100–200 random illuminations at an excitation wavelength of $488nm$. The emission wavelength is about $522nm$ and the NA of the objective is 1.49. The averaged raw speckled images (similar to 3D widefield microscopy using homogeneous illumination) and the 3D-RIM reconstruction are shown in Fig. 1.12. 3D-RIM brings about a spectacular improvement in the transverse and axial resolutions, up to $120nm$ and $300nm$ respectively.

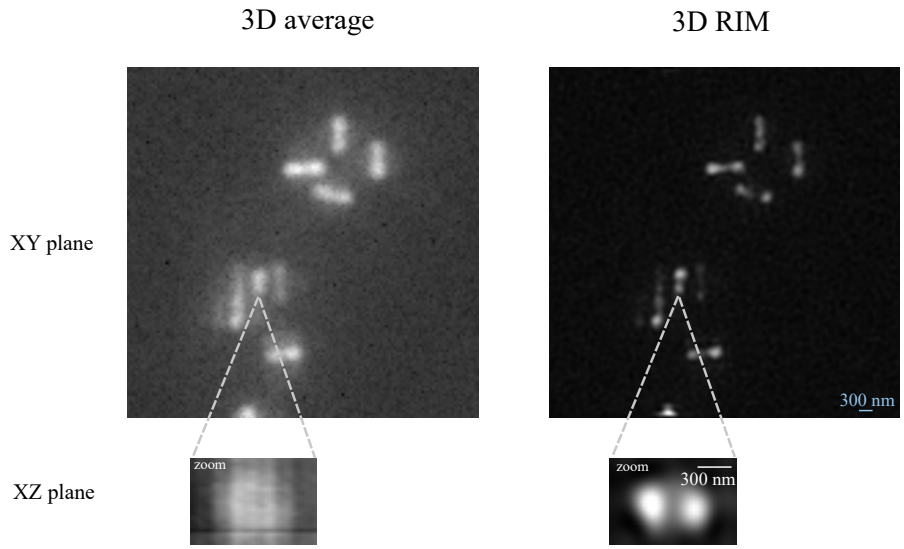


FIGURE 1.12 – The comparison of average image and RIM image in 3D. FtsZ :GFP fusion in a live Streptococcus pneumonia bacterium during cell division (the excitation and emission wavelengths are $\lambda_{exc} = 488nm$ and $\lambda_{em} = 522nm$ respectively, the objective numerical aperture (NA) is 1.49). Images at xy plane : one XY cut of the deconvolved widefield 3D image, the same cut imaged by 3D-RIM. Images at xz plane : one XZ cut of one ring for the averaged image, the same cut in 3D-RIM image. In sharp contrast with the deconvolved widefield images, the ring structure is well seen in the 3D RIM images and the internal hole can even be suspected when the ring structure shrinks to a total diameter of 230 nm.

To compare the differences between iterative filtering and Wiener filtering, we clipped three layers from the top and bottom of the original data in Fig. 1.12 to ensure sufficient data at the edges of the raw image, better aligning with biological sample data. Fig. 1.13 shows the results from both methods. The left image, similar to Fig. 1.12, achieved an axial resolution of approximately $300nm$. The right image, however, shows two structures due to edge data, but only one actually exists. This further underscores the importance of iterative algorithms in 3D RIM preprocessing, as obtaining the entire z-axis information is often challenging.

Next, we compare the transverse and axial resolutions of 3D RIM to those of the slice by slice reconstruction using 2D RIM, in Fig. 1.14. In the previously analyzed 2D-RIM approach (MANGEAT et al. 2021), a lateral resolution similar to that of periodic-SIM (about 120 nm) was already achieved. 3D-RIM not only maintains this high transverse resolution without loss but also delivers a significantly higher axial resolution and contrast than slice by slice 2D-RIM.

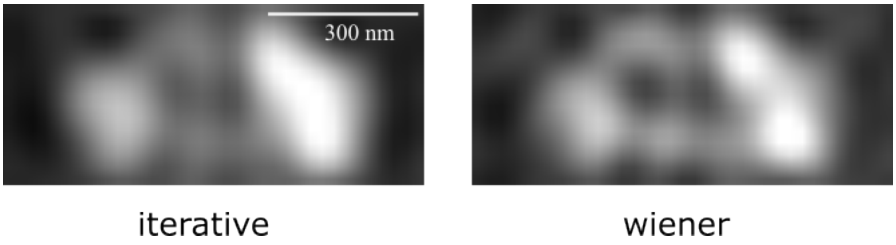


FIGURE 1.13 – Comparison of 3D RIM with iterative filter and Wiener filter by clipping three layers from the top and bottom of the original data in Fig. 1.12. The left figure : 3D RIM result obtained by iterative filter, which is very similar to the right figure in Fig. 1.12. The right figure : 3D RIM result obtained by Wiener filter, we observed two non-existent structures due to the Wiener filter's susceptibility to edge data.

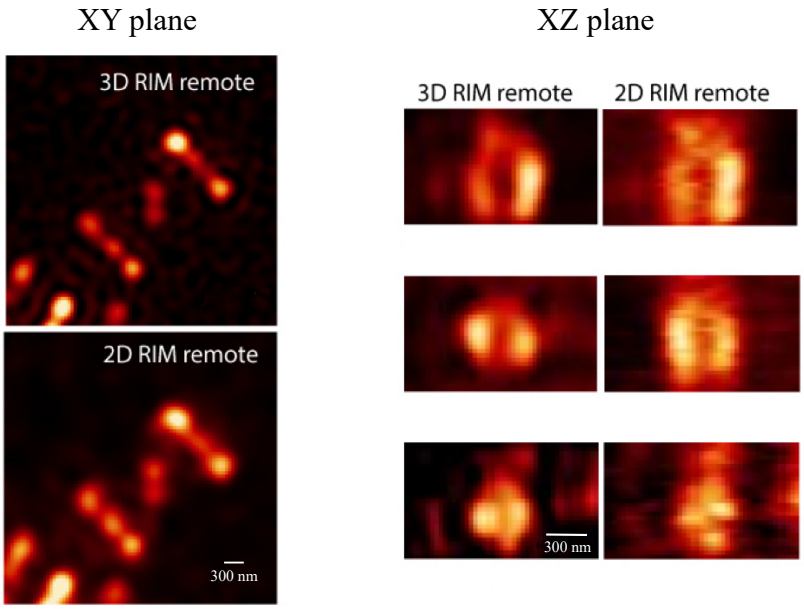


FIGURE 1.14 – Comparison of 3D RIM and 2D RIM with the same sample as in Fig. (1.12). The left figures : the comparison of 2D RIM and 3D RIM at the xy plane, both of them provide a super-resolution at the xy plane. The right figures : the comparison of 2D RIM and 3D RIM at the xz plane, where 3D-RIM provided a better image contrast and resolution.

## 1.5 Conclusion

In this chapter, I recalled the principles of RIM for super-resolved fluorescence imaging and detailed RIM inversion procedure. In the first part, I adapted the reconstruction scheme to the two-photon configuration. This adaptation required the

modeling of the autocorrelation of the square intensity of speckles. It was observed that two-photon RIM resolution was not as good as that of one-photon RIM because of the fastest decay of the two-photon autocorrelation spectrum compared to the one-photon one. Actually, two-photon RIM is mainly interesting for its better imaging of dense thick samples than one-photon RIM. Indeed the two-photon speckles being sparser than the one-photon one, it causes less out-of-focus background and less associated noise. Now the background noise is the main issue of RIM. When its variance is higher than the variance due to the speckle change, the reconstruction fails. This point is detailed in Assia Benachir thesis who conducted the experiments and studied the two-photon configuration in details.

In the second part, I have addressed an issue in the adaptation of RIM to 3D configurations. The key feature of 3D-RIM data processing lays in the 3D Wiener prefiltering of the 3D images. To preprocess images where the collected z-layer of images is typically less than the actual z-axis information length of the sample, I have developed an iterative prefiltering technique based on the minimization of a cost functional that dissociates the observation domain from the sample domain and removes the edge artefacts. This iterative preprocessing has been included in the 3D-RIM reconstruction technique and applied to experimental data. We show that a global 3D-RIM data processing improves significantly the 3D super-resolved image of a sample than a slice by slice 2D-RIM reconstruction.

# 2 Scalable isotropic resolution in scanning two-photon microscopy using focused random illumination

## Sommaire


2.1 Introduction . . . . . 44
2.2 Scanning two-photon microscopy . . . . . 46
2.3 Enlarging the excitation volume quasi-isotropically using speckled focused beams . . . . . 48
2.3.1 Modeling a focused speckled beam and its analytical optical sectioning . . . . . 50
2.3.2 Simulations . . . . . 52
2.4 Experiments . . . . . 55
2.4.1 A diffuser is placed at a conjugated Fourier plane before a field diaphragm . . . . . 55
2.4.2 The diffuser is moved throughout a slightly focused beam to control the speckle correlation at the pupil plane . . . . . 58
2.5 Conclusion . . . . . 62


## 2.1 Introduction

2PM is a major tool for biological applications thanks to its ability to image hundreds of microns deep into live biological tissues with sub-micrometric resolution in the three dimensions of space (HELMCHEN et al. 2005; SVOBODA et al. 2006; RUBART 2004). In most 2PM, the sample is scanned by a focused pulsed laser, and the emitted fluorescent light is detected on a large unique detector (often a photomultiplier). The main assets of scanning 2PM are its optical sectioning ability, its insensitivity to aberrations and scattering on the collection side and the penetration depth of the incident infrared light which is less sensitive to scattering than its visible counterpart (DENK et al. 1990). The resolution of scanning 2PM is dictated by the dimensions of the infrared light spot. Scanning 2PM is usually implemented in an epifluorescence configuration with high NA objectives able to concentrate the infrared photons in tiny volumes (about $0.3\mu m$ and $1\mu m$ in the transverse and axial directions respectively for

$\lambda \approx 1\mu m$ and NA $\approx 1$). High NA objectives reduce the collection loss of fluorescence photons due to their large acceptance angle, and yield highly resolved images but are plagued by relatively small FOV (a few microns) due to their short working distance. In addition, the detected fluorescence signal scaling with the tiny excitation volume, the pixel acquisition time must be long enough to get a sufficient signal-to-noise ratio. As a result, scanning 2PMs are hardly adapted to the fast imaging of large areas (MERTZ 2019).

This major issue has stirred a wealth of research either oriented towards camera-based widefield two-photon microscopy techniques (WOLF et al. 2017; PAPAGIAKOUMOU, RONZITTI et al. 2020) or complex instrumentations for imaging simultaneously or sequentially different regions of the sample (OTA et al. 2022; SOFRONIEW et al. 2016; TERADA et al. 2018). Unfortunately, the former is not adapted to deep imaging due to the scattering-induced degradation of the collection PSF while the latter remains hampered by the mounting complexity and still limited by the scanning speed (OTA et al. 2022; SOFRONIEW et al. 2016; TERADA et al. 2018).

Now, fast, gentle imaging of large sample areas could be obtained using standard scanning 2PMs by simply increasing the size of the excitation volume. Enlarging the transverse and axial dimensions of the light probe from $0.3 \times 0.3 \times 0.8\mu m^3$ to $3 \times 3 \times 3\mu m^3$, for example, would increase the number of excited fluorophores by more than two orders of magnitude and allow reducing the power density (or the integration time) and the number of scan steps.

The ability to increase the two-photon excitation volume is all the more interesting than important applications, such as the observation of neurons' activity (the neuron volume is about $1000\mu m^3$), do not require the present sub-micrometric resolutions (SITÀ et al. 2022). Yet, even for these applications, the excitation spot transverse width of the scanning 2PM is seldom chosen above one micron (TSAI et al. 2015). The historical reason for this high-focus mode was to achieve sufficient local power density with the pulsed lasers of the time. Now that high-power lasers are commercially available, the main reason is that one cannot enlarge the transverse dimension of a focused beam without affecting the axial one. The former is inversely proportional to the NA, whereas the latter is inversely proportional to the square of the NA (THEER et al. 2005). A focused beam of waist $0.3\mu m$ (with $\lambda \approx 1\mu m$) excites the two-photon fluorescence over a depth of about $0.8\mu m$. A focused beam of waist $3\mu m$ excites the two-photon fluorescence over a depth of about $81\mu m$.

In this chapter, we show how quasi-isotropic two-photon excitation volumes of any micrometric size can be formed using high-NA objectives and random speckled illumination. We analyze theoretically and experimentally the properties of focused random illumination. This approach paves the way towards scanning 2PM with scalable isotropic micrometric resolution, high collection efficiency, and fast scanning over large FOVs.

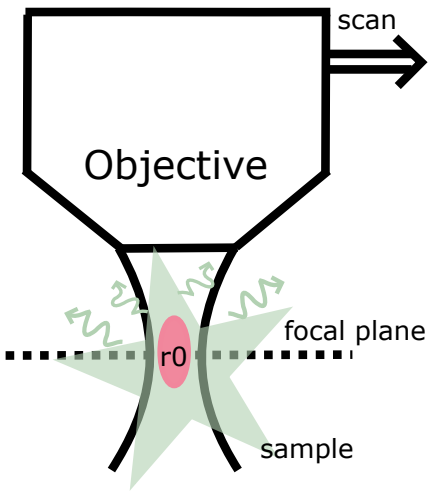


FIGURE 2.1 – Configuration of scanning 2PM. A high NA objective focuses the light into a sub-micrometric volume and scans the sample.

## 2.2 Scanning two-photon microscopy

In scanning 2PM, the sample is labeled with fluorophores and illuminated with a focused infrared light pulse. When two infrared photons hit a fluorophore simultaneously, the latter may emit a visible photon, which corresponds to the fluorescence signal, as Fig. 2.1 shows. Moreover, the signal collected by the detector in a scanning 2PM is proportional to the volume integral of the fluorescence density $\rho$ times the square of the field intensity $I_{2\mathrm{PE}} = |E|^4$, where $E$ is the complex representation of the incident electric field (which is assumed to be scalar and monochromatic of center wavelength $\lambda$, the pulse duration being orders of magnitude longer than the wave period) (MERTZ 2019). More precisely, the signal recorded at the focus position $(\boldsymbol{x}_0, z_0)$ can be written as [1],

$$S(\boldsymbol{x}_0, z_0) \propto \int |E|^4(\boldsymbol{x}' - \boldsymbol{x}_0, z' - z_0)\rho(\boldsymbol{x}', z')\mathrm{d}\boldsymbol{x}'\mathrm{d}z', \tag{22}$$

where $(\boldsymbol{x}', z')$ presents the position in the sample space.

Thus, the PSF of scanning 2PM is given by the square of the incident field intensity $|E|^4$. The incident field reads,

$$E(\boldsymbol{x}, z) = \int p(\boldsymbol{\kappa}) e^{i(\boldsymbol{\kappa}\cdot\boldsymbol{x} + \gamma(\boldsymbol{\kappa})z)}\mathrm{d}\boldsymbol{\kappa}, \tag{23}$$

where $p(\boldsymbol{\kappa})$ corresponds to the pupil function of the objective [2], $\gamma(\boldsymbol{\kappa}) = \sqrt{k^2 - \boldsymbol{\kappa}^2}$, $k = \frac{2\pi}{\lambda}$ and $z = 0$ corresponds to the objective focal plane. To simplify the derivation,

1. In this Chapter, $\boldsymbol{x}$ and $z$ denote the transverse variable and axial variable respectively.
2. $p(\boldsymbol{\kappa}) = 1$ for $\boldsymbol{\kappa} < \frac{2\pi \mathrm{NA}}{\lambda}$ and 0 elsewhere.

we use a Gaussian approximation for the pupil function

$$p(\boldsymbol{\kappa}) \approx e^{-m^2\boldsymbol{\kappa}^2} \tag{24}$$

with $m = \frac{\lambda}{2\pi \mathrm{NA}}$, and the paraxial approximation $\gamma(\boldsymbol{\kappa}) \approx k - \frac{\boldsymbol{\kappa}^2}{2k}$ (MERTZ 2019). Therefore, Eq. (23) can be simplified as a complex Gaussian integral :

$$E(\boldsymbol{x}, z) = \int p(\boldsymbol{\kappa}) e^{i[\boldsymbol{\kappa}\cdot\boldsymbol{x} + (k - \frac{\boldsymbol{\kappa}^2}{2k})z]} d\boldsymbol{\kappa} \tag{25}$$

The analytical expression for the PSF reads,

$$|E|^4(\boldsymbol{x}, z) \propto \frac{1}{q^2(z)} e^{-\frac{4}{q(z)}\boldsymbol{x}^2} \tag{26}$$

where $q(z) = 4m^2 + \mathrm{NA}^2 z^2$.

The transverse resolution $L$ is defined as the Full Width at Half Maximum (FWHM) of the PSF at the focal plane, $|E|^4(\boldsymbol{x}, 0)$, and can be written as inversely proportional to NA :

$$L = \frac{\sqrt{\ln 2}\lambda}{\pi \mathrm{NA}} \tag{27}$$

To estimate the optical sectioning, we now consider that the sample is a homogeneous fluorescent plane placed at $z$ from the focal plane and we calculate the fluorescence signal $S(z)$ which is the integration of the PSF over the transverse coordinate $\boldsymbol{x}$.

$$S(z) \propto \int |E|^4(\boldsymbol{x}, z) \mathrm{d}\boldsymbol{x} \propto \frac{1}{q(z)}. \tag{28}$$

This expression shows that the signal reaches its maximum when the fluorescent plane is at the focal plane $z = 0$. In addition, the optical sectioning $\Delta z$ defined as the FWHM of $S(z)$ can be calculated as inversely proportional to the square of NA, and is related to transverse resolution $L$ as follows

$$\begin{aligned} \Delta z &= \frac{2\lambda}{\pi \mathrm{NA}^2} \\ &= \frac{2\pi L^2}{\lambda \ln 2} \\ &\approx 10 \frac{L^2}{\lambda}. \end{aligned} \tag{29}$$

The relationship between optical sectioning and the transverse resolution $L$ (Eq. (29)) confirms that a slight increase of $L$ results in a significant deterioration of the optical sectioning. Using a NA of 1, the transverse resolution is about $0.3\mu m$ and its optical sectioning is about $0.81\mu m$. However, if we diminish NA to 0.1, the transverse resolution is about $3\mu m$, but the optical sectioning deteriorates up to about $100\mu m$. As Fig. 2.2 shows, this configuration can provide an acceptable optical sectioning only with a high NA.

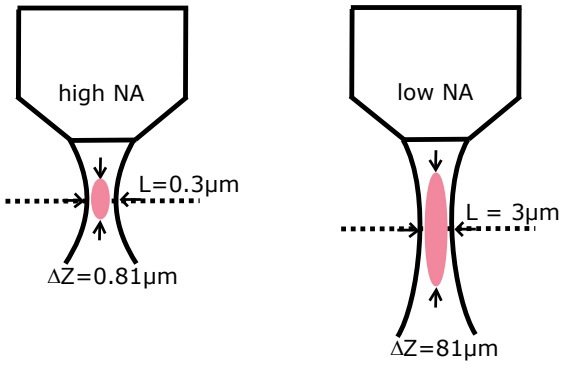


FIGURE 2.2 – Excitation volume for different NAs when $\lambda = 1\mu m$. Left image : NA is about 1, this is a sub-micrometric volume around the focus position in the sample space ; right image : NA is about 0.1, L increases to 3 $\mu m$, its optical sectioning becomes ineffective as it attenuates to 81 $\mu m$.

In addition, low NA objective is not as efficient as high NA objective for collecting the emitted light. These important drawbacks may explain why scanning 2PM is never used with low NA objectives, even if high power lasers are now available for triggering two-photon signal on a large domain, and sub-micrometric resolution is not necessary. One solution for enlarging the excitation volume while maintaining a reasonable axial resolution is to scan the sample with a highly focused beam over a predetermined micrometer domain during the detector integration time. However, this technique is expected to be slow and difficult to implement.

## 2.3 Enlarging the excitation volume quasi-isotropically using speckled focused beams

One intuitive idea for forming a quasi-isotropic excitation volume of micrometer size in 2PM would be to replace the coherent illumination by incoherent light sources placed at a conjugated image plane of a high NA objective. The field of each incoherent point source would fill the whole pupil and be focused on the sample plane with a good axial resolution. By setting the transverse width of the incoherent source equal to the targeted micrometric resolution, one would obtain a micrometric excitation volume with good optical sectioning, see Fig. 2.3. However, there are no incoherent point sources that are powerful enough to generate two-photon fluorescence, so our proposition consists in mimicking the incoherent point sources by scattering the laser pulse into rapidly changing speckle grains.

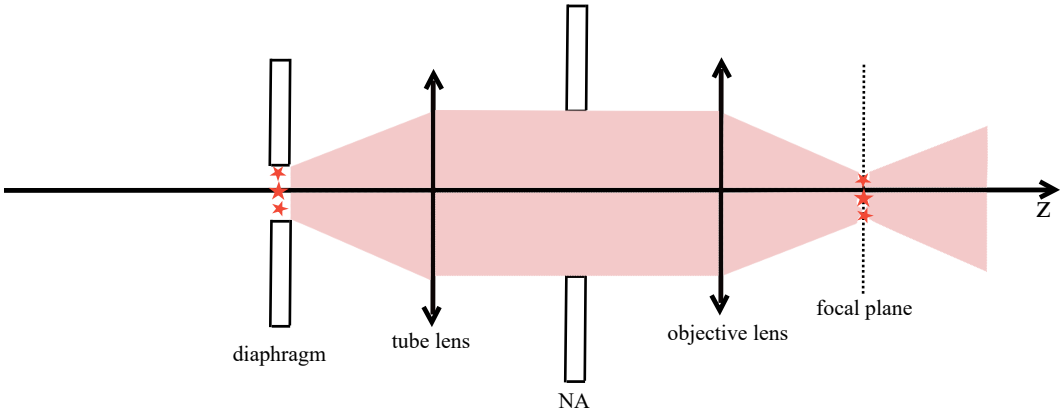


FIGURE 2.3 – The field at the objective focal plane is generated by multiple incoherent point sources diffracting, filling the whole pupil plane, and refocusing onto the sample plane.

Fig. 2.4 illustrates a possible experimental configuration for forming a speckled focused beam by mimicking the incoherent sources of finite width : we use a diffuser to project an uncorrelated random field onto a field diaphragm (placed at a plane conjugated to the objective focal image plane).

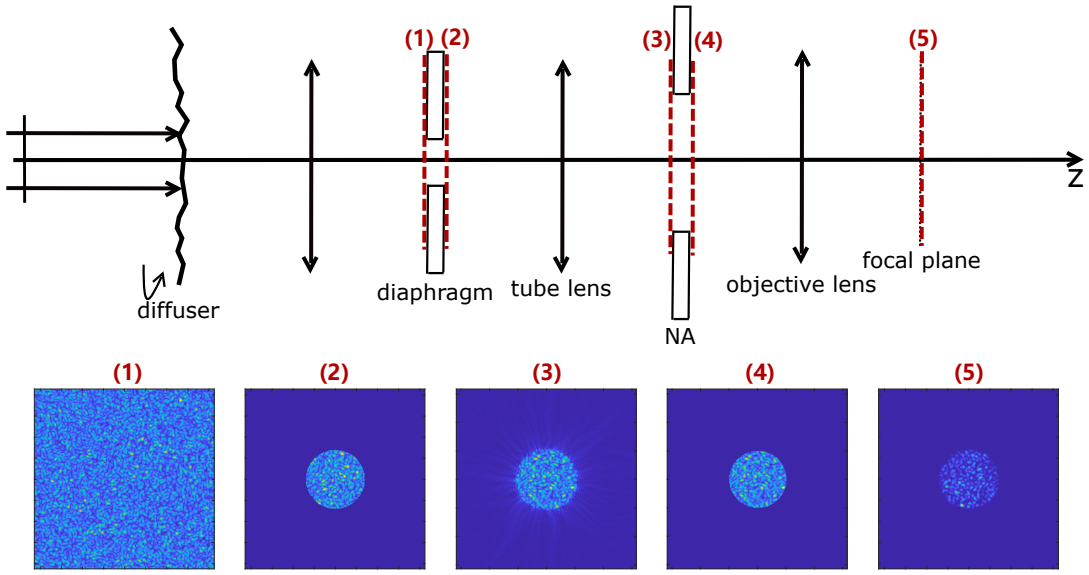


FIGURE 2.4 – Proposed configuration for forming a focused speckled illumination. A diffuser generates a random field that is cut by a field diaphragm. The field diaphragm is imaged by the objective on the sample space. The bottom row displays the simulated field intensity at the different planes indicates by numbers 1 to 5. The focused speckled beam can be observed at the objective focal plane (5).

In the following section, we model the excitation volume that is obtained with a

focused speckled beam.

### 2.3.1 Modeling a focused speckled beam and its analytical optical sectioning

We consider the configuration depicted in Fig. 2.4 where the diffuser and field diaphragm are placed at the back and front focal planes of a lens respectively. The diffuser is illuminated by a plane wave and generates an uncorrelated random complex field $E$ at the diaphragm plane, $\langle E(\boldsymbol{x}_1)E^*(\boldsymbol{x}_2)\rangle = \delta(\boldsymbol{x}_1-\boldsymbol{x}_2)$ where $\langle\rangle$ stands for averaging over many realizations of the diffuser roughness. The diaphragm is conjugated to the objective image focal plane. Just after the diaphragm, the field reads $D \times E$[3] where $D$ is the diaphragm characteristic function. Hereafter, to simplify the analytical calculations, the diaphragm function is assumed to be a Gaussian, $D(\boldsymbol{x}) = e^{-\frac{4x^2}{l^2}}$ where $l$ is the diaphragm size. At the pupil plane (Fourier plane) of the objective, we get the Fourier transform of $E \times D$. It is a correlated random variable $\eta$ which satisfies,

$$\langle \eta(\boldsymbol{\kappa}_1)\eta^*(\boldsymbol{\kappa}_2)\rangle = C(\boldsymbol{\kappa}_1-\boldsymbol{\kappa}_2) \propto e^{-d^2|\boldsymbol{\kappa}_1-\boldsymbol{\kappa}_2|^2}. \tag{30}$$

with $d^2 = \frac{l^2}{32}$.

Thus, the diaphragm transforms the uncorrelated field at the diaphragm plane into a correlated random field $\eta$ at the pupil plane. Then, after the objective, in the sample space, (and assuming a magnification of one), the field reads,

$$E_{\mathrm{FS}}(\boldsymbol{x},z) = \int p(\boldsymbol{\kappa})\eta(\boldsymbol{\kappa})e^{i(\boldsymbol{\kappa}\cdot\boldsymbol{x}+\gamma(\boldsymbol{\kappa})z)}\mathrm{d}\boldsymbol{\kappa} \tag{31}$$

where we recall that $\gamma(\boldsymbol{\kappa}) = \sqrt{k^2-\boldsymbol{\kappa}^2}$. In Fig. 2.5, we simulate the field at the pupil plane and at the objective focal plane for various correlation widths (speckle grain size at the Fourier plane) of the random field at the pupil plane, Eq. (30), corresponding to various widths of the diaphragm $l$.

Fig. 2.5 illustrate the correspondence between the field correlation at the pupil (or Fourier) plane and the size of the focused beam at the sample plane. If the field at the pupil plane is a constant (corresponding to a diaphragm almost closed), the field at the sample plane is a tiny focused spot. If the field at the pupil plane is an uncorrelated variable (corresponding to a entirely opened diaphragm), the field at the sample plane is a widefield speckle. The larger the correlation width, the smaller the focused spot.

We now study the fluorescence signal stemming from a sample depicted by $\rho$, that is recorded by the detector when the excitation is averaged over many realizations of the random field,

$$\langle S\rangle(\boldsymbol{x},z) \propto \int \langle |E_{\mathrm{FS}}|^4\rangle(\boldsymbol{x}'-\boldsymbol{x},z'-z)\rho(\boldsymbol{x}',z')\mathrm{d}\boldsymbol{x}'\mathrm{d}z'. \tag{32}$$

3. × denotes multiplication

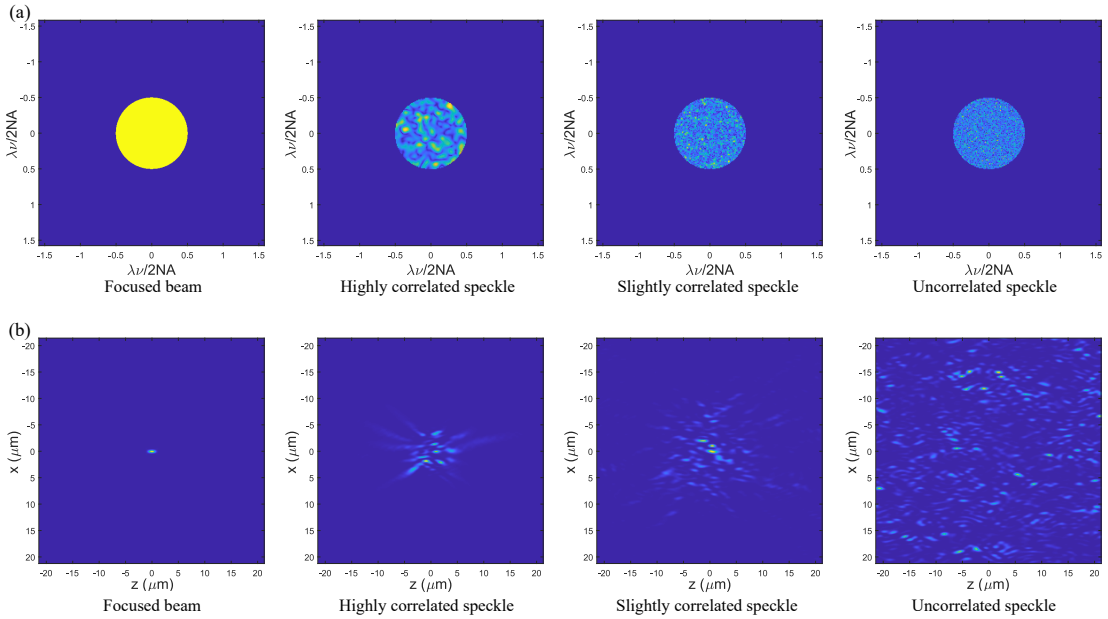


FIGURE 2.5 – Field modulus at the pupil plane $|\mathscr{F}(E_{\mathrm{FS}}(x,y,0))|$ and square of the light intensity (two photon intensity : $|E_{\mathrm{FS}}|^4(x,0,z)$) formed by a high NA objective (NA=0.95) for different correlation lengths. (a) : $|\mathscr{F}(E_{\mathrm{FS}}(x,y,0))|$ simulated by Eq. (31) for various correlation lengths. From left to right : the first image shows that the field is uniform at the pupil plane, $\nu(\boldsymbol{\kappa})$ is a constant. The second and third images illustrate the cases where the field is a correlated random variable at the pupil plane; The last image displays that the field is an uncorrelated random variable at the pupil plane. (b) : The two-photon intensity $|E_{\mathrm{FS}}|^4(x,0,z)$ simulated by Eq. (31), following the same sequence as in Fig. a. The first image : two-photon excitation is a tiny spot located at the focal plane. The second image : speckles are highly correlated. The third image : speckles are slightly correlated. The last image : one obtains statistically uniform random speckles in the object space.

where $\langle\rangle$ indicates the average taken over many realizations of the speckles. We observe that $\langle|E_{\mathrm{FS}}|^4\rangle$ plays the role of PSF.

Using the property of the circular complex random variable, $\langle|E_{\mathrm{FS}}|^4\rangle = 2\langle|E_{\mathrm{FS}}|^2\rangle^2$, and using the paraxial approximation, we obtain and analytic expression for the PSF,

$$\langle|E_{\mathrm{FS}}|^4\rangle(\boldsymbol{x},z) \propto \frac{1}{A^2(z)} e^{-\frac{\boldsymbol{x}^2}{2A(z)}} \tag{33}$$

where $A(z) = \frac{\mathrm{NA}^2 z^2}{8} + d^2 + \frac{m^2}{2}$.

To estimate the optical sectioning, we consider a sample made of a homogeneous

fluorescent plane placed at $z$. The collected signal for each $z$ position is given by,

$$S_{\mathrm{FS}}(z) \propto \int \langle |E_{\mathrm{FS}}|^4 \rangle(\boldsymbol{x}, z) \mathrm{d}\boldsymbol{x} \propto \frac{1}{A(z)}. \tag{34}$$

Then, the optical sectioning can be expressed as a function of NA and the correlation as,

$$\Delta z_{\mathrm{FS}} = \frac{4\sqrt{2d^2 + m^2}}{\mathrm{NA}} \tag{35}$$

We observe that $\Delta z_{\mathrm{FS}}$ tends towards infinity when $d$ tends to infinity (i.e. when the diaphragm is entirely opened and the field becomes uncorrelated at the Fourier plane). Indeed, in this case, the random field in the sample space corresponds to that of a fully developed speckle and its statistics are the same whatever the $z$ position, so that there is no optical sectioning.

We now define the transverse resolution of the PSF as the FWHM of $\langle |E_{\mathrm{FS}}|^4(\boldsymbol{x}, 0) \rangle$,

$$L = 2\sqrt{\ln 2 (2d^2 + m^2)} \tag{36}$$

As expected, we observe that $L$ increases with increasing $d$. Therefore, the relationship between the transverse resolution and optical sectioning can be given by

$$\Delta z_{\mathrm{FS}} = \frac{2L}{\mathrm{NA}\sqrt{\ln 2}} \approx 2.4 \frac{L}{\mathrm{NA}}. \tag{37}$$

where NA is controlled by the objective.

By comparing Eqs. (29, 37), we observe that the optical sectioning of a focused beam has a quadratic relationship with the transverse resolution, while the optical sectioning of a focused speckled beam has a linear relationship with the transverse resolution. Thus, the axial resolution of a scanning 2PM using a focused speckled beam remains reasonable even for micrometric transverse resolution as long as the objective NA is high. In the next section, we confirm these theoretical results with rigorous simulations without paraxial approximation and with realistic pupil functions.

### 2.3.2 Simulations

In this section, we simulate the field obtained under the configuration Fig. 2.4 with NA = 0.95 and $\lambda = 1\mu m$. Unlike theoretical derivations, we do not assume paraxial approximation. The pupil function is not Gaussian but a disk characteristic function, and the diaphragm can be simulated as a Gaussian or disk function. We observe that the shape of the diaphragm influences the shape of the focused speckled beam. When the diaphragm follows a Gaussian function, the average of hundreds of speckles at the sample plane also exhibits a Gaussian distribution, and the transverse resolution (FOV) is the FWHM of the intensity at the focal plane for a focused Gaussian speckle ($\langle |E_{\mathrm{FS}}|^4 \rangle(x, 0, 0)$). As shown in the left image of Fig. 2.6, with a diaphragm FWHM of approximately 11.9 micrometers, a Gaussian focused speckle with a FOV of roughly

5 micrometers can be generated. However, when the diaphragm is a disk function, the observed averaged speckles no longer follow a Gaussian distribution, but instead a top-hat distribution. For this top-hat focused speckle, its FOV is defined as the non-zero width of the focused top-hat speckle, which is approximately equal to the diaphragm width in the configuration (Fig. 2.4). For example, as illustrated in the right image of Fig. 2.6, both the diaphragm and FOV are 5 micrometers.

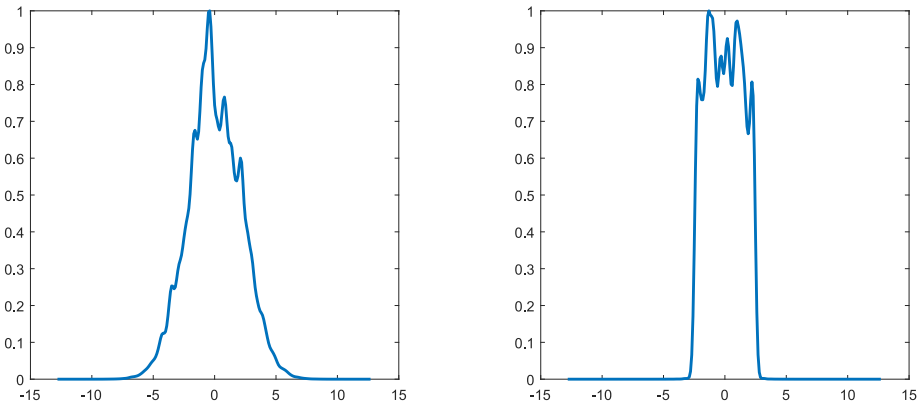


FIGURE 2.6 – Numerical simulation for average of 500 Gaussian focused speckles or top-hat focused speckles with the FOV of $5\mu m$ : $\langle |E_{\mathrm{FS}}|^4 \rangle (x,0,0)$, $\lambda = 1\mu m$, NA = 1. In the left image, the diaphragm follows a Gaussian distribution with the FWHM of the diaphragm is approximately 11.9 micrometers, yielding a Gaussian-focused speckle with a FWHM of 5 micrometers at the sample plane. However, the diaphragm in the right image is a disk whose size matches that of the focused speckle of the top-hat distribution, both being 5 micrometers.

For both shapes of the focused speckles, we consider the FWHM of integrated averaged intensity over xy plane ($\int \langle |E_{\mathrm{FS}}|^4 \rangle (\boldsymbol{x}, z) \mathrm{d}\boldsymbol{x}$) as optical sectioning (axial resolution). To investigate the relationship between the transverse resolution and axial resolution in Gaussian-focused speckles and top-hat focused speckles, we simulate 300 images with varying transverse dimensions for each shape. The results (Fig. 2.7) indicate that the optical sectioning of both types exhibits a linear relationship with the transverse resolution, differing only in their slopes : 0.6 and 2.3, respectively. In particular, the slope of Gaussian-focused speckles matches the theoretical slope of 2.4.

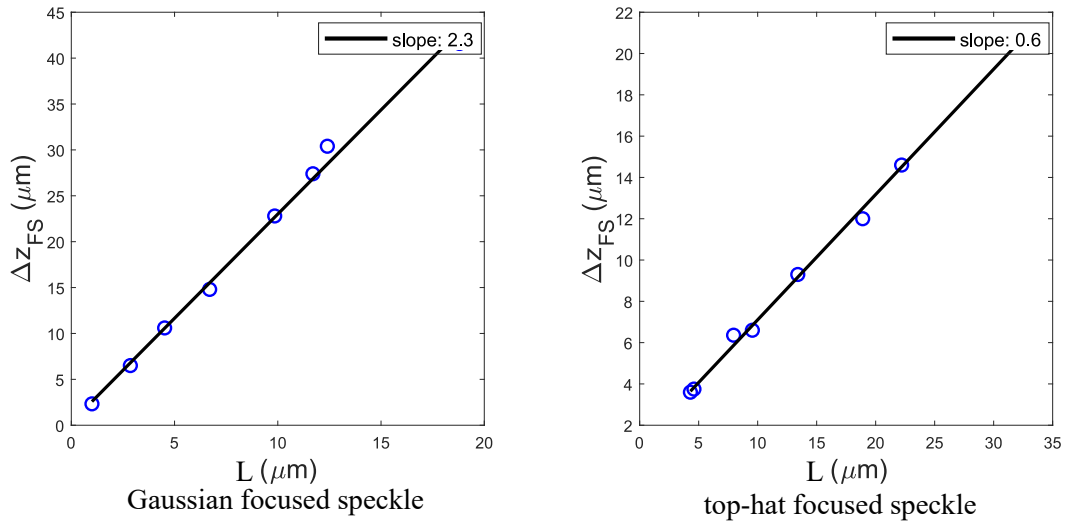


FIGURE 2.7 – The linear dependence between $L$ (transverse resolution) and $\Delta z_{FS}$ with NA = 0.95 and $\lambda = 1\mu m$ in numerical simulation. The left figure shows the focused speckle with a Gaussian shape : the slope is close to the theoretical constant in formula (Eq. (37)) : 2.4; if the focused speckles follow a top-hat shape, the constant is about 0.6, displayed in the right image. The slope ($\Delta z_{FS}/L$) really depends on the shape of focused speckle and the way to define $L$.

## 2.4 Experiments

The theoretical and numerical analysis was completed with experimental data. The experiments were realized by Federico Vernuccio, post doctorant and Assia Benachir, PhD student of Hervé Rigneault at Fresnel Institute.

### 2.4.1 A diffuser is placed at a conjugated Fourier plane before a field diaphragm

The first experiments were conducted using the configuration depicted in Fig. 2.4. The collimated beam is incident on the diffuser and collected by the objective lens after passing through a diaphragm. The transverse resolution is adjusted by manually tuning the aperture of the diaphragm, Fig. 2.8 shows the configuration.

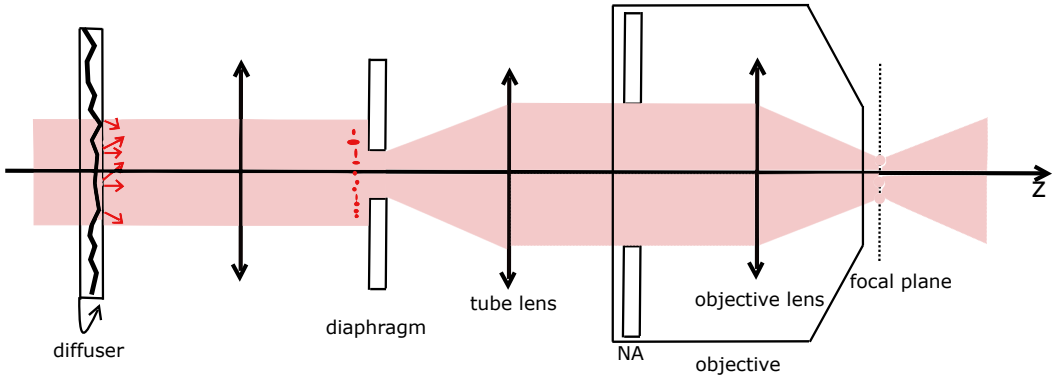


FIGURE 2.8 – Experimental configuration for focused speckle when the diffuser is placed at the Fourier plane in front of the diaphragm. Following the idea illustrated in Fig. 2.4.

To investigate the relationship between transverse resolution and optical sectioning capability, we recorded images at 200 z-positions with a step size of 1 micrometer. And we considered the average of 200 speckles. In the measurement of the focused beam, we removed the diffuser and measured transverse dimension and optical sectioning of the focused beam, as shown in Fig. 2.9(a). When the transverse dimension of the Gaussian beam is approximately $4\mu m$, its optical sectioning is poor, at about $160\mu m$, which is totally consistent with the formula (Eq. (29)). At the narrowest diaphragm width, we obtained an averaged speckle conforming to a Gaussian distribution. The averaged speckle, the transverse resolution, and decayed signal are shown in the Fig. 2.9(b). When $L$ is about $13\mu m$, we obtain an optical sectioning of $35\mu m$, which is perfect agreement with the theoretical calculations (Eq. (37)).

However, as the diaphragm width gradually increases, the beam no longer conforms to a Gaussian distribution but tends toward a top-hat distribution. Here, we observe that when $L$ is intermediate or large, the collected random illumination edges are

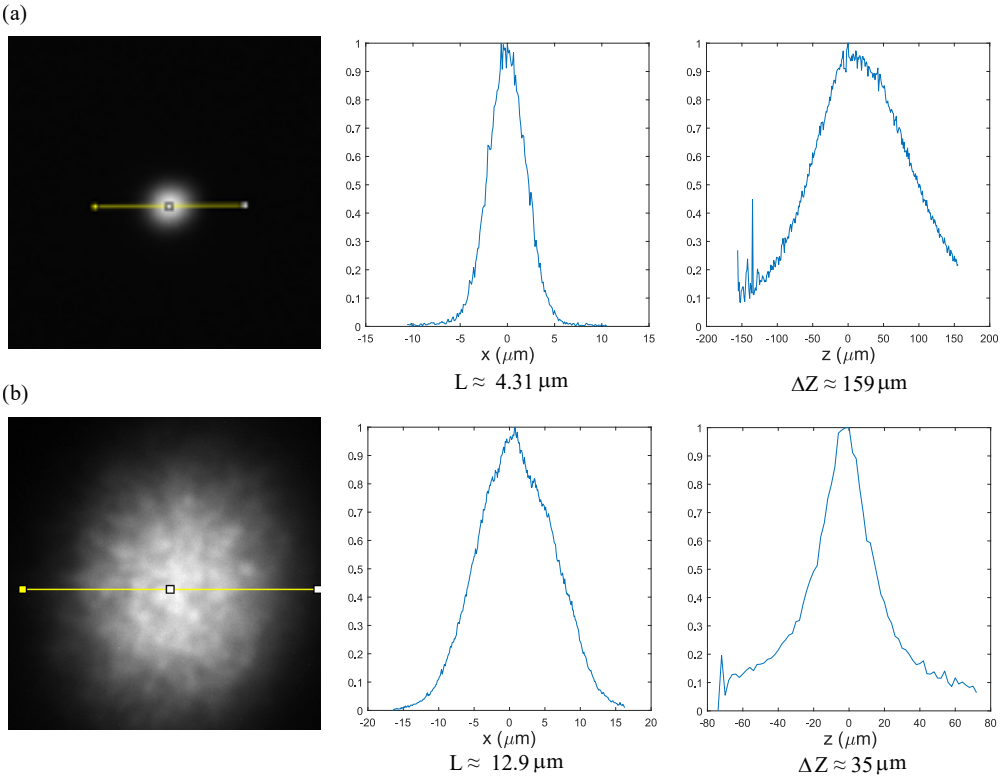


FIGURE 2.9 – Experimental data for Gaussian focused beam and Gaussian focused speckle. Fig (a) : the left image shows the Gaussian focused beam at the focal plane; the middle and right images illustrate the transverse resolution of approximately 4 micrometers and an optical sectioning of approximately 160 micrometers, respectively. This measurement perfectly matches the formula, equ(29). Fig (b) shows the Gaussian focus speckle at the objective focal plane, and when $L$ is about 13 micrometers, its optical sectioning is approximately 35 micrometers. This also matches the theory (Eq. (37)) exactly.

extremely sharp, as depicted in Fig. 2.10. At these points, the ratio of optical sectioning to $L$ is less than 1.

Due to the difficulty of manually adjusting the aperture of the pupil and protecting the objective lens from damage, we were only able to collect a few sets of data with this approach. For this reason, we developed another experimental configuration for controlling the transverse width of the focused speckled beam which did not require the use of a field diaphragm.

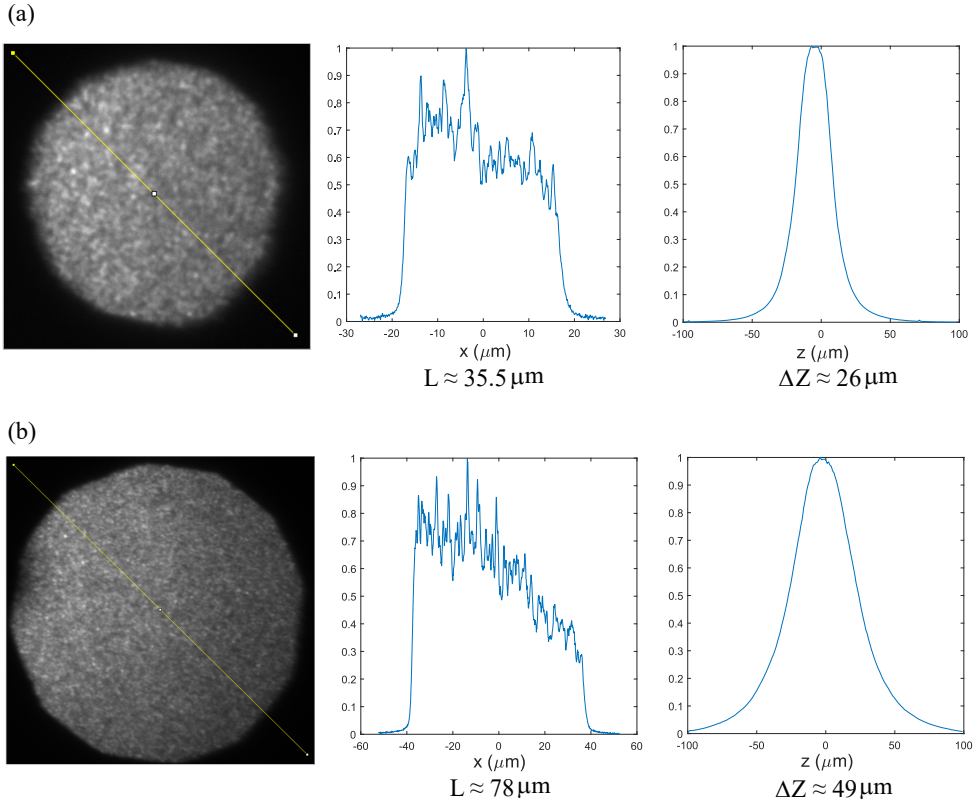


FIGURE 2.10 – Experimental top-hat focused speckles with larger transverse resolution (tens of micrometers). Fig a illustrate the top-hat focus speckle at the objective focal plane, and the transverse resolution and optical sectioning are 35.5 $\mu m$ and 26 $\mu m$ respectively; Fig b show the top-hat speckle with a larger transverse dimension compared with Fig a, with $L = 78\mu m$ and $\Delta z_{FS} = 49\mu m$. The optical sectioning ratio to the transverse resolution is less than 1, closely resembling the numerically simulated slope of 0.6.

### 2.4.2 The diffuser is moved throughout a slightly focused beam to control the speckle correlation at the pupil plane

The second method, which does not require the use of a field diaphragm, is depicted in Fig. 2.11. We recall that the transverse size of the speckled focused spot is inversely proportional to the width of the speckle grains (or field correlation length) at the objective pupil plane (as shown in Fig. 2.5). The idea is to control the size of the speckle grains at the pupil plane of the objective. We slightly focus a laser beam such that the focus spot takes place at a plane conjugated with the objective focal plane. The magnification is adjusted so that, without diffuser, this beam illuminates the whole pupil with a constant field and generates a tiny spot in the sample space. We now position the diffuser on the illumination path of the slightly focused beam.

As illustrated in Fig. 2.11, we illuminate the diffuser with a focused beam in the Fourier plane, generating a correlated speckle, where the speckle grain size will increase during the propagation. Therefore, when the diffuser is placed close to L1, the focused speckles generated by the diffuser propagate over a longer distance to reach the plane conjugate to the pupil plane, resulting in larger speckle grain sizes. On the contrary, if the diffuser is placed far from the L1, the random illumination behind the diffuser propagates over a relatively shorter distance, resulting in smaller speckle grains. Thus, one can tune the diffuser position to enlarge or diminish the speckle field correlation length as shown in Fig. 2.11.

In this section, we conduct experiments with the same method as in configuration (Fig. 2.11), where the transverse resolution varies with the position of the diffuser, as illustrated in Fig. 2.12. The advantage of this configuration is that it is possible to acquire multiple data sets with various $L$, as adjusting the position o diffusers is quite straightforward. Fig. 2.13 illustrates the examples of focused speckles for different transverse dimensions.

In actual measurements, the beam shape is neither strictly Gaussian nor strictly top-hat distributed because we study the performance only from one speckle. Therefore, it is difficult to ensure that the incident beam produces random illumination with a Gaussian or top-hat distribution. Even in numerical simulations, when the number of random illumination images is limited, it is challenging to distinguish whether a given speckle pattern belongs to a Gaussian or top-hat distribution. We choose the signal's FWHM as the transverse resolution and optical sectioning to obtain the following linear relationship (Fig. 2.14), with a slope of approximately 1.3.

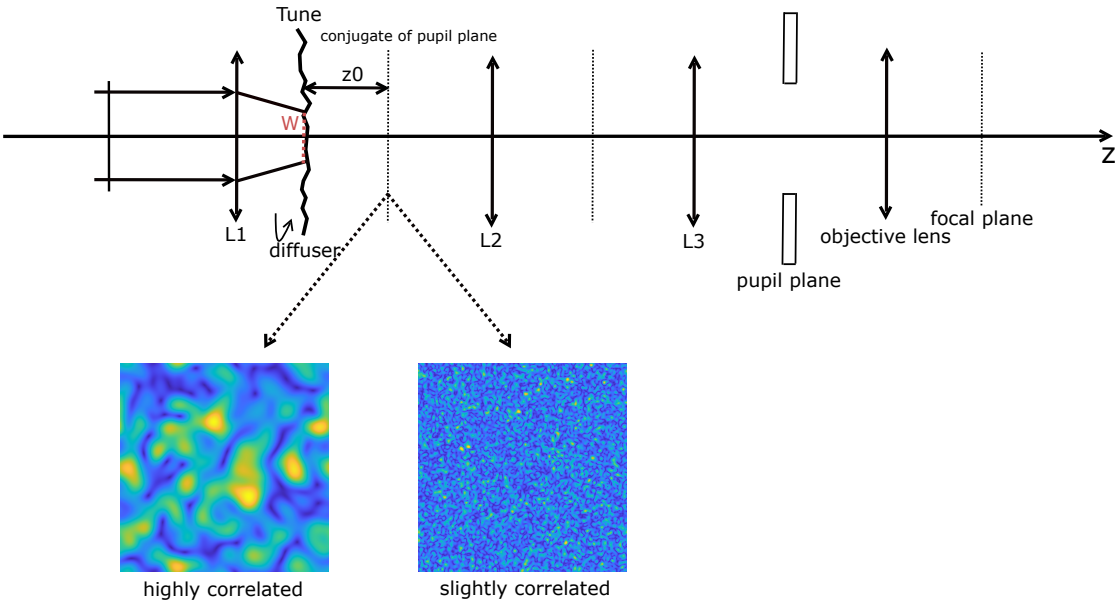


FIGURE 2.11 – Forming the focused speckled beam by adjusting the diffuser position. This configuration does not require the use of a diaphragm, unlike the configurations in Fig. 2.4. The speckle grain size is adjusted by modifying the position of the diffuser. Since the diffuser generates the speckle of a certain size, but the speckle grain gradually increases during propagation, different speckle grain sizes are observed at the pupil plane. Moreover, the pupil plane is always filled, resulting in focused speckle with different FOVs. The lower left image shows the situation when the diffuser is close to L1, while the lower right image shows the situation when the diffuser is far from L1.

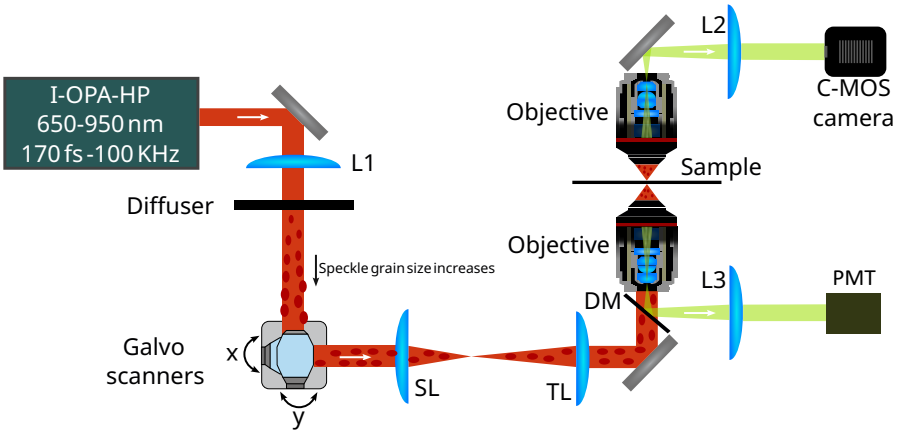


FIGURE 2.12 – Experimental configuration for generating focused speckle with different FOVs, a similar idea as in Fig. 2.11. To generate the focused speckle with different FOVs, while filling the whole pupil, the key point is to generate different speckle grain sizes at the pupil plane. Additionally, the speckle grain size is increasing while the correlated speckle is propagating towards the Fourier plane.

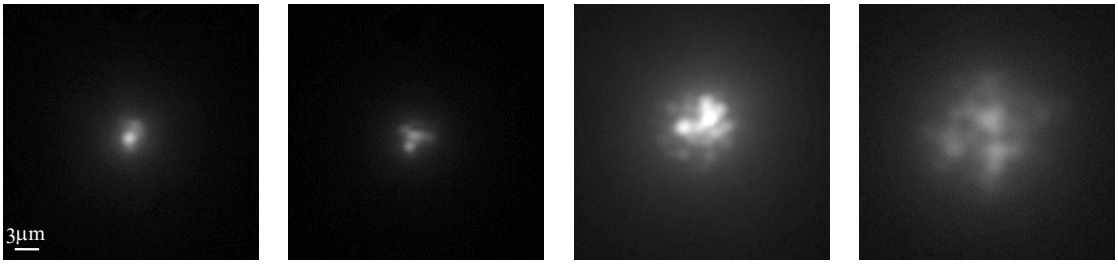


FIGURE 2.13 – Focused speckles with various transverse resolutions generating from the set-up (Fig. 2.12), from left to right : $L$ is increasing.

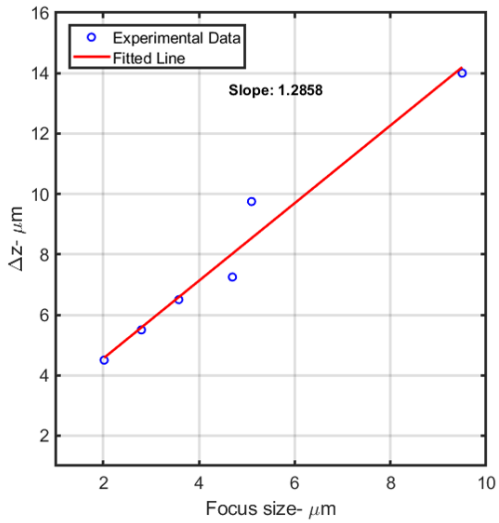


FIGURE 2.14 – The relationship between $L$ and optical sectioning with the configuration (Fig. 2.12), the slope lies between the top-hat constant of 0.6 (simulated slope) and the Gaussian constant of 2.4 (analytical slope), as the beam shape does not perfectly conform to either a Gaussian or top-hat distribution.

## 2.5 Conclusion

In this chapter, we first analyzed how traditional 2PE scanning microscopes are constrained to sub-micrometric transverse resolution to obtain micrometric optical sectioning, demonstrating that the optical sectioning is proportional to the square of transverse dimension. This indicates that standard 2PE scanning microscopes are unsuitable for rapid, large FOV imaging with micrometric resolution.

Next, we propose replacing the focused beam with a focused speckled beam to obtain an quasi-isotropic micrometric excitation volume. The focused speckled beam can be obtained thanks to a diffuser and a field diaphragm. We present a simple formula showing the linear relationship between the optical sectioning and the transverse waist of a Gaussian focused speckled beam. Our analytical expression is confirmed with simulations and experiments. We have shown that focused speckled beam can create quasi-isotropictwo-photon excitation volume of micrometric size (from 3 to 10 microns transversally and 6 to 20 microns axially)

This study paves the way towards scanning 2PM with scalable isotropic micrometric resolution, high collection efficiency, and fast scanning over large FOVs.

# 3 Improving optical sectioning in widefield two-photon microscopy by combining temporal focusing with random illumination

## Sommaire


3.1 Introduction . . . 64
3.2 Principle of grating TF . . . 65
3.2.1 Modeling Temporally Focused laser pulses . . . 66
3.2.2 Exciting the fluorescence with a temporally focused laser pulse . 70
3.2.3 Numerical Simulation . . . 72
3.2.4 Grating TF with a chirped pulse . . . 76
3.3 Collecting two or many orders diffracted by the grating : Multi-order-grating TF . . . 77
3.3.1 multi-order grating TF : Two diffracted orders are collected . . . 77
3.3.2 multi-order grating TF : Three diffracted orders are collected . . 85
3.4 Optical sectioning obtained from a pulse diffracted by a rough surface : Roughness TF . . . 90
3.5 Improving optical sectioning by combining grating TF with random illumination : Roughness-grating TF . . . 94
3.5.1 Theory of Temporal-Focused Speckle (TF-speckle) . . . 94
3.6 Experiments . . . 104
3.6.1 Modeling grating TF when using a reflection grating in Littrow configuration . . . 104
3.6.2 Modeling roughness-grating TF using a reflection grating in Littrow configuration . . . 106
3.6.3 Experimental implementation of grating TF and roughness-grating TF . . . 107
3.7 Using temporal-focused speckles in Random Illumination Microscopy 110
3.8 Conclusion . . . 114

## 3.1 Introduction

Images obtained in one-photon or two-photon fluorescence microscopes using widefield illumination are generally highly deteriorated by out-of-focus fluorescence due to the lack of optical sectioning (BEWERSDORF et al. 1998). To solve this issue in widefield 2PM, it has been proposed to use a Temporal Focusing (TF) technique (ORON, TAL et al. 2005; ZHU et al. 2005) for confining sample excitation to a thin slice about the focal plane. Since TF-2PM provides optical sectioning while keeping the fast gentle widefield illumination, it appears as an interesting alternative to the standard scanning 2PM (DENK et al. 1990), which provides good optical sectioning but is hindered by slow scanning speeds and possible sample photodamage. TF consists in diffracting the wavelengths (or colors) of a collimated pulsed laser beam by illuminating a grating, placed at an image plane of the microscope, under a certain angle. After passing through the tube lens and objective, the different colors interfere constructively only at the focal plane of the microscope, yielding a short pulse with a high peak intensity. As one moves away from the focal plane, the increasing phase mismatch between the colors stretches the pulse and decreases the peak intensity. As a result, the two-photon excitation occurs essentially in a thin layer surrounding the focal plane, which reduces phototoxicity and enables optical sectioning. It is interesting to note that during beam diffraction and recombination, the pulse duration varies between ultrashort and long pulses while its spatial dimension remains constant, rendering this method adaptable for wide-field microscopy (remaining large FOV). Therefore, by combining optical sectioning to the speed advantage of the widefield configuration, TF has rendered scanless-2PE a compelling alternative to scanning 2PE (ORON, TAL et al. 2005; ZHU et al. 2005).

Generally, in TF, an axial resolution of a few microns is obtained with femtosecond pulses (100 fs) and magnification greater than 50. The high magnification limits the use of TF to relatively small FOV (a few tens of microns) and the large frequency bandwidth to non-spectroscopic applications. Decreasing the magnification and the spectral bandwidth yields a rapid deterioration of the axial resolution (or optical sectioning) as the latter is inversely proportional to the square of the frequency bandwidth and microscope magnification (YEW et al. 2013). In this chapter, we propose different configurations for improving the optical sectioning of TF-2PM when the microscope magnification or/and the pulse frequency bandwidth are small.

TF uses the temporal frequency diversity for confining the 2PE excitation volume to a thin slice. On the other hand, spatial focusing provides optical sectioning in scanning configurations thanks to the spatial frequency diversity. Mixing spatial and temporal focusing has been proposed for exciting specific targets (in an optogenetic context) or, in conjunction with a confocal detection, for removing further the out-of-focus blur (ZHU et al. 2005; HERNANDEZ et al. 2016; LESHEM et al. 2014; PAPAGIAKOUMOU, DE SARS, EMILIANI et al. 2009; PAPAGIAKOUMOU, DE SARS, ORON et al. 2008; CHOI et al. 2013), but it has never been studied specifically for improving optical sectioning in a widefield configuration when the microscope magnification is small (corresponding to large FOV) or the laser frequency bandwidth is small.

Here, we propose an approach combining spatial and temporal frequency diversity to overcome the limitations of standard TF for small magnifications and long pulses. The core concept lies in illuminating a grating with many pulses propagating along different directions. This illumination is obtained by scattering a collimated pulse with a diffuser that is thin enough so for the amplitudes of the scattered plane waves not to depend on the pulse wavelengths. This condition allows the generated speckled field to be physically understood as a sum of multiple pulses with random phases. We will show that this approach achieves optical sectioning of a few micrometers even with picosecond pulses or in low magnification configurations.

In this chapter, we first model the standard grating TF, hereafter note grating TF, obtained a simple theoretical solution, and verified it through numerical simulations. Furthermore, we also recovered an analytical solution for the chirped pulse. Then we analyze the improved optical sectioning capability when multiple chirp-free pulses are incident at different angles onto the same grating or when a single pulse is incident on the grating but the microscope objective collects multiple diffraction orders. Hereafter this technique will be called multi-order grating TF. Next, for comparison, we analyze the optical sectioning ability of many random pulses propagating in different directions. This pulsed speckle is obtained when a pulse is diffracted by a thin diffuser, a rough surface, or Spatial Light Modulator displaying random mask, which act as a grating with random periods and introduces some color dispersion. This approach will be called roughness TF.

Subsequently, we discovered that combining grating TF with random illumination stemming from roughness TF can significantly the enhance optical sectioning, particularly for configurations where grating TF alone yields poor optical sectioning. The roughness-grating TF not only expands the parametric conditions (from fs pulse to ps pulse, from large magnification to small magnification) for TF to function, but also reduces the potential damage to the objective lens. Numerical simulations and experiments are shown that confirm the validity of our analytical models.

## 3.2 Principle of grating TF

In wide-field two-photon fluorescence microscopy, the images captured by the camera resemble the expression in Eq. (1) :

$$I(\boldsymbol{R}) = \int h(\boldsymbol{R}-\boldsymbol{r})\rho(\boldsymbol{r})I_p(\boldsymbol{r})\mathrm{d}\boldsymbol{r} \tag{38}$$

where we recall that $\boldsymbol{R}$ and $\boldsymbol{r}$ represent the coordinates in the camera space and object space, respectively, $\rho$ is the sample, $I_p$ is the illumination square intensity. To analyze the property of TF, we consider the property of the pulsed beam square intensity $I_p$.

### 3.2.1 Modeling Temporally Focused laser pulses

TF is a method that can provide optical sectioning of a few micrometers in a wide-field two-photon microscope. The configuration consists in sending a femtosecond pulse (100fs) laser beam at an angle $\theta_0$ onto a grating , as shown in Fig. 3.1. The grating period is generally about 1 micrometer, the microscope's magnification is about 50 and the pulse central wavelength close to 1 micrometer.

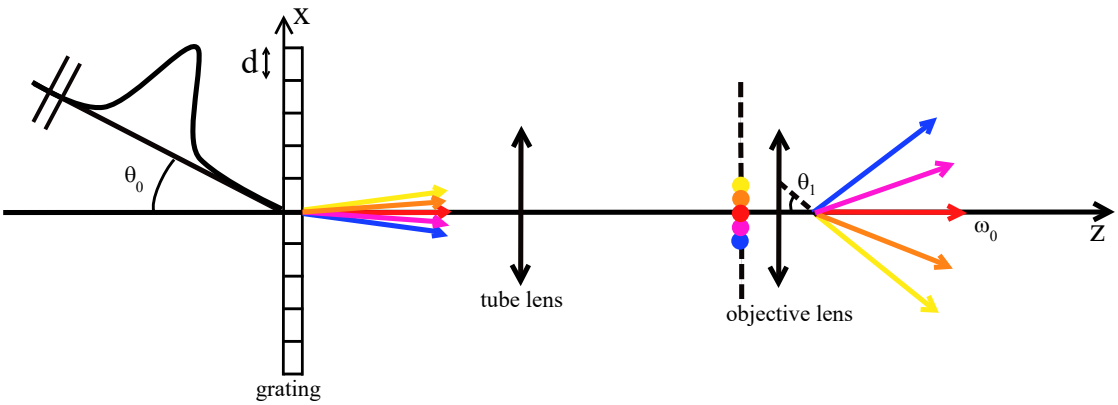


FIGURE 3.1 – Configuration of two-photon microscopy with TF using a transmission grating. The incident pulse is directed at an angle onto a transmission grating, which disperses the light such that plane waves of different wavelengths propagate in distinct directions. The angle of the incident pulse $\theta_0$ is chosen so that the diffracted component at the central wavelength is aligned along the z-axis.

We first start by recalling the theory of a collimated TF beam illustrated in Fig. 3.1. We consider a microscope with a magnification $M$, a numerical aperture $\mathrm{NA_O}$. The introduce the orthonormal basis $(\hat{\boldsymbol{x}}, \hat{\boldsymbol{y}}, \hat{\boldsymbol{z}})$ with $\hat{\boldsymbol{z}}$ the optical axis. A grating of period $\boldsymbol{d} = d\hat{\boldsymbol{x}}$ is placed at a conjugated image plane. It is illuminated by a short pulse propagating in the $(x, z)$ plane under an angle $\theta_0$ with respect to the optical axis.

The field of the incident pulse at position $\boldsymbol{r} = (\boldsymbol{r}_\perp, z) = (x, y, z)$ and time $t$, can be written (in the scalar approximation) as the real part of a sum of plane waves for different angular frequencies $\omega$ :

$$E_{\mathrm{inc}}(\boldsymbol{r}, t) = \int_{-\infty}^{+\infty} h(\omega) e^{i[\boldsymbol{k}_{\mathrm{inc}} \cdot \boldsymbol{r} - \omega t]} \mathrm{d}\omega \tag{39}$$

where $\boldsymbol{k}_{\mathrm{inc}}$, $\omega$, $t$, $c$ represent the frequency-dependent wavevector, the angular frequency, time, and speed of light, respectively. It is firstly assumed that the pulse has a Gaussian shape without chirping : $h(\omega) = e^{-T^2\nu^2}$ with $\nu = \omega - \omega_0$ [1], where $\omega_0$ is the central angular frequency, and $T$ controls the duration of the pulse. For convenience, we also introduce $\Delta\omega = \omega_{\max} - \omega_{\min} = \frac{2}{T}$ and $\Delta\lambda = \frac{\lambda_0^2}{c\pi T}$ the angular frequency and wavelength bandwidths of the pulse.

1. The radius waist of a zero-centered Gaussian distribution $g$ is defined as $x$ such that $g(x) = g(0)/e$

Due to Helmholtz equation, any frequency dependent wavevector $\boldsymbol{k}$ can be written as $\boldsymbol{k} = \boldsymbol{\kappa} + q(\omega, \boldsymbol{\kappa})\hat{\boldsymbol{z}}$ where $\boldsymbol{\kappa}$ is the transverse wavevector and $q(\boldsymbol{\kappa}, \omega) = \sqrt{\frac{\omega^2}{c^2} - \kappa^2}$. In our configuration, the incident pulse wavevector $\boldsymbol{k}_{\text{inc}}$ in Eq. (39) can be expressed as :

$$\boldsymbol{k}_{\text{inc}} = \boldsymbol{\kappa}_{\text{inc}}(\omega) + q(\boldsymbol{\kappa}_{\text{inc}}, \omega)\hat{\boldsymbol{z}} \tag{40}$$

where $\boldsymbol{\kappa}_{\text{inc}} = \frac{\omega}{c}\sin\theta_0\hat{\boldsymbol{x}}$.

Using the analytical integration of complex Gaussian functions, $\int_{-\infty}^{+\infty} e^{-ax^2+ibx}dx = \sqrt{\frac{\pi}{a}}e^{-\frac{b^2}{4a}}$, the incident complex field can be expressed as

$$E_{\text{inc}}(\boldsymbol{r}, t) = \sqrt{\frac{\pi}{T^2}}e^{i[\boldsymbol{k}_0\cdot\boldsymbol{r}-\omega_0 t]}e^{-\frac{[\frac{\boldsymbol{k}_0\cdot\boldsymbol{r}}{\omega_0}-t]^2}{4T^2}} \tag{41}$$

where $\boldsymbol{k}_0 = \boldsymbol{\kappa}_{\text{inc}}(\omega_0) + q(\boldsymbol{\kappa}_{\text{inc}}(\omega_0), \omega_0)\hat{\boldsymbol{z}}$.

Now we assume that the grating acts as a periodic transmittance along the $x$ axis, the relationship between the complex fields just before and after the grating (placed at $z = 0$) is given by

$$E(\boldsymbol{r}_\perp, 0^+) = E(\boldsymbol{r}_\perp, 0^-)g(x) \tag{42}$$

with $g(x) = e^{\frac{2\pi i m x}{d}}$ if we only take into account $m$th order diffracted field (PALMER et al. 2005). Typically, the $-1$ order diffraction field is chosen in grating TF.

The complex field ($-1$ order) diffracted by the grating reads

$$E_{\text{d}}(\boldsymbol{r}, t) = \int_{-\infty}^{+\infty} h(\omega)e^{i[\boldsymbol{k}_d\cdot\boldsymbol{r}-\omega t]}\text{d}\omega \tag{43}$$

where $\boldsymbol{k}_d = \boldsymbol{\kappa}_d + q(\boldsymbol{\kappa}_d, \omega)\hat{\boldsymbol{z}}$ with $\boldsymbol{\kappa}_d = \boldsymbol{\kappa}_{\text{inc}}(\omega) - \frac{2\pi}{d}\hat{\boldsymbol{x}}$.

The field diffracted by the grating and passing through the tube lens and objective lens can be modeled as the real part of the following complex field :

$$E_{\text{G}}(\boldsymbol{r}, t) = \int_{-\infty}^{+\infty} h(\omega)p(\boldsymbol{\kappa}_g, \omega)e^{i[\boldsymbol{k}_g\cdot\boldsymbol{r}-\omega t]}\text{d}\omega \tag{44}$$

where $\boldsymbol{k}_g = \boldsymbol{\kappa}_g + q(\boldsymbol{\kappa}_g, \omega)\hat{\boldsymbol{z}}$, $\boldsymbol{\kappa}_g = M\boldsymbol{\kappa}_d$, $M$ is the magnification, $p$ corresponds to the pupil function of the objective, $p(\nu, \omega) = 1$ for $\nu < \frac{\omega}{c}\text{NA}_{\text{O}}$ and 0 elsewhere, $\text{NA}_{\text{O}}$ denotes the objective NA.

To maximize the collection of the diffracted light, the grating period and angle of incidence of the pulse are chosen so that the minus one order diffracted field at the central wavelength propagates along the $z-$axis :

$$\boldsymbol{\kappa}_g(\omega_0) = \boldsymbol{0} \tag{45}$$

Under this assumption, $\boldsymbol{\kappa}_g$ can be simplified as a linear function of $\nu$ :

$$\boldsymbol{\kappa}_g = MQ\nu\hat{\boldsymbol{x}} \tag{46}$$

where $Q = \frac{\lambda_0}{cd}$.

Moreover, since the angular frequency bandwidth of the pulse, $\Delta\omega$, is small compared to $\omega_0$, it is possible to apply the Taylor expansion for the z-component of spatial frequency $q(\boldsymbol{\kappa}_g, \omega)$ on $\omega_0$ :

$$q(\boldsymbol{\kappa}_g, \omega) \approx q(\mathbf{0}, \omega_0) + a\nu + b\nu^2 \tag{47}$$

where $a = \frac{1}{c}$, $b = -\frac{cM^2Q^2}{2\omega_0}$.

We note that the different directions of the wavevectors $\boldsymbol{k}_g$ of the plane waves forming the diffracted beam after the grating and microscope objective belong to the $(x,z)$ plane and depend only on their temporal frequency $\omega$. If we define $\theta_1$ (shown in Fig. 3.1) as the angle between the wavevectors and the z-axis, we obtain $\boldsymbol{\kappa}_g \cdot \hat{\boldsymbol{x}} = MQ\nu = \frac{\omega}{c}\sin\theta_1$, where we recall that $\nu = \omega - \omega_0$. Thus, there is a one-to-one correspondence between $\theta_1$ and $\omega$. We recall that in an achromatic objective, a point of coordinate $(p_x, p_y)$ at the pupil plane of the objective defines the polar $(\theta)$ and azimuthal $(\phi)$ angles of the wavevector of the exit plane wave, following, $p_x = \sin\theta\cos\phi$, $p_y = \sin\theta\sin\phi$. In our configuration, the wavevectors are all in the $(x,z)$ plane ($\phi = 0$), which correspond to a line at the pupil plane. Each illuminated point of the line, of coordinate $(p_x, 0)$ with $p_x = \sin\theta_1 = MQvc/\omega$ corresponds to a specific frequency $\omega$, as illustrated in Fig. 3.2. Recalling that the spectral bandwidth is centered about $\omega_0$, we observe that $\sin\theta_1^{\max} = MQc(\omega^{\max} - \omega_0)/\omega^{\max} \approx -MQc(\omega^{\min} - \omega_0)/\omega^{\min} \approx MQ\Delta\omega c/2\omega_0$. Thus, we introduce the effective NA of the grating as $\mathrm{NA_G} = \sin\theta_1^{\max} = MQ\Delta\omega c/2\omega_0$ which yields after simplification,

$$\mathrm{NA_G} = \frac{M\Delta\lambda}{2d}. \tag{48}$$

For the objective to collect all the grating dispersed plane waves, one needs to have $\mathrm{NA_G} < \mathrm{NA_O}$.

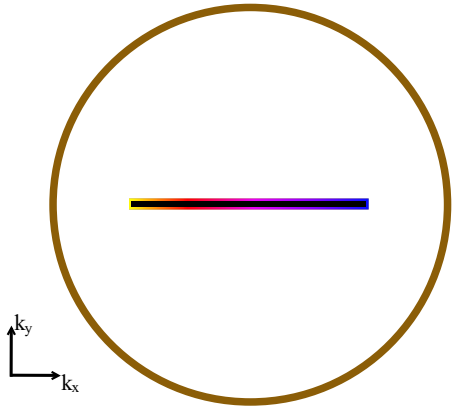


FIGURE 3.2 – Illustration of the objective pupil plane illuminated by a laser pulse that has been diffracted by a grating in a TF scheme. The circle represents the back aperture of the objective lens. We observe a rainbow line, the different colors represent the different wavelengths forming the pulse.

In most TF-2PM, the objective back aperture can collect all the wavelengths. Indeed, with a pulse duration of about $100fs$ ($\Delta\lambda \approx 40nm$ at central wavelength $\lambda_0 = 1\mu m$), a magnification about 50, a grating period of about $3\mu m$, one obtains $\mathrm{NA_G} \approx 0.33$, which is smaller than most NAs of the objective, $\mathrm{NA_O}$. However, if the duration of the pulses is very short, about $10fs$, the magnification greater than 100 or the grating period less than $1\mu m$, it is possible to have $\mathrm{NA_G} > \mathrm{NA_O}$. In these cases, the pupil will cut out the extreme wavelengths of the pulse.

Here, we consider configurations in which $\mathrm{NA_O} > \mathrm{NA_G}$ so that the product $h(\omega)p(M\boldsymbol{\kappa}_g, \omega)$ simplifies in $h(\omega)$. Thus, the complex field $E_\mathrm{G}(\boldsymbol{r}, t)$ can be considered as the integral of a complex Gaussian over $v$, which can be derived as following :

$$\begin{aligned} E_\mathrm{G}(\boldsymbol{r}, t) &= e^{iC(z,t)} \int_{-\infty}^{+\infty} e^{-A(z)v^2 + iB(\boldsymbol{r},t)v} \mathrm{d}v \\ &= e^{iC(z,t)} \sqrt{\frac{\pi}{A(z)}} e^{-\frac{B^2(\boldsymbol{r},t)}{4A(z)}} \\ &= E_{\omega_0}(\boldsymbol{r}, t) E_\mathrm{pulse}(\boldsymbol{r}, t) \end{aligned} \tag{49}$$

with $E_{\omega_0}(\boldsymbol{r}, t) = e^{iC(z,t)}$ and $E_\mathrm{pulse}(\boldsymbol{r}, t) = \sqrt{\frac{\pi}{A(z)}} e^{-\frac{B^2(\boldsymbol{r},t)}{4A(z)}}$ where $C(z, t) = q(\boldsymbol{0}, \omega_0)z - \omega_0 t$, $A(z) = T^2 + i\frac{cM^2Q^2z}{2\omega_0}$, $B(\boldsymbol{r}, t) = \boldsymbol{u}\cdot\boldsymbol{r}/c - t$, $\boldsymbol{u} = McQ\hat{\boldsymbol{x}} + \hat{\boldsymbol{z}}$, $Q = \lambda_0/(cd)$.

We interpret $E_\mathrm{pulse}(\boldsymbol{r}, t)$ as a pulse that moves along the direction $\boldsymbol{u}$ with the speed $v$. Typically, the grating period $d$ is similar to $\lambda_0$, so the speed of pulse can be approximated by $v = c/u \approx c/M$[2] and $\boldsymbol{u} \approx \hat{\boldsymbol{x}}$. One can explain the traveling speed $c/M$ with Fig. 3.3 : in the real space, the pulse first reaches the upper point of the grating and then touches the lower point. Due to the demagnification, the grating image dimension after the objective is $M$ times smaller, so in the sample plane, the pulse travels along the x-axis at a speed $M$ times slower than that in the grating space.

2. $u$ presents the modulus of $\boldsymbol{u}$

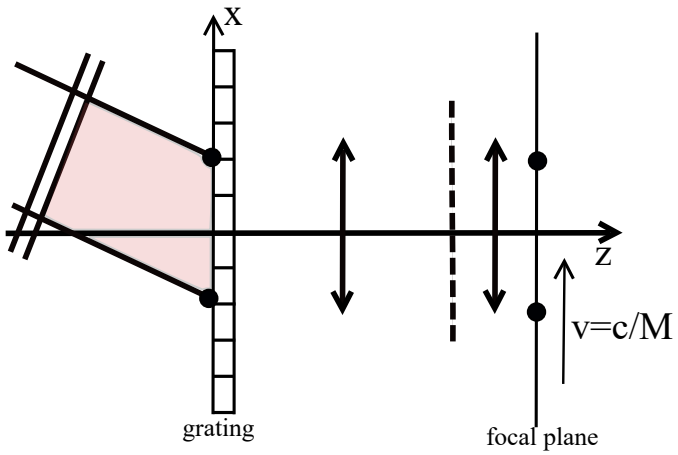


FIGURE 3.3 – Physical understanding of collimated TF beam propagation. The pulse first reaches the upper point of the grating and then contacts the lower point, causing the pulse to move upward along the x-axis on the sample plane.

### 3.2.2 Exciting the fluorescence with a temporally focused laser pulse

To model the interaction between a pulse and the fluorophores, we calculate the instantaneous field intensity at the fluorophore position, defined as $I_{\text{ins}}(\boldsymbol{r},t) = \text{Re}\,[E_{\text{G}}(\boldsymbol{r},t)]^2$. The one-photon excitation fluorescence radiation is proportional to the average instantaneous intensity over $T_0$. Importantly, we observe that $E_{\text{pulse}}(\boldsymbol{r},t)$ varies much slower in time than $E_{\omega_0}(\boldsymbol{r},t)$. Thus it is possible to assume $E_{\text{pulse}}(\boldsymbol{r},t)$ is a constant during one period of time $T_0 = \frac{2\pi}{\omega_0}$. Then the average incident intensity over $T_0$ reads,

$$I(\boldsymbol{r},t) = \frac{1}{T_0}\int_{t-\frac{T_0}{2}}^{t+\frac{T_0}{2}} I_{\text{ins}}(\boldsymbol{r},t')\mathrm{d}t' \approx \frac{|E_{\text{pulse}}(\boldsymbol{r},t)|^2}{2} \tag{50}$$

The fluorescence radiation of a fluorophore placed at $\boldsymbol{r}$, under a one-photon excitation, is proportional to the intensity $I(\boldsymbol{r},t)$. On the other hand, the two-photon excitation fluorescence radiation is proportional to the average of $I_{2\text{ins}}(\boldsymbol{r},t) = \text{Re}\,[E_{\text{G}}(\boldsymbol{r},t)]^4$ over $T_0$,

$$I_{\text{TF}}(\boldsymbol{r},t) = \frac{1}{T_0}\int_{t-\frac{T_0}{2}}^{t+\frac{T_0}{2}} I_{2\text{ins}}(\boldsymbol{r},t')\mathrm{d}t' \approx \frac{3|E_{\text{pulse}}(\boldsymbol{r},t)|^4}{4} \tag{51}$$

As a result, the two-photon excitation intensity $I_{\text{TF}}(\boldsymbol{r},t)$ can be calculated as

$$I_{\text{TF}}(\boldsymbol{r},t) \propto \frac{1}{|A(z)|^2} e^{-\frac{\text{Re}[A(z)]B^2(\boldsymbol{r},t)}{|A(z)|^2}} \tag{52}$$

The camera records the light emitted from fluorophore over a long time while the pulse travels, we can assume that the recorded fluorescent intensity is proportional

to the excitation intensity integrated over time from $-\infty$ to $+\infty$. It is seen that the one-photon intensity integrated over time $\int |E_{\text{pulse}}(\boldsymbol{r},t)|^2 \mathrm{d}t$ is a constant that does not depend on $\boldsymbol{r}$. Thus, illuminating the sample with a pulsed laser in a one-photon fluorescence experiment is equivalent to illuminating the sample with a homogeneous intensity. On the other hand, the fluorescence signal in the two-photon case $S_{\text{G}}(z)$ which is proportional to the two-photon intensity integrated over time : $\int I_{\text{TF}}(\boldsymbol{r},t)\mathrm{d}t$,

$$\begin{aligned} S_{\text{G}}(z) &\propto \frac{1}{|A(z)|} \\ &\propto \frac{1}{\sqrt{\frac{\lambda_0^2}{\pi^2 \text{NA}_{\text{G}}^4} + z^2}} \end{aligned} \tag{53}$$

depends on the axial position of the fluorophore. It is worth mentioning that the collected signal for one-photon or two-photon is only a function of $z$ because the space variables $x$ and $y$ disappear when we integrate the intensities over time.

When $\text{NA}_{\text{O}} < \text{NA}_{\text{G}}$, the objective will cut some light, $h(\omega)p(M\boldsymbol{\kappa}_g,\omega)$ can be approximated as a new Gaussian $h'(\omega) = e^{-T_N^2 \nu^2}$ with $T_N = \frac{M\lambda_0^2}{2\pi c d \text{NA}_{\text{O}}}$, because $\text{NA}_{\text{O}}$ provides an effective wavelength bandwidth (effective pulse duration). Consequently, we account for the pupil function simply by modifying the pulse wavelength bandwidth to $\Delta\lambda = \text{NA}\frac{2d}{M}$, where $\text{NA} = \min(\text{NA}_{\text{G}}, \text{NA}_{\text{O}})$.

Thus, the collected signal $S_{\text{G}}(z)$ in grating TF can be expressed as

$$S_{\text{G}}(z) \propto \frac{1}{\sqrt{\frac{\lambda_0^2}{\pi^2 \text{NA}^4} + z^2}} \tag{54}$$

where $\text{NA} = \min(\text{NA}_{\text{G}}, \text{NA}_{\text{O}})$, we recall $\text{NA}_{\text{G}} = \frac{M\Delta\lambda}{2d}$.

Since the signal decays with $z$, we define the optical sectioning as the FWHM of the $S_{\text{G}}(z)$. This is equivalent to placing a thin homogeneous fluorescent plane at the z-position in the sample space, where any point on this fluorescent plane follows the Eq. (54) as $z$ varies, with $z = 0$ representing the focal plane.

Given the magnification $M$, grating period $d$, the wavelength bandwidth $\Delta\lambda$, central wavelength $\lambda_0$, and $\text{NA}_{\text{O}}$, the analytical optical sectioning reads

$$\Delta z_{\text{G}} = \frac{2\sqrt{3}\lambda_0}{\pi \text{NA}^2} \tag{55}$$

where $\text{NA} = \min(\text{NA}_{\text{G}}, \text{NA}_{\text{O}})$.

From this theoretical solution, it can be concluded that the optical sectioning ability of the grating TF is quadratically related to the parameters magnification $M$, grating period $d$, wavelength bandwidth $\Delta\lambda$, or $\text{NA}_{\text{O}}$, this quadratic relationship between optical sectioning and different parameters shows that a slight change in the parameters will change dramatically the optical sectioning ability.

For example, when the central wavelength $\lambda_0 = 800nm$, $d = 1\mu m$, and $\text{NA}_{\text{O}} = 0.75$,

effective NA and the analytical optical sectioning variations for different wavelength bandwidth $\Delta\lambda$ and $M$ can be shown in Fig. 3.4. The left figure shows that NA increases with increasing $M$ and bandwidth $\Delta\lambda$, and $NA_G$ is partially clipped when it exceeds the objective NA. The right figure illustrates how optical sectioning varies with $M$ and bandwidth. When M is less than 40 and the bandwidth is about $10nm$, the optical sectioning degrades and reaches $40\mu m$.

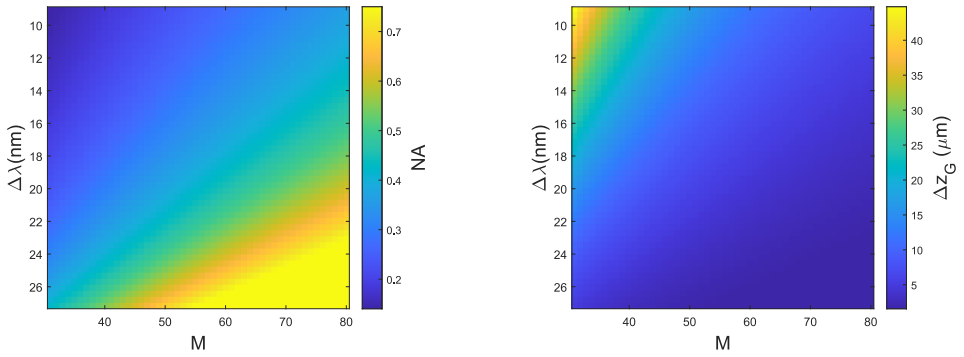


FIGURE 3.4 – (Left) NA = min($NA_G$, $NA_O$) and (right) optical sectioning as a function of the magnification $M$ and bandwidth $\Delta\lambda$. The parameters of the configuration are $\lambda_0 = 800nm$, $d = 1\mu m$, $NA_O = 0.75$. The left image shows that $NA_G$ increases with increasing bandwidth ($\Delta\lambda$) and magnification ($M$). When $NA_G > NA_O$ the extreme wavelengths of the pulse are cut by the objective pupil. The right figure shows that the optical sectioning $\Delta z_G$ improves with increasing $M$ and $\Delta\lambda$.

As mentioned before, in most existing grating TF configurations, pulses of approximately 100 femtoseconds and high-magnification microscopes ($\geq 50$) are used to obtain optical sectioning of a few micrometers, resulting in large $NA_G$ ($\geq 0.5$) but with a FOV limited to a few tens of micrometers due to the high magnification. If a larger FOV is desired, the magnification must be reduced, which will diminish $NA_G$ and cause a huge deterioration of the optical sectioning. In addition, we recall that most of the energy is concentrated in one 'rainbow' line at the Fourier plane of the objective, as illustrated in Fig. 3.2. The width of this line is inversely proportional to the width of the FOV. Thus, a gradual increase in the FOV will cause this line to get thinner and thinner, and the increased power density could potentially break the objective lens.

### 3.2.3 Numerical Simulation

In this section, we illustrate the behavior of TF by numerically simulating the field Eq. (44) and forming the two-photon intensity which is proportional to the square intensity $|E_G|^4(\boldsymbol{r}, t)$.

Two-photon excitation intensity at the focal plane $|E_G|^4(x, y, 0, t)$ for different times is shown in Fig. 3.26, for a magnification of 40, central wavelength of $800nm$, grating

period of $1\mu m$, wavelength bandwidth $\Delta\lambda = 18.1nm$ ($150fs$ pulse), yielding $NA_G = 0.36$, and $NA_O$ is 0.75. This figure shows how the pulse moves along $x$ axis. The field simulation at the pupil plane is shown in Fig. 3.6a, and shows a rainbow line, the colors corresponding to the different wavelengths. The two-photon intensity integrated over time as a function of $(x, y, z)$ is displayed in Fig. 3.6b. It indicates an optical sectioning of about $6.4\mu m$.

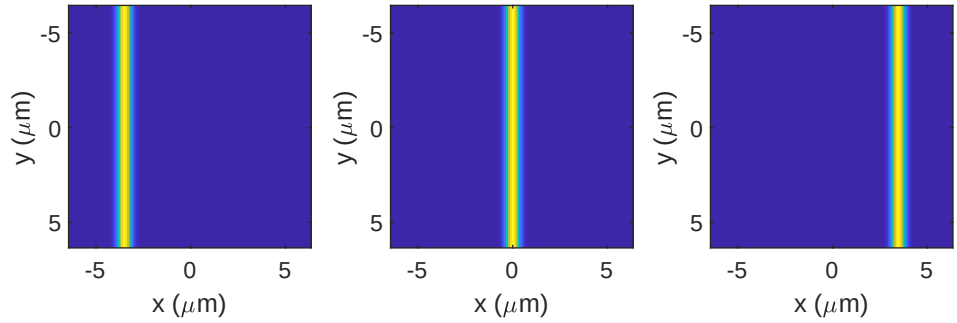


FIGURE 3.5 – Two photon excitation intensity $|E_G|^4(x, y, 0, t)$ at the XY focal plane for different times, from left to right : time increases.

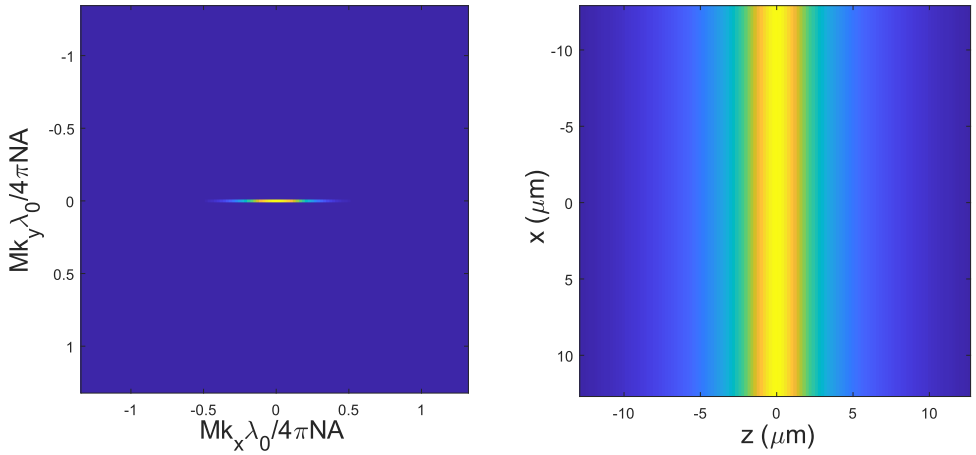


(a) $|\mathcal{F}(E_G(x, y, 0, 0))|$ (b) $\int |E_G(x, 0, z, t))|^4 dt$

FIGURE 3.6 – Simulation of TF collimated beam in the Fourier plane (left image) and in the image plane (right image) for a 40x magnification, 800 $nm$ central wavelength, 18.1 $nm$ bandwidth, $d = 1\mu m$, and $NA_O = 0.75$.

To estimate the optical sectioning, we assume that we have a homogeneous fluorescent plane placed at $z$ from the focal plane. The recorded signal at each z-position is the integration of the two-photon intensity over time and the FOV : $\int |E_G|^4(\boldsymbol{r}, t) dx dy dt$. To check the validity of the analytical expression of the optical sectioning Eq. (55), we simulated the recorded fluorescence signal using Eq. (44) with $\lambda_0 = 800nm$, $d = 1\mu m$

for different magnifications and bandwidths. Fig. 3.7(a) displays the optical sectioning obtained for a fixed pulse bandwidth, $\Delta\lambda = 18.1nm$ as function of the microscope magnification; Fig. 3.7(b) displays the optical sectioning for a fixed microscope magnification $M = 40$ as a function of $\Delta\lambda$. We observe a very good agreement between the analytical result and the simulations.

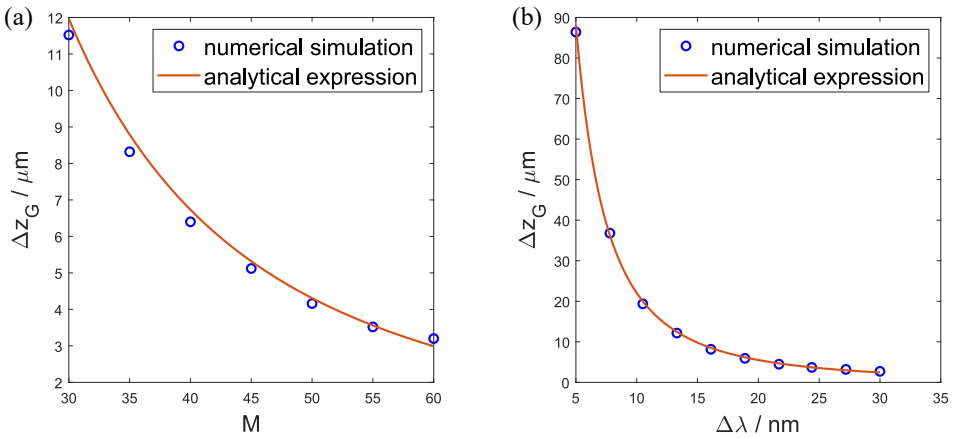


FIGURE 3.7 – Estimation of the optical sectioning for different microscope magnifications and pulse bandwidths with $\lambda_0 = 800nm$, $d = 1\mu m$. We simulated the temporally focused collimated TF beam using Eq. (44). The optical sectioning was estimated by computing the fluorescence signal detected on a camera when the sample is a thin homogeneous fluorescent plane that is translated through the focal plane. The simulated optical sectioning was compared to the analytical expression Eq. (55). The simulated results agree with the analytical ones.

Additionally, we set the magnification to 20 (corresponding to a large FOV) and investigate the behavior of the optical sectioning ($\lambda_0 = 800nm$, $d = 1\mu m$, $\mathrm{NA_O} = 0.75$) as a function of different wavelength bandwidths in Fig. 3.8. As expected, we observe that when the magnification is low, extremely short pulses must be used to achieve optical sections of several micrometers. We need bandwidths smaller than $30nm$ (about 90 fs), which is difficult to do in practice.

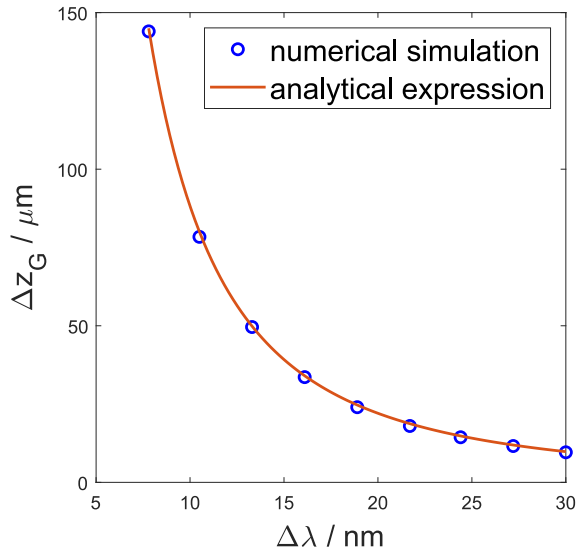


FIGURE 3.8 – Same as Fig. 3.7(a) but with a smaller magnification ($M = 20$).

### 3.2.4 Grating TF with a chirped pulse

In this subsection, we discuss the behavior of grating TF when the incident pulse is chirped. The field at the objective plane has the same expression as Eq. (44), the only difference lies in the angular frequency distribution $h(\omega) = e^{-(T^2+i\alpha)v^2}$, where $\alpha$ represents the chirp term.

Here, we only consider the case when the objective pupil is large enough to collect all the light ($NA_O$ is large enough). After processing a similar calculation procedure as the non-chirped pulse, the recorded signal with the chirped pulse reads

$$S_c(z) \propto \frac{1}{\sqrt{\frac{\lambda_0^2}{\pi^2 {NA_G}^4} + (\frac{\alpha}{b} - z)^2}} \tag{56}$$

where we recall that $NA_G = \frac{M\Delta\lambda}{2d}$, $b = -\frac{cM^2Q^2}{2\omega_0}$

Eq. (56) suggests that the pulse reaches its maximum intensity when $z = \frac{\alpha}{b}$, which indicates the plane of maximum excitation intensity now depends on the chirp parameter and is not limited to the focal plane. This property suggests that chirped TF allows a remote control of the z-position of the illuminated sample slice.

The optical sectioning $\Delta z_c$ of a chirped pulse can be calculated as :

$$\Delta z_c = \frac{2\sqrt{3}\lambda_0}{\pi {NA_G}^2} - \frac{2\alpha}{b} \tag{57}$$

where the first term on the right-hand side is the same as the grating TF, while the second term is due to the chirp. If $\alpha$ is a negative value, the focused plane translates towards positive $z$, and the optical sectioning gets better. If $\alpha$ is a positive value, the focused plane tranlates towards negative $z$ and the optical sectioning gets slightly worse. These expressions are very similar to that obtained in the bibliography (Michael E DURST et al. 2006; Michael Earle DURST et al. 2008).

## 3.3 Collecting two or many orders diffracted by the grating : Multi-order-grating TF

In this section, we theoretically and numerically analyze what happens when two or more grating orders are collected by the objective pupil. This paragraph introduces some ideas which will be helpful when studying temporal-focused random illumination and for applying TF to CARS.

### 3.3.1 multi-order grating TF : Two diffracted orders are collected

In standard grating TF configurations, we found that the optical sectioning stems from the second-order derivative of the axial wavevector component $q$ with respect to $\omega_0$ ($b$ in the Taylor expansion Eq. (47) leads to optical sectioning). In other terms, the optical sectioning of grating TF results from the pulse's Group Velocity Dispersion (GVD), which explains why it depends quadratically on the grating $NA_G$. Grating TF is generally limited to high magnifications (small FOV), short-duration pulses, and grating periods such that $NA_G < NA_O$ : The objective pupil is seldom filled. In this paragraph, we show that TF can be obtained without playing on the pulse GVD. In addition, our approach allows for better filling of the NA of the objective lens ($NA_O$).

We propose a configuration that makes two sets of rainbow lines appear simultaneously at the pupil plane after the diffraction by the grating. The physical picture of the pupil plane is shown in Fig. 3.9.

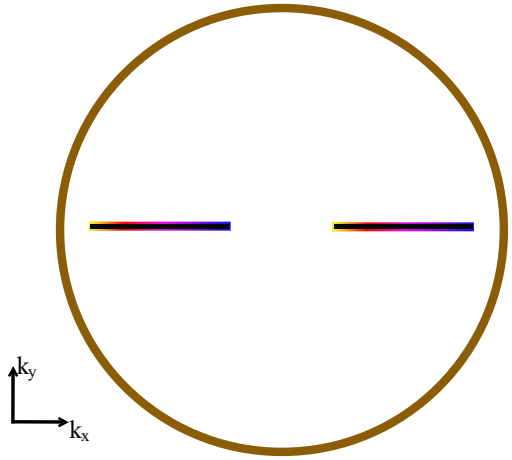


FIGURE 3.9 – The image helps clarify the configuration's purpose by illustrating the understanding of the pupil plane, where the objective collects two diffracted order fields from the grating. Each rainbow line in the image represents a pulse, with different colors indicating different wavelengths.

There are two ways to obtain such a configuration. The first possibility is to send simultaneously two pulses on the same grating under different angles, so that both

their −1 diffracted order are collected. The other technique involves sending one pulse on the grating and collecting the diffracted fields of two orders simultaneously. Fig. 3.10 shows these two possibilities.

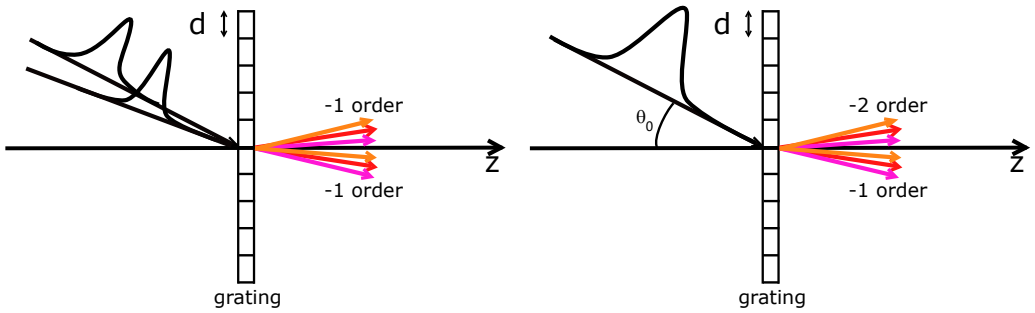


(a) Two pulses are incident on a grating at different angles. The angles are chosen so that their minus-one diffraction beams at the central wavelength propagate at angles symmetrical about the z-axis. Both beams are collected by the objective lens.

(b) A pulse is incident on a grating at an angle that is chosen so that the minus one and minus two diffraction orders at the central wavelength propagate along angles that are symmetrical around the z-axis. The objective lens collects both the minus one and minus two diffracted beams.

FIGURE 3.10 – Two possible configurations where the two grating diffraction fields are simultaneously collected by the objective lens

Both configurations enable the collection of two diffraction fields. For simplicity, we will only consider the second case, whose configuration is shown in the Fig. 3.11.

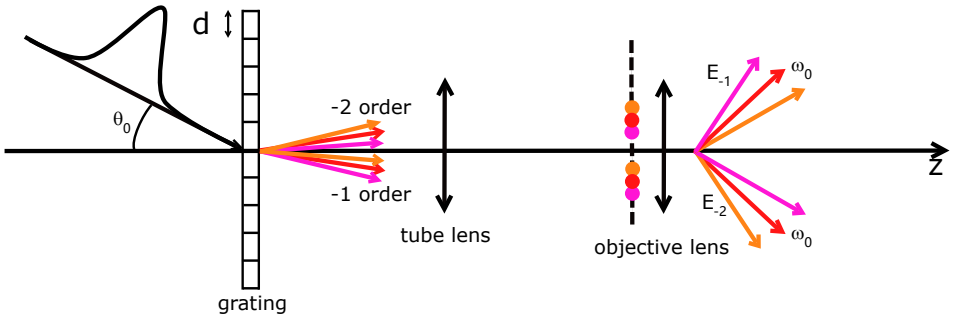


FIGURE 3.11 – The configuration shown in Fig. 3.10(b), featuring the pupil plane and magnification. The minus two diffraction field just after the grating propagates towards positive $x$. The minus one diffraction field propagates towards negative $x$. Both orders are collected by the objective lens.

To simplify the model, it is assumed that the two orders at the central wavelength propagate along symmetric angles about the z-axis. As Fig. 3.11 shows, the −2 order diffraction field at the central wavelength propagates in the positive direction along the x-axis, while the corresponding −1 order diffraction field propagates in the opposite

direction along the x-axis. Note that this symmetric configuration is also interesting for collecting as much light as possible from the two orders. Since the incident pulse field has the same expression as Eq. (39), the field diffracted by the grating and passing through the magnification for different orders can be modeled as :

$$E_n(\boldsymbol{r},t)=\int_{-\infty}^{+\infty}h(\omega)p(M\boldsymbol{\kappa}_n,\omega)e^{i[\boldsymbol{k}_n\cdot\boldsymbol{r}-\omega t]}\mathrm{d}\omega \tag{58}$$

where $\boldsymbol{k}_n=M\boldsymbol{\kappa}_n+q(M\boldsymbol{\kappa}_n,\omega)\hat{z}$, $\boldsymbol{\kappa}_n=(\frac{\omega}{c}\sin\theta_0+\frac{2\pi n}{d})\hat{\boldsymbol{x}}$, $n$ represents the different order, $h(\omega)=e^{-T^2\nu^2}$ and $T=\frac{\lambda_0^2}{c\pi\Delta\lambda}$ are recalled again.

Since both orders at the central wavelength propagate along symmetric directions with respect to the z-axis, we have,

$$\boldsymbol{\kappa}_{-1}(\omega_0)+\boldsymbol{\kappa}_{-2}(\omega_0)=\boldsymbol{0} \tag{59}$$

Thus, the relationship between the incident angle, grating period, and central wavelengths becomes :

$$\frac{\sin\theta_0}{\lambda_0}=\frac{3}{2d} \tag{60}$$

Under these assumptions, we relate the maximum transverse spatial frequency to the effective grating numerical aperture $\mathrm{NA_{G2}}$ via,

$$M\left(\frac{\omega_{\max}}{c}\sin\theta_0-\frac{2\pi}{d}\right)=\frac{\omega_{\max}}{c}\mathrm{NA_{G2}} \tag{61}$$

where $\omega_{\max}=\omega_0+\frac{1}{T}$.

The effective $\mathrm{NA_{G2}}$ can be expressed as :

$$\mathrm{NA_{G2}}=M\sin\theta_0-\frac{M}{d}\left(\lambda_0+\frac{\Delta\lambda}{2}\right) \tag{62}$$

For simplicity, here, we assume that $\mathrm{NA_{G2}}<\mathrm{NA_O}$ so $h(\omega)p(M\boldsymbol{\kappa}_n,\omega)\approx h(\omega)$.

In grating TF, optical sectioning comes only from the second-order derivative of $q$ with respect to $\omega$. Here, we show that we obtain optical sectioning by forming the Taylor expansion of $q(M\boldsymbol{\kappa}_n,\omega)$ with respect $\omega_0$ only to first order,

$$q(M\boldsymbol{\kappa}_n,\omega)\approx q(M\boldsymbol{\kappa}_n,\omega_0)+a_n(\omega_0)\nu \tag{63}$$

where $a_n(\omega_0)=\frac{\omega_0}{c^2}-M^2\frac{\sin\theta_0}{c}(\frac{\omega_0}{c}\sin\theta_0+\frac{2\pi n}{d})/\sqrt{\frac{\omega_0^2}{c^2}-M^2(\frac{\omega_0}{c}\sin\theta_0+\frac{2\pi n}{d})^2}$.

Therefore, the $n^{\text{th}}$ order field in Eq. (58) can be simplified and calculated as :

$$\begin{aligned} E_n(\boldsymbol{r},t) &= \int_{-\infty}^{+\infty} h(\omega) e^{i[\boldsymbol{k}_n\cdot\boldsymbol{r}-\omega t]} \mathrm{d}\omega \\ &= \sqrt{\frac{\pi}{T^2}} e^{i[M(\frac{\omega_0}{c}\sin\theta_0+\frac{2\pi n}{d})x+q(M\boldsymbol{\kappa}_n,\omega_0)z-\omega_0 t]} e^{-[\boldsymbol{u}_n\cdot\boldsymbol{r}/c-t]^2/(4T^2)} \\ &= E^n_{\omega_0}(\boldsymbol{r},t) E^n_{\text{pulse}}(\boldsymbol{r},t) \end{aligned} \tag{64}$$

where $\boldsymbol{u}_n = M\sin\theta_0\hat{\boldsymbol{x}} + ca_n(\omega_0)\hat{\boldsymbol{z}}$.

We interpret $E^n_{\omega_0}(\boldsymbol{r},t)$ as a simple phase term while $E^n_{\text{pulse}}(\boldsymbol{r},t)$ is a Gaussian pulse propagating along direction $\boldsymbol{u}_n$ with speed $v_n = c/u_n$. Importantly, we note that the speed propagation along the $x$ axis is the same whatever the order.

The field in the sample space $E_{\text{TO}}(\boldsymbol{r},t)$ is the sum of the -1 and -2 field pulses,

$$E_{\text{TO}}(\boldsymbol{r},t) = E_{-1}(\boldsymbol{r},t) + E_{-2}(\boldsymbol{r},t) \tag{65}$$

For example, when $\lambda_0 = 800nm$, the bandwidth is about $\Delta\lambda \approx 13.5nm$ (200fs), $M = 20$, $d = 10\mu m$, $\sin\theta_0 = 0.12$, $\text{NA}_{\text{O}} = 0.95$, this yields $\text{NA}_{\text{G2}} \approx 0.8$ indicates that the objective can collect all the wavelengths under those parameters. The normalized propagated directions of $E_{-1}(\boldsymbol{r},t)$ and $E_{-2}(\boldsymbol{r},t)$ read

$$\begin{aligned} \boldsymbol{u}_{-1} &= 0.84\hat{\boldsymbol{x}} - 0.54\hat{\boldsymbol{z}} \\ \boldsymbol{u}_{-2} &= 0.44\hat{\boldsymbol{x}} + 0.9\hat{\boldsymbol{z}} \end{aligned} \tag{66}$$

Thus, the -2 order beam propagates towards positive $z$ while the -1 order beam propagates towards negative $z$. At $z = 0$, all the beams propagate along the $x$ axis with the same speed. We illustrate this behavior in Fig. 3.12.

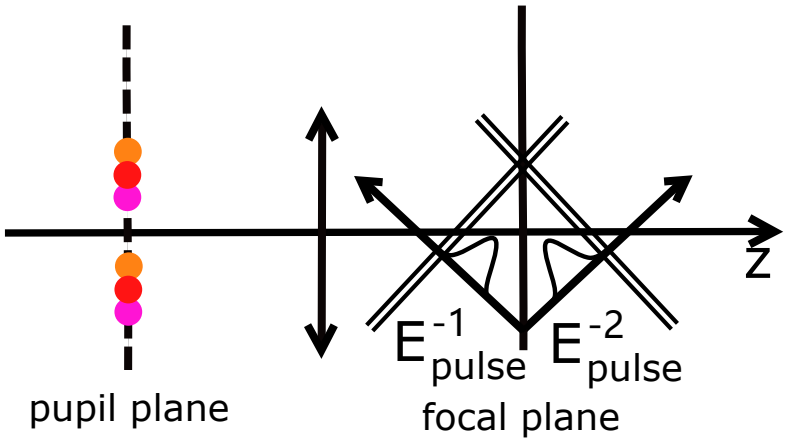


FIGURE 3.12 – Physical understanding of multi-order grating TF when $\lambda_0 = 800nm$, $\Delta\lambda \approx 13.5$, $M = 20$, $d = 10\mu m$, $\sin\theta_0 = 0.12$, $\text{NA}_{\text{O}} = 0.95$. The $-2$ diffracted order pulse $E^{-2}_{\text{pulse}}$ propagates along positive z-axis, whereas the $-1$ diffracted order pulse $E^{-1}_{\text{pulse}}$ propagates along negative z-axis.

The field square intensity of $E^{-1}_{\text{pulse}}(\boldsymbol{r},t)$ and $E^{-2}_{\text{pulse}}(\boldsymbol{r},t)$ at different times are shown in Fig. 3.13. It is observed that at a given time, the field overlap only for $z$ close to 0, and the overlap moves along the x-axis as time increases.

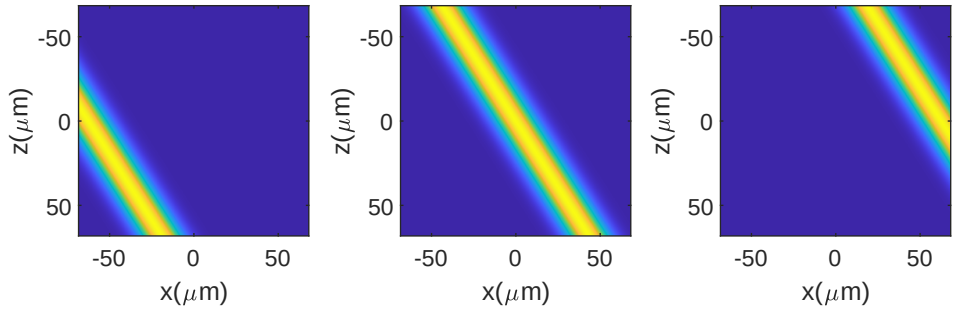


(a) Simulation of the minus one amplitude $|E^{-1}_{\text{pulse}}|(\boldsymbol{r},t)$ for increasing time from left to right

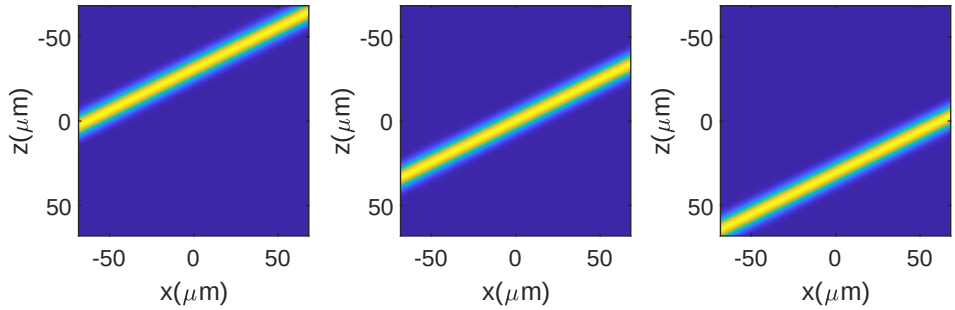


(b) Simulation of the minus two amplitude $|E^{-2}_{\text{pulse}}|(\boldsymbol{r},t)$for increasing time from left to right

FIGURE 3.13 – Multi-order grating TF with $\lambda_0 = 800nm$, $\Delta\lambda \approx 13.5nm$ (200fs), $M = 20$, $d = 10\mu m$, $\sin\theta_0 = 0.12$, $\text{NA}_\text{O} = 0.95$.

We now study the optical sectioning of multi-order grating TF. We first consider one-photon fluorescence excitation of a homogeneous plane placed at $z$ from the focal plane. The one-photon intensity $I_{\text{TO}}(\boldsymbol{r},t)$ is proportional to $|E_{\text{TO}}|^2(\boldsymbol{r},t)$, which can be simplified as

$$|E_{\text{TO}}|^2(\boldsymbol{r},t) = |E_{-1}|^2(\boldsymbol{r},t) + |E_{-2}|^2(\boldsymbol{r},t) + 2\,\text{Re}[E_{-1}(\boldsymbol{r},t)E^*_{-2}(\boldsymbol{r},t)] \tag{67}$$

The collected signal $S_{\text{TO}}(\boldsymbol{r})$ is proportional to the intensity integrated over a long time, and can be derived as follows :

$$\begin{aligned} S_{\text{TO}}(\boldsymbol{r}) &= \int |E_{\text{TO}}|^2(\boldsymbol{r},t)\mathrm{d}t \\ &= \int |E_{-1}|^2(\boldsymbol{r},t)\mathrm{d}t + \int |E_{-2}|^2(\boldsymbol{r},t)\mathrm{d}t + \int 2\,\text{Re}[E_{-1}(\boldsymbol{r},t)E^*_{-2}(\boldsymbol{r},t)]\mathrm{d}t \end{aligned} \tag{68}$$

According to the field derivation in Eq. (64), the first two integrals $\int |E_n|^2(\boldsymbol{r},t)\mathrm{d}t$ in

Eq. (68) are constant and equal to $\frac{2\sqrt{\pi^3}}{T}$. Since we have assumed that the propagation directions of the $-1$ diffracted order and $-2$ diffracted order about the central wavelength are symmetric (see assumption Eq. (59)) about the z-axis, $q(M\boldsymbol{\kappa}_{-1},\omega_0)$ equal to $q(M\boldsymbol{\kappa}_{-2},\omega_0)$, the last term in Eq. (68) can be calculated as,

$$\int 2\,\mathrm{Re}[E_{-1}(\boldsymbol{r},t)E^*_{-2}(\boldsymbol{r},t)]\mathrm{d}t = \frac{\sqrt{8\pi^3}}{T}e^{-\frac{[a_{-1}(\omega_0)-a_{-2}(\omega_0)]^2z^2}{8T^2}}\cos\frac{2\pi}{d}x \tag{69}$$

Even though $\int 2\,\mathrm{Re}[E_{-1}(\boldsymbol{r},t)E^*_{-2}(\boldsymbol{r},t)]\mathrm{d}t$ decreases with $z$, this is not sufficient for getting optical sectioning. Indeed, the latter requires that the signal coming from a homogeneous fluorescent plane decreases with $z$. Thus, we need to integrate the intensity over the whole plane (note that, contrary to the present configuration, in grating TF, the intensity is homogeneous along a transverse plane). Now the average of the interference term over the FOV tends to zero, $\propto \int_L \cos\frac{2\pi}{d}x/L$ when $L$ the FOV size increases. Therefore, multi-order grating TF does not exhibit optical sectioning in one-photon microscopy. To confirm our analysis, we display the XY map of $S_{\mathrm{TO}}(\boldsymbol{r})$ in Fig. 3.14. We see that the intensity oscillates continuously along the x-axis, which is in line with our expectations.

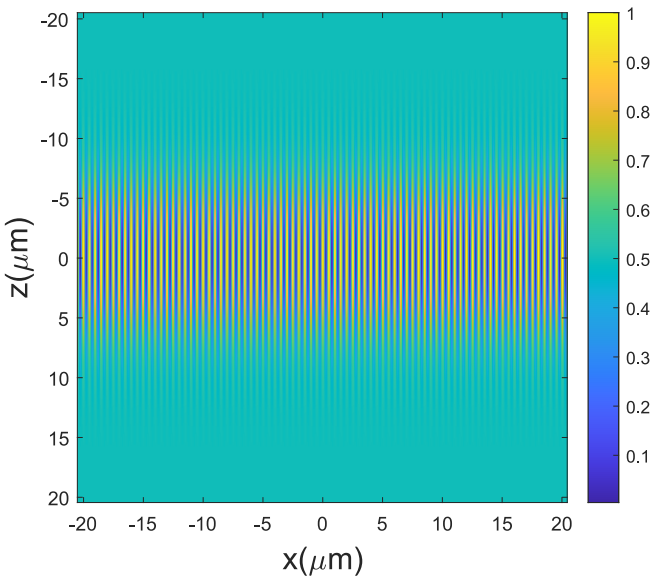


FIGURE 3.14 – XZ map of normalized one-photon intensity $\int |E_{\mathrm{TO}}|^2(x,0,z,t)\mathrm{d}t$ when two diffracted orders are collected. The parameters are the same as in Fig. 3.13.

We now study the optical sectioning capability of multi-order grating TF in two-photon microscopy.

We estimate the two-photon intensity $|E_{\mathrm{TO}}|^4(\boldsymbol{r},t)$ as,

$$|E_{\mathrm{TO}}|^4(\boldsymbol{r},t) = |E_{-1}|^4(\boldsymbol{r},t) + |E_{-2}|^4(\boldsymbol{r},t) + 2|E_{-1}|^2(\boldsymbol{r},t)|E_{-2}|^2(\boldsymbol{r},t) + 4\,\mathrm{Re}[E_{-1}(\boldsymbol{r},t)E^*_{-2}(\boldsymbol{r},t)]^2 + 4\,\mathrm{Re}[E_{-1}(\boldsymbol{r},t)E^*_{-2}(\boldsymbol{r},t)][|E_{-1}|^2(\boldsymbol{r},t) + |E_{-2}|^2(\boldsymbol{r},t)] \tag{70}$$

The integration over time for each term of the above expression can be expressed as

$$\begin{aligned}
\int |E_{-1}|^4(\boldsymbol{r},t)\mathrm{d}t &= \frac{\sqrt{\pi^5}}{T^3} \\
\int |E_{-2}|^4(\boldsymbol{r},t)\mathrm{d}t &= \frac{\sqrt{\pi^5}}{T^3} \\
\int 2|E_{-1}|^2(\boldsymbol{r},t)|E_{-2}|^2(\boldsymbol{r},t)\mathrm{d}t &= \frac{2\sqrt{\pi^5}}{T^3} e^{-\frac{[a_{-1}(\omega_0)-a_{-2}(\omega_0)]^2 z^2}{4T^2}} \\
4\,\mathrm{Re}[E_{-1}(\boldsymbol{r},t)E^*_{-2}(\boldsymbol{r},t)]^2 &= \frac{4\sqrt{\pi^5}}{T^3} e^{-\frac{[a_{-1}(\omega_0)-a_{-2}(\omega_0)]^2 z^2}{4T^2}} \cos\frac{4\pi}{d}x \\
4\,\mathrm{Re}[E_{-1}(\boldsymbol{r},t)E^*_{-2}(\boldsymbol{r},t)][|E_{-1}|^2(\boldsymbol{r},t) + |E_{-2}|^2(\boldsymbol{r},t)] &= \frac{8\sqrt{\pi^5}}{T^3} e^{-\frac{3[a_{-1}(\omega_0)-a_{-2}(\omega_0)]^2 z^2}{16T^2}} \cos\frac{2\pi}{d}x
\end{aligned} \tag{71}$$

Similar to the analysis in the one-photon case, we notice that the average integral of $\cos(x)$ along the x-axis is negligible, so the effects of the last two terms can be neglected. Only the first three terms should be considered. We first observe that the third term, $\int 2|E_{-1}|^2(\boldsymbol{r},t)|E_{-2}|^2(\boldsymbol{r},t)\mathrm{d}t$, decays with $z$, and the extent of its decay depends on $a_n(\omega_0)$ which depends on the (different) velocities of the two pulses. On the other hand, the first two terms provide a constant background. For example, when $\lambda_0 = 800nm$, $\Delta\lambda = 18.1nm$, $M = 20$, $\sin\theta_0 = 0.12$, $\mathrm{NA}_{\mathrm{objective}} = 0.95$, $d = 10\mu m$, the third term provide an optical sectioning of $7.8\mu m$, its intensity is shown in Fig. 3.15. However, the background terms cause the two-photon signal $|E_{\mathrm{TO}}|^4(\boldsymbol{r},t)$ to decay to only half its maximum value. Thus, collecting two diffracted orders cannot provide optical sectioning capability, but we obtain an 'overintensity' about the focal plane when the two pulses propagating along different directions overlap via $\int 2|E_{-1}|^2(\boldsymbol{r},t)|E_{-2}|^2(\boldsymbol{r},t)\mathrm{d}t$. The origin of the overintensity localized about the focal plane in multi-order grating TF differs significantly from the optical sectioning property of grating TF as it does not depend on the group velocity dispersion of the pulse. Here, only the first derivative of $q$ with respect to $\omega$ was accounted for. The analytical result and the simulations are in agreement.

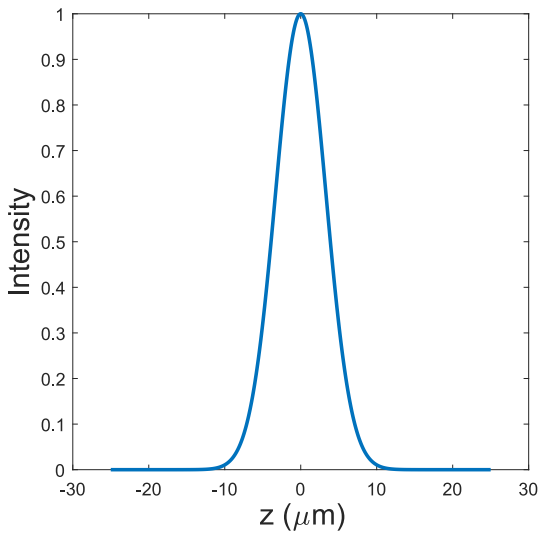


FIGURE 3.15 – Simulation of $\int 2|E_{-1}|^2(\boldsymbol{r},t)|E_{-2}|^2(\boldsymbol{r},t)\mathrm{d}t$ from Eq. (71) as a function of the distance $z$ to the focal plane. If this term was along, we would get an optical sectioning about $7.8\mu m$. However, the two-photon excitation intensity, Eq. (71), includes also two additional terms $\int |E_{-1}|^4(\boldsymbol{r},t)\mathrm{d}t$ and $\int |E_{-2}|^4(\boldsymbol{r},t)\mathrm{d}t$ which provide a constant background. Thus, the signal attenuates to half its maximum value as $z$ increases. The two-order grating TF depicted in Fig. (3.11) does not provide optical sectioning.

### 3.3.2 multi-order grating TF : Three diffracted orders are collected

To reduce the influence of the background ($\int |E_{-1,-2}|^4(\boldsymbol{r},t)\mathrm{d}t$) when two diffracted orders are collected, we analyze the case when three orders $E_{-1}(\boldsymbol{r},t)$, $E_{-2}(\boldsymbol{r},t)$, $E_{-3}(\boldsymbol{r},t)$ are simultaneously collected by the objective lens, as shown in Fig. 3.16.

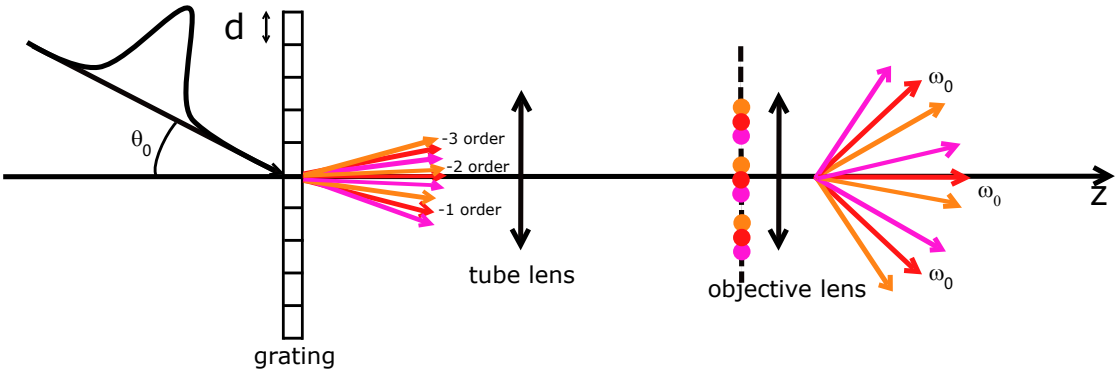


FIGURE 3.16 – Configuration when three diffraction orders are collected. We assume the minus-two diffraction light (at the central wavelength) propagates along the z-axis, while the minus-three and minus-one diffraction light propagate along the positive and negative directions of the grating, respectively.

According to the formula $|a+b+c|^4 = [|a|^2+|b|^2+|c|^2]^2+4(|a|^2+|b|^2+|c|^2)[\mathrm{Re}(ab^*)+\mathrm{Re}(ac^*)+\mathrm{Re}(bc^*)]+4[\mathrm{Re}(ab^*)+\mathrm{Re}(ac^*)+\mathrm{Re}(bc^*)]^2$, after ignoring the real part that will introduce the cosine functions as discussed in Eq. (69), the only effective contributions to the two-photon excitation intensity are,

$$
\begin{aligned}
\int |E_{-1}|^4(\boldsymbol{r},t)\mathrm{d}t &= \frac{\sqrt{\pi^5}}{T^3} \\
\int |E_{-2}|^4(\boldsymbol{r},t)\mathrm{d}t &= \frac{\sqrt{\pi^5}}{T^3} \\
\int |E_{-3}|^4(\boldsymbol{r},t)\mathrm{d}t &= \frac{\sqrt{\pi^5}}{T^3} \\
\int 2|E_{-1}|^2(\boldsymbol{r},t)|E_{-2}|^2(\boldsymbol{r},t)\mathrm{d}t &= \frac{2\sqrt{\pi^5}}{T^3} e^{-\frac{[a_{-1}(\omega_0)-a_{-2}(\omega_0)]^2 z^2}{4T^2}} \\
\int 2|E_{-1}|^2(\boldsymbol{r},t)|E_{-3}|^2(\boldsymbol{r},t)\mathrm{d}t &= \frac{2\sqrt{\pi^5}}{T^3} e^{-\frac{[a_{-1}(\omega_0)-a_{-3}(\omega_0)]^2 z^2}{4T^2}} \\
\int 2|E_{-2}|^2(\boldsymbol{r},t)|E_{-3}|^2(\boldsymbol{r},t)\mathrm{d}t &= \frac{2\sqrt{\pi^5}}{T^3} e^{-\frac{[a_{-2}(\omega_0)-a_{-3}(\omega_0)]^2 z^2}{4T^2}}
\end{aligned}
\tag{72}
$$

We see that when we consider three orders, the background intensity becomes

only one-third of the maximum intensity. For instance, when $d = 10\mu m$, $\sin\theta_0 = 0.16$, $\lambda_0 = 800nm$, $M = 10$, $\mathrm{NA_O} = 0.95$, $\Delta\lambda = 12.3nm$, we simulate two-photon excitation intensity with the complex field

$$E_{\mathrm{P3}}(\boldsymbol{r},t) = E_{-1}(\boldsymbol{r},t) + E_{-2}(\boldsymbol{r},t) + E_{-3}(\boldsymbol{r},t) \tag{73}$$

(Eq. (58) gives the expression of $E_n(\boldsymbol{r},t)$), the collected signal is proportional to $\int |E_{\mathrm{P3}}|^4(\boldsymbol{r},t)\mathrm{d}t$.

Fig. 3.17 displays the xz-map of the two-photon excitation intensities for the three-order grating TF (three orders are collected) and one-order grating TF (one order is collected), with the same parameters $d = 10\mu m$, $\sin\theta_0 = 0.16$, $\lambda_0 = 800nm$, $M = 10$, $\mathrm{NA_O} = 0.95$, $\Delta\lambda = 12.3nm$. We observe that with these particular parameters, the optical sectioning produced by a single pulse is negligible, while multiple pulses (multiple orders) yield an optical sectioning of approximately 15 micrometers (with still a background about one third of the maximum intensity as expected with the analytical model).

In the three-order grating TF configuration, the field in the backfocal plane of the objective appear as three short rainbow lines that tend to fill the pupil as illustrated in Fig. 3.18a). Thus, introducing multiple pulses compensates for the limitations of $\mathrm{NA_G}$. It enables optical sectioning even in configurations with low magnification and small wavelength bandwidths through the speed and propagation direction mismatch between the different pulses.

We illustrate the mechanism subtending the temporal focusing in the three-order grating TF configuration in Fig. 3.18b.The pulse is diffractedthree short rainbow lines at the pupil plane transforms into three beams in the sample space that propagate along different directions (one towards positive $z$, one towards negative $z$ and one along the $x$ axis). Yet, in the $z = 0$ plane, all the beams propagate with the same speed along the $x$ axis. Thus, the overlap of the beam at $z = 0$ forms a Y line that moves along $x$. It is worth noting that with the same parameters as Fig. 3.17, any beam alone cannot provide optical sectioning as the magnification and wavelength bandwidth are too small. It is the overlapping between the three pulses that generate the overintensity about the focal plane.

We have seen that when the number of orders increases from two to three, the influence of the background diminishes. It can be shown that increasing further the number of orders will gradually diminish the background influence by using the formula

$$\begin{aligned} |\sum_{i=1}^{n} z_i|^4 = \sum_i |z_i|^4 + 2\sum_{i\neq j} |z_i|^2|z_j|^2 \\ +4\sum_{i\neq j} |z_i|^2\,\mathrm{Re}(z_j z_i^*) + 4\sum_{i\neq j, i<k, j<l} \mathrm{Re}(z_i z_j^*)\,\mathrm{Re}(z_k z_l^*). \end{aligned} \tag{74}$$

. In the estimation of the optical sectioning we neglect the oscillating interference terms as their influence is negligible when they are integrated over the FOV, as dis-

cussed in Eqs. 71 and 72). Then, according to Eqs. 71 and 72, the terms $\int |E_n|^4(\boldsymbol{r},t)\mathrm{d}t$ provides a constant background equal to $\frac{\sqrt{\pi^5}}{T^3}$, and the term $\int_{i\neq j} 2|E_i|^2(\boldsymbol{r},t)|E_j|^2(\boldsymbol{r},t)\mathrm{d}t$ provides an overintensity at $z=0$ with a maximum value of $\frac{2\sqrt{\pi^5}}{T^3}$. Therefore, if multi-order fields could be considered, the impact of background intensity compared to the overintensity would become negligible. However, controlling parameters to ensure multiple pulses or multiple orders propagate along the given directions becomes experimentally challenging. Therefore, replacing multi-order illumination with random illumination proves to be a sound alternative.

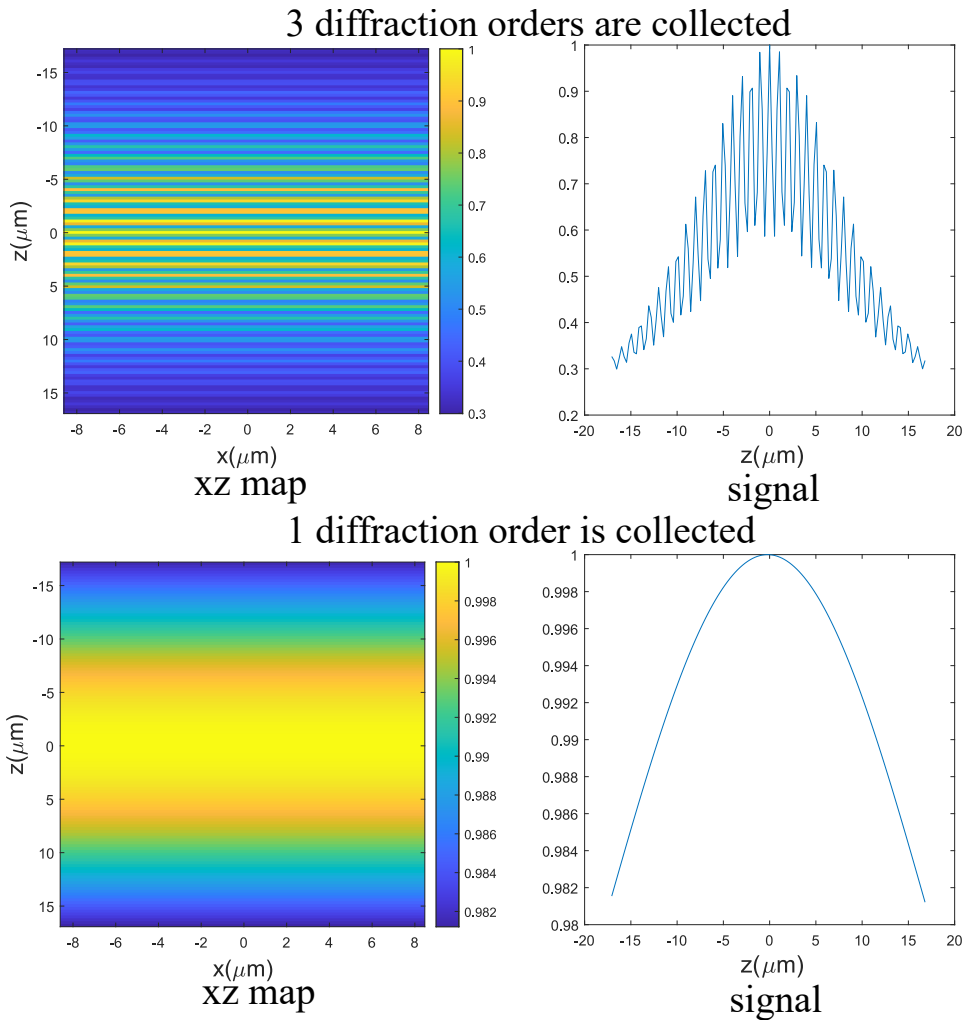


FIGURE 3.17 – XZ map of the two-photon excitation intensity for the following parameters : $d = 10\mu m$, $\sin\theta_0 = 0.16$, $\lambda_0 = 800nm$, $M = 10$, $\mathrm{NA_O} = 0.95$, $\Delta\lambda = 12.3nm$ (220 fs). (a) : two photon excitation intensity in the three-order grating TF, $\int |E_{\mathrm{P3}}|^4(x,0,z,t)\mathrm{d}t$, in the XZ plane. Fringes appear because of the interference between the three orders. (b) : Cut of (a) taken at $x = 0$. The optical sectioning is estimated to about 15 microns. A residual background of one third the maximum intensity is also observed. (c) : XZ map of the two-photon excitation intensity $\int I_{\mathrm{TF}}(x,0,z,t)\mathrm{d}t$ for grating TF (only one diffracted order is collected) for the same microscope and pulse parameters. (d) Cut of (c) taken at $x = 0$. For these parameters, the two-photon excitation intensity of the one-order grating TF is almost constant with respect to $z$ (no optical sectioning).

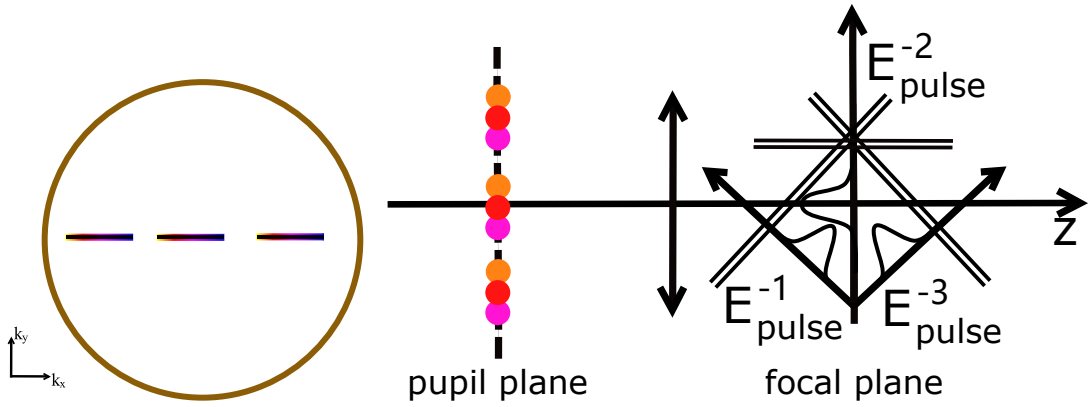


(a) Pupil plane (b) Pulse propagation

FIGURE 3.18 – Physical pictures of the pupil plane and the pulse propagation. Fig a : Illustration of the pupil plane when three diffraction orders are collected simultaneously. The pulse of each order is stretched into a short rainbow line. Fig b : physical understanding of three-order-grating TF beam with the parameters in Fig. 3.17. −2 diffracted order moves along the x-axis, while −1 and −3 diffracted orders move along the negative and positive directions of the z-axis, respectively.

## 3.4 Optical sectioning obtained from a pulse diffracted by a rough surface : Roughness TF

After modeling and analyzing grating TF and multiorder-grating TF, we intend to combine random illumination with grating TF. However, before exploring this configuration, we first analyze the optical sectioning capability of a pulse diffracted by a rough surface or a thin diffuser.

Generally, a rough surface can be considered as a superposition of gratings with different periods. When a monochromatic plane wave with transverse wavevector $\boldsymbol{\kappa}_{\text{inc}}$ and frequency $\omega$ is incident on a rough surface, the scattered field reads,

$$E(\boldsymbol{r},t) = \text{Re}\left(\int \eta(\boldsymbol{\kappa}) e^{i[\boldsymbol{k}\cdot\boldsymbol{r}-\omega_0 t]} \text{d}\boldsymbol{\kappa}\right) \tag{75}$$

where $\eta(\boldsymbol{\kappa})$ is a random complex variable that depends on the surface roughness (under first order diffraction approximation, $\eta(\boldsymbol{\kappa}) = \tilde{h}(\boldsymbol{\kappa} - \boldsymbol{\kappa}_{\text{inc}})$ where $\tilde{h}$ is the Fourier transform of the rough surface height and $\boldsymbol{\kappa}_{\text{inc}}$ is the projection of the incident wavevector onto the surface plane).

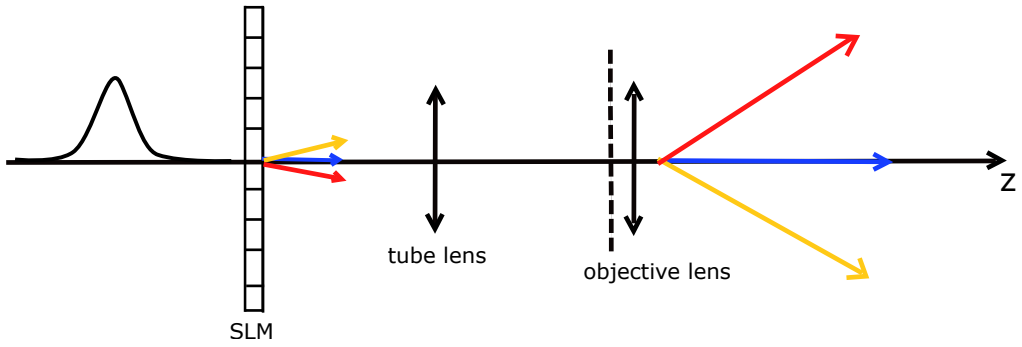


FIGURE 3.19 – A pulse incident on a rough surface is slightly dispersed. However, this dispersion appears weaker than that obtained using a grating with a small period. The rough surface can be understood as a superposition of gratings with different periods, among which, the large ones are not efficient for dispersing the pulse.

We now consider a pulse that illuminates a rough surface, placed at the image plane of a microscope, under normal incidence as shown in Fig. 3.19. We assume that the complex amplitudes of the diffracted waves generated by the rough surface can be written as $\eta = e^{i\phi}$ where $\phi$ is an uncorrelated random variable between $[0, 2\pi]$. In other terms, we assume that the rough surface (or diffuser) generates a fully developed speckle. Importantly, we further assume that the random phases do not depend on the wavelength (within the limited bandwidth of the pulse). Under these hypothesis,

the field at the focal plane can be written as the real part of,

$$E_{\mathrm{r}}(\boldsymbol{r},t)=\int\int_{-\infty}^{+\infty}h(\omega)g(\boldsymbol{\kappa})p(M\boldsymbol{\kappa},\omega)e^{i\phi(\boldsymbol{\kappa})}e^{i[\boldsymbol{k}_S\cdot\boldsymbol{r}-\omega t]}\mathrm{d}\boldsymbol{\kappa}\mathrm{d}\omega \tag{76}$$

where $\boldsymbol{k}_S=M\boldsymbol{\kappa}+q(M\boldsymbol{\kappa},\omega)\hat{\boldsymbol{z}}$, $g(\boldsymbol{\kappa})=e^{-R^2\boldsymbol{\kappa}^2}$ with $R=\frac{M\lambda_0}{2\pi\mathrm{NA_S}}$ and $\mathrm{NA_S}$ is the effective NA of the diffuser (which is related to the scattering distribution function of the diffuser) after the magnification by the microscope, $e^{\phi(\boldsymbol{\kappa})}$ satisfies $\langle e^{i\phi(\boldsymbol{\kappa})}e^{-i\phi(\boldsymbol{\kappa}')}\rangle=\delta(\boldsymbol{\kappa}-\boldsymbol{\kappa}')$, and zero mean : $\langle e^{i\phi(\boldsymbol{\kappa})}\rangle=0$ , where $\langle\rangle$ is the averaging, we recall that $h(\omega)=e^{T^2\nu^2}$, $p(\boldsymbol{\kappa},\omega)=1$ for $\boldsymbol{\kappa}<\frac{\omega}{c}\mathrm{NA_O}$ and 0 elsewhere. From Eq. (76), we can interpret the speckled pulse as a collection of plane-wave pulses with random phases propagating along multiple directions within a solid angle depending on the NA of the diffuser, $\mathrm{NA_S}$.

We now assume that all the light can be collected by the objective, $\mathrm{NA_S}<\mathrm{NA_O}$, so $g(\boldsymbol{\kappa})p(M\boldsymbol{\kappa},\omega)\approx g(\boldsymbol{\kappa})$ and Eq. (76) can be seen as the integral of a complex Gaussian. To obtain an analytical expression, we use the paraxial approximation : $q(M\boldsymbol{\kappa},\omega)=\sqrt{\frac{\omega^2}{c^2}-M^2\boldsymbol{\kappa}^2}\approx\frac{\omega}{c}-\frac{cM^2}{2\omega}\boldsymbol{\kappa}^2$ and Taylor expansion of $q(M\boldsymbol{\kappa},\omega)$ with respect to $\omega$ at $\omega_0$ :

$$q(M\boldsymbol{\kappa},\omega)\approx q(M\boldsymbol{\kappa},\omega_0)+\alpha(\boldsymbol{\kappa})(\omega-\omega_0) \tag{77}$$

where $\alpha(\boldsymbol{\kappa})=\frac{1}{c}+\frac{cM^2\boldsymbol{\kappa}^2}{2\omega_0^2}$.

The complex field $E_{\mathrm{r}}(\boldsymbol{r},t)$ becomes

$$E_{\mathrm{r}}(\boldsymbol{r},t)=\int e^{iC_S(z,t)}g(\boldsymbol{\kappa})e^{-\frac{[\alpha(\boldsymbol{\kappa})z-t]^2}{4T^2}}e^{i\phi(\boldsymbol{\kappa})}e^{iM\boldsymbol{\kappa}\cdot\boldsymbol{x}}\mathrm{d}\boldsymbol{\kappa} \tag{78}$$

where $\boldsymbol{x}=[x,y]$ is the transverse space variable, $C_S(z,t)=e^{i[q(M\boldsymbol{\kappa},\omega_0)z-\omega_0 t]}$.

The pulse diffracted by the diffuser only moves along the z-axis with the speed of $1/\alpha(\boldsymbol{\kappa})$. Thus, the diffraction is not enough as in grating TF, multi-order TF cases, as illustrated in Fig. 3.20.

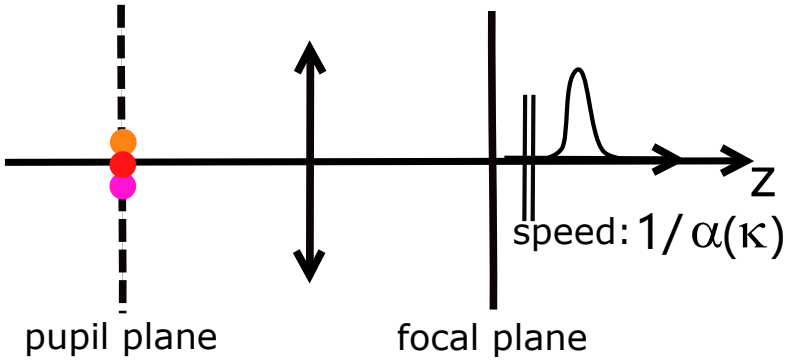


FIGURE 3.20 – Pulse diffracted only by the diffuser propagates along z axis, with the positive speed $v=1/\alpha(\boldsymbol{\kappa})$.

To estimate the optical sectioning of the speckled pulse, it is necessary to integrate the excitation intensity over a transverse plane at a given $z$. Now the latter is equiva-

lent to forming the ensemble average at $(\boldsymbol{r}, t)$ (due to the transverse ergodicity). The random phase being uncorrelated, $\langle e^{i\phi(\boldsymbol{\kappa})} e^{-i\phi(\boldsymbol{\kappa}')}\rangle = \delta(\boldsymbol{\kappa}-\boldsymbol{\kappa}')$, the averaged excitation intensity in the one-photon case can be expressed as

$$\langle |E|_{\mathrm{r}}^2\rangle(\boldsymbol{r}, t) \propto \int g^2(\boldsymbol{\kappa}) e^{-\frac{[\alpha(\boldsymbol{\kappa})z-t]^2}{2T^2}} \mathrm{d}\boldsymbol{\kappa} \tag{79}$$

While, due to the property of circular complex Gaussian random variable : $\langle |E|^4\rangle(\boldsymbol{r}, t) = 2\langle |E|^2\rangle^2(\boldsymbol{r}, t)$ (GOODMAN 1985), the averaged intensity in two-photon case reads

$$\langle |E|_{\mathrm{r}}^4\rangle(\boldsymbol{r}, t) \propto \int\int g^2(\boldsymbol{\kappa}) e^{-\frac{[\alpha(\boldsymbol{\kappa})z-t]^2}{2T^2}} g^2(\boldsymbol{\kappa}') e^{-\frac{[\alpha(\boldsymbol{\kappa}')z-t]^2}{2T^2}} \mathrm{d}\boldsymbol{\kappa}\mathrm{d}\boldsymbol{\kappa}' \tag{80}$$

As usual, in one-photon fluorescence microscopy, the speckled pulse can not provide optical sectioning because the averaged one-photon excitation intensity integrated over time is a constant. On the other hand, the averaged two-photon excitation intensity integrated over time can be simplified as

$$\int \langle |E|_{\mathrm{r}}^4\rangle(\boldsymbol{r}, t) dt \propto \int\int g^2(\boldsymbol{\kappa}) g^2(\boldsymbol{\kappa}') e^{-P(z)[\boldsymbol{\kappa}^2-\boldsymbol{\kappa}'^2]^2} \mathrm{d}\boldsymbol{\kappa}\mathrm{d}\boldsymbol{\kappa}' \tag{81}$$

where $P(z) = \frac{M^4\Delta\lambda^2 z^2}{256\pi^2}$

Writing $\boldsymbol{\kappa}$ in polar coordinates $\kappa$, $\theta$ : $\boldsymbol{\kappa} = \kappa[\cos\theta, \sin\theta]$, the recorded 2PE signal becomes

$$\begin{aligned} I_{\mathrm{r}}(z) &= \int |E|_{\mathrm{r}}^4(\boldsymbol{r}, t)\mathrm{d}t\mathrm{d}\boldsymbol{x} \\ &= \int \langle |E|_{\mathrm{r}}^4\rangle(\boldsymbol{r}, t)\mathrm{d}t \\ &\propto \int_0^{+\infty}\int_0^{+\infty} e^{-2R^2\kappa^2} e^{-2R^2\kappa'^2} e^{-P(z)[\kappa^2-\kappa'^2]^2} \kappa\kappa' \mathrm{d}\kappa\mathrm{d}\kappa' \end{aligned} \tag{82}$$

which, thanks to the additional coordinate change, $a = \kappa^2$, $b = \kappa'^2$, yields,

$$\begin{aligned} I_{\mathrm{r}}(z) &\propto \int_0^{+\infty}\int_0^{+\infty} e^{-2R^2 a} e^{-2R^2 b} e^{-A(z)(a-b)^2} \mathrm{d}a\mathrm{d}b \\ &= \frac{\sqrt{\pi}}{4R^2\sqrt{P(z)}} \end{aligned} \tag{83}$$

The expression Eq. (83) shows that, at $z = 0$, the signal reaches its maximum $I_S(0) = \frac{1}{4R^2}$ and the optical sectioning (FWHM of $I_{\mathrm{r}}(z)$) is,

$$\Delta Z_{\mathrm{S}} = \frac{16\lambda_0^2}{\sqrt{\pi}\Delta\lambda \mathrm{NA_S}^2} \tag{84}$$

From Eq. (84), we observe that the optical sectioning only depends on the pulse

wavelength bandwidth $\Delta\lambda$ (pulse duration) and $NA_S$. Unlike grating TF, $M$ is unimportant because magnification does not increase the pulse dispersion, the only dispersion is generated by the roughness. For example, if the incident wavelength bandwidth is about $18.1nm$, $\lambda_0 = 800nm$, $NA_S = 0.95$, the optical sectioning of a pulsed fully developed speckle diffracted by a rough surface is about $300\mu m$ as illustrated in Fig. 3.21. Note that the grating TF can provide an optical sectioning of $6.4\mu m$ (see Fig. 3.6b) with the same parameters and a magnification of 40. Thus, if the pulse duration is about several hundred femtoseconds, the optical sectioning of the pulsed speckle is negligible and can even be approximated as a monochromatic plane wave without optical sectioning. In other words, if we want to obtain optical sectioning of a few micrometers, a broader wavelength bandwidth is required, and such short duration pulse is obviously difficult to obtain. This observation aligns with the remark given in TF's original paper (ORON, TAL et al. 2005), which proposed to replace the rough surface with a tilted grating due to the much better dispersion property of the latter.

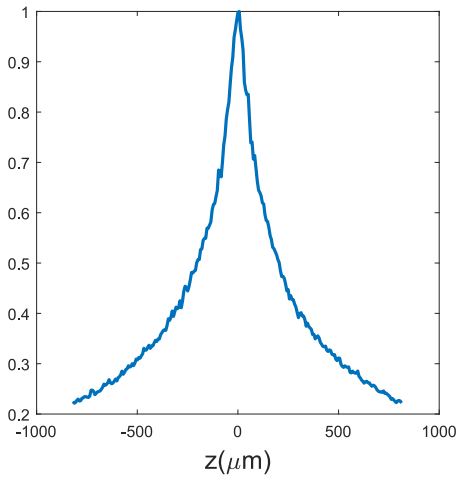


FIGURE 3.21 – Integrated signal for a homogeneous fluorescent plane in a 2PM as a function of the distance to the focal plane, $I_S(z)$, when the pulsed illumination is diffracted by a rough surface. The parameters are $\Delta\lambda = 18.1nm$, $\lambda_0 = 800nm$, and $NA_S = 0.95$. The optical sectioning is estimated to $300\mu m$.

## 3.5 Improving optical sectioning by combining grating TF with random illumination : Roughness-grating TF

In this section, we study the optical sectioning obtained with temporal-focused speckles (TF-speckle) obtained by combining grating TF with random illumination obtained using a diffuser. This idea originated from the previous sections showing that multiple pulses incident on a grating (multi-order grating TF) can improve the optical sectioning capability as compared to grating TF (in this case optical sectioning does not stem only from the GVD), while illuminating a thin diffuser with a collimated beam pulse generates multiple pulses propagating along different directions.

### 3.5.1 Theory of Temporal-Focused Speckle (TF-speckle)

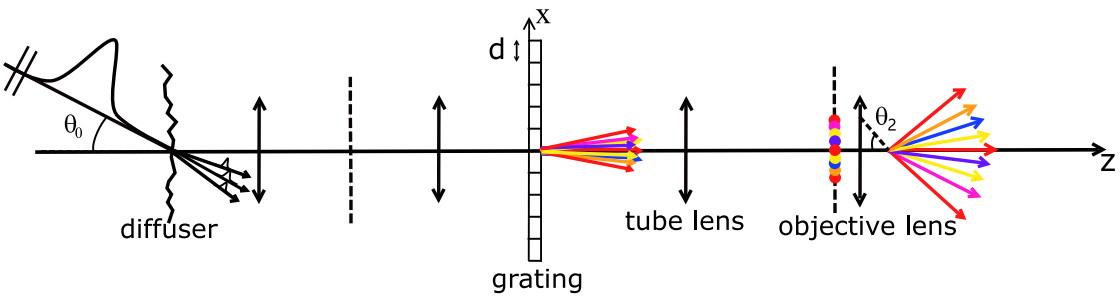


FIGURE 3.22 – Configuration of temporal-focused speckle with a transmission grating. The incident laser pulse first passes through a diffuser, which scatters it into speckle pattern where plane waves of all wavelengths acquire the same random phase distribution. This speckled illumination is then directed at an angle onto a transmission grating, which disperses the light such that different wavelengths propagate in distinct directions.

The roughness-grating TF configuration is shown in Fig. 3.22. We consider a microscope with magnification $M$. A collimated pulsed beam illuminates a thin diffuser with numerical aperture $\mathrm{NA_S}/M$ at an angle $\theta_0$. As in the previous paragraph, the thin diffuser scatters light into multiple plane-wave pulses with random phases propagating within a certain solid angle related to $\mathrm{NA_S}/M$. Similarly to Eq. (76), the field after the diffuser can be modeled as,

$$E_S(\boldsymbol{r},t) = \int\int_{-\infty}^{+\infty} h(\omega)g(\boldsymbol{\kappa})e^{i\phi(\boldsymbol{\kappa})}e^{i[\boldsymbol{k}_S\cdot\boldsymbol{r}-\omega t]}\mathrm{d}\boldsymbol{\kappa}\mathrm{d}\omega \tag{85}$$

where we recall that $\boldsymbol{k}_S = \boldsymbol{\kappa}_{\mathrm{inc}}(\omega)+\boldsymbol{\kappa}+q(\boldsymbol{\kappa}_{\mathrm{inc}}+\boldsymbol{\kappa},\omega)\hat{\boldsymbol{z}}$, $\boldsymbol{\kappa}_{\mathrm{inc}} = \frac{\omega\sin\theta_0}{c}\hat{\boldsymbol{x}}$, $h(\omega) = e^{-T^2\nu^2}$, and $g(\boldsymbol{\kappa}) = e^{-R^2\boldsymbol{\kappa}^2}$ with $R = \frac{M\lambda_0}{2\pi\mathrm{NA_S}}$.

Then, the multiple pulse beams illuminate a grating of period $\boldsymbol{d} = d\hat{\boldsymbol{x}}$ placed at a plane conjugated to the objective image focal plane. Only the minus one diffracted order of the grating is collected by the objective. The grating and the microscope magnification transform the transverse wavevector $\boldsymbol{\kappa} + \boldsymbol{\kappa}_{\text{inc}}(\omega)$ into $\boldsymbol{\kappa}_s(\omega) = M(\boldsymbol{\kappa} + \boldsymbol{\kappa}_{\text{inc}}(\omega) - \frac{2\pi}{d}\hat{\boldsymbol{x}})$ so that the pulse field after the objective, in the sample space reads :

$$E_{\text{SG}}(\boldsymbol{r}, t) = \int\int_{-\infty}^{+\infty} h(\omega) g(\boldsymbol{\kappa}) p(\boldsymbol{\kappa}_s, \omega) e^{i\phi(\boldsymbol{\kappa})} e^{i[\boldsymbol{k}_{SG}\cdot\boldsymbol{r} - \omega t]} \mathrm{d}\boldsymbol{\kappa}\mathrm{d}\omega \tag{86}$$

where $\boldsymbol{k}_{SG} = \boldsymbol{\kappa}_s(\omega) + q(\boldsymbol{\kappa}_s, \omega)\hat{\boldsymbol{z}}$.

For collecting most of the dispersed waves, we keep the same assumption as in grating TF, $\boldsymbol{\kappa}_{\text{inc}}(\omega_0) - \frac{2\pi}{d}\hat{\boldsymbol{x}} = 0$. Then, we can write,

$$\boldsymbol{\kappa}_s(\omega) = M(Qv\hat{\boldsymbol{x}} + \boldsymbol{\kappa}). \tag{87}$$

where we recall that $Q = \frac{\lambda_0}{cd}$.

Taking the first-order Taylor expansion with respect to $\omega$ of $q(\boldsymbol{\kappa}_s, \omega)$ at $\omega_0$ gives,

$$q(\boldsymbol{\kappa}_s, \omega) \approx q(M\boldsymbol{\kappa}, \omega_0) + \beta(\boldsymbol{\kappa})v \tag{88}$$

with $\beta(\boldsymbol{\kappa}) = (\frac{\omega_0}{c^2} - M^2 Q\kappa_x)/\sqrt{\frac{\omega_0^2}{c^2} - M^2\boldsymbol{\kappa}^2}$, $\boldsymbol{\kappa} = \kappa_x\hat{\boldsymbol{x}} + \kappa_y\hat{\boldsymbol{y}}$.

Since the transverse spatial frequency $\boldsymbol{\kappa}_s(\omega)$ is a sum of $Qv\hat{\boldsymbol{x}}$ and $\boldsymbol{\kappa}$, we can understand that the field at the pupil plane consists of a superposition of rainbow lines, as illustrated in Fig. 3.23. This interpretation is confirmed by the simulation of the field amplitude at the pupil plane, $|\int E_{\text{SG}}(x, y, 0, 0) e^{-i(\kappa_x x + i\kappa_y y)} \mathrm{d}x\mathrm{d}y|$, shown in Fig. 3.24.

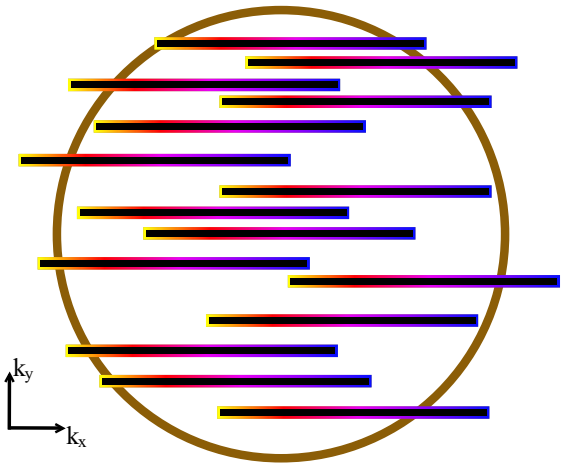


FIGURE 3.23 – Illustration of the pupil plane for temporal-focused speckle. The pulse is diffracted by a thin diffuser into multiple pulsed beams with different directions and random phases. Then, the multiple pulses are stretched by the grating into multiple rainbow lines.

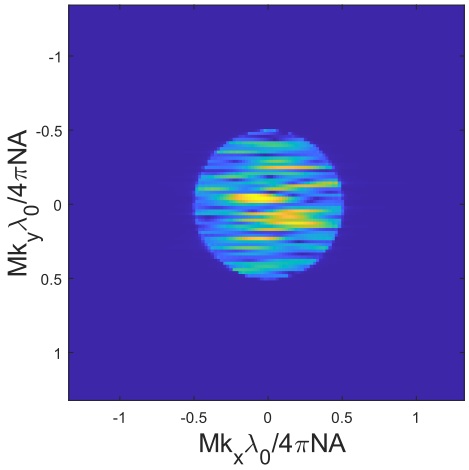


FIGURE 3.24 – Simulation of the field amplitude at the Fourier (pupil) plane $|\int E_{SG}(x,y,0,0)e^{-i(\kappa_x x+i\kappa_y y)}\mathrm{d}x\mathrm{d}y|$ in a roughness-grating TF configuration : $M = 40$, $\lambda_0 = 800nm$, $d = 1\mu m$, $\Delta\lambda = 18.1nm$, $\mathrm{NA_O} = 0.75$, $\mathrm{NA_S} = 0.75$.

A first expected benefit of roughness-grating TF is that it reduces the damage the pulsed illumination can cause to the objective. In grating TF, all the energy is concentrated in a single line in the Fourier (backfocal) plane of the objective, see Fig. 3.2. Roughness-grating TF allows the energy to be distributed across the entire Fourier plane, decreasing the power surface density as illustrated in Figs. 3.23, 3.24.

To pursue our analytical study, we now assume that all the plane waves are collected by the pupil. This condition is roughly satisfied if $\mathrm{NA_G} + \mathrm{NA_S} < \mathrm{NA_O}$. In this case, $g(\boldsymbol{\kappa})p(\boldsymbol{\kappa}_s,\omega)$ can be approximated as $g(\boldsymbol{\kappa})$. In this way, after calculating the integral over $\omega$, $E_{SG}(\boldsymbol{r},t)$ can be expressed as :

$$E_{SG}(\boldsymbol{r},t) = \int_{-\infty}^{+\infty} g(\boldsymbol{\kappa})e^{i\phi(\boldsymbol{\kappa})}e^{i[\boldsymbol{\kappa}_0\cdot\boldsymbol{r}-\omega_0 t]}e^{-\frac{W^2(\boldsymbol{\kappa})}{4T^2}}\mathrm{d}\boldsymbol{\kappa} \tag{89}$$

where $W(\boldsymbol{\kappa}) = MQx + \beta(\boldsymbol{\kappa})z - t$, $\boldsymbol{\kappa}_0 = M\boldsymbol{\kappa}\hat{\boldsymbol{x}} + q(M\boldsymbol{\kappa},\omega_0)\hat{\boldsymbol{z}}$.

Furthermore, if the diffuser NA and magnification are small enough, $(M\kappa << k_0)$, it is possible to use the first order Taylor expansion with respect to $\boldsymbol{\kappa}$ of $\beta(\boldsymbol{\kappa})$ at $\boldsymbol{\kappa} = \mathbf{0}$,

$$\beta(\boldsymbol{\kappa}) \approx \frac{1}{c} - \frac{cM^2Q}{\omega_0}\kappa_x \tag{90}$$

In this case, $\beta(\boldsymbol{\kappa})$ becomes a linear function of $\kappa_x$, so $W(\boldsymbol{\kappa})$ can be simplified as :

$$\begin{aligned} W(\kappa_x) &= MQx + (\frac{1}{c} - \frac{cM^2Q}{\omega_0}\kappa_x)z - t \\ &= \frac{\boldsymbol{u}_{\kappa_x}\cdot\boldsymbol{r}}{c} - t \end{aligned} \tag{91}$$

with $\boldsymbol{u}_{\kappa_x} = McQ\hat{\boldsymbol{x}} + (1 - \frac{c^2M^2Q}{\omega_0}\kappa_x)\hat{\boldsymbol{z}}$.

Unlike the pulse described in Eq. (49) in grating TF, which propagates along direction $\boldsymbol{u}_{\text{ref}} = McQ\hat{\boldsymbol{x}} + \hat{\boldsymbol{z}}$ (mainly along $\hat{\boldsymbol{x}}$) and velocity $v_{\text{ref}} = c/u_{\text{ref}}$, the TF-speckle beam can be interpreted as the superposition of multiple pulses propagating in normalized directions $\boldsymbol{u}_{\kappa_x}/u_{\kappa_x}$ with speed $c/u_{\kappa_x}$. Since $\kappa_x$ varies in a range dictated by the diffuser strength, $g$, $\kappa_x \in [-1/(\sqrt{2}R), 1/(\sqrt{2}R)]$, we can extract the extreme directions and velocities : for $\boldsymbol{\kappa}_x = -1/(\sqrt{2}R)$, $\boldsymbol{u}_{\min} = McQ\hat{\boldsymbol{x}} + \left(1 + \frac{McQ\text{NA}_S}{\sqrt{2}}\right)\hat{\boldsymbol{z}}$ and $v_{\min} = c/u_{\min}$, for $\boldsymbol{\kappa}_x = 1/(\sqrt{2}R)$, $\boldsymbol{u}_{\max} = McQ\hat{\boldsymbol{x}} + \left(1 - \frac{McQ\text{NA}_S}{\sqrt{2}}\right)\hat{\boldsymbol{z}}$ and $v_{\max} = c/u_{\max}$. The pulses forming the temporal-focus speckle field propagate along directions between $\boldsymbol{u}_{\min}$ and $\boldsymbol{u}_{\max}$ with speeds between $v_{\min}$ and $v_{\max}$. Thus, we notice that some pulses propagate towards positive $z$ while others propagate towards negative $z$ as in multi-order-grating TF. They superpose only at $z = 0$ where all the pulses move along the $x$ direction with the same speed $1/(MQ)$, as in grating and multi-order grating TF.

We try to give a geometrical illustration of this behavior in Fig. 3.25 and complete this interpretation with a simulation of the field square intensity at $z = 0$ as a function of time, $|E_{\text{SG}}(x, y, 0, t)|^4$ is given by Eq. (86), in Fig. 3.26. We observe that, as expected, the field square intensity is a random line that moves along the $x$ direction.

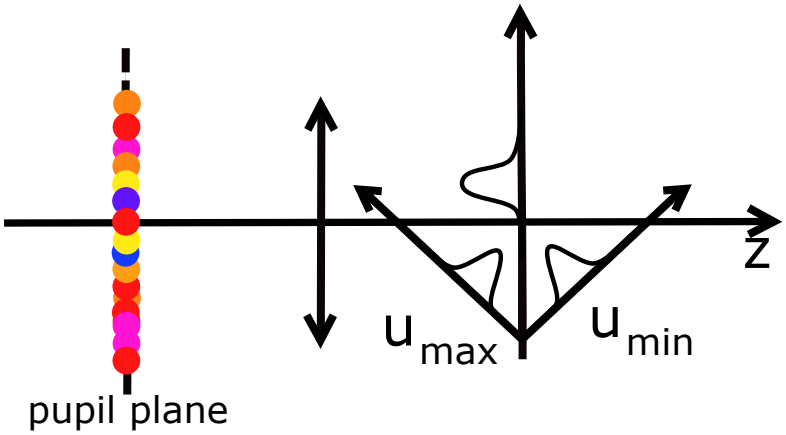


FIGURE 3.25 – Physical insight into the field created in the sample space by the roughness-grating TF. The field is a superposition of pulses, some propagate towards positive $z$ and others towards negative $z$. At $z = 0$ all the pulses move along the $x$ axis with the same speed.

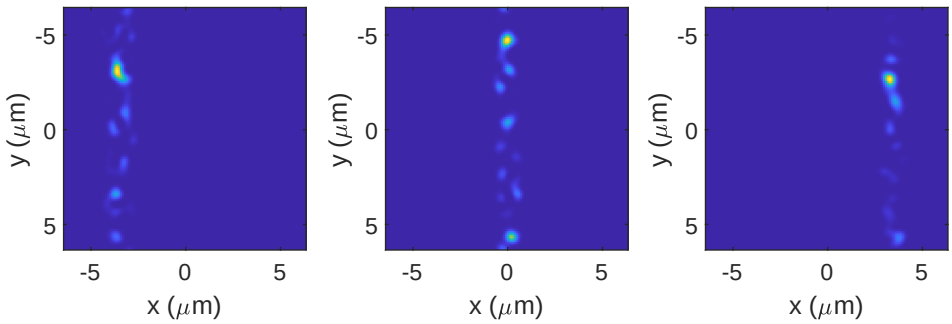


FIGURE 3.26 – Square intensity in the XY plane at $z = 0$ of the temporal-focused speckle beam. $|E_{SG}(x, y, 0, t)|^4$ is simulated with Eq. (86) for increasing times $t$ (from left to right). In the $z = 0$ plane, the square intensity forms a line that moves along $x$ as $t$ increases.

In the XY plane at $z = 0$, whatever $y$, one can find a time $t$ for which all the pulses coincide at a given $x$. Thus, a field enhancement in the shape of a Y-line moving along the $x$ direction is expected at $z = 0$ as in multi-order grating TF. However, contrary to this configuration, the square intensity line in the XY plane is not homogeneous. Indeed, when the pulses coincide (at $z = 0$ and $MQx - t = 0$), they can interfere destructively or constructively as each pulse is affected by a random fixed phase $e^{i\phi(\boldsymbol{\kappa})}$ and a varying phase $e^{i\boldsymbol{\kappa}_0 \cdot \boldsymbol{r}}$.

When modeling two-photon microscopy images, Eq. (38) we need to estimate $I_p$, the two-photon excitation function, which is related to the square field intensity integrated over time. The time integration is due to the fact that the camera recording time is very long compared to the field variation. Thus, we now study the square intensity of the TF-speckle beam integrated over time, defined as $i_{SG}(\boldsymbol{r}) = \int |E_{SG}|^4(\boldsymbol{r}, t)\mathrm{d}t$. In Fig. 3.27, we show simulations of $i_{SG}(\boldsymbol{r})$ in the XZ plane for different $NA_S$. We observe that the transverse width of the speckle grain increases with decreasing $NA_S$. Indeed, it is directly linked to the range of available $\boldsymbol{\kappa}$ (in other words to the diffuser NA, $NA_S$. When $NA_S \approx 0$, the diffuser does not play any role anymore and we recover the behavior of grating TF. We also note that the excitation function is confined in a slice about the focal plane, where the pulses coincide, thus yielding optical sectioning. When $NA_S \approx 0$, we recover the behavior of grating TF as expected and when $NA_S$ is increased, the axial width of the speckle grains decreases.

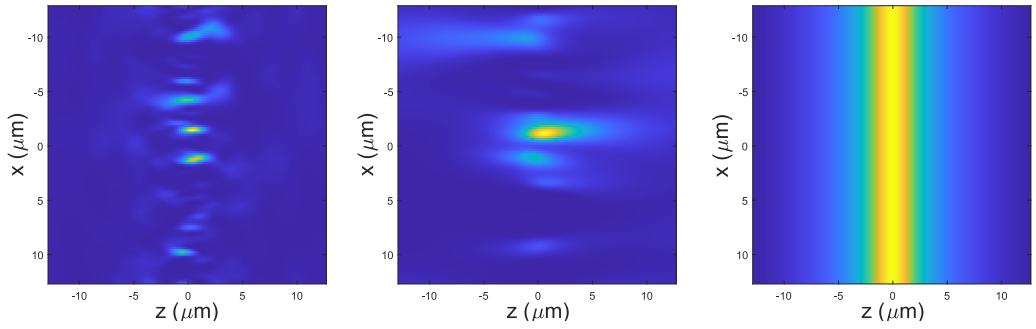


FIGURE 3.27 – Simulations in the XZ plane of the two-photon excitation function for one realization of the speckle, $i_{SG}(x,0,z) = \int |E_{SG}(x,0,z,t)|^4 \mathrm{d}t$, for different $NA_S$. The parameters are the same as those in Fig 3.24 with $NA_S$ taking the values 0.75, 0.2 and 0.01. When $NA_S = 0.75$, the transverse (along x) speckle grain size is approximately equal to $\lambda_0/(2NA_S)$. When $NA_S$ is close to zero (the diffuser does not play any role), the line is homogeneous and its axial width is similar to that of grating TF. As $NA_S$ increases, the axial width of the speckle grains decreases.

This observation is confirmed in Fig. (3.28) where we plot the empiric average over 50 speckles of $i_{SG}(\boldsymbol{r})$ for $NA_S = 0.75$ and compare it to grating-TF ($NA_S = 0$ for two different microscope parameters (small wavelength bandwidth or small magnification). In both cases, the roughness-grating TF brings a huge improvement in the excitation confinement.

We now provide an analytical derivation that permits to estimate the optical sectioning of roughness-grating TF as a function of the microscope, grating, and diffuser parameters. We consider the total signal that is obtained from a homogeneous fluorescent plane placed at $z$ from the focal plane. In one-photon fluorescence microscopy, the instantaneous signal is proportional to the ensemble average (corresponding to the integration over the XY plane) one-photon excitation intensity $\langle |E_{SG}|^2 \rangle(\boldsymbol{r},t)$,

$$\langle |E_{SG}|^2 \rangle(\boldsymbol{r},t) = \int_{-\infty}^{+\infty} g^2(\boldsymbol{\kappa}) e^{-\frac{W^2(\boldsymbol{\kappa})}{2T^2}} \mathrm{d}\boldsymbol{\kappa} \tag{92}$$

Eq. (92) shows that the instantaneous average one-photon intensity of the TF-speckle beam integrated over time $\int \langle |E_{SG}|^2 \rangle(\boldsymbol{r},t)dt$ is a constant. Thus, similarly to grating TF and roughness-TF, roughness-grating TF can not provide optical sectioning in one-photon fluorescence microscopy. Optical sectioning appears only with two-photon microscopy. Using the property of circular complex Gaussian random variable, the averaged instantaneous two-photon excitation intensity, $\langle |E_{SG}|^4 \rangle(\boldsymbol{r},t) = 2\langle |E_{SG}|^2 \rangle^2$ can be written as,

$$\langle |E_{SG}|^4 \rangle(\boldsymbol{r},t) = 2\left| \int g^2(\boldsymbol{\kappa}) e^{-\frac{W^2(\boldsymbol{\kappa},t)}{2T^2}} \mathrm{d}\boldsymbol{\kappa} \right|^2 \tag{93}$$

By replacing $W(\boldsymbol{\kappa})$ with $W(\kappa_x)$, Eq. (93) can be simplified as,

$$\langle |E_{\mathrm{SG}}|^4 \rangle(\boldsymbol{r},t) \propto \int\int_{-\infty}^{+\infty} e^{-2R^2(\kappa_x^2+\kappa_x'^2)} e^{-\frac{W^2(\kappa_x)+W^2(\kappa_x')}{2T^2}} \mathrm{d}\kappa_x \mathrm{d}\kappa_x' \tag{94}$$

We estimate the recorded signal $I_{\mathrm{SG}}(z)$ as the averaged two-photon intensity integrated over time,

$$\begin{aligned} I_{\mathrm{SG}}(z) &\propto \int \langle |E|_{\mathrm{SG}}^4 \rangle(\boldsymbol{r},t)\mathrm{d}t \\ &= \int\int_{-\infty}^{+\infty} e^{-2R^2(k_x^2+k_x'^2)} e^{-N(z)(k_x-k_x')^2} \mathrm{d}k_x \mathrm{d}k_x' \\ &= (\frac{\lambda_0^2}{\pi^2 \mathrm{NA_S}^2 \mathrm{NA_G}^2} + z^2)^{-1/2} \end{aligned} \tag{95}$$

where $N(z) = \frac{c^2 M^4 Q^2 z^2 \Delta\lambda^2}{16\lambda_0^2}$.

From $I_{\mathrm{SG}}(z)$ we extract the optical sectioning,

$$\Delta z_{\mathrm{SG}} = \frac{2\sqrt{3}\lambda_0}{\pi \mathrm{NA_S} \mathrm{NA_G}}. \tag{96}$$

We observe that the optical sectioning of roughness-grating TF is inversely proportional to $\mathrm{NA_G}$, which means that it is less affected by a change in the magnification or wavelength bandwidth than the optical sectioning of grating TF (which varies as $1/\mathrm{NA_G}^2$). In Fig. 3.29, we compare the analytical expression for the optical sectioning Eq. (96) with the numerical optical sectioning obtained by estimating the FWHM of the line in the XZ plane of $i_{\mathrm{SG}}$ averaged along the $s$ axis. We obtain a very good agreement, with a slight difference when $M$ and $\Delta\lambda$ are large and the assumption $\mathrm{NA_G} + \mathrm{NA_S} < \mathrm{NA_O} = 1$ does not hold anymore. In Fig. (3.30, right), we plot the optical sectioning as a function of the magnification $M$ and $\Delta\lambda$ obtained with the analytical expression Eq. (96). The roughness-grating TF parameters were : central wavelength $\lambda_0 = 800nm$, $d = 1\mu m$, $\mathrm{NA_S} = 0.75$. We also plotted $\mathrm{NA_G} = \lambda_0/(cd)$ for each configuration in Fig. (3.30, left) to indicate when the assumption $\mathrm{NA_G} + \mathrm{NA_S} < \mathrm{NA_O} = 1$ roughly holds.

Comparing the optical sectioning of grating TF, Fig. 3.4 to that in roughness-grating TF, Fig. (3.30, right), we observe a dramatic improvement of the optical sectioning of roughness-grating TF under conditions of low magnifications and narrow bandwidths, as was expected from the simulations in Fig. (3.28).

To conclude, with the introduction of random illumination, the optical sectioning capability is significantly improved, especially for a small magnification and a narrow bandwidth, potential damage to the objective lens can be reduced, and the FOV can be expanded.

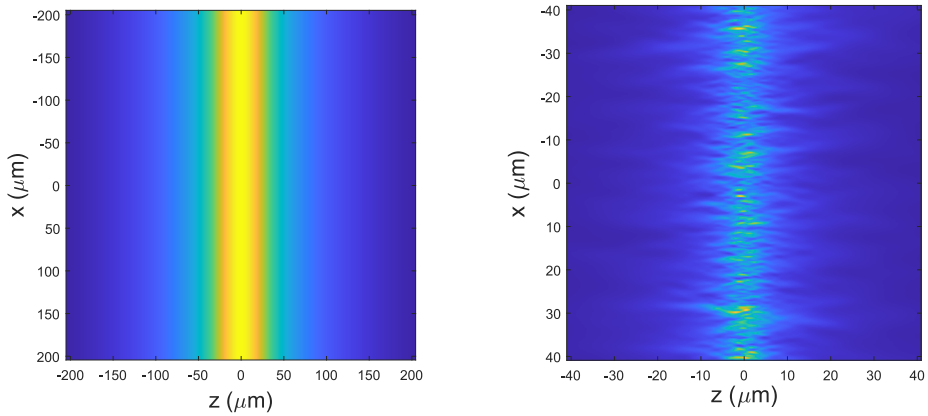


(a) Small magnification

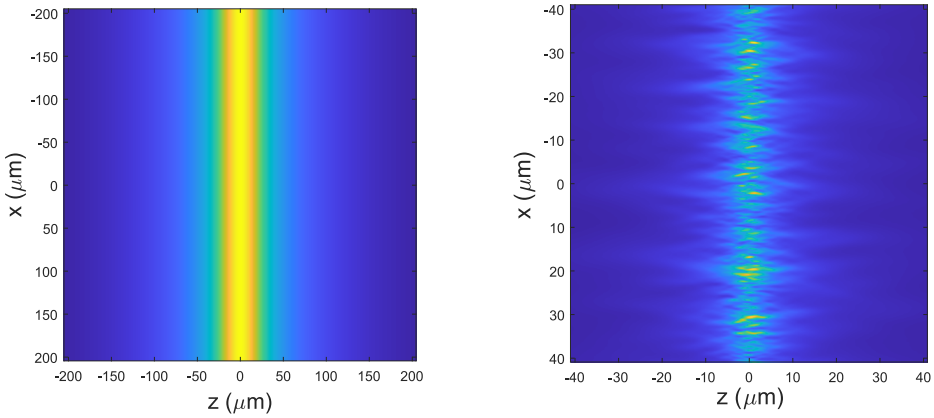


(b) Narrow bandwidth

FIGURE 3.28 – Simulation in the XZ plane of the two-photon excitation function for grating-TF ($NA_S = 0$) (left images) and empiric average over 50 speckles of the two-photon excitation function $i_{SG}(\boldsymbol{r})$ for the roughness-grating TF $NA_S = 0.75$ (right images). (a) : $\Delta\lambda = 18.1nm$, M : 10. $\Delta z_G : 105.6\mu m$, $\Delta z_{SG} : 12\mu m$. (b) : $\Delta\lambda = 2.7nm$, M : 80. $\Delta z_G : 73.6\mu m$, $\Delta z_{SG} : 10.8\mu m$.

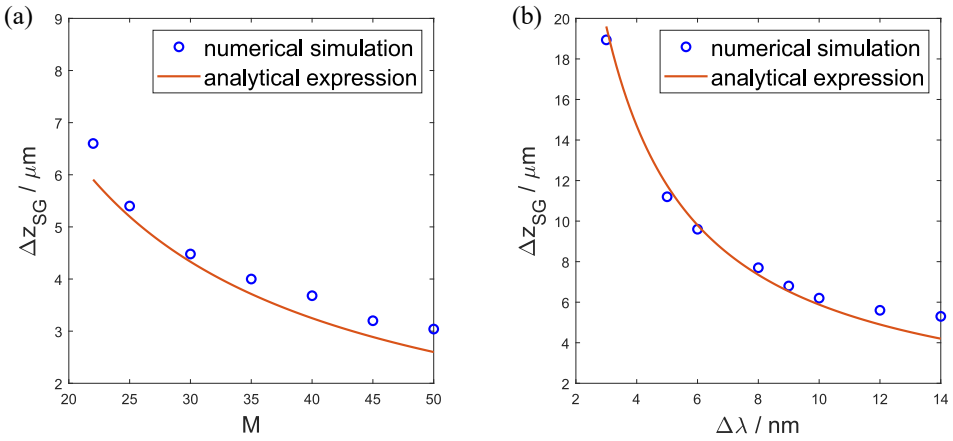


FIGURE 3.29 – Estimation of the optical sectioning for different microscope magnifications and pulse bandwidths when the illumination is a speckle, with $\lambda_0 = 800nm$, $d = 1\mu m$, $\mathrm{NA_S} = 0.75$, $\mathrm{NA_O} = 0.75$. We simulated the temporally focused speckled illumination with Eq. (86). The optical sectioning was estimated by computing the fluorescence signal detected on a camera when the sample is a thin homogeneous fluorescent plane that is translated through the focal plane. The simulated optical sectioning was compared to the analytical expression Eq. (96). The simulated results agree with the analytical ones except when the optical sectioning gets smaller than $5\mu m$. Indeed, in this case, one cannot assume that all the diffracted waves are collected by the objective pupil. The pupil cuts the extreme wavelengths thus reducing the effective bandwidth of the pulse and deteriorating the optical sectioning.

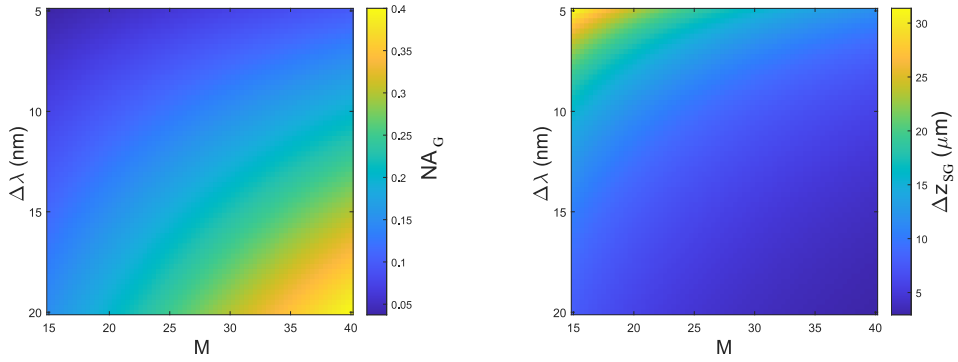


FIGURE 3.30 – Analytical optical sectioning in roughness-grating TF as a function of the magnification and wavelength bandwidth. The microscope parameters are $\lambda_0 = 800nm$, $d = 1\mu m$, $\mathrm{NA_S} = 0.75$, $\mathrm{NA_O} = 1$. Left : $\mathrm{NA_G}$ is plotted for indicating the regions were $\mathrm{NA_G} + \mathrm{NA_S} < \mathrm{NA_O}$ and the analytical expression holds. Right : $\Delta z_{\mathrm{SG}}$ as calculated from Eq. (96). This plot should be compared to Fig. 3.4, both the magnification and bandwidth required to achieve a similar optical sectioning of several micrometers are reduced.

## 3.6 Experiments

In the previous section, we presented simple analytical expressions of the optical sectioning for each of the following cases : grating TF, multi-order grating TF, roughness TF, and roughness-grating TF. The latter is considered the most promising method due to its better optical sectioning capability performance, protection of the objective, and the ability to be combined with RIM. In the following, we confirm the theory by experiments. However, due to slight differences between the theoretical configuration and the experimental setup, where it employed a reflective grating in Littrow configuration, we firstly model the roughness-grating TF optical sectioning for the experimental setup.

### 3.6.1 Modeling grating TF when using a reflection grating in Littrow configuration

In the modeling, we considered a TF configuration with a transmission grating. The grating is placed on a plane conjugated to the image plane and the pulse is illuminates the grating under a certain angle so that the (-1) order diffracted light propagates along the z-axis. In the experimental configuration, the pulse propagates along the $-z$ direction, the grating is tilted (the angle between the grating and the x-axis is $\theta_0$) and the diffracted light propagates towards positive $z$. Fig. 3.31 shows the configuration.

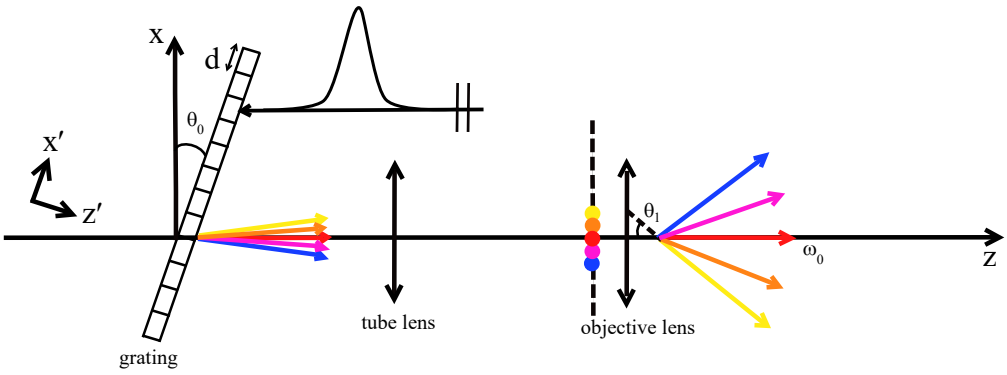


FIGURE 3.31 – Experimental configuration used for grating TF, where the transmission grating is replaced by a reflection grating used in Littrow configuration

Firstly, we model the complex field of the incident pulse :

$$E^{\mathrm{r}}_{\mathrm{inc}}(\boldsymbol{r},t)=\int_{-\infty}^{+\infty}h(\omega)e^{i[\boldsymbol{k}_{\mathrm{inc}}\cdot\boldsymbol{r}-\omega t]}\mathrm{d}\omega \tag{97}$$

where $\boldsymbol{k}_{\mathrm{inc}}=-q(\boldsymbol{0},\omega)\hat{\boldsymbol{z}}$ because the pulse is assumed to illuminate the grating in the negative $z$ direction.

Hereafter, we introduce the orthonormal basis $\hat{\boldsymbol{x}}^{'}$, $\hat{\boldsymbol{y}}^{'}$, $\hat{\boldsymbol{z}}^{'}$ where $\hat{\boldsymbol{z}}^{'}$ is normal to the grating plane and $\hat{\boldsymbol{x}}^{'}$ indicates the direction of periodicity of the grating, $\boldsymbol{d}=d\hat{\boldsymbol{x}}^{'}$ being

the period of the grating. We introduce the rotation matrix $J = \begin{pmatrix} \cos\theta_0 & 0 & \sin\theta_0 \\ 0 & 1 & 0 \\ -\sin\theta_0 & 0 & \cos\theta_0 \end{pmatrix}$ and we call
$\boldsymbol{k}'_{\text{inc}} = J\boldsymbol{k}_{\text{inc}} = \boldsymbol{\kappa}'_{\text{inc}} - q(\boldsymbol{\kappa}'_{\text{inc}},\omega)\hat{\boldsymbol{z}}' = -\sin\theta_0 q(\boldsymbol{0},\omega)\hat{\boldsymbol{x}}' - \cos\theta_0 q(\boldsymbol{0},\omega)\hat{\boldsymbol{z}}'$, and $\boldsymbol{r}^{'} = J\boldsymbol{r}$.

The incident field can be rewritten using the variables $\boldsymbol{k}'_{\text{inc}}$ and $\boldsymbol{r}'$ which are more adapted to the diffraction operation by the tilted grating,

$$E^{\text{r}}_{\text{inc}}(\boldsymbol{r},t) = \int_{-\infty}^{+\infty} h(\omega) e^{i[\boldsymbol{k}^{'}_{\text{inc}}\cdot\boldsymbol{r}'-\omega t]}\mathrm{d}\omega \tag{98}$$

Noting that $\boldsymbol{k}^{'}_{\text{inc}}$ lies in the $(x',y')$ plane, the field diffracted by the grating can be cast as

$$E^{\text{r}}_{d}(\boldsymbol{r},t) = \int_{-\infty}^{+\infty} h(\omega) e^{i[\boldsymbol{k}'_{d}\cdot\boldsymbol{r}^{'}-\omega t]}\mathrm{d}\omega \tag{99}$$

where $\boldsymbol{k}^{'}_{d} = \boldsymbol{\kappa}^{'}_{d} + q(\boldsymbol{\kappa}^{'}_{d},\omega)\hat{\boldsymbol{z}}^{'}$ with $\boldsymbol{\kappa}^{'}_{d} = \boldsymbol{\kappa}^{'}_{\text{inc}} + \frac{2\pi}{d}\hat{\boldsymbol{x}}^{'}$ lays in the $(x^{'},y^{'})$ plane.

Now we assume that the minus first order diffracted plane wave at the central wavelength propagates along the $z$ axis : $\boldsymbol{\kappa}^{'}_{\text{inc}}(\omega_0) = -\boldsymbol{\kappa}^{'}_{d}(\omega_0)$, thus $\boldsymbol{\kappa}^{'}_{d}(\omega)$ can be simplified as $(-\frac{2\pi\omega}{d\omega_0} + \frac{2\pi}{d})\hat{\boldsymbol{x}}^{'}$, and it is possible to apply Taylor expansion of $q(\boldsymbol{\kappa}^{'}_{d},\omega)$ on $\omega_0$ : $q(\boldsymbol{\kappa}^{'}_{d},\omega) \approx m + \frac{n}{m}\nu$ with $m = \sqrt{\frac{\omega_0^2}{c^2} - \frac{\pi^2}{d^2}}$, $n = \frac{\omega_0}{c^2} + \frac{\pi\sin\theta_0}{cd}$.

Next, we rewrite the field $E^{\text{r}}_{d}(\boldsymbol{r},t)$ using the $\boldsymbol{k}_d = J^{-1}\boldsymbol{k}'_d$ and $\boldsymbol{r} = J^{-1}\boldsymbol{r}'$ variables that are adapted to the objective and pupil operations,

$$E^{\text{r}}_{d}(\boldsymbol{r},t) = \int_{-\infty}^{+\infty} h(\omega) e^{i[\boldsymbol{k}_d\cdot\boldsymbol{r}-\omega t]}\mathrm{d}\omega \tag{100}$$

where $\boldsymbol{k}_d = \boldsymbol{\kappa}_d + q(\boldsymbol{\kappa}_d,\omega)\hat{\boldsymbol{z}}$ with $\boldsymbol{\kappa}_d$ lays now in the pupil $(x,y)$ plane.

After magnification in the sample space after the objective, the complex field at the objective space reads :

$$E^{\text{r}}_{\text{G}}(\boldsymbol{r},t) = \int_{-\infty}^{+\infty} h(\omega)\, p(\boldsymbol{\kappa}_g,\omega) e^{i[\boldsymbol{k}_g\cdot\boldsymbol{r}-\omega t]}\mathrm{d}\omega \tag{101}$$

where $\boldsymbol{k}_g = \boldsymbol{\kappa}^{\text{r}}_g + q(\boldsymbol{\kappa}^{\text{r}}_g,\omega)\hat{\boldsymbol{z}}$, $\boldsymbol{\kappa}^{\text{r}}_g = M\boldsymbol{\kappa}_d$.

After some calculations, we can show that the transverse component $\boldsymbol{\kappa}^{\text{r}}_g$ can be expressed as :

$$\boldsymbol{\kappa}^{\text{r}}_g = MQ\nu\hat{\boldsymbol{x}} \tag{102}$$

where $Q = \frac{2\lambda_0}{c\sqrt{4d^2-\lambda_0^2}}$.

Compared to Eq. (46), the only difference between the reflection grating model and the transmission grating configuration is the expression for $Q$, yielding a different

effective $\mathrm{NA_G}$ in reflection configuration,

$$\mathrm{NA_G} = \frac{M\Delta\lambda}{\sqrt{4d^2 - \lambda_0^2}}. \tag{103}$$

Then, the optical sectioning for the reflection configuration has the same expression as that obtained with a transmission grating, Eq. (55) except that one should change $\mathrm{NA_G}$ to the expression given by Eq. (103).

### 3.6.2 Modeling roughness-grating TF using a reflection grating in Littrow configuration

Fig. 3.32 shows the configuration of TF speckle using a reflection grating. The collimated beam propagates along the $(-z)$ axis and is scattered by a diffuser before illuminating the tilted reflection grating. The collimated beam propagates along the $z$ axis so that the wavevector of one plane wave forming the collimated beam is $\boldsymbol{k}_{\mathrm{inc}} = -q(\mathbf{0},\omega)\hat{\boldsymbol{z}}$. After scattering by the diffuser, the wavevector gains a transverse $(x,y)$ component $\boldsymbol{\kappa}$ and becomes $\boldsymbol{k}(\omega) = \boldsymbol{\kappa} - q(\boldsymbol{\kappa},\omega)\hat{\boldsymbol{z}}$. Hereafter, we assume that $\kappa << \omega/c$ so that $\boldsymbol{k}(\omega) \approx \boldsymbol{\kappa} - q(\mathbf{0},\omega)\hat{\boldsymbol{z}}$.

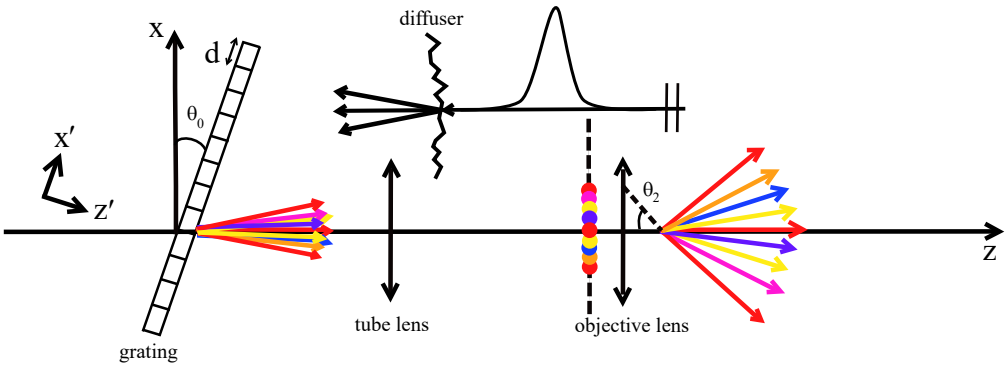


FIGURE 3.32 – Configuration for tempoal-focused speckle with reflection grating in Littrow configuration

Then, the complex field of the pulse diffracted by diffuser is modeled as,

$$E_{\mathrm{S}}^{\mathrm{r}}(\boldsymbol{r},t) = \int \mathrm{d}\omega h(\omega) e^{-i\omega t} \int g(\boldsymbol{\kappa})\eta(\boldsymbol{\kappa}) e^{i\boldsymbol{k}\cdot\boldsymbol{r}} \mathrm{d}\boldsymbol{\kappa} \tag{104}$$

Following the previous section, we introduce $\boldsymbol{k}' = J[\boldsymbol{\kappa} - q(\mathbf{0},\omega)\hat{\boldsymbol{z}}] = \boldsymbol{\kappa}'_s + q(\boldsymbol{\kappa}'_s,\omega)\hat{\boldsymbol{z}}'$ where $\boldsymbol{\kappa}'_s$ lies in the $(x',y')$ plane, and $\boldsymbol{r}' = J\boldsymbol{r}$ with,

$$E_{\mathrm{S}}^{\mathrm{r}}(\boldsymbol{r},t) = \iint h(\omega) g(\boldsymbol{\kappa})\eta(\boldsymbol{\kappa}) e^{i[\boldsymbol{k}'\cdot\boldsymbol{r}' - \omega t]} \mathrm{d}\omega \mathrm{d}\boldsymbol{\kappa} \tag{105}$$

The field diffracted by the grating can be expressed as :

$$E^{\mathrm{r}}_{\mathrm{Sg}}(\boldsymbol{r},t)=\iint h(\omega)g(\boldsymbol{\kappa})\eta(\boldsymbol{\kappa})e^{i[\boldsymbol{k}'_{Sg}\cdot\boldsymbol{r}'-\omega t]}\mathrm{d}\omega\mathrm{d}\boldsymbol{\kappa} \tag{106}$$

where $\boldsymbol{k}'_{Sg}=\boldsymbol{\kappa}'_{Sg}+q(\boldsymbol{\kappa}'_{Sg},\omega)\hat{\boldsymbol{z}}'$, $\boldsymbol{\kappa}'_{Sg}=\boldsymbol{\kappa}'_{s}+\frac{2\pi}{d}\hat{\boldsymbol{x}}'$.

Rewriting the field $E^{\mathrm{r}}_{\mathrm{Sg}}$ using the $\boldsymbol{k}_{Sg}=J^{-1}\boldsymbol{k}'_{Sg}$ and $\boldsymbol{r}=J^{-1}\boldsymbol{r}'$ variables that are adapted to the objective and pupil operations, one obtains,

$$E^{\mathrm{r}}_{\mathrm{Sg}}(\boldsymbol{r},t)=\iint h(\omega)g(\boldsymbol{\kappa})\eta(\boldsymbol{\kappa})e^{[\boldsymbol{k}\cdot\boldsymbol{r}-\omega t]}\mathrm{d}\omega\mathrm{d}\boldsymbol{\kappa} \tag{107}$$

where $\boldsymbol{k}=\boldsymbol{\kappa}^{\mathrm{r}}_{Sg}+q(\boldsymbol{\kappa}^{\mathrm{r}}_{Sg},\omega)\hat{\boldsymbol{z}}$ and $\boldsymbol{\kappa}^{\mathrm{r}}_{Sg}$ lies in the $(x,y)$ plane.

Hence, after magnification and pupil cut-off, the field at the objective space can be written as :

$$E^{\mathrm{r}}_{\mathrm{SG}}(\boldsymbol{r},t)=\iint h(\omega)g(\boldsymbol{\kappa})p(M\boldsymbol{\kappa}^{\mathrm{r}}_{Sg},\omega)\eta(\boldsymbol{\kappa})e^{i[\boldsymbol{k}_{SG}\cdot\boldsymbol{r}-\omega t]}\mathrm{d}\omega\mathrm{d}\boldsymbol{\kappa} \tag{108}$$

where $\boldsymbol{k}_{SG}=M\boldsymbol{\kappa}^{\mathrm{r}}_{Sg}+q(M\boldsymbol{\kappa}^{\mathrm{r}}_{Sg},\omega)\hat{\boldsymbol{z}}$.

After some calculations, we can show that the transverse component $M\boldsymbol{\kappa}^{\mathrm{r}}_{Sg}$ is,

$$M\boldsymbol{\kappa}^{\mathrm{r}}_{Sg}=M(Q\nu\hat{\boldsymbol{x}}+\boldsymbol{\kappa}) \tag{109}$$

with $Q=\frac{2\lambda_0}{c\sqrt{4d^2-\lambda_0^2}}$. Comparing this expression of $M\boldsymbol{\kappa}^{\mathrm{r}}_{Sg}$ with Eq. (87) yields a novel effective grating numerical aperture, $\mathrm{NA_G}$, which is same as that given in Eq. (103).

Thus, the axial sectioning of temporal focusing using speckled illumination with a reflection grating has the same expression as the optical sectioning obtained with a transmission grating Eq. (96), except that $\mathrm{NA_G}$ is now equal to

$$\mathrm{NA_G}=\frac{M\Delta\lambda}{\sqrt{4d^2-\lambda_0^2}}. \tag{110}$$

### 3.6.3 Experimental implementation of grating TF and roughness-grating TF

In order to confront the analytical optical sectioning of grating and roughness-grating TF, we perform a two-photon microscopy experiment using a $220fs$ light pulse with a $100KHz$ repetition rate centered about $850nm$, and two microscope objectives with same NA but different magnifications (20× and 40× with $\mathrm{NA_O}=0.75$). In the grating TF experiment, the pulse is first incident into a reflective diffraction grating with a grating period of 0.83 microns. The light is reflected by a pick-up mirror and passes through a tube lens and objective lens to the sample plane. For the temporal-focused speckle configuration, we place a 1-degree diffuser before the grating, Fig. 3.33 shows the configuration.

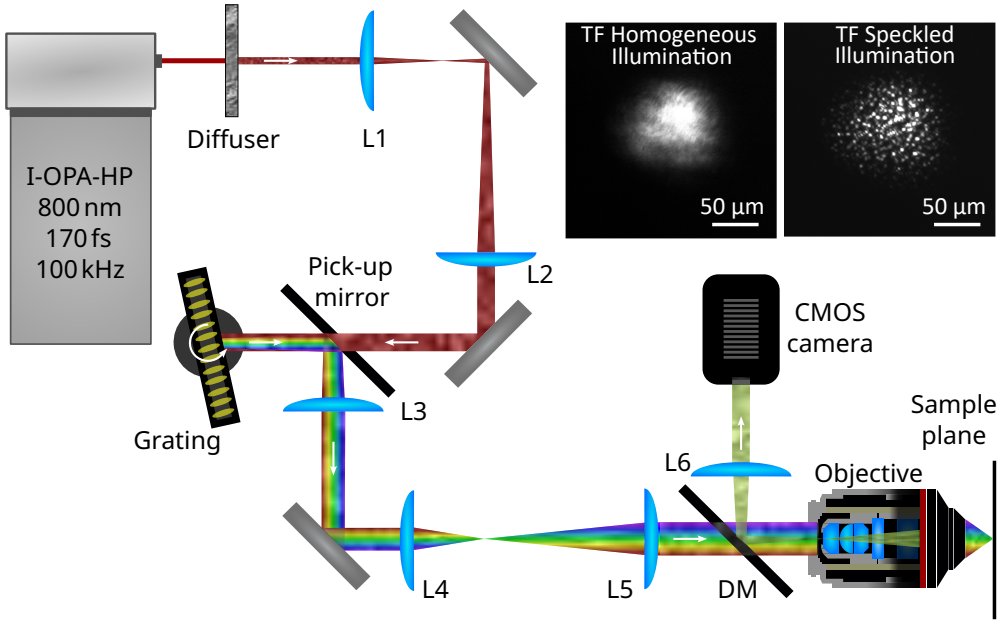


FIGURE 3.33 – (a) Experimental setup for TF microscopy with a thin diffuser and a reflection grating in Littrow configuration. Legend : L, lens; DM, dichroic mirror. The top panels (b-c) show the recorded image at the focal plane for collimated TF (b) and TF with speckle (c) for a 20 ×, NA = 0.75, objective lens.

To estimate the diffuser NA, $NA_S$, we placed a lens in front of the diffuser and compared the size of the speckle intensity repartition in the Fourier plane to the pupil size of the objective. We found $NA_S \approx 0.23$ for the 20× objective and $NA_S \approx 0.36$ for the 40× objective.

To check the behavior of their optical sectioning with respect to the wavelength bandwidth without changing the central wavelength, we introduce two tunable low and high-pass filters at the output of laser. Because it is difficult to constantly change the grating period and the magnification. To extract the optical sectioning, we translated the sample through the focal plane by steps of $1\mu m$ and recorded the integrated fluorescence signal as a function of $z$. We show in Figs. 3.33(b,c) the fluorescence images of the sample placed at the focal plane when the illumination is the temporally focused collimated beam or the temporally focused speckled beam. The illuminated areas (FOV) are roughly the same in both cases and the speckled bright grains are nicely visible in the speckle configuration, Fig. 3.33(c).

Next, we substitute all the experiment parameters into the analytical calculations for reflection grating to minimize the difference between the theoretical and experimental results by fitting the constants in formulas.The linear and quadratic behaviors of the optical sectioning with respect to the wavelength bandwidths, depending on the collimated, are well reproduced, Figs. 3.34 (c,d). By adjusting the constant of proportionality $A = 2\sqrt{3}\lambda_0/\pi$ appearing in Eqs. (55, 96) by 14% for the 20x objective and 30% for the 40x objective, we obtained a remarkable agreement between the

experimental and theoretical curves.

In Fig. 3.34(a), we chose a 20× objective and the wavelength bandwidth of 1.49 $nm$, and the random illumination allowed the optical sectioning to be raised from about 160 microns in the grating TF to about 40 microns. Meanwhile, in the Fig. 3.34(b), we chose a 40× objective lens, the wavelength bandwidth is 2.44 $nm$, and the random illumination improves the optical sectioning from about 17 microns to about 10 microns.

This discrepancy between the theoretical and experimental proportionality constant can be explained by the fact that the experimental beam is not rigorously Gaussian, as assumed in the derivation, and that some wavelengths may be clipped by the pupil, especially with the 40× objective.

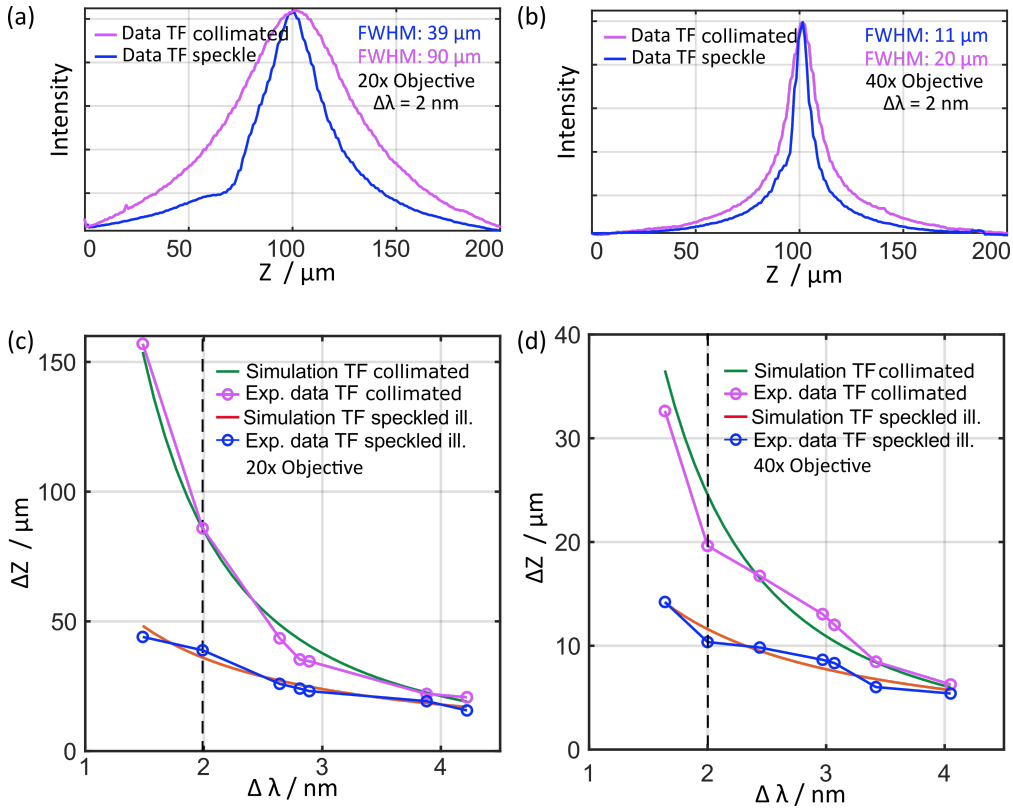


FIGURE 3.34 – Collimated and speckle TF optical sectioning : experimental data and simulations. (a-b) Comparison of the experimental intensity profile along the optical axis z for the case of collimated TF (purple curve) and TF with speckle illumination (blue curve) with a 20×, NA = 0.75, objective (a) and a 40×, NA = 0.75, objective (b) and a bandwidth $\Delta\lambda = 2nm$ corresponding to a 500 fs pulse duration (case of the vertical black-dashed line in (c-d)). (c-d) Experimental and simulated data for collimated TF and TF with speckle illumination of the optical sectioning as a function of the wavelength bandwidth for 20×, NA = 0.75, objective (c) and for 40×, NA = 0.75, objective (d).

## 3.7 Using temporal-focused speckles in Random Illumination Microscopy

In the above analysis, we theoretically, numerically, and experimentally analyzed the exceptional optical sectioning capability of temporal-focused speckles. Furthermore, another benefit of temporal-focused speckles is that it can be combined with 2D RIM to provide super-resolved images. Indeed, RIM main issue in thick densely labeled samples is that the background noise variance may overcome the variance due to the change of speckles. In this case, the reconstruction scheme fails. Thanks to the optical sectioning capability of temporal-focused speckles we can expect reducing the background and its relevant noise, thus increasing the applicability of RIM. In this subsection, we combine TF with 2D RIM (TF-RIM) to enable super-resolution reconstruction of thick samples.

Unlike the configuration shown in Fig. 3.33, we incorporate a galvo-mirror in the Fourier plane behind the grating to scan the sample and obtain a larger range of sample imaging (FOV without fast scan is about $50\mu m \times 50\mu m$, FOV with Galvo is about $200\mu m \times 200\mu m$). Fig. 3.35 shows its configuration. In this experiment, the temporal-focused speckle covering a small FOV is scanned across the sample. In the following, this pattern translation is used to form different images of the same sample region. Note that this method requires to use more images then those required in traditional RIM technique where different realizations of the speckles covering a large FOV are used.

We conducted experiments on RIM and TF-RIM separately. To obtain randomly illuminated images without TF, we replaced the grating in the configuration with a mirror. We imaged a rhodamine-labeled mouse intestinal villi sample using an excitation wavelength of 800 nm to obtain about 5000 images with the fast scanning random illumination (traditional RIM needs about 200 images). This is reasonable because the FOV area of the image is 16 times that of a single speckle FOV area, and the number of images required is nearly the same. Fig. 3.36 illustrates several examples of speckles, where the speckle pattern is continuously scanned by the galvo scanner.

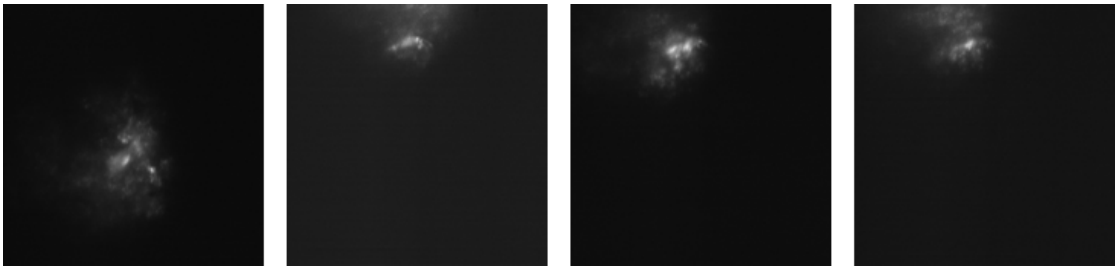

FIGURE 3.36 – Examples of several temporal focused speckles. The FOV of one speckle in the image is approximately $50\mu m \times 50\mu m$, the temporal focused speckles rapidly scan an area with a FOV of $200\mu m \times 200\mu m$.

The averaged image and RIM reconstruction image without TF can be found in Fig.

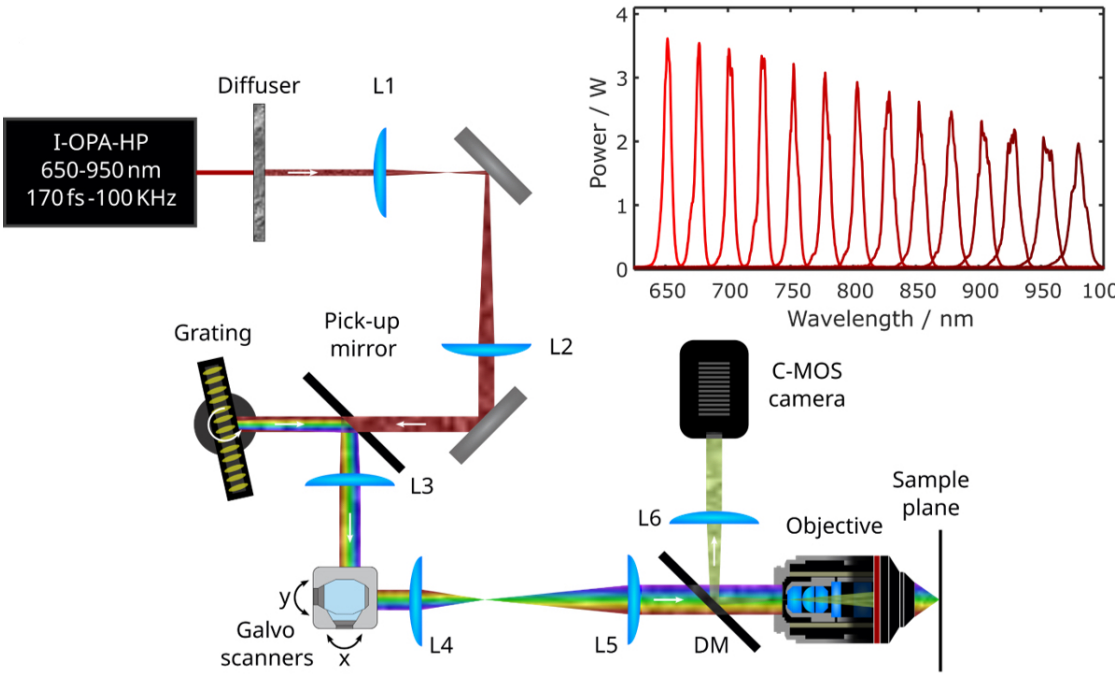


FIGURE 3.35 – Configuration of combining temporal-focused speckle with RIM. The only difference from Fig. 3.33 is that we insert a Galvo scanner at the Fourier plane to obtain a larger FOV.

3.37. Even though RIM provides super-resolution (as evidenced by the Fourier support for the mean and RIM images in the right image of Fig. 3.37(c)), the background noise still prevents us from discerning the specific structures within the sample.

Fig. 3.38 shows the comparison of averaged image and RIM image for temporal-focused random illumination, RIM also provide a good super-resolution about $300nm$. However, due to the introduction of TF, the random illumination is confined to a very thin plane, allowing us to clearly observe the internal structure of the sample, as shown in the lower image of Fig. 3.38(b).

It is evident that RIM achieved a resolution of approximately 300 nm in both cases (see their Fourier supports). However, thanks to the optical sectioning capability in temporal-focused speckle, the TF-RIM result is capable of visualizing more details in the specimen.

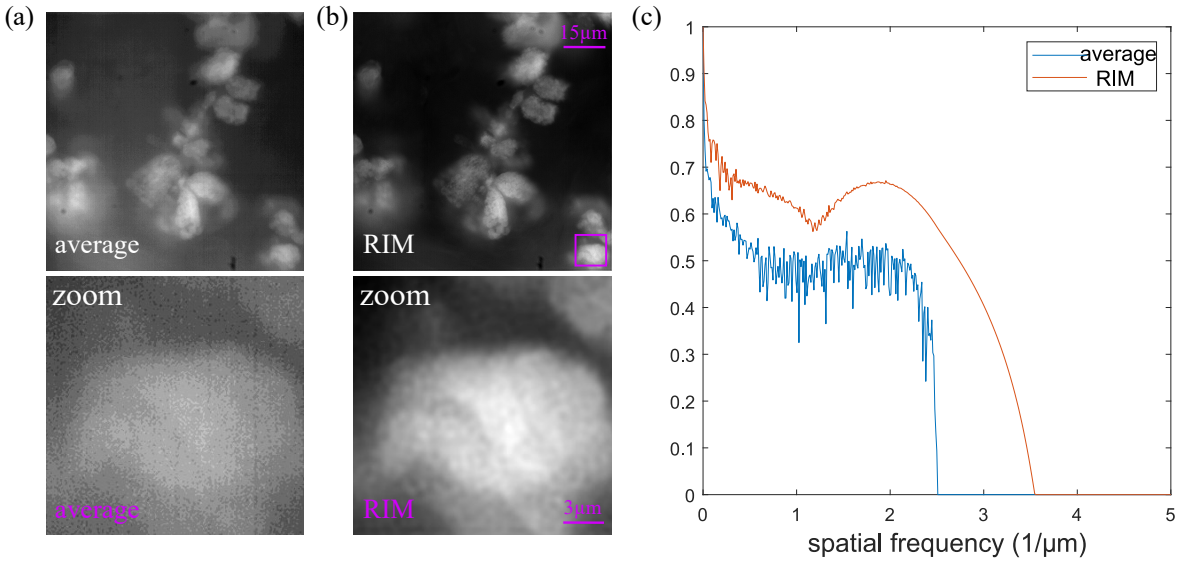


FIGURE 3.37 – The averaged image (identical to the image obtained with wide-field two-photon microscopy), RIM image, and their Fourier supports in RIM. Here, we replace the grating in Fig. 3.35 by a mirror, and recorded 5000 images by illuminating a rhodamine-labeled mouse intestinal villi sample with an excitation central wavelength of 800 nm pulse. Noting that this configuration has a FOV of $50\mu m \times 50\mu m$, so this is equivalent to recording 300 speckled images with a $200\mu m \times 200\mu m$ FOV. The top images in Fig. (a, b) show the averaged image and RIM image, respectively, while the bottom images display the zoom of the purple range. Fig c presents the Fourier support for the mean and RIM results, indicating the super-resolution in RIM image.

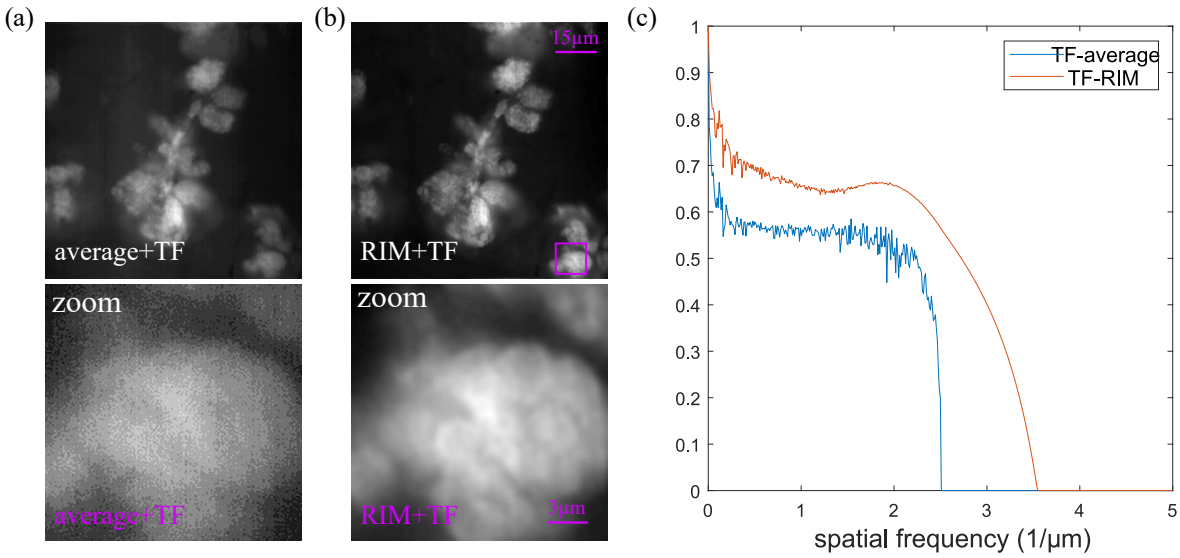


FIGURE 3.38 – Similar to Fig. 3.37, we recorded 5000 temporally focused speckled images, and show the averaged image (the same image as in grating TF microscopy), RIM-TF image, and their Fourier supports. Comparing with the images in Fig. 3.37 and the averaged temporally focused image, RIM-TF reveals more of the internal structure of the sample, which is more pronounced in the purple areas.

## 3.8 Conclusion

In this chapter, we analysed the optical sectioning of temporal-focusing, generated by stretching and recombining pulses in the time domain. We first reinstate the theoretical modeling of both chirp-free and chirped pulses in the standard grating TF. We recalled that the optical sectioning in this configuration is governed by the second derivative with respect to the temporal frequency of the axial spatial frequency component (also known as GVD). We then develop a novel configuration in which multiple pulses are incident on the grating (or equivalently, when multiple orders diffracted by the grating are collected by the microscope objective). We show that, in this case, the optical sectioning depends mainly on the speed mismatch between the different pulses, i.e. on the first derivative with respect to the temporal frequency of the axial spatial frequency. To generate these multiple pulses, we propose to use a thin diffuser to scatter the pulse beam before the grating. We theoretically, numerically, and experimentally demonstrate that the optical sectioning of roughness-grating TF is significantly better than that of standard grating TF when the microscope magnification and/or the laser spectral bandwidth are small. In addition, roughness-grating TF reduces the potential damage to the objective lens, especially when wide FOVs (small magnification) are used. Finally, we combined the super-resolution method 2D-RIM with the temporal-focused speckle. By reducing the out-of-focus noise, TF-RIM could provide better contrasted images than RIM in thick densely labeled samples.

# 4 Adapting temporal focusing to Coherent Anti-Stokes Raman Scattering microscopy (TF-CARS)

## Sommaire


4.1 Introduction . . . 115
4.2 Applying TF-CARS using two gratings . . . 120
4.2.1 Theory of TF-CARS with two gratings . . . 121
4.2.2 Simulations . . . 124
4.2.3 Experiments on the optical sectioning of TF-CARS using two gratings . . . 125
4.3 Spectroscopy in the TF-CARS configuration with two gratings . . . 128
4.3.1 Analysis of the pupil plane . . . 128
4.3.2 How to select configuration parameters to improve spectral resolution? . . . 131
4.3.3 Experiments on TF-CARS spectral resolution . . . 133
4.4 Forming TF-CARS using only one grating . . . 134
4.4.1 Theory of TF-CARS with one grating . . . 134
4.4.2 How can an objective collect all the light in TF-CARS using one grating? . . . 137
4.4.3 Field behavior at the pupil plane . . . 137
4.4.4 Simulations . . . 138
4.5 Conclusion and perspective . . . 141


## 4.1 Introduction

CARS is a non-linear four-wave mixing process. The sample is illuminated with two powerful laser beams at two different wavelengths (pump and Stokes). This illumination triggers a non-linear response of the material which emits light at another wavelength (anti-Stokes). The strength of the non-linear response depends on the chemical bonds of the sample and on the frequency difference of the lasers (MAKER et al. 1965), More precisely, noting the pump field $E_p$ at frequency $\omega_p$ and the Stokes field $E_S$ at frequency $\omega_S$, when the frequency difference $\omega_p - \omega_S$ matches the molecular vibration frequency $\Omega$, a CARS signal at frequency $\omega_{aS} = 2\omega_p - \omega_S$ is generated. This property makes CARS microscopy an interesting tool for chemical imaging without

staining. In particular, it has been considered as an alternative to brightfield transmission microscopy for label-free histology applications (CHENG et al. 2002; EVANS et al. 2008).

Most CARS microscopes work in a scanning configuration (ZUMBUSCH et al. 1999). The CARS signal is generated in the very small volume where the pump and Stokes focused beams overlap and is detected on a bucket detector (generally a photomultiplier). The 3D resolution of scanning CARS is dictated by the excitation volume (about one micron transversally and a few microns axially). Thanks to the non-linear excitation process, CARS scanning microscope provides optical sectioning. The main drawback of the scanning configuration appears when large FOVs need to be imaged at high temporal resolution. In order to speed up the scanning process and shorten the detector's integration time, the laser power must be increased to obtain an effective signal from the tiny excitation volume. But increasing the laser power can induce photodamage to the sample. This physical limit prevents the use of CARS scanning microscopes for large-area, fast imaging applications.

A less common configuration, wide-field CARS microscopy, consists in exciting the CARS signal simultaneously over a large region of the sample, using weakly focused or collimated beams, and recording the anti-Stokes light on a camera (HEINRICH et al. 2004; BERTO et al. 2012; TOYTMAN et al. 2007). Now that powerful lasers are available, this approach appears promising for speeding the imaging of large FOVs without increasing the phototoxicity. Compared to scanning CARS microscopy, wide-field CARS microscopy reduces the phototoxicity and shortens the integration time, but it loses the optical sectioning capability and may damage the objective's back pupil plane where the beams are focused. Up to now, these drawbacks have prevented the use of the widefield CARS imaging configuration. To address the issue of poor optical sectioning in wide-field CARS microscopy, a first solution was given by CARS-RIM (FANTUZZI et al. 2023) in which the sample is illuminated by speckled Stokes and pump beams. The pump speckles are rotated rapidly during the camera integration time while the Stokes patterns are kept fixed. This configuration was shown to be close to fluorescence RIM. By forming the variance of multiple images recorded under different Stokes patterns, one could reconstruct an image of the sample exhibiting the same optical sectioning and resolution of a scanning CARS microscope. However, CARS-RIM requires the recording of hundreds of speckled images, which can limit the temporal resolution.

In this chapter, we propose another approach for bringing optical sectioning to widefield CARS microscopy while keeping the rapidity of the one-shot recording. The idea is to introduce TF in a widefield CARS microscope. To our knowledge, TF has never been associated with CARS imaging, the wide-field configuration having attracted very little interest on itself its coupling with a complex technique even less. However, as will be shown, we believe that this approach is promising, especially for imaging large FOVs.

To analyse the optical sectioning in a widefield CARS microscope using temporal focused Stokes and pump beams, we first write the general formula for the instanta-

neous anti-Stokes intensity $I_{aS}$ recorded at position $\boldsymbol{R}$ in the camera space,

$$\begin{aligned} I_{\mathrm{aS}}(\boldsymbol{R},t) &= |E_{\mathrm{CARS}}|^2(\boldsymbol{R},t) \\ &= \left| \int G_{aS}(\boldsymbol{R},\boldsymbol{r},\omega_{aS})\chi_{aS}(\boldsymbol{r},\omega_{aS})E_p(\boldsymbol{r},\omega_p^1)E_p(\boldsymbol{r},\omega_p^2)E_S^*(\boldsymbol{r},\omega_S)e^{-i\omega_{aS}t}\mathrm{d}\omega_p^1\mathrm{d}\omega_p^2\mathrm{d}\omega_S\mathrm{d}\boldsymbol{r} \right|^2 \end{aligned} \tag{111}$$

where $\omega_{aS} = \omega_p^1 + \omega_p^2 - \omega_S$, $\chi_{aS}$ is the third-order susceptibility tensor of the sample (reduced to a scalar, for easing the calculation), $G_{aS}(\boldsymbol{R},\boldsymbol{r},\omega_{aS})$ is the Green function of the microscope at frequency $\omega_{aS}$, $G_{aS}(\boldsymbol{R},\boldsymbol{r},\omega_{aS}) = \int h_{aS}(\boldsymbol{\kappa})e^{i\boldsymbol{k}_{aS}\cdot(\boldsymbol{R}-\boldsymbol{r})}\mathrm{d}\boldsymbol{\kappa}$ with $\boldsymbol{k}_{aS} = \boldsymbol{\kappa} + q(\boldsymbol{\kappa},\omega_{aS})\hat{\boldsymbol{z}}$, $h_{aS}$ is the pupil function whose Fourier support is a disk of radius approximately $\mathrm{NA}_{\mathrm{aS}}/\lambda_{0aS}$, $h_{aS} = 1$ for $\nu < \frac{\lambda_{0aS}}{\mathrm{NA}_{\mathrm{aS}}}$ ($\lambda_{0aS}$ is the central wavelength for anti-Stokes beam) and 0 elsewhere, $E_{p,S}(\boldsymbol{r},\omega)$ represents the pump or Stokes fields in the temporal frequency domain, which is the Fourier transform of the field in time domain $E_{p,S}(\boldsymbol{r},t)$.

For investigating the optical sectioning property of wide-field CARS microscopy, we assume the sample is a thin homogeneous layer at $z_0$ in the sample space : $\chi(\boldsymbol{r},\omega_{aS}) \propto \delta(r_z - z_0)$. The recorded signal will be $\int I_{\mathrm{aS}}(\boldsymbol{R},t)\mathrm{d}t$ and do not depend on $\boldsymbol{R}$. Hereafter, we assume that the objective collects all the light emitted by the layer, and that $q(\boldsymbol{\kappa},\omega_{aS}) \approx 2\pi/\lambda_{0aS}$ so that $G_{aS}$ is a constant. Under these assumptions, we have,

$$I_{\mathrm{CARS}}(z_0) = \int I_{\mathrm{aS}}(\boldsymbol{R},t)\mathrm{d}t \approx \int |E_p(x,y,z_0,t)|^4|E_S(x,y,z_0,t)|^2\mathrm{d}x\mathrm{d}y\mathrm{d}t \tag{112}$$

In the rest of the chapter, we will consider configurations in which the pulse beams do not depend on $y$ (the grating period is along the $x$ axis). In addition, from the previous analysis on TF, we know that the integration along time permits to remove the $x$ dependence. Thus, for simplicity we pursue our study by only studying,

$$S_{aS}(z) = \int |E_p(0,0,z_0,t)|^4 E_S(0,0,z_0,t)|^2\mathrm{d}t. \tag{113}$$

Eq. (113) shows that the CARS signal is related to the fourth power of the pump field. We now recall that the two-photon intensity recorded in grating TF is proportional to the modulus of the field to the power of 4. So, the first idea that comes to mind when adapting TF in CARS microscopy is to apply TF to the pump beam only. However, this configuration prevents the pump beam and the Stokes beam from overlapping in time and space, as shown in Fig. 4.1. As mentioned in the section discussing grating TF, the temporally focused pulsed beam generates a Y line that moves along the x-axis with the speed of light divided by the magnification. In contrast, the collimated Stokes beam illustrated in Fig. 4.1 moves along the z-axis with the speed of light, so this configuration is not capable of generating an effective CARS signal.

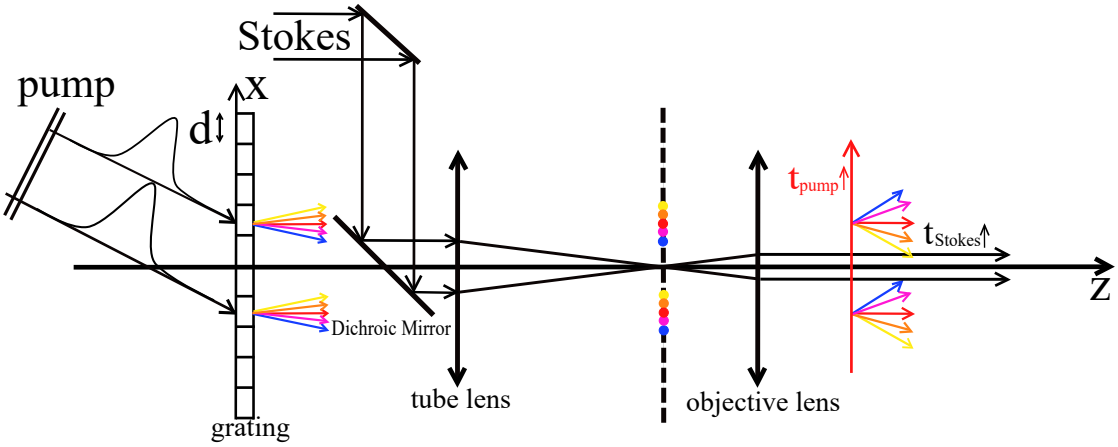


FIGURE 4.1 – An intuitive (but inefficient) configuration for adapting TF to CARS, where the pump beam is temporally focused and the Stokes beam is not temporally focused. The pump beam will be stretched by the grating and recombined at the focal plane, but it will propagate along the x-axis at the sample plane. However, the Stokes pulse is propagating along the z-axis. Therefore, the effective CARS signal can not be observed due to the mismatch between pump pulse and Stokes pulses.

Ensuring that the pump and Stokes beams superimpose temporally and spatially to produce a useful CARS signal is essential. Therefore, we must temporally focus the Stokes beam so that it also forms a Y line that moves along the $x$ axis with the same speed as the pump Y line. This introduces the next question : how to design the configuration so that both lines can overlap in the sample space while being temporally focused?

We assume that the grating parameters (period and angle of incidence) are adapted to the pump beam : the central wavelength of the pump pulsed beam propagates along the z-axis after diffraction by the grating, then the period of the grating satisfies the condition $\boldsymbol{\kappa}_g(\omega_{0p}) = M(\frac{\omega_{0p}}{c}\sin\theta_0 - \frac{2\pi}{d})\hat{\boldsymbol{x}} = \mathbf{0}$ (where $\omega_{0p}$ is the central temporal frequency of pump pulse). In this case, if the Stokes pulse is incident into the same grating with the same incident angle, then the objective will probably not be able to collect the Stokes beam. This issue is illustrated in Fig. 4.2a. For example, if the pump central wavelength $\lambda_{0p} = 800nm$, the Stokes central wavelength $\lambda_{0S} = 1030nm$, grating period $d = 1\mu m$, magnification $M = 50$, thus the incident angle $\sin\theta_0 = 0.8$. Therefore, the diffracted angle $\theta_S$ for Stokes central wavelength can be expressed as

$$\frac{\omega_{0S}}{c}\sin\theta_0 - \frac{2\pi}{d} = \frac{\omega_{0S}}{c}\sin\theta_S \tag{114}$$

Under those parameters, the angle $\theta_S^M$ between the wavevector and optical axis in the sample plane can be expressed as : $\sin\theta_S^M = M\sin\theta_S = -11.5$, which indicates that the wavelength $\lambda_{0S}$ can not be collected by the objective.

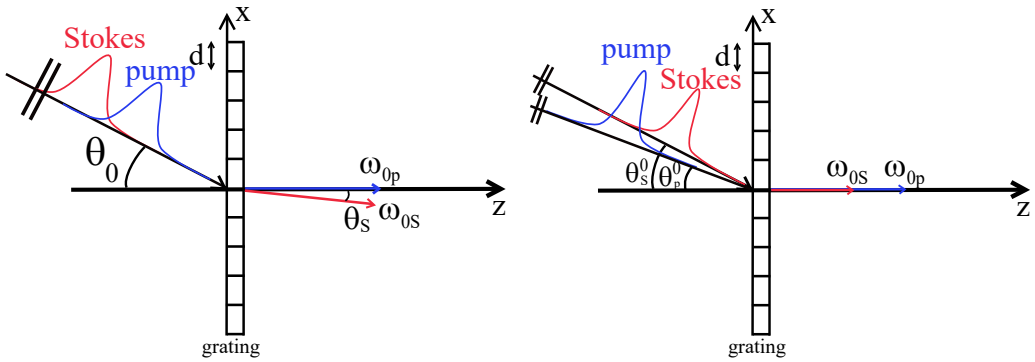


(a) If the pump and Stokes pulses are incident into the grating with the same direction, where the grating period satisfies the assumption ($\boldsymbol{\kappa}_g(\omega_{0p}) = M(\frac{\omega_{0p}}{c}\sin\theta_0 - \frac{2\pi}{d})\hat{\boldsymbol{x}} = \mathbf{0}$ mentioned in Eq. (45)) in two-photon TF for the pump pulse. The $-1$ diffraction order for Stokes pulse will not be collected by the objective.

(b) If the pump and Stokes pulses are incident into the grating with two different directions, the incident angles ensure that the central wavelengths ($\lambda_{0p}$, $\lambda_{0S}$) are propagating along the optical axis. However, as described by Eq. (49), the collimated TF beams propagate along the direction $\boldsymbol{u}$ at a velocity $v$, both of which depend on $M$, $d$, $\lambda_0$. Therefore, the pump and Stokes pulses will not overlap in the sample plane due to their differing wavelengths.

FIGURE 4.2 – Two unsuccessful attempts in combining TF with CARS

To collect both pump and Stokes pulses, another possibility is to tune the incident angle for Stokes pulse so that the diffraction field of its central wavelength $\omega_{0S}$ also propagates along z axis, as Fig. 4.2b shows. Yet, even if the objective lens is able to collect Stokes pulse, another problem arises in that they have different orientations and velocities in the objective space. This is because in the Chapter 3 dealing with grating TF, it was mentioned that the pulse propagates with velocity $v = c/u_{\text{ref}}$ along direction $\boldsymbol{u}_{\text{ref}} = McQ\hat{\boldsymbol{x}} + \hat{\boldsymbol{z}}$. For the configuration in Fig. 4.2b, the pump pulse and Stokes pulse have the same $d$, $M$, but different central wavelengths, which means that they can not coincide in space and time because the pump and Stokes line pulses will propagate in different directions and at different speeds.

In the following sections, we present two schemes to ensure that the pump and Stokes temporally focused beams propagate at the same speed and in the same direction within the sample plane, thereby generating an effective CARS signal and achieving micrometric optical sectioning.

In the first configuration, we employ two distinct gratings and different magnifications to temporally focus the pump pulse and Stokes pulse separately, ensuring that both beams propagate at precisely identical velocities and directions within the sample plane under the appropriate parameters. Subsequently, they are superimposed at the pupil plane to generate the CARS signal. The generation of each beam in this method is analogous to grating TF techniques, with its optical sectioning capability enhanced by GVD (the second order derivative in Eq. (47) induces the optical sectioning).

Another approach is to send the pump and Stokes pulses simultaneously on one grating, but select the incident angle and grating period so that the diffraction angles of their central wavelengths are symmetric about the z-axis. This concept originates from the analysis of multi-order grating TF, where pulses propagate in different directions, and their overlap achieves optical sectioning (Fig. 3.17) illustrates this case). As discussed in the multi-order grating TF section, optical sectioning can benefit from the different pulse speeds (the first order derivative in Eq. (63) provides the optical sectioning), enabling the TF method to be achieved using picosecond pulses without being limited to femtosecond pulses. However, to ensure that as much light as possible can be collected, the magnification should be relatively low, which will result in a larger FOV.

In the next section we investigate theoretically, numerically, and experimentally the optical sectioning capabilities of these two configurations.

## 4.2 Applying TF-CARS using two gratings

In this section, we present a technique for generating temporally-focused CARS signals in which pump pulse and Stokes pulses are incident on two gratings, and the incident angle and magnification are adjusted so that they have the same propagation direction and velocity in the sample plane, where they are combined in the Fourier plane to create a CARS signal. The configuration is depicted in Fig. 4.3.

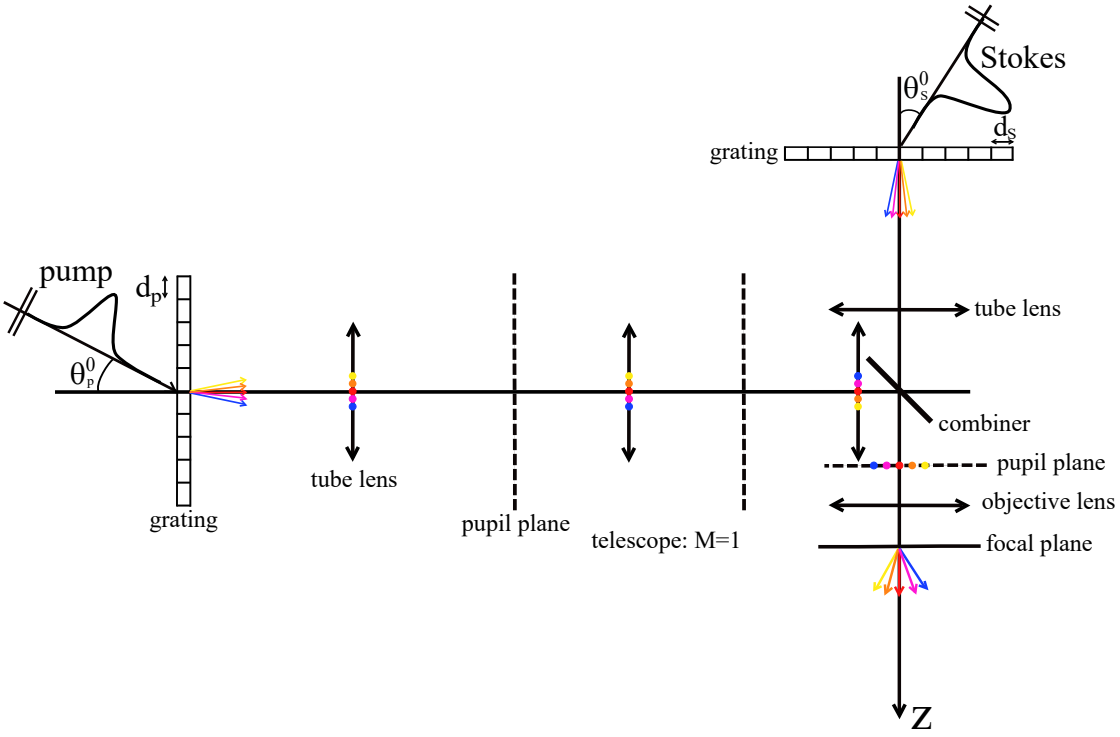


FIGURE 4.3 – TF-CARS configuration with two transmission gratings. The pump beam and Stokes beam are temporal-focused through two separate gratings, and the parameters are selected such that they are combined at the pupil plane and propagate along the same direction with the same velocity at the sample plane to generate the effective CARS signal.

### 4.2.1 Theory of TF-CARS with two gratings

The complex fields of pump and Stokes pulses at the sample plane have the same expression as in two-photon TF (Eq. (44)) and can be expressed as follows :

$$\begin{aligned} E^G_{p,S}(\boldsymbol{r},t) &= \int_{-\infty}^{+\infty} h_{p,S}(\omega)\, p(M_{p,S}\boldsymbol{\kappa}_d^{p,S},\omega)\, e^{i[\boldsymbol{k}_{p,S}\cdot\boldsymbol{r}-\omega t]}\,\mathrm{d}\omega \\ &= \int_{-\infty}^{+\infty} E^G_{p,S}(\boldsymbol{r},\omega)\, e^{-i\omega t}\,\mathrm{d}\omega \end{aligned} \tag{115}$$

where $h_{p,S}(\omega) = e^{-T_{p,S}^2 \nu^2}$, $\boldsymbol{k}_{p,S} = M_{p,S}\boldsymbol{\kappa}_d^{p,S} + q(M_{p,S}\boldsymbol{\kappa}_d^{p,S},\omega)\hat{\boldsymbol{z}}$, $\boldsymbol{\kappa}_d^{p,S} = (\frac{\omega}{c}\sin\theta^0_{p,S} - \frac{2\pi}{d_{p,S}})\hat{x}$, we recall that $d_{p,S}$ and $\sin\theta^0_{p,S}$ are grating periods and incident angles, and the relationship between pulse duration and wavelength bandwidth is $T_{p,S} = \frac{\lambda_0^2}{c\pi\Delta\lambda_{p,S}}$.

Similar to the grating TF case (Eq. (45)), one assumes that the diffracted field at each

central wavelength propagates along the optical axis,

$$\begin{aligned} \boldsymbol{\kappa}_g^p(\omega_{0p}) &= \mathbf{0} \\ \boldsymbol{\kappa}_g^S(\omega_{0S}) &= \mathbf{0} \end{aligned} \tag{116}$$

The first order Taylor expansion is applied to both axial frequency component $q$,

$$q(M_{p,S}\boldsymbol{\kappa}_d^{p,S}, \omega) \approx q(\mathbf{0}, \omega_{0p,0S}) + a\nu_{p,S} + b_{p,S}\nu_{p,S}^2 \tag{117}$$

where $a = \frac{1}{c}$, $b_{p,S} = -\frac{cM_{p,S}^2 Q_{p,S}^2}{2\omega_{0p,0S}}$, we recall $Q_{p,S} = \frac{\lambda_{0p,0S}}{cd}$ is for transmission grating, $Q_{p,S} = \frac{2\lambda_{0p,0S}}{c\sqrt{4d^2 - \lambda_{0p,0S}^2}}$ is for reflection grating.

And the pulse durations (pulse wavelength bandwidths) define the effective NA as :

$$\begin{aligned} \mathrm{NA}_p &= \frac{M_p \Delta\lambda_p}{2d_p} \\ \mathrm{NA}_S &= \frac{M_S \Delta\lambda_S}{2d_S} \end{aligned} \tag{118}$$

In addition, we assume the pupil can collect all the wavelengths of the pump pulse and the Stokes pulse, which means the objective NA ($\mathrm{NA_O}$) is larger than $\mathrm{NA}_p$ and $\mathrm{NA}_S$. Therefore, according to the two-photon TF derivation process (Eq. (49)), the fields of pump pulse and Stokes pulse in Eq. (115) can be calculated as

$$E_{p,S}^G(\boldsymbol{r}, t) = E_{\omega_{0p,0S}}(\boldsymbol{r}, t) E_{\mathrm{pulse}}^{p,S}(\boldsymbol{r}, t) \tag{119}$$

where $E_{\omega_{0p,0S}}(\boldsymbol{r}, t) = e^{iC_{p,S}(z,t)}$, $E_{\mathrm{pulse}}^{p,S}(\boldsymbol{r}, t) = \sqrt{\frac{\pi}{A_{p,S}(z)}} e^{-\frac{B_{p,S}^2(\boldsymbol{r},t)}{4A_{p,S}(z)}}$, $C_{p,S}(z, t) = q(\mathbf{0}, \omega_{0p,0S})z - \omega_{0p,0S}t$, $A_{p,S}(z) = T_{p,S}^2 + i\frac{cM_{p,S}^2 Q_{p,S}^2 z}{2\omega_{0p,0S}}$, $B_{p,S}(\boldsymbol{r}, t) = \frac{\boldsymbol{u}_{p,S}\cdot\boldsymbol{r}}{c} - t$, $\boldsymbol{u}_{p,S} = M_{p,S}cQ_{p,S}\hat{\boldsymbol{x}} + \hat{\boldsymbol{z}}$.

To ensure that the pump pulse and Stokes pulse can overlap temporally and spatially in the sample plane, it is essential to make sure they have the same speed and the same propagation direction, meaning $\boldsymbol{u}_p = \boldsymbol{u}_S$. Thus, the following condition should be maintained :

$$M_p Q_p = M_S Q_S \tag{120}$$

Based on Eq. (113), the optical sectioning of the wide-field CARS microscopy can be analyzed by calculating,

$$|E_p^G|^4(\boldsymbol{r}, t)|E_S^G|^2(\boldsymbol{r}, t) \propto \frac{1}{|A_p(z)|^2 |A_S(z)|} e^{-\frac{\mathrm{Re}[A_p(z)]B^2(\boldsymbol{r},t)}{|A_p(z)|^2}} e^{-\frac{\mathrm{Re}[A_S(z)]B^2(\boldsymbol{r},t)}{2|A_S(z)|^2}} \tag{121}$$

The collected signal $S_{\mathrm{aS}}$ is obtained through,

$$\begin{aligned} S_{\mathrm{aS}}(z) &\propto \int |E_p^G|^4(\mathbf{0},z,t)|E_S^G|^2(\mathbf{0},z,t)\mathrm{d}t \\ &= \int |E_p^G|^4(\boldsymbol{r},t)|E_S^G|^2(\boldsymbol{r},t)\mathrm{d}t \\ &= \frac{1}{|A_p(z)|}\frac{1}{\sqrt{T_p^2|A_S(z)|^2+\frac{T_S^2}{2}|A_p(z)|^2}} \end{aligned} \tag{122}$$

The optical sectioning of this configuration, which is defined as the FWHM of $S_{\mathrm{aS}}(z)$, reads

$$\Delta z_{\mathrm{CARS}} = 2\sqrt{U} \tag{123}$$

where $U = \frac{-B_{\mathrm{CARS}}+\sqrt{B_{\mathrm{CARS}}^2+12T_p^4J_pN(T_S^4T_p^2+T_p^4T_S^2/2)}}{2J_pN}$, $B_{\mathrm{CARS}} = J_p(T_S^4T_p^2+T_S^2T_p^4/2)+NT_p^4$, $N = T_p^2J_S+T_S^2J_p/2$, $J_{p,S} = \frac{\lambda_{0p,0S}^2M_{p,S}^4Q_{p,S}^4}{16\pi^2}$.

Given the difficulty in analyzing the optical sectioning performance of this configuration from the complicated formula (Eq. (123)), we consider three distinct pulse duration cases.

— The first case to be analyzed is when $T_p \ll T_S$, which means the Stokes pulse duration is very long[1]. Thus, the second term of Eq. (122) tends to a constant even the pump pulse bandwidth is changing, so the signal $S_{\mathrm{CARS}}(z)$ becomes similar to that of obtained in two-photon microscopy using grating TF. The optical sectioning reads;

$$\Delta z_{\mathrm{CARS}} \approx \frac{2\sqrt{3}\lambda_0}{\pi \mathrm{NA}_p^2} \tag{124}$$

— In the second case, we assume $T_p$ is much longer than $T_S$, and the signal $S_{\mathrm{aS}}(z)$ can be simplified as

$$S_{\mathrm{CARS}}(z) \approx \frac{1}{\sqrt{T_p^2|A_S(z)|^2+\frac{T_S^2}{2}|A_p(z)|^2}} \tag{125}$$

The optical sectioning will be

$$\Delta z_{\mathrm{CARS}} \approx 2\sqrt{3}T_P\sqrt{\frac{T_S^4+\frac{T_S^2T_p^2}{2}}{T_p^2J_S+\frac{T_S^2J_p}{2}}} \tag{126}$$

In this case, the optical sectioning almost disappears if the pump pulse duration $T_p$ is very long, indicating that the pump pulse bandwidth is critical for the optical sectioning of TF-CARS.

1. Here, we can not assume $T_S \to +\infty$ because if the second term tends to 0, which means there is no optical sectioning, and it would be meaningless.

— The last case is when $T_p = T_S$, the optical sectioning expression is identical to the one in Eq. (123) : $\Delta z_{\text{CARS}} = 2\sqrt{U}$, but $U$ can be simplified as

$$U = \frac{-T^4[J_S + 2J_p] + T^4\sqrt{16J_p^2 + 28J_pJ_S + J_S^2}}{J_p[2J_S + J_p]} \tag{127}$$

By analyzing its theoretical optical sectioning, we can conclude that the pump pulse duration dominates in the CARS configuration. Furthermore, if we consider Eq. (122), even if the second term $\frac{1}{\sqrt{T_p^2|A_S(z)|^2 + \frac{T_S^2}{2}|A_p(z)|^2}}$ does not induce attenuation and remains merely a small constant, the collected signal in this configuration still matches that obtained in the two-photon microscope using grating TF (Eq. (53)) and the pump pulse as the excitation beam. However, if the Stokes pulse duration is comparable to that of CARS, the second term does induce some decay. Thus, the optical sectioning in this configuration outperforms the one obtained in two-photon grating TF using the pump pulse as the excitation beam.

### 4.2.2 Simulations

To check the optical sectioning capability of TF-CARS with two gratings, we performed numerical simulations of its field (Eq. (115)) and intensity (Eq. (121)) and compared the simulations of optical sectioning for two-photon TF with pump parameters. Here, we analyze the effect of different pulse durations on optical sectioning, because the assumptions we made previously to allow the pump and Stokes to overlap in space and time make it difficult to change the other parameters.

Firstly, we maintain the pump bandwidth constant and adjust only the Stokes bandwidth to compare the optical sectioning for TF-CARS and grating TF, as shown in Fig. 4.4(a). For grating period equal $0.83\mu m$, $\lambda_{0p} = 800nm$, $\lambda_{0S} = 1030nm$, $M_p = 60$, so $M_S = 46.6$, $\Delta\lambda_p = 12.3nm$ (pulse duration is about 220 fs), we observe an improvement on optical sectioning for TF-CARS $\Delta z_{\text{CARS}}$ when the Stokes pulse bandwidth increases. When $\Delta\lambda_S = 25nm$, the optical sectioning can be improved to $2\mu m$ (TF-CARS) whereas it is only $4.4\mu m$ in two-photon TF. However, if the Stokes pulse bandwidth narrows (its pulse duration increases), the optical sectioning of CARS will converge to the two-photon case.

This behavior is consistent with the analytical analysis when $T_p \ll T_S$ ($\Delta\lambda_p \gg \Delta\lambda_S$), which suggests that when the pump and Stokes pulses overlap temporally and spatially, the introduction of the Stokes pulse improves the optical sectioning compared to that of the two-photon TF.

In Fig. 4.4(b), we choose pump and Stokes pulses to have the same bandwidth, and the comparison with grating TF shows that the TF-CARS optical sectioning mainly depends on the pump pulse bandwidth, which is also consistent with the analytical analysis (the pump pulse dominates $\Delta z_{\text{CARS}}$, while the Stokes pulse brings only a slight improvement).

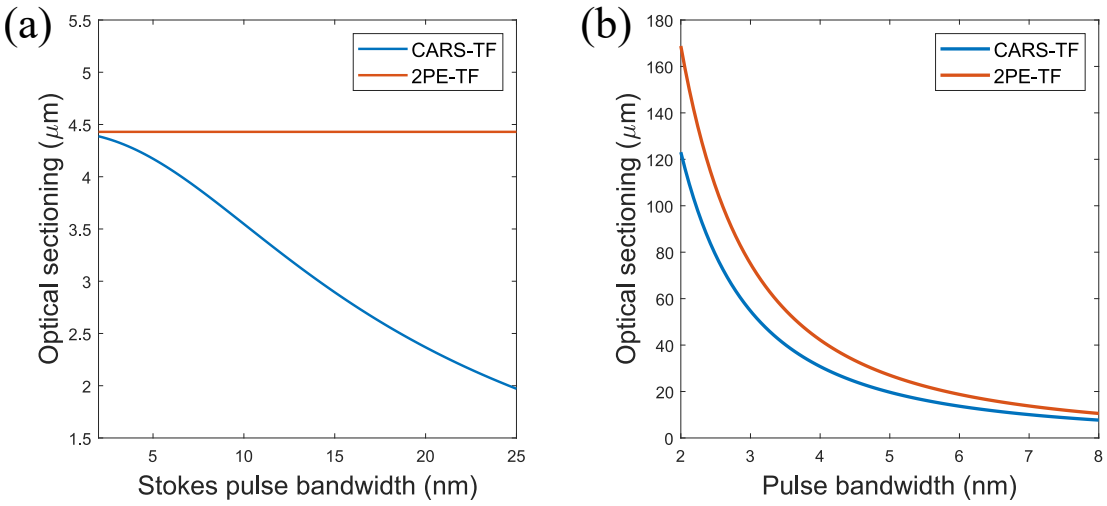


FIGURE 4.4 – Comparing the simulated optical sectioning of TF-CARS (in the two-gratings configuration) and grating TF. (a) : for different Stokes pulse bandwidths, the comparison of optical sectioning for TF-CARS $\Delta z_{\mathrm{CARS}}$ and two-photon TF $\Delta z_{\mathrm{G}}$ (using the pump pulse as the excitation beam in the two-photon simulation) ; this indicates that the introduction of temporal-focused Stokes beam slightly improves the optical sectioning as compared to two-photon TF. (b) : when pump pulse and Stokes pulse have the same wavelength bandwidth, the optical sectioning comparison of TF-CARS and two-photon TF with varying bandwidth shows that the pump pulse dominant in TF-CARS. However, the Stokes pulse still exerts some influence.

### 4.2.3 Experiments on the optical sectioning of TF-CARS using two gratings

To confront our theoretical expressions with experimental data, a TF-CARS microscopy experiment with two gratings was implemented at the Fresnel Institute by Michal Marynowski (PhD student of H. Rigneault) and Federico Vernuccio. The experimental configuration is depicted in Fig. 4.5. The sample is a coverslip that has been stained by a black marker. With $M_p = 60$, $\lambda_{0p} = 790nm$, $\lambda_{0S} = 1030nm$, $d = 0.83\mu m$, $M_S = 41$ is obtained from the condition $M_p Q_p = M_S {Q_S}^2$[2], pulse durations are both about $220fs$, Fig. 4.6 illustrates that the optical sectioning of CARS is about $2.1\mu m$, whereas the optical sectioning of two-photon TF using the pump pulse is about $3.43\mu m$.

If we substitute the above parameters into the grating TF formula (Eq. (55)) and CARS

2. The experiment uses reflection gratings. The transmission gratings are used for modeling, while reflection gratings are used for experiments. We have shown in the previous chapter on grating TF that the only difference lies in the distinct numerical apertures $\mathrm{NA_G}$ introduced by the differing expressions for $Q$

optical sectioning with the same pulse durations (Eqs. (123, 127)) with $Q = \frac{2\lambda_0}{c\sqrt{4d^2-\lambda_0^2}}$ respectively, we obtain the analytical optical sectioning as : $\Delta z_G = 3.56\mu m$, $\Delta z_{CARS} = 2.01\mu m$. Hence, the experimental optical sectionings totally match the theory. In the following, we will study another benefit of TF-CARS, its spectral resolution.

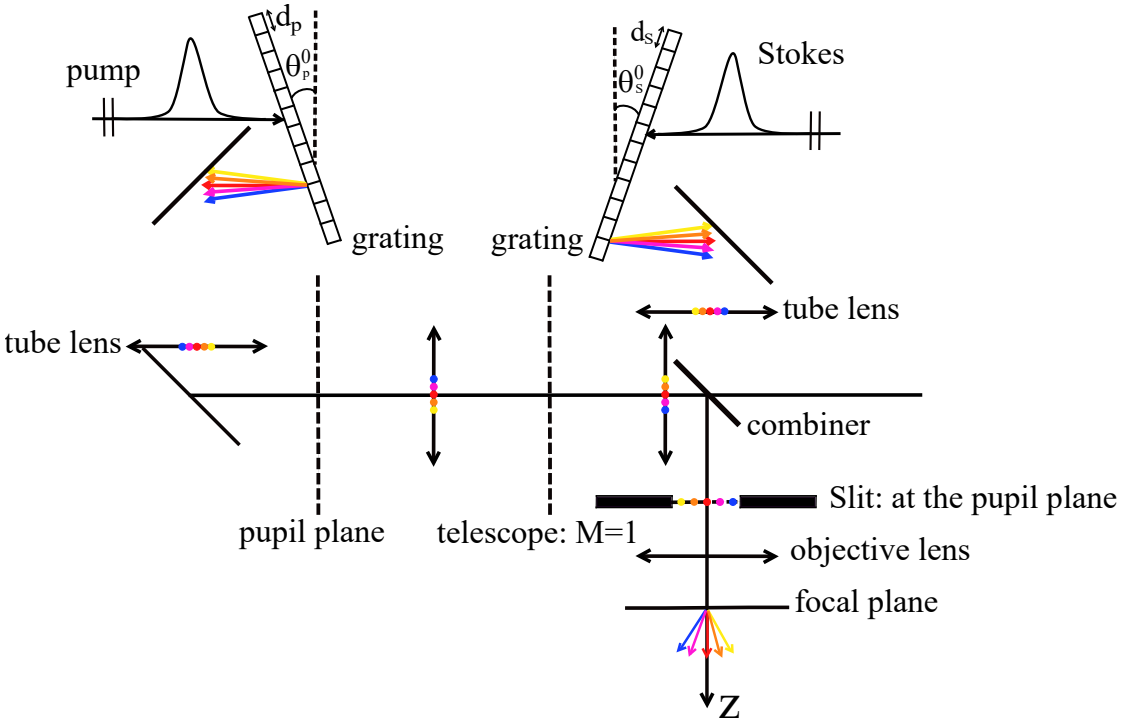


FIGURE 4.5 – Experimental setup for TF-CARS configuration with two reflection gratings in Littrow configuration. Two pulses are incident onto the reflective grating, with their central wavelengths propagating in the opposite direction to the incident direction. The two pulses are diffracted into plane waves with different wavelengths and then combined at the pupil plane. The only difference from the modeling configuration (Fig (4.3)) is that we employ a reflective grating to achieve temporal focusing of the pulses, not the transmission gratings. However, the slit placed at the pupil plane is used to measure the best achievable spectral resolution, which will be discussed in the next subsection.

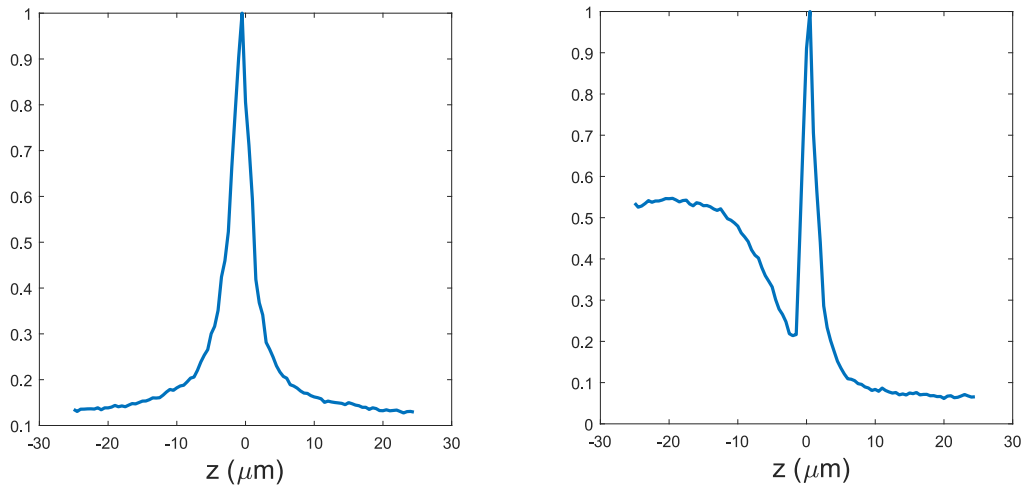


(a) Optical sectioning for two-photon TF : $\Delta z_{\mathrm{G}} \approx 3.43\mu m$

(b) Optical sectioning for TF-CARS : $\Delta z_{\mathrm{CARS}} \approx 2.1\mu m$

FIGURE 4.6 – Experimental optical sectioning obtained for two-photon grating TF using the pump pulse and TF-CARS. $M_p = 60$, $\lambda_{0p} = 790nm$, $\lambda_{0S} = 1030nm$, $d = 0.83\mu m$, $M_S = 41$, pulse durations are both about $220fs$. TF-CARS optical sectioing is better than that of two-photon TF (left image : $\Delta z_{\mathrm{G}} \approx 3.43\mu m$) (right image : $\Delta z_{\mathrm{CARS}} \approx 2.1\mu m$), which is consistent with the analytical expression. In the CARS experiment, we measure the signal from a coverslip stained with a black marker that is translated through the focal plane to obtain the optical sectioning. The CARS intensity curve (right plot) shows a peak when the marker's ink is excited but also some asymmetric background. We suppose that this non-resonant background (NRB) signal is generated by the glass. The asymmetry can be explained by the fact that, during the translation, we first detect the signal of the glass, then, that of the black marker layer and then that of the air.

## 4.3 Spectroscopy in the TF-CARS configuration with two gratings

In this section, we demonstrate that TF-CARS using two gratings not only provides an optical sectioning that is better than that obtained in two-photon grating TF, but it also has a superior spectral resolution compared to conventional CARS scanning microscopes.

### 4.3.1 Analysis of the pupil plane

As shown in Figs. (4.3, 4.5), the pump and Stokes pulses are combined in the pupil plane after being diffracted by different gratings, and then pass through the same objective lens to form the CARS signal. So in the pupil plane, we should observe two overlapping rainbow lines, each one representing a pulse, as illustrated in the right image of Fig. 4.7.

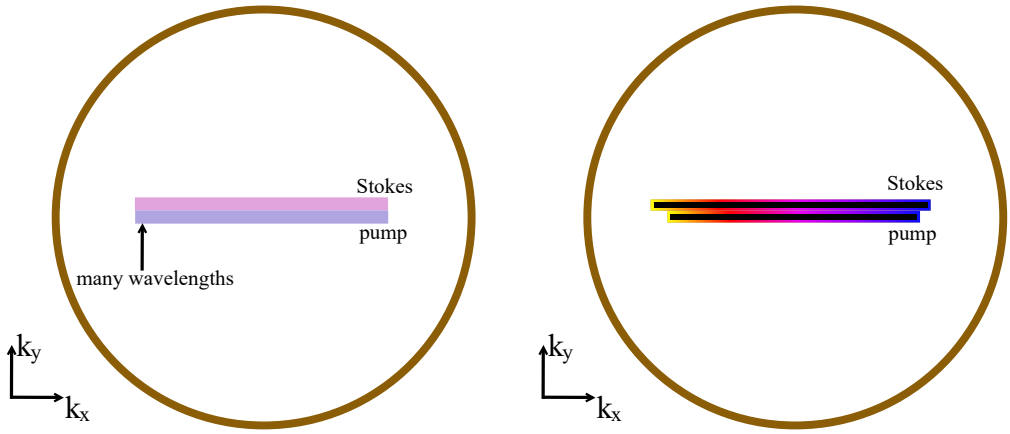


FIGURE 4.7 – The field behavior in the pupil plane for a line-scanning CARS configuration and for the TF-CARS with two gratings. The left image illustrates the pupil plane in a line-scanning CARS microscope in which two line-focused beams spanning multiple wavelengths are incident on the conjugate plane of the sample plane. Consequently, both pulses are stretched at the pupil plane, with each point along the line containing all wavelengths of the incident pulses. The right image represents the pupil plane in a TF-CARS configuration using two gratings. Both the pump pulse and the Stokes pulse are stretched by two sets of independent gratings into two rainbow lines, where the different colors on the rainbow line represent different wavelengths. They overlap but differ slightly in length, and the reasons for the difference in length will be discussed.

The illustration of the pupil plane in line-scanning CARS microscopy and TF-CARS using two gratings displayed in Fig. 4.7 show that, at a given point of the pupil (cor-

responding to a given direction of the plane wave in the sample space) the range of frequency differences $\Omega = (\omega_p - \omega_S)$ between the two pulses is much larger in the line-scanning CARS than in the TF-CARS. In the latter case, one point in the pupil plane corresponds to one specific $\Omega$. This will have a major impact on the TF-CARS spectral resolution.

Generally, the spectral resolution $\Delta\nu$ of a standard scanning CARS microscope is obtained by the cross-correlation of two pulses, and can be expressed as

$$\Delta\nu = \sqrt{\Delta\nu_p^2 + \Delta\nu_S^2} \tag{128}$$

where $\Delta\nu_{p,S} = \frac{\nu_{p,S}}{2\pi c} = \frac{\omega_{p,S} - \omega_{0p,0S}}{2\pi c}$.

A technique that can significantly improve the spectral resolution of femtosecond pulses in CARS scanning microscopes is Spectral focusing (SF) (HELLERER et al. 2004). SF is able to provide high spectral resolution by applying identical chirps to two femtosecond pulses, thereby stretching their pulse duration to picosecond pulses. This induces a linear relationship between pulse frequency $\omega_{p,S}$ and time $t$ with the same slope, yielding an extremely narrow frequency difference and attaining high spectral resolution of approximately tens of $cm^{-1}$, and this range of frequency difference can be tuned by adding the time delay, as illustrated in Fig. 4.8. The enhanced spectral resolution can be calculated from Eq. (128) by the chirped pulse duration. This approach has been applied in both CARS (ANDRESEN, BIRKEDAL et al. 2006) and stimulated Raman scattering (SRS) (ANDRESEN, BERTO et al. 2011).

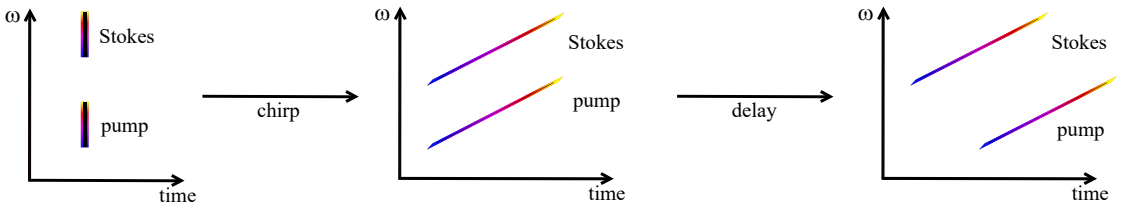


FIGURE 4.8 – The principle of SF. Left, illustration of the short-time Fourier transform of standard pump and Stokes fs pulses. Middle, illustration of the short-time Fourier transform of chirped picosecond pump and Stokes pulses. The spectral resolution is enhanced significantly. Right, illustration of the short-time Fourier transform of chirped picosecond pump and Stokes pulses when a delay is introduced between the pulses. The range of spectral resolution ($\Delta\nu$) can be tuned depending on the delay.

In our TF-CARS configuration (Figs. 4.3, 4.5), there are two overlapping rainbow lines on the pupil plane. One position on the horizontal line of the pupil plane (which is proportional to $\sin(\theta)$ where $\theta$ is the angle between the propagation direction of the plane wave in the sample space and the $z$ axis) is related to a temporal frequency $\omega_{S,p}$ following,

$$M_{p,S} Q_{p,S} (\omega_{p,S} - \omega_{0p,0S}) / \frac{\omega_{p,S}}{c} = \sin\theta_{p,S} \tag{129}$$

Thus, $\omega$ can be approximated as a linear function of $\sin\theta$ :

$$\omega_{p,S} = \frac{cM_{p,S}Q_{p,S}\omega_{0p,0S}}{cM_{p,S}Q_{p,S} - \sin\theta_{p,S}} \approx \alpha_{p,S}\sin\theta_{p,S} + \omega_{0p,0S} \tag{130}$$

where $\alpha_{p,S} = \frac{\omega_{0p,0S}}{cM_{p,S}Q_{p,S}}$. Eq. (130) indicates a linear relationship between the angular frequency and the pupil position, with the slope determined by the selected parameters. The physical picture for the relationship between $\sin\theta$ and $\omega_{p,S}$ can be depicted in Fig. 4.9.

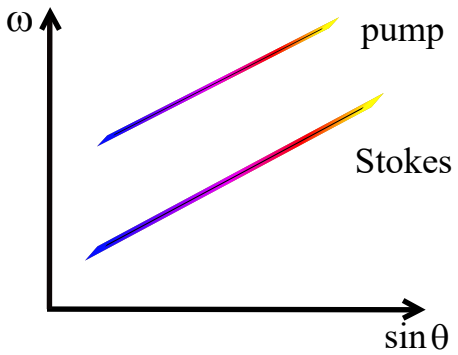


FIGURE 4.9 – Relationship between $\omega_{p,S}$ and $\sin\theta$ (indicating a point in the pupil) in TF-CARS using two gratings. As discussed in Eq. (130), the frequencies depend linearly on $\sin\theta$, and the slopes depend on the microscope and grating parameters.

From a theoretical point of view, the phase-matching condition when the pump beam and Stokes beams illuminate a homogeneous non-linear medium, imposes that two conditions be satisfied : $\boldsymbol{k}_{as} = 2\boldsymbol{k}_p - \boldsymbol{k}_S$ (wavevectors), $\omega_{as} = 2\omega_p - \omega_S$.

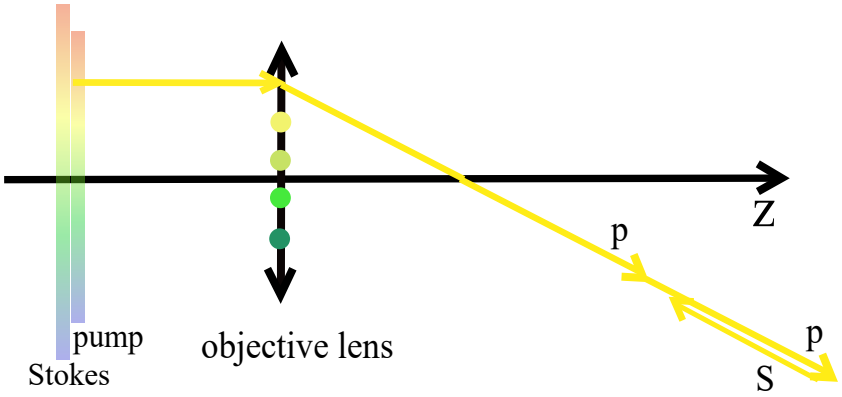


FIGURE 4.10 – When the sample is homogeneous, the phase matching condition is satisfied when the pump plane wave field and Stokes plane wave have the same propagation direction in the sample space.

Thus, the frequency difference $\nu_d = \nu_p - \nu_S$ can be expressed as

$$\nu_d = \frac{\alpha_p - \alpha_S}{2\pi c}\sin\theta + \nu_{0p} - \nu_{0S} \tag{131}$$

where $\nu_{0p,0S} = \frac{\omega_{0p,0S}}{2\pi c}$.

The ideal spectral resolution $\Delta\nu = \max(\nu_d) - \min(\nu_d)$ reads

$$\Delta\nu_{\text{CARS}} = \frac{\alpha_p - \alpha_S}{2\pi c}[\max(\sin\theta) - \min(\sin\theta)] \tag{132}$$

### 4.3.2 How to select configuration parameters to improve spectral resolution ?

To ensure that two pulses propagate at the same speed across the sample plane, $M_pQ_p = M_SQ_S$ must be maintained. However, this results in different slopes ($\alpha_{p,S} = \frac{\omega_{0p,0S}}{cM_{p,S}Q_{p,S}}$) in Eq. (130) due to their differing center frequencies. For example, when $\lambda_{0p} = 800nm$, $\lambda_{0S} = 1030nm$, $M_p = 60$, $M_S = 46.6$, $d = 0.83\mu m$, pulse durations are $220fs$ ($\Delta\lambda_p \approx 12.3nm$, $\Delta\lambda_S \approx 20.4nm$), the linear relationship between $\omega_{p,S}$ and $\sin\theta$ can be shown in Fig. 4.11, we obtain a spectral resolution (frequency difference) : $\Delta\nu_{\text{CARS}} = 42.5\text{cm}^{-1}$. Fig. 4.11(a) illustrates the relationship between $\nu$ and $\sin\theta$. Note that the spectral resolution, given by the formula (Eq. (128)), is about $273\text{cm}^{-1}$ in scanning CARS microscopy. Additionally, under these parameters, TF-CARS provide an optical sectioning of about $2.6\mu m$.

To further enhance TF-CARS spectral resolution, we can try to equalize the Stokes and pump slopes ($\alpha_p = \alpha_S$), providing a constant frequency difference $\nu_d$ whatever the plane-wave directions and theoretically an infinitely small spectral resolution. However, this would cause the two pulses to propagate at different speeds and in different directions within the sample plane (as $M_pQ_p \neq M_SQ_S$ anymore). Consequently, the effective CARS signal would only be excited on a very small FOV. For instance, with the following parameters, $\lambda_{0p} = 800nm$, $\lambda_{0S} = 1030nm$, $M_p = 60$, $d = 0.83\mu m$, pulse durations $220fs$, $M_S = 36.2$ we obtain $\alpha_p = \alpha_S$. However, due to the differing velocities of the Stokes and pump pulses, they overlap only on a reduced FOV of 5 micrometers, as seen in Fig. 4.11(d). Therefore, in order to maintain the wide-field configuration, which is the main interest for TF applications, we favor the first option, $M_pQ_p = M_SQ_S$, even though it deteriorates slightly the spectral resolution.

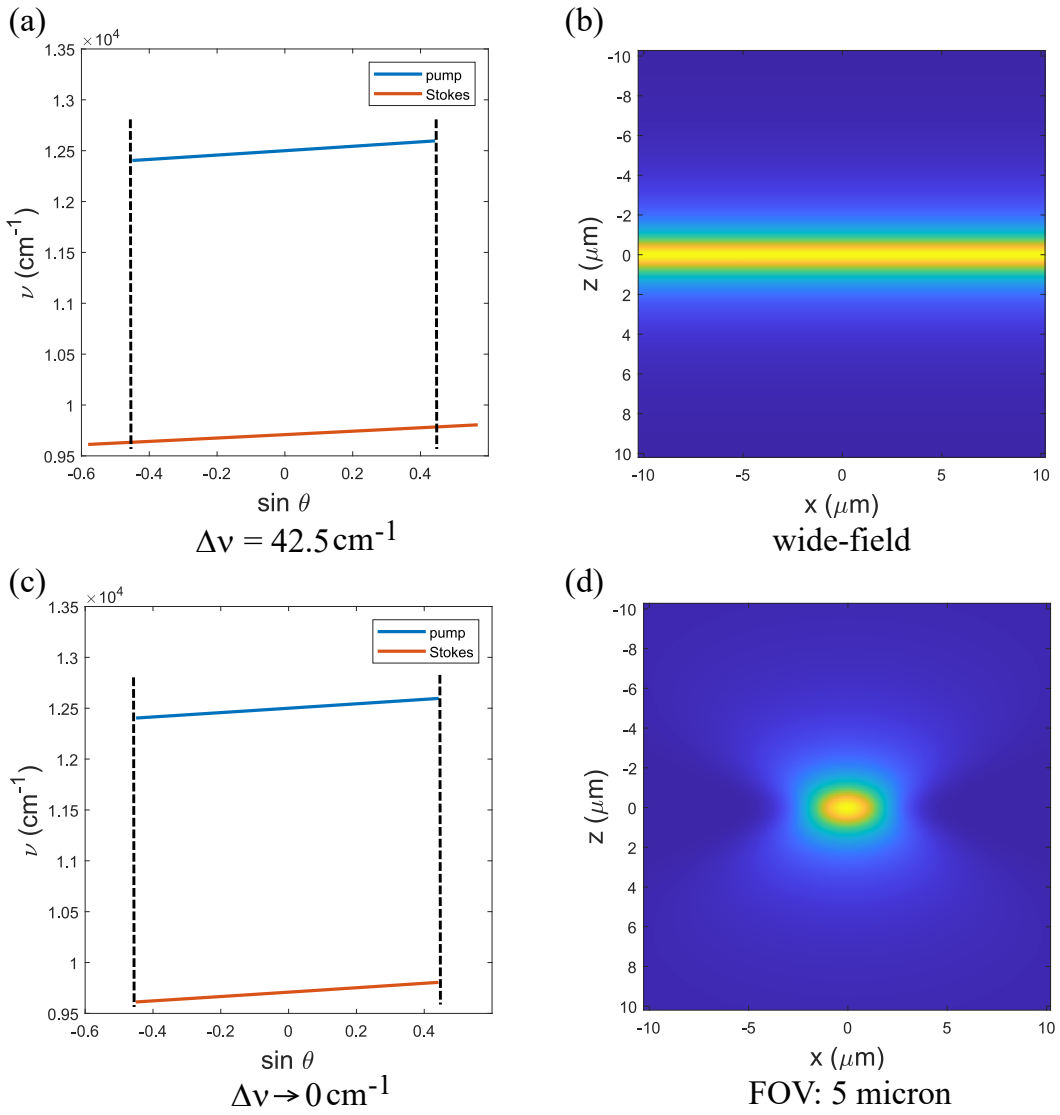


FIGURE 4.11 – Right, XZ maps of $\int |E_p|^4(x,0,z,t)|E_S|^2(x,0,z,t)dt$ in the TF-CARS configuration using two gratings, $\lambda_{0p} = 800nm$, $\lambda_{0S} = 1030nm$, $M_p = 60$, $d = 0.83\mu m$, pulse durations are $220fs$. Right, plots of $(\nu_S, \nu_p)$ as a function of $\sin\theta$. The molecular frequency $\Omega^{\min,\max} = \nu_p - \nu_S$ obtained at the extreme $\sin\theta$ points indicated by the dashed lines yields the spectral resolution of the configuration. (a,b) :The Stokes magnification is chosen ($M_S = 46.6$) so that the two pulses maintain identical velocities on the sample plane. In this case, the spectral resolution is about 42.5 $cm^{-1}$, and the excitation of the CARS signals occurs across a wide FOV. (c,d) : The Stokes magnification is chosen to obtain the same slopes for $\nu_{S,p}$ with respect to $\omega_{S,p}$ ($M_S = 46.6$). In this case $\Omega^{\min,\max}$ are equal and the spectral resolution is theoretically infinitely small. On the other hand, the FOV to about 5 microns, as the pump and Stokes pulses do not propagate at the same speed in the sample plane.

### 4.3.3 Experiments on TF-CARS spectral resolution

To confirm the theory, experiments were conducted that measured the spectral resolution of TF-CARS. In addition, to mitigate spectral resolution degradation caused by varying slopes, we placed a slit at the pupil plane in front of the objective lens and measured the spectral resolution for different slit widths, as shown in Fig. 4.5.

Regarding spectral resolution, contrary to theory, the mismatch vector $\Delta\boldsymbol{k} = \boldsymbol{k}_{as} - (2\boldsymbol{k}_p - \boldsymbol{k}_S)$ need not be exactly zero to be collected because of the difficulty with the homogeneous sample. For instance, when $M_p = 60$, $\lambda_{0p} = 790nm$, $\lambda_{0S} = 1030nm$, $d = 0.83\mu m$, $M_S = 41$ is obtained from the condition $M_pQ_p = M_SQ_S$ for the reflection grating, pulse durations are both about $220fs$, we measure a spectral resolution of $35\text{cm}^{-1}$ (Eq. 132 provides a spectral resolution of about $40\text{cm}^{-1}$ with those parameters), shown in Fig. 4.12(a).

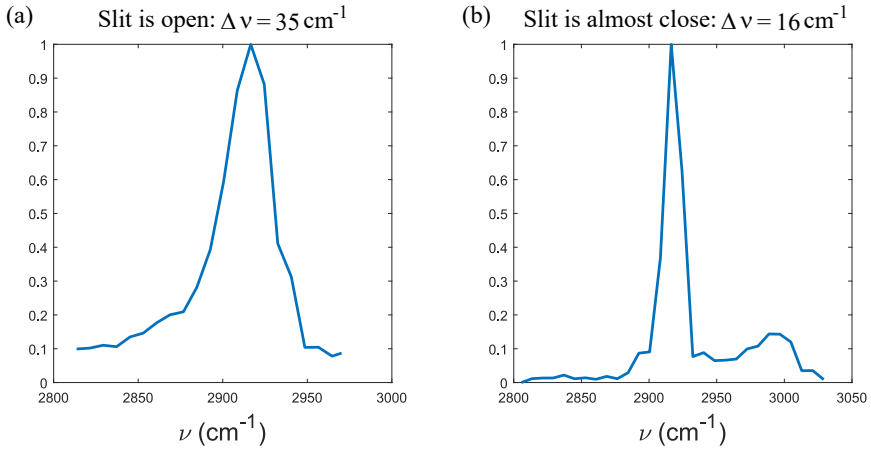


FIGURE 4.12 – Experimental spectral resolutions in TF-CARS using two reflection grating with, $M_p = 60$, $\lambda_{0p} = 790nm$, $\lambda_{0S} = 1030nm$, $d = 0.83\mu m$, $M_S = 41$. As discussed in Fig. 4.5, we place a slit at the objective pupil plane to explore the spectral resolution. The left image shows the spectral resolution when the slit is open; the right image illustrates the spectral resolution when the slit is almost closed, displaying the best spectral resolution for this configuration.

Additionally, placing a slit at the pupil plane and closing it as much as possible yields a spectral resolution of approximately $15\text{cm}^{-1}$, as shown in the Fig. 4.12(b). However, during imaging, we do not choose to close the slit because this would significantly compromise optical sectioning capability. Nevertheless, this allows us to estimate the best achievable spectral resolution. Moreover, the different spectral resolutions obtained by varying the slit will be analysed theoretically.

## 4.4 Forming TF-CARS using only one grating

In this section, we propose an approach that allows obtaining an effective TF-CARS signal with only one grating. We simultaneously send the pump and Stokes pulses along the same direction onto the same grating and choose the grating period and angle of incidence so that the pump field of the $-1$ diffraction order at the central pump wavelength propagates towards positive $x$ while the Stokes field of the $-1$ diffraction order at the central Stokes wavelength propagates towards negative $x$, as illustrated in Fig. 4.13. This configuration resembles that of the multi-order grating TF discussed in the previous Chapter.

### 4.4.1 Theory of TF-CARS with one grating

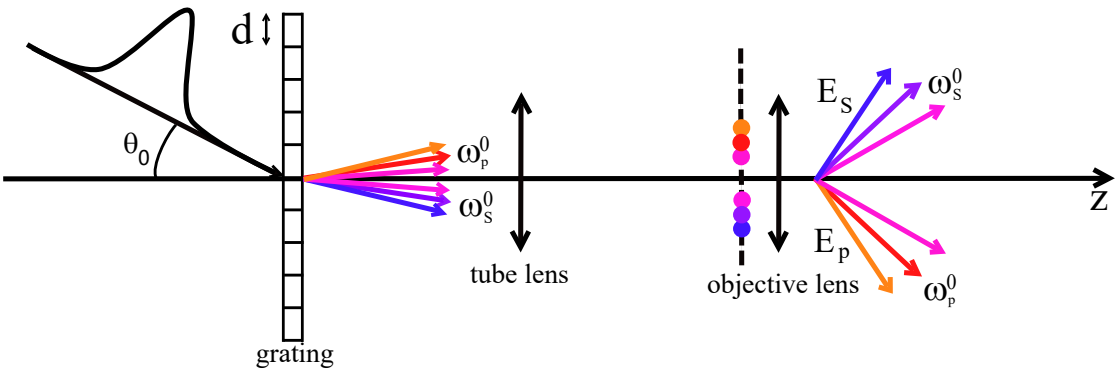


FIGURE 4.13 – Configuration of TF-CARS using one grating. Pump pulse and Stokes pulse are incident onto grating with the same angle, their $-1$ diffraction orders propagate towards the positive and negative $x$ axis, respectively. Both Stokes and pump (-1) diffracted orders are collected by the objective lens.

The $-1$ order diffraction field of pump and Stokes (a similar expression with Eq. (44)) can be expressed as :

$$E_{\mathrm{p,S}}(\boldsymbol{r},t)=\int_{-\infty}^{+\infty}h_{p,S}(\omega)\,p(M\boldsymbol{\kappa}_{p,S},\omega)\,e^{i[\boldsymbol{k}_{p,S}\cdot\boldsymbol{r}-\omega t]}\mathrm{d}\omega \tag{133}$$

where $\boldsymbol{k}_{p,S}=M\boldsymbol{\kappa}_{p,S}+q(M\boldsymbol{\kappa}_{p,S},\omega)\hat{z}$, $\boldsymbol{\kappa}_{p,S}=(\frac{\omega}{c}\sin\theta_0-\frac{2\pi}{d})\hat{x}$.

For simplicity, we assume the -1 diffracted order of the pump and Stokes beam at their central wavelengths $\omega_p^0$ and $\omega_S^0$ propagate along directions that are symmetrical

with respect to the optical axis :

$$\begin{aligned} \boldsymbol{\kappa}_p(\omega_{0p})/\frac{\omega_{0p}}{c} + \boldsymbol{\kappa}_S(\omega_{0S})/\frac{\omega_{0S}}{c} &= 0 \\ \frac{\omega_{0p}\sin\theta_0/c - 2\pi/d}{\omega_{0p}/c} + \frac{\omega_{0S}\sin\theta_0/c - 2\pi/d}{\omega_{0S}/c} &= 0 \end{aligned} \tag{134}$$

To obtain this property, the following condition should be satisfied,

$$2\sin\theta_0 = \frac{\lambda_{0p} + \lambda_{0S}}{d} \tag{135}$$

Following the derivation performed in the section concerning multi-order grating TF, we then assume the objective lens can collect all the light so that $h_{p,S}(\omega)p(M\boldsymbol{\kappa}_{p,S},\omega) \approx h_{p,S}(\omega)$. In this case the pump and Stokes fields in the sample space can be modeled as a complex Gaussian integrals. Applying the first-order Taylor expansion with respect to $\omega$ of the axial spatial component $q$ yields,

$$q(M\boldsymbol{\kappa}_{p,S},\omega) \approx q(M\boldsymbol{\kappa}_{p,S},\omega_{0p,0S}) + a(\omega_{0p,0S})\nu \tag{136}$$

where $a(\omega_0) = [\frac{\omega_0}{c^2} - M^2\frac{\sin\theta_0}{c}(\frac{\omega_0}{c}\sin\theta_0 - \frac{2\pi}{d})]/\sqrt{\frac{\omega_0^2}{c^2} - M^2(\frac{\omega_0}{c}\sin\theta_0 - \frac{2\pi}{d})^2}$. Note that the sign of $a(\omega_{0p}), a(\omega_{0S})$ are opposite in virtue of Eq. (134).

Thus, the pump and Stokes fields in the sample space can be modeled as Gaussian pulses propagating in different directions with different speeds,

$$\begin{aligned} E_{\mathrm{p,S}}(\boldsymbol{r},t) &= e^{iC_{p,S}(x,z,t)}\int h(\omega)e^{i\nu[\boldsymbol{u}_{p,S}\cdot\boldsymbol{r}/c - t]}\mathrm{d}\nu \\ &= e^{iC_{p,S}(x,z,t)}e^{-\frac{[\boldsymbol{u}_{p,S}\cdot\boldsymbol{r}/c-t]^2}{4T_{p,S}^2}} \\ &= E_{\omega_{0p,0S}}(\boldsymbol{r},t)E_{\mathrm{pulse}}^{p,S}(\boldsymbol{r},t) \end{aligned} \tag{137}$$

where $C_{p,S}(x,z,t) = M(\frac{\omega_{0p,0S}}{c}\sin\theta_0 - \frac{2\pi}{d})x + q(M\boldsymbol{\kappa}_{p,S},\omega_{0p,0S})z - \omega_{0p,0S}t$, $\boldsymbol{u}_{p,S} = M\sin\theta_0\hat{\boldsymbol{x}} + ca(\omega_{0p,0S})\hat{\boldsymbol{z}}$.

As discussed in the introduction to this chapter, the optical sectioning capability of CARS can be obtained by analyzing the CARS signal,

$$\begin{aligned} S_{\mathrm{aS}}(z) &= \int |E_p|^4(\boldsymbol{r},t)|E_S|^2(\boldsymbol{r},t)\mathrm{d}t \\ &= e^{-\frac{[a(\omega_{0p})-a(\omega_{0S})]^2z^2}{2T_S^2+T_p^2}} \end{aligned} \tag{138}$$

Therefore, the optical sectioning defined as the FWHM of $S_{\mathrm{aS}}(z)$ is,

$$\Delta z_{\mathrm{CARS}} = \frac{2\sqrt{\ln 2(2T_S^2 + T_p^2)}}{|a(\omega_{0p}) - a(\omega_{0S})|} \tag{139}$$

We observe that if $T_p = T_S$, the analytical optical sectioning, Eq. (139), depends linearly on the pulse duration,

$$\Delta z_{\mathrm{CARS}} = \frac{2\sqrt{3\ln 2}T}{|a(\omega_{0p}) - a(\omega_{0S})|} \tag{140}$$

and is influenced by the parameters $a(\omega_{0p,0S})$. Now, the latter governs the propagation speed and direction of the pulses (shown in Eq. (137)). Similarly to the multi-order grating TF and the roughness-grating TF configurations, the optical sectioning arises from the difference between the Stokes and pump pulse propagation direction (one propagates towards positive $z$ and the other one towards negative $z$). Fig. 4.14 illustrates the opposite propagation directions of pump and Stokes pulses along the $z$ axis.

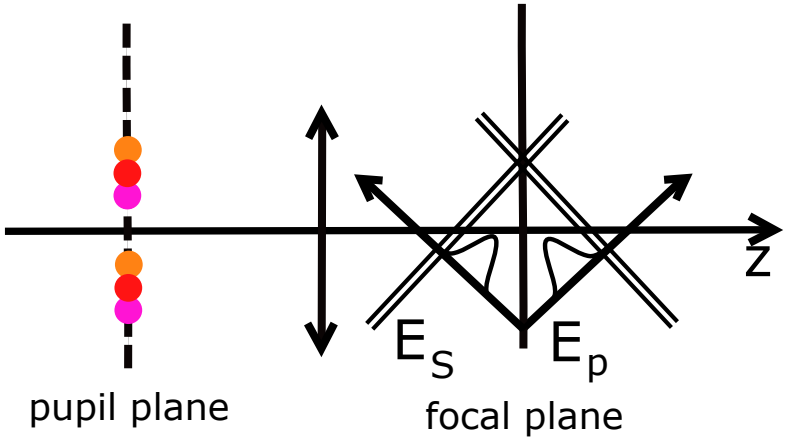


FIGURE 4.14 – Physical picture of pump pulse and Stokes pulse propagation in the TF-CARS configuration with only one grating. Similar to the analysis in Eq. (137), both pulses propagate along the $x$ at the same velocity and direction, while their speeds and direction along the z-axis are influenced by $a(\omega_{0p,0S})$. The pump pulse propagates along the positive $z$, while the Stokes pulse moves along the negative $z$.

Thus, contrary to TF-CARS using two gratings, whose optical sectioning depends on the GVD of the pulses, TF-CARS using one-grating is expected to provide a good optical sectioning even with long-duration (picosecond) pulses.

### 4.4.2 How can an objective collect all the light in TF-CARS using one grating ?

We define the maximum diffraction angles of pump and Stokes as $\mathrm{NA}_p^M$ and $\mathrm{NA}_S^M$ :

$$\begin{aligned} |M(\frac{\omega_p^{\max}}{c}\sin\theta_0 - \frac{2\pi}{d})| &= \frac{\omega_p^{\max}}{c}\mathrm{NA}_p^M \\ |M(\frac{\omega_S^{\min}}{c}\sin\theta_0 - \frac{2\pi}{d})| &= \frac{\omega_S^{\min}}{c}\mathrm{NA}_S^M \end{aligned} \tag{141}$$

where $\omega_p^{\max} = \omega_{0p} + \frac{1}{T_p}$, $\omega_S^{\min} = \omega_{0S} - \frac{1}{T_S}$.

Therefore, when selecting parameters, we need to ensure that the NA of the objective is greater than both $\mathrm{NA}_p^M$ and $\mathrm{NA}_S^M$, enabling the objective to collect all the light. Additionally, a lower magnification should be selected, as excessive magnification can cause light to be cut by the pupil.

### 4.4.3 Field behavior at the pupil plane

As illustrated in Figs. 4.13, 4.14, the diffracted pump or Stokes pulses occupy half of the pupil plane. Thus two rainbow lines should be observed at the pupil plane, as Fig. 4.15 shows.

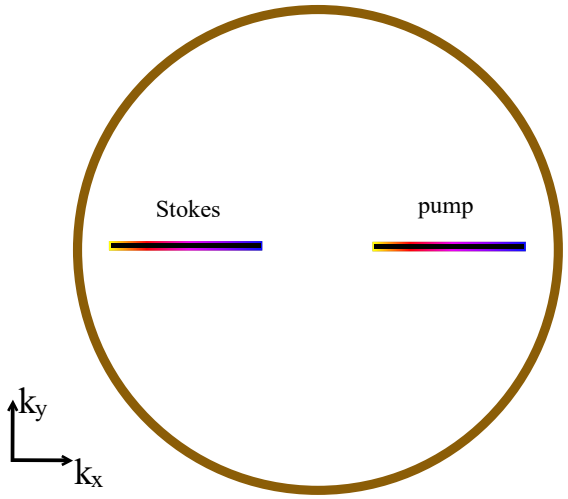


FIGURE 4.15 – Illustration of the field behavior at the pupil plane in a TF-CARS using one grating configuration. Pump pulse and Stokes pulse are each diffracted into a rainbow line, with each pulse occupying half of the pupil.

### 4.4.4 Simulations

In this subsection, we verify the theoretical optical sectioning by simulating the fields Eq. (133) and the CARS intensity Eq. (138). As discussed earlier, this configuration requires long-duration pulses and a small magnification for the objective to collect all the light. When $d = 1.6\mu m$, $\lambda_{0p} = 800nm$, $\lambda_{0S} = 1030nm$, $\mathrm{NA_O} = 0.95$, $M = 12.5$ and both pulse durations are 1ps, we find $\sin\theta_0 = 0.57$ for Eq. (135) to be satisfied. Under those parameters, $\mathrm{NA}_p^M$ and $\mathrm{NA}_S^M$ are about 0.91, thus the objective can collect the light. Figs. (4.16a, b) illustrates the XZ maps of the pump and Stokes pulse intensities ($|E_p|^4(\boldsymbol{r},t)$, $|E_S|^2(\boldsymbol{r},t)$) at different times. We observe that the pump pulse moves towards negative $z$, while the Stokes pulse moves towards positive $z$. Additionally, Fig. 4.16(c) shows that each of pulses occupy a small portion of the pupil plane, in the same way as Fig. 4.15.

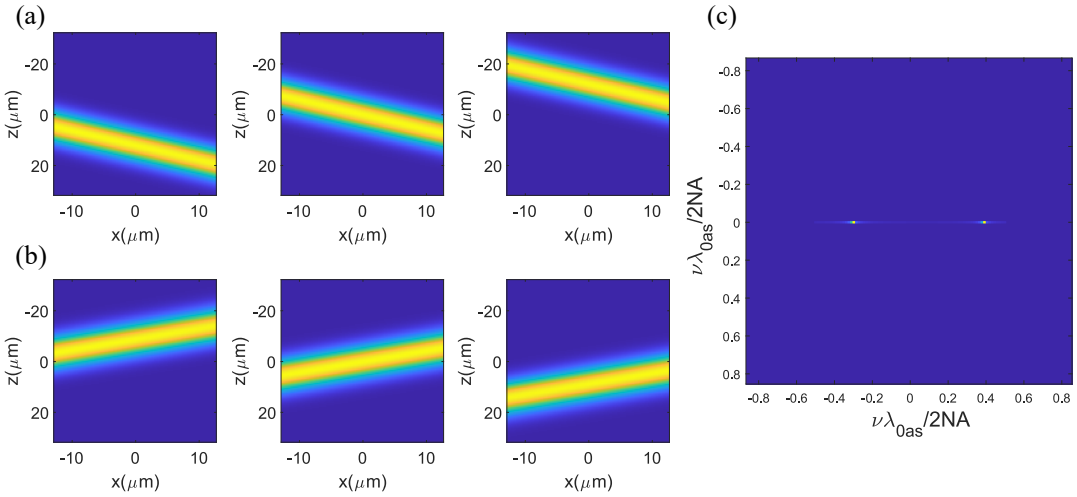


FIGURE 4.16 – Simulation of the pump and Stokes pulses at the sample and Fourier planes, with the parameters : $d = 1.6\mu m$, $\lambda_{0p} = 800nm$, $\lambda_{0S} = 1030nm$, $\mathrm{NA_O} = 0.95$, $M = 12.5$, $\sin\theta_0 = 0.57$, pulse durations : 1ps. (a) : simulation of $|E_\mathrm{p}|^4(x,0,z,t)$ for increasing time (from left to right), the pump pulse propagates towards negative $z$. (b) : simulation of $|E_\mathrm{S}|^2(x,0,z,t)$ for increasing time (from left to right). The Stokes pulse propagates towards positive $z$. (c) : Field intensity at the pupil plane. Noting that each picosecond pulse is slightly diffracted by the grating and low magnification into a short rainbow line. This is because the optical sectioning in this configuration benefits from the pulse velocity difference rather than GVD.

The overlapping of the pump and Stokes beams is illustrated in Fig. 4.17(a) where we plot $|E_p|^4(x,0,z,t)|E_S|^4(x,0,z,t)$ for increasing times (from top left to bottom right). In Fig. 4.17(b) we simulated the integrated excitation signal $S_{aS}(z) = \int |E_p|^4(0,0,z,t)|E_S|^4(0,0,z,t)\mathrm{d}t$. We estimate the optical sectioning to about $7.4\mu m$ which is exactly the value provided by the analytical expression for the optical sectioning, Eq. (139). Therefore, the simula-

ted optical sectioning agrees with the theoretical result, and it could be demonstrated that this configuration can achieve optical sectioning of several micrometers with two picosecond pulses and a small magnification.

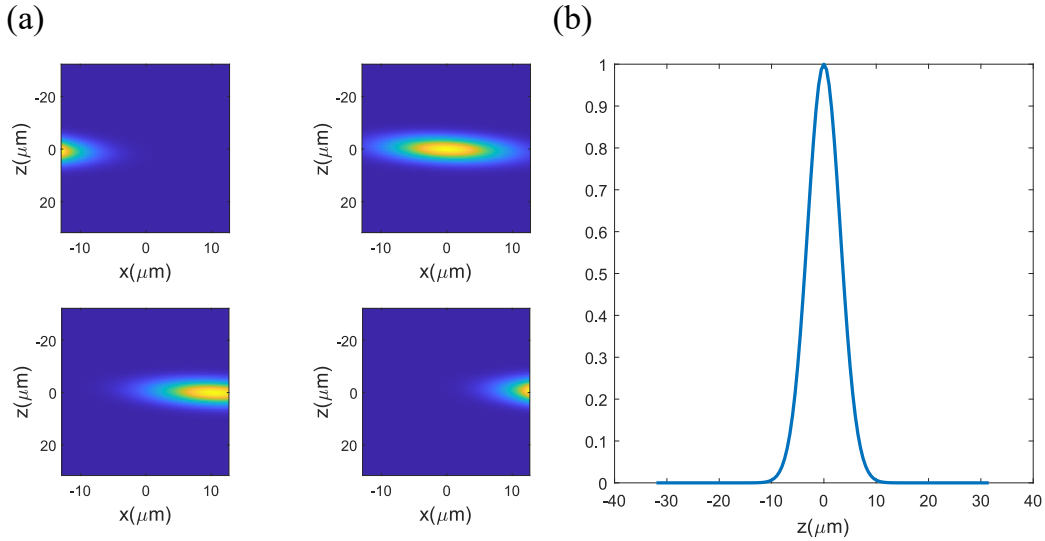


FIGURE 4.17 – (a) Simulation of the overlapping intensities $|E_p|^4(x,0,z,t)|E_S|^4(x,0,z,t)$ for increasing time (from top left to bottom right). (b) Simulation of the integrated signal $S_{aS}(z) = \int |E_p|^4(0,0,z,t)|E_S|^4(0,0,z,t)dt$. The optical sectioning is estimated to about $7.4\mu m$. The TF-CARS configuration parameters are the same as those of Fig. 4.16.

Next, we investigate the relationship between the optical sectioning $\Delta z_{\text{CARS}}$ and the pulse duration $T$ (similar for Stokes and pump beams). All the other parameters are the same as in Fig. 4.16 except for the magnification which is taken equal to 12.5 (left) and 10 (right). With these parameters the objective can collect all the diffracted light stemming from the grating. The simulations of Fig. 4.18 confirms the linear relationship between the optical sectioning and the pulses duration that had been found with the analytical expression of $\Delta z_{\text{CARS}}$, Eq. (140).

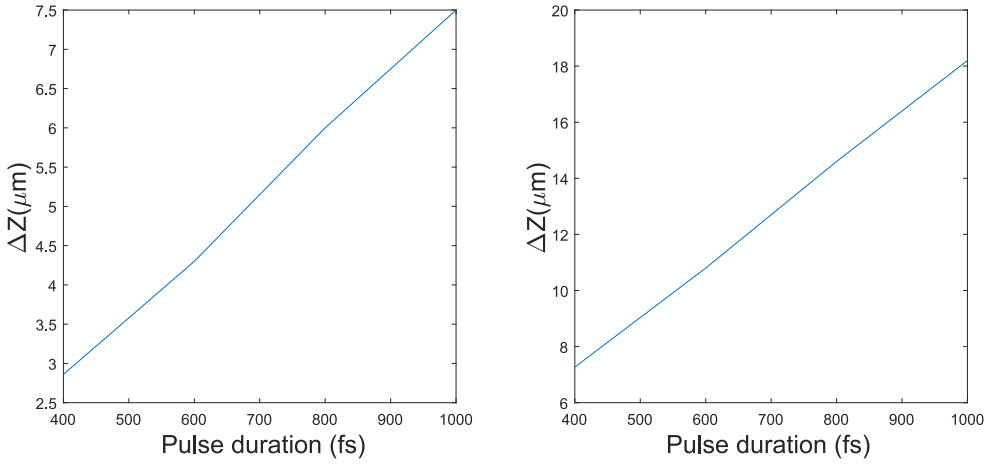


(a) $M = 12.5$ (b) $M = 10$

FIGURE 4.18 – Simulated optical sectioning $\Delta z_{\text{CARS}}$ as a function of the pulse duration (similar for the Stokes and pump beams). The TF-CARS configuration parameters are the same as in Fig. 4.18 except for the magnification. Fig. a shows a linear relationship between $\Delta z_{\text{CARS}}$ and the pulse duration when $M = 12.5$; Fig. b shows a linear relationship between $\Delta z_{\text{CARS}}$ and pulse duration when $M = 10$ as expected from the analytical expression of $\Delta z_{\text{CARS}}$, Eq. (140). Note that in both cases, the objective can collect all the diffracted light.

These preliminary results are promising as TF-CARS using one grating seems easier to implement than TF-CARS using two gratings and its optical sectioning, which does not depend on the GVD of the pulses, remains micrometric even with picosecond pulses. However, the present analysis lacks a study on the collected anti-Stokes radiation taking into account the phase-matching conditions, as the plane waves forming the pump and Stokes beams at the exit of the pupil plane propagate in different directions.

It is worth noting also, that TF-CARS using one grating bears some similarities with the concept presented in (LIN et al. 2024), though their analysis focuses on point scanning Stimulated Raman Scattering (SRS) microscopy using pump and Stokes Bessel beams that propagate along opposite directions. We believe that our approach holds significant potential : it can be applied not only to various nonlinear microscopy techniques such as SRS, CARS, and Coherent Stokes Raman scattering microscopy (CSRS), but can also be extended to incorporate random illumination scenarios (as in roughness-grating TF) and combined with super-resolution methods like RIM.

## 4.5 Conclusion and perspective

In this chapter, we propose two methods for introducing Temporal Focusing in CARS microscopy. The first method is primarily suited for femtosecond pulses and configurations with a large magnification (approximately 50). It involves using two gratings and two different magnifications to temporally focus the pump and Stokes pulses, ensuring that both pulses propagate in identical directions and at the same velocity through the sample plane. We demonstrate that this approach provides a better optical sectioning than that observed in two-photon microscopy with grating-TF (using the pump beam) from 3.5 microns to 2 microns. Indeed, the temporally focused Stokes beam enhances the action of the temporally focused pump beam. In addition, we have shown that, using the same laser beams, TF-CARS using two gratings exhibit a spectral resolution that is much better than that of scanning CARS microscopy : from several hundred $cm^{-1}$ to tens of $cm^{-1}$. The theoretical and numerical study of TF-CARS using two gratings has been confirmed with experiments.

The second TF-CARS method primarily targets picosecond pulses and smaller magnifications (about 20). It achieves CARS signal and optical sectioning capability by illuminating a single grating with the pump and Stokes pulses propagating along the same direction. The grating period and angle of incidence is optimized so that the pump and Stokes diffracted orders are symmetrical with respect to the optical axis. In the sample space, the pump and Stokes beams propagate towards positive and negative $z$, respectively. Their overlapping, about $z = 0$, determines the optical sectioning. As the latter do not depend on the GVD of the pulses (as in the two-gratings configuration), one can use longer pulses and smaller magnifications.

Both methods could be extended to random illumination using a diffuser and to other nonlinear microscopy techniques.

# Conclusion and perspective

The analytical and numerical studies developed in this thesis have shown that it is possible to improve the optical sectioning of widefield linear and non-linear microscopies using innovative illumination schemes combining random speckles and spatial or temporal focusing. Importantly, most of the theoretical results have been confirmed with preliminary experiments. A global perspective would be to optimize the different microscopes' configurations (1PM, 2PM, CARS) for demonstrating specifically the interest of the proposed illuminations for fast imaging of large FOVs.

From a theoretical point of view, two important global developments are foreseen. First, it would be interesting to take into account the vectorial nature of the field in the models of the speckled field and of the temporal focused beams (presently, all the theoretical developments are based on the scalar approximation). This study may be particularly interesting for CARS imaging as the CARS signal is polarization dependent and for extending the technique to polarization fluorescence imaging. Secondly, a key issue in optical microscopy is how far inside a sample we can obtain a meaningful image. Thus, it would be interesting to study how the inhomogeneities of the sample deteriorate the property of the different proposed illumination schemes.

More specifically, in chapter one we have shown that RIM adapted to 3D-imaging is more efficient than the slice by slice reconstruction. 3D-RIM is now implemented in a fluorescence microscope adapted to biological applications at the CBI. However, the 3D-RIM reconstruction algorithm, and especially the 3D iterative deconvolution applied to each of the raw speckled images are time and memory consuming. For this code to be practical for applications requiring large FOVs, it would be necessary to optimize its speed and memory requirements.

In chapter two, we have shown that a focused speckle beam can generate a two-photon excitation volume with transverse and axial dimensions of a few microns. It would be great to implement this illumination scheme in a standard scanning 2PM and verify that it can indeed fasten the scanning of large samples (at the cost, of course, of a deterioration in the resolution).

In chapter three, we have proposed different temporal focusing schemes, the standard grating TF, the multi-order grating TF, the roughness TF and the roughness-grating TF. Here we did not verify experimentally the performances of the multi-order grating TF. Such experiments would permit to confirm our analytical model and our physical interpretation involving two (or more) pulses propagating in different directions. Also, to complete the theory, it would be interesting to model the Poynting vector of the multi-order grating TF to understand how the electromagnetic energy is flowing.

Last, in chapter four, we show how temporal focusing can be adapted to widefield

CARS imaging for providing optical sectioning. Our work dealt essentially with the modeling of an excitation intensity equal to the square intensity of the pump field times the intensity of the Stokes field. This simplified model was justified for a sample reduced to a thin homogeneous layer. If we want to do imaging with such an illumination scheme, it is necessary to develop a more complete model of the recorded signal that involves the space-variant non-linear susceptibility of the sample, along the line presented in (HEUKE et al. 2019). Also, TF-CARS has been studied with a simple grating TF scheme or a multi-order grating scheme. It could also be studied with the roughness-grating TF scheme. By providing more wavevectors in the illumination, this configuration may be more efficient for triggering the non-linear signal and should yield better resolved images (as seen in (FANTUZZI et al. 2023)). Last, the optically sectioned widefield approach that has been made possible with the proposed TF illumination schemes could be adapted to other non-linear contrasts such as Stimulated Raman Scattering or Second Harmonic Generation.

# Bibliographie


[Aff+23] Kévin AFFANNOUKOUÉ, Simon LABOUESSE, Guillaume MAIRE et al. « Super-resolved total internal reflection fluorescence microscopy using random illuminations ». In : *Optica* 10.8 (2023), p. 1009-1017 (cf. p. 25).

[ABR11] Esben Ravn ANDRESEN, Pascal BERTO et Hervé RIGNEAULT. « Stimulated Raman scattering microscopy by spectral focusing and fiber-generated soliton as Stokes pulse ». In : *Optics letters* 36.13 (2011), p. 2387-2389 (cf. p. 129).

[And+06] Esben Ravn ANDRESEN, Victoria BIRKEDAL, Jan THØGERSEN et al. « Tunable light source for coherent anti-Stokes Raman scattering microspectroscopy based on the soliton self-frequency shift ». In : *Optics letters* 31.9 (2006), p. 1328-1330 (cf. p. 129).

[Ber+12] Pascal BERTO, David GACHET, Pierre BON et al. « Wide-field vibrational phase imaging ». In : *Physical Review Letters* 109.9 (2012), p. 093902 (cf. p. 116).

[BPH98] Jörg BEWERSDORF, Rainer PICK et Stefan W HELL. « Multifocal multiphoton microscopy ». In : *Optics letters* 23.9 (1998), p. 655-657 (cf. p. 64).

[Che+02] Ji-Xin CHENG, Y Kevin JIA, Gengfeng ZHENG et al. « Laser-scanning coherent anti-Stokes Raman scattering microscopy and applications to cell biology ». In : *Biophysical journal* 83.1 (2002), p. 502-509 (cf. p. 116).

[Cho+13] Heejin CHOI, Elijah YS YEW, Bertan HALLACOGLU et al. « Improvement of axial resolution and contrast in temporally focused widefield two-photon microscopy with structured light illumination ». In : *Biomedical optics express* 4.7 (2013), p. 995-1005 (cf. p. 12, 22, 64).

[DSW90] Winfried DENK, James H STRICKLER et Watt W WEBB. « Two-photon laser scanning fluorescence microscopy ». In : *Science* 248.4951 (1990), p. 73-76 (cf. p. 44, 64).

[Der+09] Thomas DERTINGER, Ryan COLYER, Gopal IYER et al. « Fast, background-free, 3D super-resolution optical fluctuation imaging (SOFI) ». In : *Proceedings of the National Academy of Sciences* 106.52 (2009), p. 22287-22292 (cf. p. 24).

[DZX06] Michael E DURST, Guanghao ZHU et Chris XU. « Simultaneous spatial and temporal focusing for axial scanning ». In : *Optics express* 14.25 (2006), p. 12243-12254 (cf. p. 9, 12, 20, 21, 76).

[DZX08] Michael Earle DURST, G ZHU et C XU. « Simultaneous spatial and temporal focusing in nonlinear microscopy ». In : *Optics communications* 281.7 (2008), p. 1796-1805 (cf. p. 76).

[EX08] Conor L EVANS et X Sunney XIE. « Coherent anti-Stokes Raman scattering microscopy : chemical imaging for biology and medicine ». In : *Annu. Rev. Anal. Chem.* 1.1 (2008), p. 883-909 (cf. p. 116).

[Fan+23] Eric M FANTUZZI, Sandro HEUKE, Simon LABOUESSE et al. « Wide-field coherent anti-Stokes Raman scattering microscopy using random illuminations ». In : *Nature Photonics* 17.12 (2023), p. 1097-1104 (cf. p. 9, 13, 20, 22, 116, 143).

[Gir24] Guillaume GIROUSSENS. « Microscopie par éclairements aléatoires (RIM) : Nouvelles méthodes d'inversion et extensions ». Thèse de doct. Aix marseille université, 2024 (cf. p. 37, 38).

[Gir+24] Guillaume GIROUSSENS, Simon LABOUESSE, Marc ALLAIN et al. « Fast super-resolved reconstructions in fluorescence random illumination microscopy (RIM) ». In : *IEEE Transactions on Computational Imaging* (2024) (cf. p. 10, 20, 21, 25-27, 35).

[GG13] Israel GOHBERG et Seymour GOLDBERG. *Basic operator theory*. Birkhäuser, 2013 (cf. p. 26).

[Goo75] Joseph W GOODMAN. « Statistical properties of laser speckle patterns ». In : *Laser speckle and related phenomena*. Springer, 1975, p. 9-75 (cf. p. 25, 26).

[Goo85] Joseph W GOODMAN. « Statistical optics ». In : *New York, Wiley-Interscience, 1985, 567 p.* 1 (1985) (cf. p. 92).

[Goo07] Joseph W GOODMAN. *Speckle phenomena in optics : theory and applications*. Roberts et Company Publishers, 2007 (cf. p. 32).

[Gus00] Mats GL GUSTAFSSON. « Surpassing the lateral resolution limit by a factor of two using structured illumination microscopy ». In : *Journal of microscopy* 198.2 (2000), p. 82-87 (cf. p. 24).

[Gus+08] Mats GL GUSTAFSSON, Lin SHAO, Peter M CARLTON et al. « Three-dimensional resolution doubling in wide-field fluorescence microscopy by structured illumination ». In : *Biophysical journal* 94.12 (2008), p. 4957-4970 (cf. p. 9, 20).

[HBR04] Christoph HEINRICH, Stefan BERNET et Monika RITSCH-MARTE. « Wide-field coherent anti-Stokes Raman scattering microscopy ». In : *Applied physics letters* 84.5 (2004), p. 816-818 (cf. p. 13, 22, 116).

[HEZ04] Thomas HELLERER, Annika MK ENEJDER et Andreas ZUMBUSCH. « Spectral focusing : High spectral resolution spectroscopy with broad-bandwidth laser pulses ». In : *Applied Physics Letters* 85.1 (2004), p. 25-27 (cf. p. 129).

[HD05] Fritjof HELMCHEN et Winfried DENK. « Deep tissue two-photon microscopy ». In : *Nature methods* 2.12 (2005), p. 932-940 (cf. p. 44).

[Her+16] Oscar HERNANDEZ, Eirini PAPAGIAKOUMOU, Dimitrii TANESE et al. « Three-dimensional spatiotemporal focusing of holographic patterns ». In : *Nature communications* 7.1 (2016), p. 11928 (cf. p. 64).

[Heu+19] Sandro HEUKE, Kevin UNGER, Samira KHADIR et al. « Coherent anti-stokes Raman Fourier ptychography ». In : *Optics Express* 27.16 (2019), p. 23497-23514 (cf. p. 143).

[Idi+18] Jérôme IDIER, Simon LABOUESSE, Penhuan LIU et al. « On the super-resolution capacity of imagers using unknown speckle illuminations ». In : 4.1 (mars 2018), p. 87-98. DOI : 10.1109/TCI.2017.2771729 (cf. p. 25, 28).

[Im+05] Kang-Bin IM, Sumin HAN, Hwajoon PARK et al. « Simple high-speed confocal line-scanning microscope ». In : *Optics express* 13.13 (2005), p. 5151-5156 (cf. p. 8, 19).

[Lab+24] Simon LABOUESSE, Jérôme IDIER, Marc ALLAIN et al. « Superresolution capacity of variance-based stochastic fluorescence microscopy : From random illumination microscopy to superresolved optical fluctuation imaging ». In : *Physical Review A* 109.3 (2024), p. 033525 (cf. p. 25, 27).

[Lab+21] Simon LABOUESSE, Jérôme IDIER, Anne SENTENAC et al. « Random illumination microscopy from variance images ». In : *2020 28th European Signal Processing Conference (EUSIPCO)*. IEEE. 2021, p. 785-789 (cf. p. 27, 29).

[Lak06] Joseph R LAKOWICZ. *Principles of fluorescence spectroscopy*. Springer, 2006 (cf. p. 8, 19).

[Les+14] Ben LESHEM, O HERNANDEZ, E PAPAGIAKOUMOU et al. « When can temporally focused excitation be axially shifted by dispersion? » In : *Optics Express* 22.6 (2014), p. 7087-7098 (cf. p. 12, 22, 64).

[LGH24] Shulang LIN, Li GONG et Zhiwei HUANG. « Time-of-flight resolved stimulated Raman scattering microscopy using counter-propagating ultraslow Bessel light bullets generation ». In : *Light : Science & Applications* 13.1 (2024), p. 148 (cf. p. 140).

[MT65] PD MAKER et RW TERHUNE. « Study of optical effects due to an induced polarization third order in the electric field strength ». In : *Physical Review* 137.3A (1965), A801 (cf. p. 115).

[Man+21] Thomas MANGEAT, Simon LABOUESSE, Marc ALLAIN et al. « Super-resolved live-cell imaging using random illumination microscopy ». In : *Cell Reports Methods* 1.1 (2021) (cf. p. 9, 10, 20, 25, 36, 41).

[Maz+24] Lorry MAZZELLA, Thomas MANGEAT, Guillaume GIROUSSENS et al. « Extended-depth of field random illumination microscopy, EDF-RIM, provides super-resolved projective imaging ». In : *Light : Science & Applications* 13.1 (2024), p. 285 (cf. p. 25).

[Mer19] Jerome MERTZ. *Introduction to Optical Microscopy*. Juill. 2019. ISBN : 9781108428309. DOI : 10.1017/9781108552660 (cf. p. 45-47).

[Neg+18] Awoke NEGASH, Simon LABOUESSE, Patrick C CHAUMET et al. « Two-photon speckle illumination for super-resolution microscopy ». In : *Journal of the Optical Society of America A* 35.6 (2018), p. 1028-1033 (cf. p. 31).

[Oh+13] Joo-Eon OH, Young-Wook CHO, Giuliano SCARCELLI et al. « Sub-Rayleigh imaging via speckle illumination ». In : *Optics letters* 38.5 (2013), p. 682-684 (cf. p. 28).

[OS05] Dan ORON et Yaron SILBERBERG. « Harmonic generation with temporally focused ultrashort pulses ». In : *JOSA B* 22.12 (2005), p. 2660-2663 (cf. p. 9, 20).

[OTS05] Dan ORON, Eran TAL et Yaron SILBERBERG. « Scanningless depth-resolved microscopy ». In : *Optics express* 13.5 (mars 2005), p. 1468-1476. DOI : 10.1364/OPEX.13.001468 (cf. p. 12, 21, 64, 93).

[Ota+22] Keisuke OTA, Hiroyuki UWAMORI, Takahiro ODE et al. « Breaking trade-offs : Development of fast, high-resolution, wide-field two-photon microscopes to reveal the computational principles of the brain ». In : *Neuroscience Research* 179 (2022), p. 3-14. ISSN : 0168-0102. DOI : https://doi.org/10.1016/j.neures.2022.03.010. URL : https://www.sciencedirect.com/science/article/pii/S0168010222001079 (cf. p. 45).

[PL05] Christopher PALMER et Erwin G LOEWEN. « Diffraction grating handbook ». In : (2005) (cf. p. 67).

[Pap+09] Eirini PAPAGIAKOUMOU, Vincent DE SARS, Valentina EMILIANI et al. « Temporal focusing with spatially modulated excitation ». In : *Optics express* 17.7 (2009), p. 5391-5401 (cf. p. 64).

[Pap+08] Eirini PAPAGIAKOUMOU, Vincent DE SARS, Dan ORON et al. « Patterned two-photon illumination by spatiotemporal shaping of ultrashort pulses ». In : *Optics Express* 16.26 (2008), p. 22039-22047 (cf. p. 64).

[PRE20] Eirini PAPAGIAKOUMOU, Emiliano RONZITTI et Valentina EMILIANI. « Scanless two-photon excitation with temporal focusing ». In : *Nature Methods* 17.6 (2020), p. 571-581 (cf. p. 9, 20, 45).

[Paw06] James PAWLEY. *Handbook of biological confocal microscopy*. T. 236. Springer Science & Business Media, 2006 (cf. p. 8, 19).

[Rub04] Michael RUBART. « Two-photon microscopy of cells and tissue ». In : *Circulation research* 95.12 (2004), p. 1154-1166 (cf. p. 44).

[Sit+22] Luca SITÀ, Marco BRONDI, Pedro LAGOMARSINO DE LEON ROIG et al. « A deep-learning approach for online cell identification and trace extraction in functional two-photon calcium imaging ». In : *Nature Communications* 13.1 (2022), p. 1529 (cf. p. 45).

[Sof+16] Nicholas James SOFRONIEW, Daniel FLICKINGER, Jonathan KING et al. « A large field of view two-photon mesoscope with subcellular resolution for in vivo imaging ». In : *elife* 5 (2016), e14472 (cf. p. 45).

[Ste+21] Ernst HK STELZER, Frederic STROBL, Bo-Jui CHANG et al. « Light sheet fluorescence microscopy ». In : *Nature Reviews Methods Primers* 1.1 (2021), p. 73 (cf. p. 9, 20).

[SY06] Karel SVOBODA et Ryohei YASUDA. « Principles of two-photon excitation microscopy and its applications to neuroscience ». In : *Neuron* 50.6 (2006), p. 823-839 (cf. p. 44).

[Ter+18] Shin-Ichiro TERADA, Kenta KOBAYASHI, Masamichi OHKURA et al. « Super-wide-field two-photon imaging with a micro-optical device moving in post-objective space ». In : *Nature communications* 9.1 (2018), p. 3550 (cf. p. 45).

[The+05] Patrick THEER, Bernd KUHN, Dorine KEUSTERS et al. « Two-photon microscopy and imaging ». In : *Neurobiology* 77 (2005), p. 5-2 (cf. p. 45).

[Toy+07] I TOYTMAN, K COHN, T SMITH et al. « Wide-field coherent anti-Stokes Raman scattering microscopy with non-phase-matching illumination ». In : *Optics letters* 32.13 (2007), p. 1941-1943 (cf. p. 116).

[Tsa+15] Philbert S TSAI, Celine MATEO, Jeffrey J FIELD et al. « Ultra-large field-of-view two-photon microscopy ». In : *Optics express* 23.11 (2015), p. 13833-13847 (cf. p. 45).

[Val02] B VALEUR. *Molecular Fluorescence : Principles and Applications*. 2002 (cf. p. 8, 19).

[VM05] Cathie VENTALON et Jerome MERTZ. « Quasi-confocal fluorescence sectioning with dynamic speckle illumination ». In : *Optics letters* 30.24 (2005), p. 3350-3352 (cf. p. 9, 20, 28).

[Wol+17] Sébastien WOLF, Alexis M DUBREUIL, Tommaso BERTONI et al. « Sensorimotor computation underlying phototaxis in zebrafish ». In : *Nature communications* 8.1 (2017), p. 651 (cf. p. 45).

[YSS13] Elijah YS YEW, Colin JR SHEPPARD et Peter TC SO. « Temporally focused wide-field two-photon microscopy : Paraxial to vectorial ». In : *Optics express* 21.10 (2013), p. 12951-12963 (cf. p. 64).

[Zhu+05] Guanghao ZHU, James VAN HOWE, Michael DURST et al. « Simultaneous spatial and temporal focusing of femtosecond pulses ». In : *Optics express* 13.6 (2005), p. 2153-2159 (cf. p. 12, 21, 64).

[ZHX99] Andreas ZUMBUSCH, Gary R HOLTOM et X Sunney XIE. « Three-dimensional vibrational imaging by coherent anti-Stokes Raman scattering ». In : *Physical review letters* 82.20 (1999), p. 4142 (cf. p. 13, 22, 116).